eXPRESS Polymer Letters Vol.5, No.10 (2011) 838
Available online at www.expresspolymlett.com
DOI: 10.3144/expresspolymlett.2011.82

Editorial corner – a personal view
Recycling of thermoset structural composites: Would textile technology bring a high added-value solution?

*P. Krawczak**

Department of Polymers and Composites Technology & Mechanical Engineering, Ecole des Mines de Douai, 941 rue Charles Bourseul, BP 10838, 59508 Douai, France

Substantial amounts of composite end-of-life and manufacturing waste are still being landfilled or incinerated. Most of them are made of long or endless glass or carbon fibres and cross-linked thermosetting resin matrices, which are not easily recycled and remoulded. Recent changes to waste management legislation are however powerful drivers to identify more environmental friendly and economically viable recycling routes for such thermoset composites.

Many attempts have been made over the past twenty years to develop recycling processes (mechanical grinding, different variants of pyrolysis, cement kiln route, solvolysis …) and seek ways of cost-effectively using recycled material (glass or carbon fibres, resin chemicals) in various applications (moulding compounds for automotive and sanitary ware, concrete and rubber compounds for the construction industry, ceramic composites for friction applications).

In spite of the huge research efforts, the industrial achievements are globally disappointing up to now as far as closed-loop recycling of structural composites (i.e. high performance unidirectional or textile composites) is concerned. Indeed, one should keep in mind that the glass or carbon fiber reinforcement has potentially the most recoverable value in a structural composite, and that fiber length and fiber alignment are key features in composites design. That means that mechanical grinding, which dramatically reduces the fiber aspect ratio and cannot preserve continuous fibers, and further re-use as random compounds are obviously inappropriate in the case of structural composites.

Textile technology may bring a solution to overcome this problem. Patented textile technologies already allow manufacturing from dry fibre waste (selvedges, offcuts …) high added-value aligned fibre products such as veils, tapes or continuous yarns which could be re-used to form fabrics. However, glass or carbon fibres recovered by pyrolysis or solvolysis are more challenging to process that way because contrary to dry fibres (i) they do not retain the sizing applied to the virgin fibres at manufacture and would require further surface treatment; (ii) they are not fully 'clean', polluting residues or small resin pieces being possibly still attached to their surface; (iii) their mechanical properties (strength, modulus) may be significantly reduced in some cases (e.g. if recovered by pyrolysis). Current research programmes address these issues. If successful, then a closed-loop recycling route for such high-performance composites will emerge.

Prof. Dr. Patricia Krawczak
Member of International Advisory Board

*Corresponding author, e-mail: patricia.krawczak@mines-douai.fr

eXPRESS Polymer Letters Vol.5, No.10 (2011) 839–848
Available online at www.expresspolymlett.com
DOI: 10.3144/expresspolymlett.2011.83

Lower critical solution temperature *versus* volume phase transition temperature in thermoresponsive drug delivery systems

M. Constantin[1], *M. Cristea*[1], *P. Ascenzi*[2], *G. Fundueanu*[1,3*]

[1]Department of Bioactive and Biocompatible Polymers, 'Petru Poni' Institute of Macromolecular Chemistry, 700487 Iassy, Romania
[2]Department of Biology and Interdepartmental Laboratory for Electron Microscopy University Roma Tre, I-00146 Roma, Italy
[3]Department of Pharmaceutical Sciences, University of Ferrara, I-44100 Ferrara, Italy

Received 20 January 2011; accepted in revised form 28 March 2011

Abstract. One of the most subtle problem in the characterization of thermoresponsive polymers is the evaluation of the relationship between the lower critical solution temperature (LCST) of the linear polymer and the volume phase transition temperature (VPTT) of the corresponding hydrogel. Here, the LCST and the onset temperature of linear poly(N-isopropylacrylamide-co-N-hydroxymethyl acrylamide) has been determined under pseudo-physiological conditions by cloud point (CP) measurements and by microcalorimetric analysis. The LCSTs, as well as the onset temperatures, determined by the CP method, decrease with increasing the concentration of the polymer solution. On the contrary, microcalorimetric analyses give almost the same values for LCSTs and the onset temperatures regardless of polymer concentration. The VPTT of the hydrogel, determined by the blue dextran method, was found to be closely similar to the LCST of the concentrated polymer solution (10%, w/v), determined by the CP method. In fact, the hydrogel could be considered as a concentrated polymer solution whose concentration could be related to the amount of water retained by the hydrogel. Hydrogel microspheres have been also reported to release diclofenac, a drug model system, in a pulsating way at temperatures slightly below and above the VPTT.

Keywords: *smart polymers, thermoresponsive hydrogels, lower critical solution temperature, volume phase transition temperature, cloud point*

1. Introduction

In the last decades, much attention has been focused on thermoresponsive drug delivery systems [1–3]. Indeed, temperature variations trigger changes of the polymer configuration, leading to the modulation of the release rate of incorporated drugs. Poly(N-isopropylacrylamide) (poly(NIPAAm)) is the most relevant thermoresponsive polymer for biomedical applications, because it possesses a sharp phase transition or a lower critical solution temperature (LCST) around 32ºC in aqueous solutions [4, 5]. Below the LCST, the polymer is in the hydrated state and therefore it is soluble. Above the LCST, the polymer is dehydrated, becomes hydrophobic, and precipitates. Accordingly, the cross-linked hydrogels obtained from this polymer swell under the critical temperature and collapse above it. The critical temperature of the hydrogel is called volume phase transition temperature (VPTT) and it is often confused with the LCST [6, 7]. For determining the LCST of linear thermoresponsive polymer, the cloud point (CP) method is used to determine

*Corresponding author, e-mail: ghefun@icmpp.ro

the CP value [8], and the differential scanning calorimetry analysis applies to obtain the endothermic transition peak [9].

Usually, the concentration of the polymer solution used for the determination of the LCST value by calorimetric and absorbance studies is low (0.5–1%, w/v) [10, 11]. The LCST value determined at low concentration is then taken as the VPTT of the hydrogel, although the physical and chemical cross-linked hydrogels used in biomedical applications are prepared starting from high concentrated polymer solutions (5–10%, w/v) [11, 12]. Moreover, cross-linked hydrogels in the swollen state could be considered as a concentrated polymer solution related to the amount of water retained by the hydrogel.

The VPTT values of thermoresponsive hydrogels are generally determined by the equilibrium swelling ratio method [13, 14]. Hydrogels (most in the form of discs or slabs) are weighed and allowed to reach their equilibrium swelling state at different temperatures. Then, the hydrogels are taken out from the solvent and the excess of solvent present on their surface is removed by blotting with filter paper. However, this method, that allows to determine the water retained at different temperatures, is unreliable since the gel is taken out at room temperature and tapped for a random time with a filter paper or laboratory tissue [15, 16]. Moreover, in the case of microspheres, this method gives wrong results, since it is not possible to discriminate between the water that is present in the microspheres and the water present between the microspheres.

On the basis of these considerations, the main purpose of this paper is to evaluate the correspondence between the LCST values of the polymer solutions at different concentrations and the VPTT values of the corresponding hydrogels. Firstly, we synthesized the poly(N-isopropylacrylamide-co-N-hydroxymethyl acrylamide) (poly(NIPAAm-co-HMAAm)) copolymer with a LCST value (under physiological conditions) closely similar to the body temperature. Secondly, we studied the influence of the solution concentration on the LCST value by DSC and CP methods. Thirdly, the linear thermoresponsive polymer was transformed in cross-linked hydrogel microspheres, and the VPTT was determined by the blue dextran method and compared with the LCST value. Finally, the release of diclofenac, a drug model system, at temperatures situated slightly below and above the VPTT was investigated.

2. Materials and methods

2.1. Materials

N-isopropylacrylamide (NIPAAm) (from Sigma-Aldrich Chemical Co., Milwaukee, WI, USA) was re-crystallized with hexane. The N-hydroxymethylacrylamide (HMAAm) aqueous solution (48 wt%), the glutaraldehyde (GA) aqueous solution (25%, w/v), 1,4-dioxane, and N,N'-azobisisobutyronitrile (AIBN) were supplied from Fluka AG (Buchs, Switzerland). 1,4-Dioxane was purified by refluxing and AIBN was purified in methanol. Light mineral oil (d = 0.84 g·ml^{-1}) and diclofenac (Na form) were purchased from Sigma-Aldrich Chemical Co. (St Louis, MO, USA). Blue dextran (BD) was provided from Pharmacia (Uppsala, Sweden). All the other chemicals were from Fluka AG (Buchs, Switzerland). All chemicals were of the highest analytical grade.

2.2 Synthesis of poly(NIPAAm-co-HMAAm)

Synthesis of linear poly(NIPAAm-co-HMAAm)) was carried out by free radical copolymerization in 1,4-dioxane with AIBN as the initiator. Typically, 1.13 g of NIPAAm (10 mmol), 0.4 ml of HMAAm (2 mmol) and 0.010 g AIBN were solubilized in 12 ml of 1,4-dioxane. Dried nitrogen was bubbled through the solution for 30 min. prior to polymerization. The reaction mixture was allowed to react at 70°C for 16 hours. The polymer was precipitated into diethyl ether, and dried under vacuum. Finally, the copolymer was solubilized in distilled water, dialyzed for 7 days at 22°C (molecular weight cut off 10 000–12,000 Da; from Medi Cell International, England), and recovered by freeze-drying.

2.3. Copolymer composition

The copolymer composition was determined by ^{1}H NMR analysis. ^{1}H NMR spectra of poly (NIPAAm-co-HMAAm) were recorded in D_2O on a Varian Mercury Plus 400/Varian VXR 200 spectrometer operating at the frequency of 400 MHz. The molar fraction of HMAAm in poly(NIPAAm-co-HMAAm) was calculated according to Equation (1):

$$3\,\text{HMAAm} = (3\,\text{HMAAm} + 3\,\text{NIPAAm} + 6\,\text{NIPAAm}) - Y \cdot 9\,\text{NIPAAm} \quad (1)$$

where Y is the molar fraction of NIPAAm calculated as the area of the methynic proton at 3.91 ppm, and (3 MAAm + 3 NIPAAm + 6 NIPAAm) is the total area of the peaks between 0.5 and 2.5 ppm, corresponding to the main backbone protons (3 HMAAm + 3 NIPAAm) and the NIPAAm methylenic protons (6 NIPAAm).

2.4. Determination of the molecular weight of poly(NIPAAm-co-NHMAAm)

The number-average (M_n) and weight-average (M_w) molecular weight of poly(NIPAAm-co-HMAAm) were determined by GPC using an instrument GPC-PL-EMD 950 from Polymer Laboratories (Shropshire, UK) (in dimethylformamide at 120°C, the flow rate was 0.7 ml/min). Calibration was carried out with monodisperse polystyrene standards.

2.5. LCST determination

LCST was determined from the absorbance at 450 nm measured against temperature using an UV-Vis spectrophotometer coupled with a temperature controller. The polymer solution was prepared in standard phosphate buffer (pH = 7.4, 50 mM Na_2HPO_4 and NaOH) (PB). The heating rate was 0.2°C every 10 minutes. CP was defined as the temperature corresponding to the absorbance value of 0.5 of the curve of the absorbance versus temperature. The onset temperature was defined as the temperature at which the first signs of turbidity occurred.

Microcalorimetric analyses were performed in PB with a DSC III microcalorimeter (Setaram, Caluire, France) at a heating rate of 0.5°C/min, under nitrogen. The transition temperature was defined as the temperature corresponding to the peak of the thermogram. The onset temperature was determined from crossing of the baseline with the leading edge of the endotherm.

2.6. Microsphere preparation

Typically, 1 g copolymer was solubilized in 10 ml distilled water, at 22°C. Then, 0.4 ml of 0.5 M H_2SO_4 and 0.5 ml of 25% GA (w/v) were added just before dispersion of the aqueous copolymer solution in the dispersion phase. The continuous phase consists in 100 ml light mineral oil containing 0.5 g soybean lecitin, as the dispersing agent. The mixture was stirred at 350 rpm by a three-blade turbine impeller. The reaction temperature was fixed below the LCST of the polymer solution (34°C); the reaction time was 24 hours. Finally, cross-linked microspheres were washed successively with diethyl ether, methanol, water, methanol, and dried diethyl ether.

2.7. Morphological and dimensional analysis of the microspheres

The morphology of the microspheres was evaluated by scanning electron microscopy (SEM) (ESEM, type Quanta 200, Netherlands) and by optical microscopy using an inverted microscope (Nikon Diaphot, Tokyo, Japan) equipped with a digital camera. The mean diameter of the microspheres was determined on digital photomicrographs, considering at least 100 microspheres for each sample. The analysis was performed by the computerized size analysis system NIH image.

2.8. Volume phase transition temperature

The volume phase transition temperature (VPTT) corresponded to the inflexion point of the curve of PB retention as a function of temperature. The PB retention values at different temperatures were determined by the BD approach based on the solute exclusion technique at equilibrium [17]. In a closed vial, 200 mg of dried microspheres were soaked in 10 ml of PB containing BD (2 mg/ml). After reaching equilibrium (24 hours), 0.5 ml of the solution were picked up and the BD content was assayed by UV-Vis spectrophotometry, at 618 nm. The PB retention (PB_R) values were determined according to Equation (2):

$$\mathbf{PB_R}[\mathbf{ml \cdot g^{-1}}] = V_i(C_e - C_i) \cdot \frac{5}{C_e} \quad (2)$$

where V_i is the initial volume of the BD solution [ml], C_i is the initial concentration of BD [mg/ml], and C_e is the BD concentration at equilibrium, in the presence of microspheres [mg/ml].

2.9. Drug loading

Drug-loaded microspheres were prepared by soaking 100 mg dried microspheres in 4 ml of ethanol containing diclofenac (2.5 mg/ml). After the complete evaporation of the solvent at 22±2°C, the

microspheres were washed with 10 ml of diethyl ether and dried under vacuum at room temperature. The amount of the retained drug, per mg of dried microspheres, was determined by solubilization of the entrapped drug in ethanol. The amount of the drug in the filtrate was determined after microsphere isolation by UV-Vis spectroscopy, using a previously made calibration curve.

2.10. *In vitro* drug release kinetics

In vitro drug release kinetic studies were performed (under thermal cycling operation), at different temperatures, by soaking an appropriate amount of loaded microspheres in 50 ml of PB solution under gentle stirring. At regular time intervals, aliquots of the released medium were withdrawn and the drug content was determined spectrophotometrically. The same volume of the released medium was added to replace the volume of the extracted samples.

3. Results and discussion

3.1. Preparation and characterization of the thermoresponsive copolymer

The biomedical applications of thermoresponsive polymers are achievable when the polymers possess a phase transition corresponding approximately to the human body temperature. Moreover, the thermal transition should be sharp when very small variations of temperature occur below and above the LCST. As it is well known, poly(NIPAAm) exhibits a LCST value at 32ºC in aqueous solution [4, 5]. Under pseudo-physiological conditions (PB at pH 7.4) the LCST decreases to lower temperatures [12]. In order to increase the LCST towards body temperature, NIPAAm is usually copolymerized with hydrophilic monomers [18, 19]. Here, HMAAm was selected to be copolymerized with NIPAAm. Note that the presence of HMAAm in the copolymer does not affect the acrylamide sequence of NIPAAM, which is responsible for thermorespon-

Table 1. Effect of the co-monomer ratio in the feed and in the copolymer on the LCST determined by the CP method under pseudo-physiological conditions (PB at pH 7.4). The concentration of the copolymer was 10%, w/v

Sample	Co-monomer composition				LCST [°C] In PB
	In the feed · 10^{-3} M [% molar ratio]		In the co-polymer [% molar ratio]		
	NIPAAm	HMAAm	NIPAAm	HMAAm	
TP_0	10	0.0	100	0.0	28.8±0.1
TP_1	10	1.0	n.d.[a]	n.d.	32.1±0.2
TP_2	10 (86.96)	1.5 (13.04)	86.18	13.82	34.5±0.2
TP_3[b]	10 (83.34)	2.0 (16.66)	82.87	17.13	36.8±0.2

Data are the results of three independent experiments.
[a]n.d. = not determined
[b]M_n = 21 200, M_w = 76 400, IP = 3.60, IP = index of polydispersity

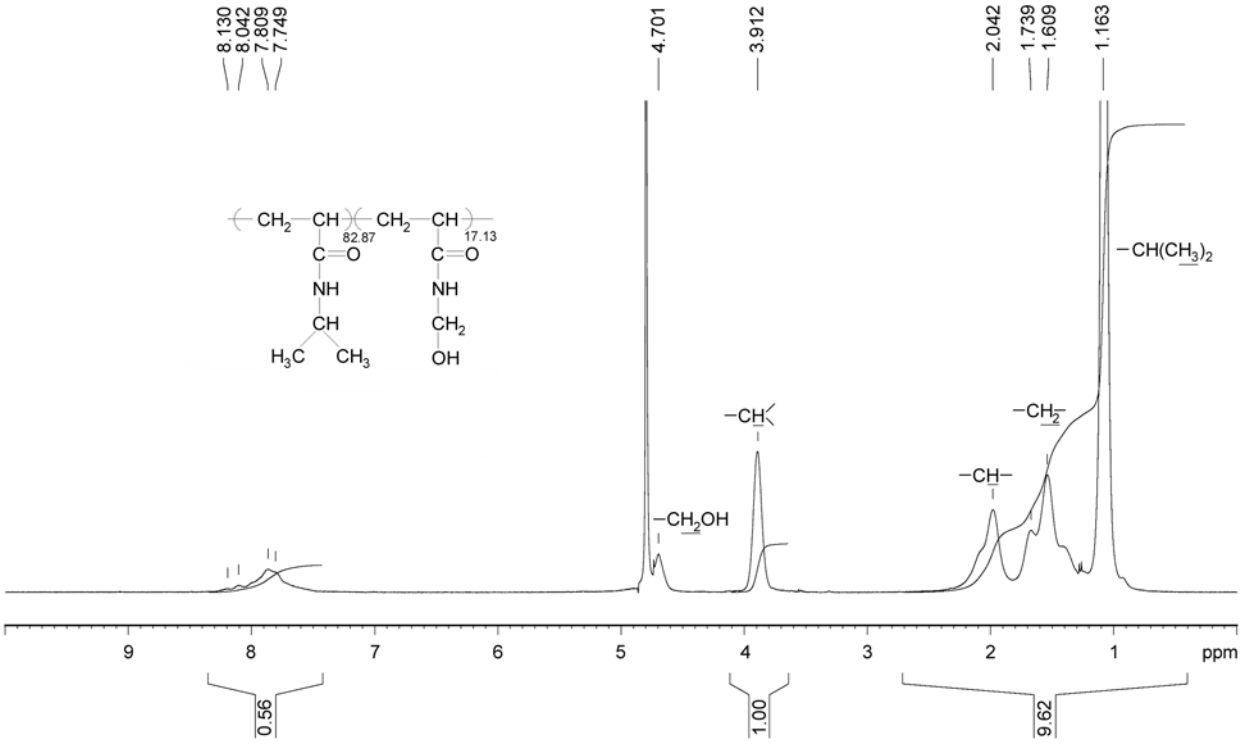

Figure 1. ^{1}H NMR spectrum of poly(NIPAAm-co-HMAAm) (sample TP_3 in Table 1)

sibility. In addition, HMAAm possesses hydroxyl groups which undergo easily to cross-linking.

As reported in Table 1 and proven by ^{1}H NMR spectra (Figure 1), the copolymer formation and the percentage of the co-monomers in the copolymer correspond approximately to those observed in the feed. It should be noted that increasing the HMAAm content of the copolymer, the LCST value increases, however it shows a sharp phase transition. The copolymer containing an initial 10/2 NIPAAm/HMAAm co-monomer molar ratio (sample TP3) possesses a LCST value of 36.8°C corresponding to the human body temperature.

3.2. Influence of the polymer concentration on LCST

Generally, the LCST value of the hydrogels is determined by the CP method at low polymer concentration (0.5–1%) [10, 11], this value is then assumed to correspond to that of the hydrogels. However, the chemically cross-linked hydrogels are prepared from highly concentrated polymer solution (5–10%) [11, 12]. Moreover, hydrogels could be considered as concentrated polymer solutions whose concentration could correspond approximately to the amount of the retained water. Therefore, from both the theoretical and practical viewpoints, the influence of the concentration of the polymer solution on the LCST value under pseudo-physiological conditions must be determined. As shown in Table 2, the LCST value of linear poly (NIPAAm-co-HMAAm) determined by CP measurements decreases as the concentration of the polymer increases.

However, in a highly concentrated solution, the solution opalescence is more accentuated than in a diluted solution. Since this discrepancy could affect the exact determination of LCST, we considered also the onset points which correspond to the first opaqueness that appeared in the solution (Table 3). In addition, the influence of polymer concentration on LCST was determined by the DSC technique (Figure 2).

The onset temperature determined by the CP method decreases on increasing the polymer concentration. In contrast, the LCST values and the onset points determined by the calorimetric method seem to be unaffected by the polymer concentration (see Tables 2 and 3). In fact, the calorimetric technique gives information on the heat released from the cleavage of hydrogen bonds between the water solvent and the polymer [20]. Therefore, it is expected that dehydration occurs at the same temperatures regardless of the polymer concentration, while the CP method detects the clouding of the solution due to the hydrophobic interactions between the polymer chains [21]. Obviously, hydrophobic interac-

Table 2. Effect of the polymer concentration on the LCST as determined by the CP method[a]

Sample	LCST [°C] at different copolymer concentration [%, w/v]					
	0.25	**0.5**	**1**	**3**	**5**	**10**
TP_0	30.8	30.6	30.3	29.5	29.1	28.8
TP_2	36.8	36.5	36.1	35.4	35.1	34.5
TP_3	39.4 (n.d.)[b]	38.6 (40.3)[c]	38.1 (40.25)	37.7 (39.9)	37.3 (n.d.)	36.8 (39.66)

[a]Data are the results of three independent experiments, standard deviation ±0.15°C
[b]n.d., not determined
[c]Data between brackets were determined by the calorimetric method

Table 3. Effect of the polymer concentration on the onset temperature as determined by the CP method[a]

Sample	Onset temperature [°C] at different copolymer concentration [%, w/v]					
	0.25	**0.5**	**1**	**3**	**5**	**10**
TP_0	30.7	30.3	29.9	29.3	28.9	28.6
TP_2	36.3	36.1	35.6	35.1	34.7	33.9
TP_3	38.0 (n.d.)[b]	37.8 (35.75)[c]	37.6 (36.3)	37.2 (35.8)	36.8 (n.d.)	36.5 (35.94)

[a]Data are the results of three independent experiments, standard deviation ±0.15°C
[b]n.d., not determined
[c]Data between brackets were determined by the calorimetric method

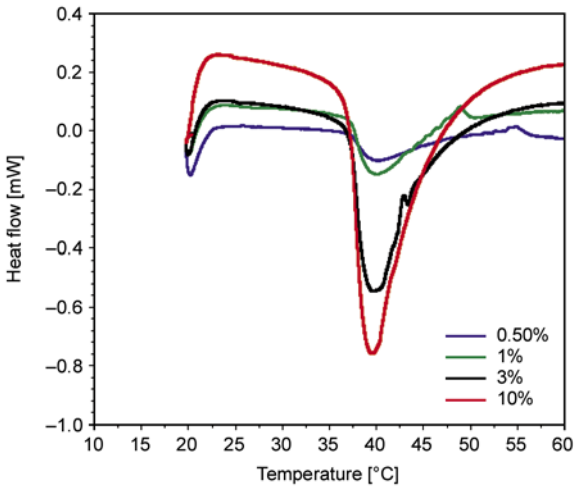

Figure 2. DSC thermograms of the poly(NIPAAm-co-HMAAm) solution (sample TP_3 in Table 1) in phosphate buffer at pH 7.4 at different concentrations. The scanning rate was 0.5°C·min^{-1}

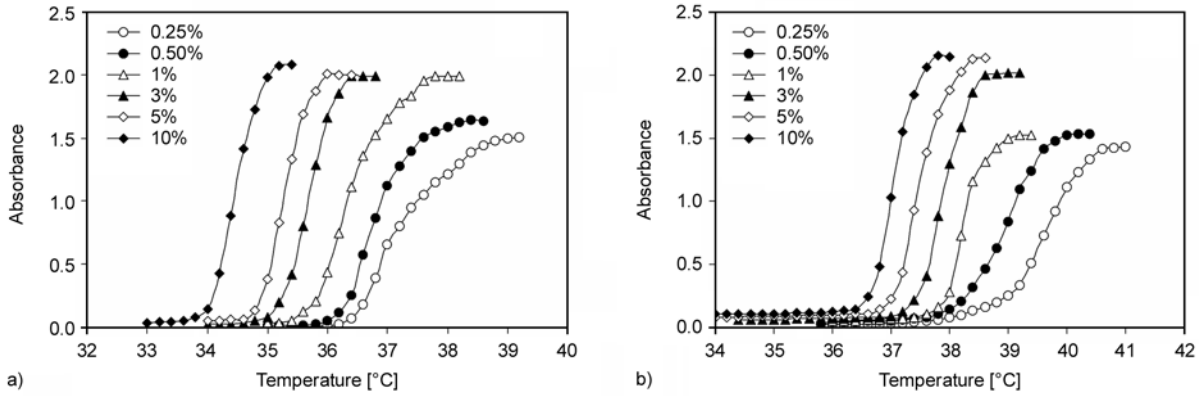

Figure 3. LCST profile of poly(NIPAAm-co-HMAAm) (sample TP_2, Panel a; sample TP_3, Panel b) dissolved in PB (pH 7.4), at different polymer concentrations (0.25%, open circles; 0.5% filled circles; 1%, open triangles; 3%, filled triangles; 5%, open diamonds, and 10%, filled diamonds)

tions are faster in a highly concentrated solution, and therefore the phase transition appears to be sharper at high polymer concentration (Figure 3a, b). In conclusion, the CP method is a more reliable technique since highlights the dehydration and the hydrophobic interactions of the polymer chains, giving information at the macroscopic level.

3.3. Preparation and characterization of thermoresponsive microspheres

Spherical poly(NIPAAm-co-HMAAm) microparticles with a mean diameter of 102 μm (Figure 4a) were prepared from preformed polymers (TP_3) by cross-linking the –OH groups of HMAAm with GA, under acidic conditions [22].

Microspheres were prepared at a temperature as high as possible, but lower than the LCST. Preliminarily, the value of the LCST of the polymer solution (= 38.5º) was determined by CP method under the same preparation conditions (i.e. in the presence of H_2SO_4 and GA). After cross-linking at a temperature below the LCST (= 34ºC), the microspheres still retain the thermoresponsive properties of the linear copolymer (Figure 4 b, c).

However, the most important question rising here concerns the coincidence of the VPTT value of the microspheres with the LCST value of the linear polymer. The VPTT of the hydrogel was determined by measuring the amount of PB retention at different temperatures. The PB retention of the microspheres was determined by an accurate method based on solute exclusion at equilibrium [17]. This method is based on measuring the increase of the BD concentration in supernatant, which occurs when dried microspheres are added to a solution of BD. Therefore, the temperature dependence of the PB retention was monitored (Figure 5). A decrease of the PB retention was observed even at temperatures lower than those of the onset points. This behavior is somewhat unexpected since no influence of temperature on the dehydration process was previously reported for the linear polymer under peak onset values when determined by calorimetric studies (Figure 2).

Nevertheless, the decrease of the PB retention profile is discontinuous around 36.5ºC, corresponding to the VPTT of the hydrogel microspheres. This value is closely similar to the LCST value of the linear polymer at the polymer concentration of 10% (w/v) as determined by the CP method (sample TP_3 in Table 2). Note that the volume of PB retained by the hydrogel microspheres at 22ºC is 11.2 ml/g, and corresponds approximately to the concentration of the polymer solution that displays the LCST value of 36.8ºC. In conclusion, the VPTT of the hydrogel is in agreement with the LCST value of the polymer solution at the concentration corresponding to the amount of PB retained by the hydrogel.

Conflicting data are reported in the literature concerning the relationships between the phase transition of the linear polymers and the hydrogels. Some authors report that both the transition temperature and the heat of collapse of the poly(NIPAAm) gel show similar values to those of the poly(NIPAAm) solutions [23]. Other authors report that the transition temperature of poly(NIPAAm) gels is slightly higher (1–2ºC) than that of the linear polymer solutions [24, 25]. This difference in the transition tem-

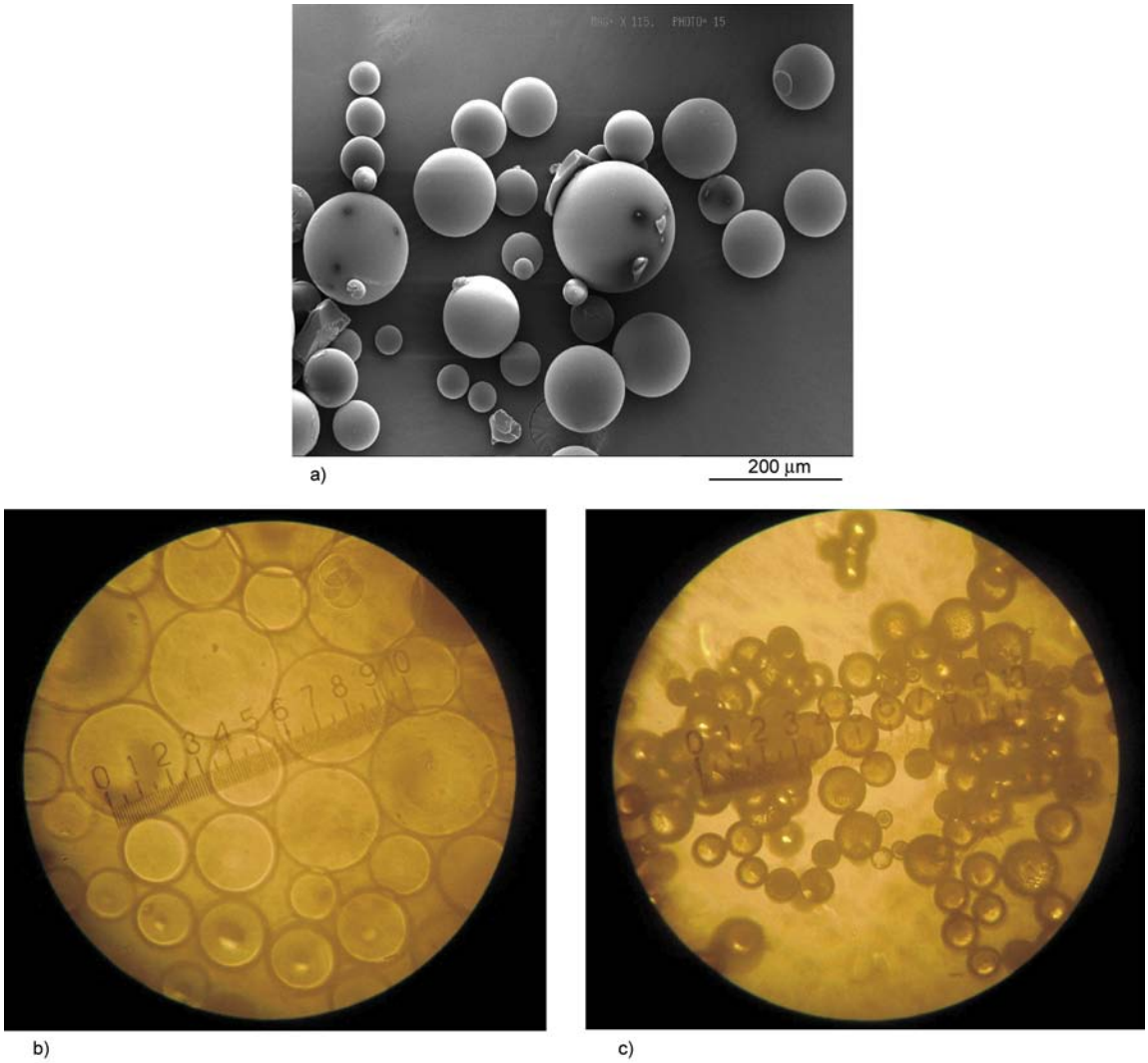

Figure 4. Scanning electron micrographs of poly(NIPAAm-co-HMAAm) microspheres (Panel a). Optical photomicrographs of thermoresponsive microspheres taken in the swollen state in water below the VPTT value at 35ºC (Panel b) and above the VPTT value at 38ºC (Panel c). The bar corresponds to 200 µm in Panel a, and 500 µm in Panels b and c.

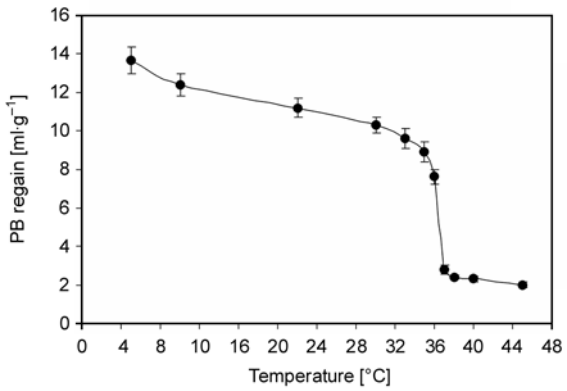

Figure 5. Effect of temperature on the PB retention by cross-linked thermoresponsive microspheres under physiological conditions. All values are the mean of three independent measurements ± SD.

perature could be explained by the reduced 'mobility' of the polymer chains in a cross-linked network. We agree with the last interpretation; however, when the cross-linking degree is enough low, its influence is negligible.

3.4. Drug loading and release studies

The release of drugs by thermal cycling was performed for most of thermoresponsive hydrogels at temperatures far below and above the LCST of the linear polymer (i.e., 25 and 40ºC) [26, 27]. The reason is to be sure that these temperatures are also situated below and above the VPTT of the hydrogel, which in fact, is not known. However, biomedical applications of the hydrogels are only possible when

the volume changes take place at temperatures slightly higher and lower than the VPTT. On the basis of these considerations, we studied the release of diclofenac from thermoresponsive microspheres at 35 and 38ºC, i.e. at temperatures closely near the VPTT (= 36.5°C) (Figure 6).

Previously, diclofenac, used as low molecular weight model drug, was loaded in thermoresponsive microspheres by the solvent evaporation method. This process was performed in ethanol since diclofenac displays a good solubility in this solvent and the thermoresponsive microspheres possess a high swelling degree in ethanol (swollen volume/dried volume = 17.9). Following this procedure, a high encapsulation efficiency (95.4±3%) was obtained, in fact almost the entire amount of the drug from solution is forced to diffuse into the microspheres during ethanol evaporation. The entrapped drug is molecularly dispersed in the network of the microspheres as proved by the absence of any fusion peak of the drug crystals in the DSC thermogram of loaded microspheres (data not shown). The release rate of diclofenac is mainly determined by diffusion of the drug through the pores of the microsphere matrix. Below the VPTT value (i.e., at 35ºC), the hydrogel microspheres are in the swollen state and no steric interaction between the drug and the microsphere matrix takes place; therefore, the release rate of the drug is high. On the contrary, when the temperature is raised above the VPTT (i.e., at 38ºC), the microsphere matrix is in a collapsed state and the diffusion of the drug is impaired. Moreover, additional hydrophobic interactions between the drug and the polymer network occur; accordingly, the release rate is dramatically reduced. Finally, a pulsating drug release was achieved under thermal cycling between 35 and 38ºC.

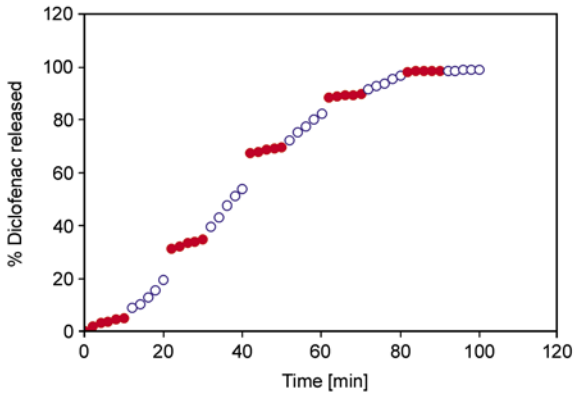

Figure 6. Effect of temperature cycling (35°C (○) and 38°C (●)) on diclofenac release from poly (NIPAAm-co-HMAAm) microspheres in phosphate buffer at pH 7.4

Notably, a fraction of the drug is expelled during the shrinkage of the microsphere matrix, when the temperature increases above the VPTT. This suggests the presence of the dissolved drug in the swollen hydrogel. Such drug fraction is mechanically squeezed out from the system when the hydrogel network collapsed.

4. Conclusions

Poly(NIPAAm-co-HMAAm)) was synthesized both as a thermoresponsive linear polymer and as cross-linked hydrogel microspheres. The LCST value, determined by the CP method, strongly depends to the polymer solution concentration. On the contrary, the LCST value determined by the calorimetric method is unaffected by the polymer concentration. The CP method was found to be a more reliable technique to characterize a hydrogel because takes in consideration both the dehydration and hydrophobic interactions of polymer chains, giving information at macroscopic level. The VPTT value of the hydrogel agrees with the LCST value of the polymer solution at the concentration corresponding to that of PB retained by the hydrogel. The pulsating release of diclofenac under thermal cycling operation at temperatures slightly below and above the VPTT, here determined, confirmed that the phase transition temperature of the hydrogel is well determined.

Abbreviations

AIBN	N,N'-azobisisobutyronitrile
BD	blue dextran
CP	cloud point
GA	glutaraldehyde
HMAAm	N-hydroxymethylacrylamide
LCST	lower critical solution temperature
NIPAAm	N-isopropylacrylamide
PB	phosphate buffer
poly(NIPAAm)	poly(N-isopropylacrylamide)
poly(NIPAAm-co-HMAAm	poly(N-isopropylacrylamide-co-N-hydroxymethyl acrylamide)
SEM	scanning electron microscopy
VPTT	volume phase transition temperature

Acknowledgements

This work was supported by CNCSIS –UEFISCSU, project number 644/19.01.2009, PNII – IDEI code 989/2008. M. Constantin acknowledges the financial support of European Social Fund – 'Cristofor I. Simionescu' Postdoctoral Fellowship Programme (ID POSDRU/89/1.5/S/55216), Sectoral Operational Programme Human Resources Development 2007 – 2013.

References

[1] Bae Y. H., Okano T., Hsu R., Kim S. W.: Thermo-sensitive polymers as on-off switches for drug release. Die Makromolekulare Chemie, Rapid Communications, **8**, 481–485 (1987).
DOI: 10.1002/marc.1987.030081002

[2] Jeong B., Bae Y. H., Lee D. S., Kim S. W.: Biodegradable block copolymers as injectable drug-delivery systems. Nature, **388**, 860–862 (1997).
DOI: 10.1038/42218

[3] Chearúil F. N., Corrigan O. I.: Thermosensitivity and release from poly *N*-isopropylacrylamide–polylactide copolymers. International Journal of Pharmaceutics, **366**, 21–30 (2009).
DOI: 10.1016/j.ijpharm.2008.08.036

[4] Boutris C., Chatzi E. G., Kiparissides C.: Characterization of the LCST behaviour of aqueous poly(N-isopropylacrylamide) solutions by thermal and cloud point techniques. Polymer, **38**, 2567–2570 (1997).
DOI: 10.1016/S0032-3861(97)01024-0

[5] Costa R. O. R., Freitas R. F. S.: Phase behavior of poly(*N*-isopropylacrylamide) in binary aqueous solutions. Polymer, **43**, 5879–5885 (2002).
DOI: 10.1016/S0032-3861(02)00507-4

[6] Zhuo R-X., Li W.: Preparation and characterization of macroporous poly(*N*-isopropylacrylamide) hydrogels for the controlled release of proteins. Journal of Polymer Science Part A: Polymer Chemistry, **41**, 152–159 (2003).
DOI: 10.1002/pola.10570

[7] Zhao Z., Li Z., Xia Q., Xi H., Lin Y.: Fast synthesis of temperature-sensitive PNIPAAm hydrogels by microwave irradiation. European Polymer Journal, **44**, 1217–1224 (2008).
DOI: 10.1016/j.eurpolymj.2008.01.014

[8] Cao Y., Zhang C., Shen W., Cheng Z., Yu L., Ping Q.: Poly(*N*-isopropylacrylamide)–chitosan as thermosensitive in situ gel-forming system for ocular drug delivery. Journal of Controlled Release, **120**, 186–194 (2007).
DOI: 10.1016/j.jconrel.2007.05.009

[9] Geever L. M., Devine D. M., Nugent M. J. D., Kennedy J. E., Lyons J. G., Hanley A., Higginbotham C. L.: Lower critical solution temperature control and swelling behaviour of physically crosslinked thermosensitive copolymers based on *N*-isopropylacrylamide. European Polymer Journal, **42**, 2540–2548 (2006).
DOI: 10.1016/j.eurpolymj.2006.06.002

[10] Serres A., Baudyš M., Kim S. W.: Temperature and pH-sensitive polymers for human calcitonin delivery. Pharmaceutical Research, **13**, 196–201 (1996).
DOI: 10.1023/A:1016026711364

[11] Ramkissoon-Ganorkar C., Liu F., Baudyš M., Kim S. W.: Modulating insulin-release profile from pH/thermosensitive polymeric beads through polymer molecular weight. Journal of Controlled Release, **59**, 287–298 (1999).
DOI: 10.1016/S0168-3659(99)00006-1

[12] Fundueanu G., Constantin M., Bortolotti F., Ascenzi P., Cortesi R., Menegatti E.: Preparation and characterisation of thermoresponsive poly[(*N*-isopropylacrylamide-*co*-acrylamide-*co*-(hydroxyethyl acrylate)] microspheres as a matrix for the pulsed release of drugs. Macromolecular Bioscience, **5**, 955–964 (2005).
DOI: 10.1002/mabi.200500099

[13] Varghese J. M., Ismail Y. A., Lee C. K., Shin K. M., Shin M. K., Kim S. I., So I., Kim S. J.: Thermoresponsive hydrogels based on poly(*N*-isopropylacrylamide)/chondroitin sulfate. Sensors and Actuators B: Chemical, **135**, 336–341 (2008).
DOI: 10.1016/j.snb.2008.09.001

[14] Zhang J-T., Bhat R., Jandt K. D.: Temperature-sensitive PVA/PNIPAAm semi-IPN hydrogels with enhanced responsive properties. Acta Biomaterialia, **5**, 488–497 (2009).
DOI: 10.1016/j.actbio.2008.06.012

[15] Zhang J-T., Petersen S., Thunga M., Leipold E., Weidisch R., Liu X., Fahr A., Jandt K. D.: Micro-structured smart hydrogels with enhanced protein loading and release efficiency. Acta Biomaterialia, **6**, 1297–1306 (2010).
DOI: 10.1016/j.actbio.2009.11.005

[16] Zhao S. P., Cao M. J., Li L. Y., Xu W. L.: Synthesis and properties of biodegradable thermo- and pH-sensitive poly[(*N*-isopropylacrylamide)-*co*-(methacrylic acid)] hydrogels. Polymer Degradation and Stability, **95**, 719–724 (2010).
DOI: 10.1016/j.polymdegradstab.2010.02.027

[17] Fundueanu G., Constantin M., Bortolotti F., Cortesi R., Ascenzi P., Menegatti E.: Poly[(*N*-isopropylacrylamide-*co*-acrylamide-*co*-(hydroxyethylmethacrylate))] thermoresponsive microspheres: An accurate method based on solute exclusion technique to determine the volume phase transition temperature. European Polymer Journal, **43**, 3500–3509 (2007).
DOI: 10.1016/j.eurpolymj.2007.05.026

[18] Eeckman F., Moës A. J., Amighi K.: Synthesis and characterization of thermosensitive copolymers for oral controlled drug delivery. European Polymer Journal, **40**, 873–881 (2004).
DOI: 10.1016/j.eurpolymj.2003.11.010

[19] Eeckman F., Moës A. J., Amighi K.: Poly(*N*-isopropylacrylamide) copolymers for constant temperature controlled drug delivery. International Journal of Pharmaceutics, **273**, 109–119 (2004).
DOI: 10.1016/j.ijpharm.2003.12.013

[20] Schild H. G., Muthukumar M., Tirrell D. A.: Cononsolvency in mixed aqueous solutions of poly(N-isopropylacrylamide). Macromolecules, **24**, 948–952 (1991).
DOI: 10.1021/ma00004a022

[21] Schild H. G.: Poly(*N*-isopropylacrylamide): Experiment, theory and application. Progress in Polymer Science, **17**, 163–249 (1992).
DOI: 10.1016/0079-6700(92)90023-R

[22] Constantin M., Fundueanu G., Bortolotti F., Cortesi R., Ascenzi P., Menegatti E.: Preparation and characterisation of poly(vinyl alcohol)/cyclodextrin microspheres as matrix for inclusion and separation of drugs. International Journal of Pharmaceutics, **285**, 87–96 (2004).
DOI: 10.1016/j.ijpharm.2004.07.025

[23] Otake K., Inomata H., Konno M., Saito S.: Thermal analysis of the volume phase transition with N-isopropylacrylamide gels. Macromolecules, **23**, 283–289 (1990).
DOI: 10.1021/ma00203a049

[24] Katayama S., Hirokawa Y., Tanaka T.: Reentrant phase transition in acrylamide-derivative copolymer gels. Macromolecules, **17**, 2641–2643 (1984).
DOI: 10.1021/ma00142a032

[25] Tanaka T.: Collapse of gels and the critical endpoint. Physical Review Letters, **40**, 820–823 (1978).
DOI: 10.1103/PhysRevLett.40.820

[26] Tokuyama H., Kato Y.: Preparation of poly(*N*-isopropylacrylamide) emulsion gels and their drug release behaviors. Colloids and Surfaces B: Biointerfaces, **67**, 92–98 (2008).
DOI: 10.1016/j.colsurfb.2008.08.003

[27] Wu J-Y., Liu S-Q., Heng P. W-S., Yang Y-Y.: Evaluating proteins release from, and their interactions with, thermosensitive poly (*N*-isopropylacrylamide) hydrogels. Journal of Controlled Release, **102**, 361–372 (2005).
DOI: 10.1016/j.jconrel.2004.10.008

eXPRESS Polymer Letters Vol.5, No.10 (2011) 849–858
Available online at www.expresspolymlett.com
DOI: 10.3144/expresspolymlett.2011.84

Crystallization kinetics of poly(lactic acid)-talc composites

D. Battegazzore, S. Bocchini, A. Frache*

Politecnico di Torino, Alessandria Site, V.le Teresa Michel 5, 15100 Alessandria, Italy

Received 18 February 2011; accepted in revised form 5 April 2011

Abstract. The crystallization kinetics of poly(lactic acid) / talc composites were determined over a range of 0 to 15 wt% of talc. Talc was found to change the crystallization kinetics. The presence of talc increases the crystallization rate and this increase is related to talc concentration and to crystallization temperature. In order to understand the effect of talc and PLA crystallinity on mechanical properties, dynamic mechanical thermal analyses were performed on poly(lactic acid) / talc composites before and after an annealing process. It was demonstrated that the presence of crystals improves thermo-mechanical properties but in order to achieve good results at high temperatures the reinforcing effect of a filler such as talc is necessary.

Keywords: *thermal properties, crystallization, polylactic acid, mechanical properties, polymer composites*

1. Introduction

Poly(lactic acid) (PLA) is a commercially available compostable biobased material that could become a material of choice, due to its high strength and moderate barrier properties. It is a highly transparent and rigid material with a relatively low crystallization rate that makes it a promising candidate for the fabrication of biaxially oriented films, thermoformed containers and stretch-blown bottles [1, 2]. Unfortunately the range of application of PLA is severely limited because of low glass transition temperature (around 55–60°C) thus research was focused on the study of PLA crystallization kinetics [3]. At temperature higher than glass transition only the PLA crystalline phase can confer useful mechanical properties. Increasing the crystallization speed of PLA is thus desired [4].

Lactic acid is optically active and thus it has a L or D form. The maximum attainable crystallinity level is obtained by minimizing the amount of the other lactide and mesolactide in the lactide used as the major monomer. The crystallinity and crystallization rate of PLA decrease as the purity decreases. The crystallization half-time was found to increase by roughly 40% for every 1 wt% increase in the mesolactide content of the polymerization mixture [5]. However even at high L-LA content PLA crystallization is typically too slow to develop significant crystallinity unless it is induced by strain such as in processes used to produce bottles. In processes such as injection molding where the orientation is limited and the cooling rate is high it is much more difficult to develop significant crystallinity and thus formulation or process changes are required. Researchers have studied the crystallization behaviour [6–9] of PLA; especially the crystallization kinetics [5, 10, 11]; the isothermal melting mechanism [12]; the effects of undercooling and the molecular weight on its morphology and crystal growth [13]; the effects of annealing on the thermal properties, morphology, and mechanical properties of PLA films [14]; and the effects of thermal treatment on compression-molded PLA at different molecular weights [15]. In order to increase crystallinity three main routes can be considered. The first one is to add a nucleating agent that will lower

*Corresponding author, e-mail: sergio.bocchini@polito.it

the surface free energy barrier towards nucleation and thus initiates crystallization at higher temperature upon cooling. A second possibility is to add a plasticizer which will increase the polymer chain mobility and will enhance the crystallization rate by reducing the energy required during crystallization for the chain folding process. The third possibility is to play with the molding conditions, in particular molding temperature and cooling time.

Several potential nucleating agents have been examined in the literature [3]. Talc is a widely used nucleating agent. It was shown that talc nucleates the crystallization of polymers through an epitaxial mechanism [16]. In the case of PLA, it is shown that the crystallization half-time can be reduced by more than one order of magnitude to less than 1 min when 1% talc is added [17]. Similarly, strong increase in nucleation density with addition of talc was found in poly(L-lactide-co-mesolactide) [5].

This paper investigated the effect of microtalc concentration on the crystalline content developed during heating-cooling-heating cycle and in isothermal condition. The crystalline content and mechanical properties achieved in different conditions are compared using differential scanning calorimetry and dynamic mechanical analysis. This information would be useful to better understand PLA/talc composites and their manufacturing and possible applications.

2. Experimental

2.1. Materials and sample preparation

Poly(L-lactic acid) 'NatureWorks® PLA Polymer 3051D', average molecular weight 160 kDa, ratio 96% L-Lactide to 4% D-Lactide units was obtained from Natureworks Minneapolis Minnesota (USA).

Industrial microtalc masterbatch 'PLA NA BIO L 6951' with 30% of talc content was purchased from Polyone Belgium SA Assesse (Belgium).

All the material was dried at least for 4 hours at 80°C under vacuum to a Karl-Fischer titration moisture content below 500 ppm before processing.

The compounds were melt blended using a co-rotating twin screw micro extruder DSM Xplore 15 ml Microcompounder. Residence time was fixed for all the runs at 5 minutes. To prevent the degradation of the polymers, N_2 purge flow was used during the processing. The screw speed was fixed at 60 rpm for the feeding and 100 rpm for the melt mixing. The heating temperature was set at 180°C. Percent of talc content is indicated by the number in the sample name (e.g., PLA1T contains 1.0 wt% talc).

2.2. Characterizations

Wide Angle X-Ray Scattering (WAXS) analyses were performed on compression moulded 3×3×0.5 mm specimens with a Thermo ARL diffractometer X-tra 48 using Cu-K_α X-ray source (λ = 1.540562 Å), step-size 0,02° at 2°C/min scanning rate.

Scanning Electron Microscope (SEM) pictures were taken with LEO 1400 VP Series (Carl Zeiss, Oberkochen, Germany) on surface of fragile fracture from film samples fractured after cooling by immersion in liquid nitrogen. The samples were metallized with gold.

Differential Scanning Calorimetry (DSC) analyses were performed with DSC Q20 TA Instruments (New Castle, DE, USA) with a double cycle of heating from 0 to 230°C at 10°C/min separated by a single cooling cycle at 10°C/min with isothermal step for 3 minutes at 230 and 0°C. The thermal history of samples was erased by the preliminary heating cycle at 10°C/min. The amount of material in the DSC samples was 6–8 mg. An empty pan was used as a reference. The glass transition temperature (T_g), crystallization temperature (T_c), cold crystallization temperature (T_{cc}), melting temperature (T_m), crystallization enthalpy (ΔH_c), cold crystallization enthalpy (ΔH_{cc}) and melting enthalpy (ΔH_m) were determined from cooling and second heating scans. The crystallinity (χ) of PLA and composites was evaluated using Equation (1):

$$\chi = \frac{\Delta H}{\Delta H_m^0 \cdot \left(1 - \frac{\%\,\text{wt filler}}{100}\right)} \cdot 100 \qquad (1)$$

where $\Delta H = \Delta H_c$ (for cooling curves, as ΔH_c is the specific crystallization enthalpy of the sample) or $\Delta H = \Delta H_m - \Delta H_{cc}$ (for second heating curves, as ΔH_m is the specific melting enthalpy of the sample, ΔH_{cc} is the specific cold crystallization enthalpy of the sample), ΔH_m^0 is the melting enthalpy of the 100% crystalline polymer matrix (93.0 J/g for PLA [18, 19]) and *%wt filler* is the total weight percentage of talc.

To evaluate isothermal crystallization values, a sample was heated from 25 to 200°C at 10 C/min and

maintained at 200°C for 5 min. Subsequently, it was rapidly cooled (–50°C/min) to the isothermal evaluation temperatures of 90, 95, 100, 105 and 110°C (T_i). The sample was held at the isothermal temperature for 120 minutes, allowing crystallization. To observe the melting behavior, the isothermally crystallized samples were reheated to 200°C at a rate of 10°C/min. The melting temperature that was observed was taken as the maximum of the endothermic transition.

Dynamic Mechanical Thermal Analysis (DMTA) was performed with DMA Q800 TA Intruments (New Castle, DE, USA). The measurements were carried out at a constant frequency of 1 Hz, at a strain amplitude of 15 µm with a preload of 0,01 N, a temperature range from 25 to 100°C with a heating rate of 3°C/min in tension mode. The samples were prepared by cutting strips from the films with a width of 6 mm, a height of 26 mm and a thickness of about 0,5 mm prepared by hot compression molding with 5 MPa at 180°C for 3 min. For each material at list three samples were characterized.

3. Results and discussion

3.1. Morphology

The WAXS spectra of talc is characterized by the presence of three diffraction peaks at $2\theta = 9.5$, 19.1 and 28.7º [20]. The WAXS pattern of PLA is characterized by a broad band with maximum at $2\theta = 16.6$º, indicating a completely amorphous structure (Figure 1). Crystalline structure of the polymer matrix is significantly affected by the presence of talc: the composites containing talc show the presence of the three talc peaks and a new peak at 16.6° due to the crystalline phase of the PLA (inset Figure 1) [21]. Thus, as expected talc enhance PLA crystallization. It is interesting to underline that the

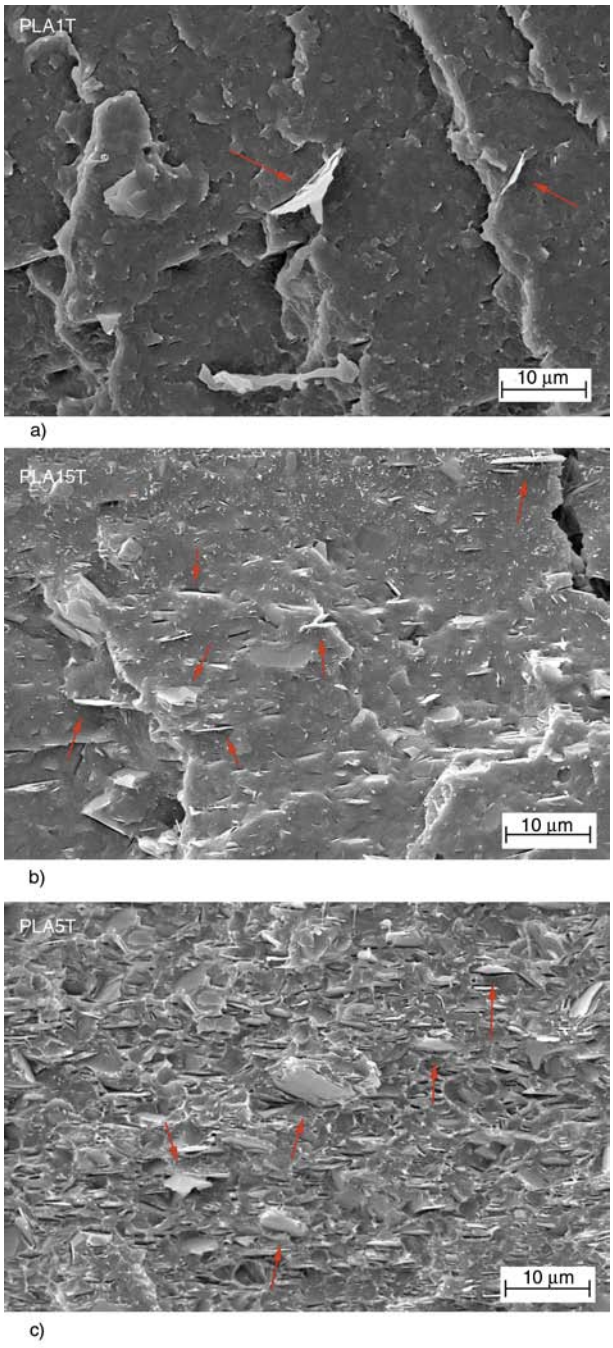

Figure 2. SEM analyses of PLA1T (a), PLA5T (b) and PLA15T (c)

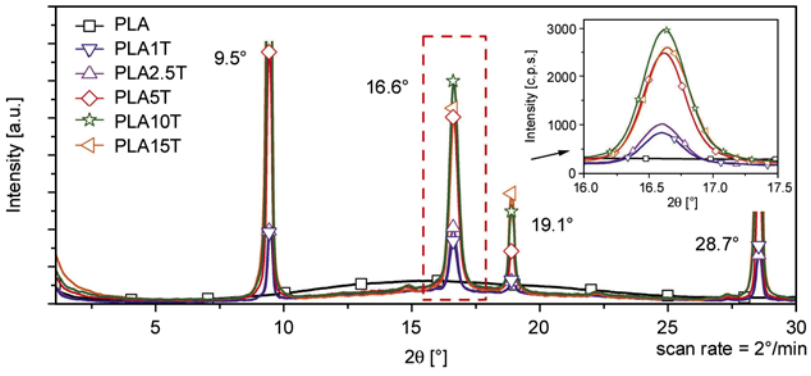

Figure 1. X-ray diffraction of melt-blended samples (inset: magnification of PLA characteristic peak)

intensities of the three talc peaks seem almost proportional to the talc content.

For the sake of brevity, only SEM analyses of PLA1T, PLA5T and PLA15T are shown because all the composites show a good dispersion. There are no aggregates and the talc lamellae are singularly dispersed. SEM analyses (Figure 2) shows also a wide size distribution of talc lamellae with maximum particle size of about 10 μm.

3.2. Thermal analysis

The thermal history of samples was erased by the preliminary heating cycle. The DSC thermograms recorded during cooling and second heating of PLA composites are reported respectively in Figure 3a and Figure 3b.

The data derived from DSC analyses are reported in Table 1. PLA alone does not crystallize during cooling. Talc induces PLA crystallization on cooling, as already reported [5], the crystallization percentage increases with the concentration of filler.

Neat PLA crystallizes on heating (cold crystallization) with a T_{cc} of 130°C (Figure 3b, Table 1). The exothermic peak of cold crystallization is partially merged with the endothermic melting peak that has a maximum at 152°C (Figure 3b). The χ_m and χ_{cc} of PLA have practically the same absolute value and this confirms that crystallization of neat PLA occurs only during heating.

The addition of 1 wt% of talc (Table 1) leads to a considerable decrease of T_{cc}, (~23°C), as well as to an increase of total crystallinity respect to neat PLA. The T_{cc} remains similar for all the samples containing talc. The PLA crystals in PLA/talc composites are formed partially during cooling and partially during cold crystallization. There is an important increase in the crystallinity percentage formed during the cooling cycle from 2.7 to 9.1% (evaluated as $\chi_m - \chi_{cc}$) with the increase of talc concentration from 1 to 15 wt%. The percentage of crystallization during heating (χ_{cc}), evaluated by heating released by cold crystallization, decreases with the increase of talc concentration. Similarly the overall crystallinity (χ_m) decreases with increasing the concentration of talc. Probably this is due to the presence of an higher percentage of crystals formed dur-

Table 1. DSC analysis of PLA, PLA/talc composites

Sample			PLA	PLA1T	PLA2.5T	PLA5T	PLA10T	PLA15T
Cooling	T_c	[°C]	–	85	86	88	88	89
	ΔH_c	[J/g]	0.0	0.9	2.4	2.6	4.2	4.4
	χ_c	[%]	0.0	0.9	2.7	2.9	5.0	5.6
2° heating	T_g	[°C]	59	57	58	59	60	60
	T_{cc}	[°C]	130	107	104	106	103	100
	ΔH_cc	[J/g]	12.0	26.2	24.2	19.7	16.4	13.9
	χ_{cc}	[%]	12.9	28.5	26.7	22.3	19.6	17.6
	T_m	[°C]	152	147–153	147–152	147–152	147–152	147–151
	ΔH_m	[J/g]	12.1	28.7	28.4	24.9	22.8	21.1
	χ_m	[%]	13.0	31.2	31.3	28.2	27.2	26.7
	$\chi_m - \chi_{cc}$	[%]	0.1	2.7	4.6	5.9	7.6	9.1

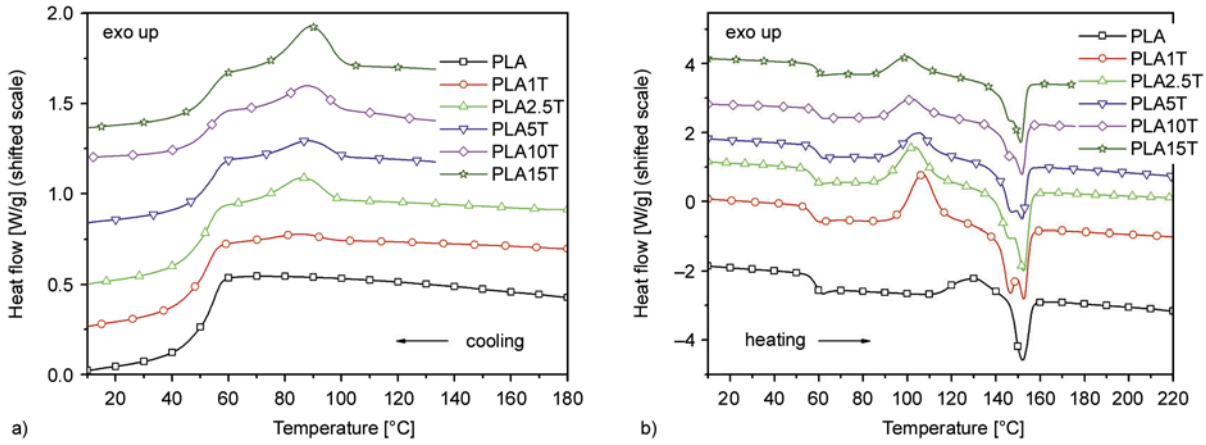

Figure 3. DSC analyses of samples a) cooling (10°C/min 230–0°C) b) second heating (10°C/min 0–230°C)

ing cooling, that reduce the chain mobility [3]. This reduction negatively affects cold crystallization process.

Two overlapping melting processes are shown by the composites containing talc (T_m: 147 and 152°C) which probably correspond to PLA crystallized respectively on heating and on cooling [11]. The low temperature melting process is reduced to a shoulder increasing talc content which indicates that crystallization on cooling gives crystals with an higher melting temperature. Thus the incorporation of talc leads to an increase of crystallization percentage during cooling and affect the total crystalline percentage obtained with an annealing process.

3.3. Isothermal crystallization behaviour

In Figure 4 the heat flow [W/*g*] versus *t* [min] at the isothermal temperature (T_i) of 110°C are plotted. Typical crystallization isotherms are obtained for pure PLA and PLA/talc composites. Adding talc the crystallization isotherm curves are shifted to left along the time axis.

In Table 2 are reported all the maximum of the curves (t_{max}) obtained at the different T_i. By plotting the T_i against the t_{max} saddle shape curves for PLA composites were obtained (Figure 5). The t_{max} for PLA/talc composites decrease as the T_i increased, then reach a minimum and start to increase. This minimum is at a T_i of 378 K (100°C) for the PLA alone and composites till 5 wt% of talc, and decrease to 95°C for talc concentration higher than 10 wt%.

Table 2. DSC isothermal analysis of PLA and PLA/talc composites

Sample	t_{max} [min]				
	90°C	95°C	100°C	105°C	110°C
PLA	120.0	106.2	81.5	86.2	118.0
PLA1T	8.9	4.9	4.3	4.7	6.8
PLA2.5T	6.9	4.6	3.0	4.3	6.2
PLA5T	4.4	2.9	2.8	3.7	4.7
PLA10T	3.0	2.2	2.2	3.0	4.2
PLA15T	2.8	2.0	2.0	3.0	4.0

The minimum t_{max} for PLA alone is 81 min. At the same temperature the talc reduces this time to 2.0–4.3 min for PLA/talc composite with various ratios. Thus the crystallization rates of the PLA containing talc were much faster than that of pure PLA. This is obtained at all experimental temperatures indicating that talc extremely increases the PLA crystallization rate. As the talc content in the PLA increased the t_{max} decreased slightly at all temperatures indicating an increase in PLA crystallization rate.

The Avrami equation [22–24] (Equation (2)) describes how solids transform from one phase to another at constant temperature. It can specifically describe the crystallization kinetics and for these is

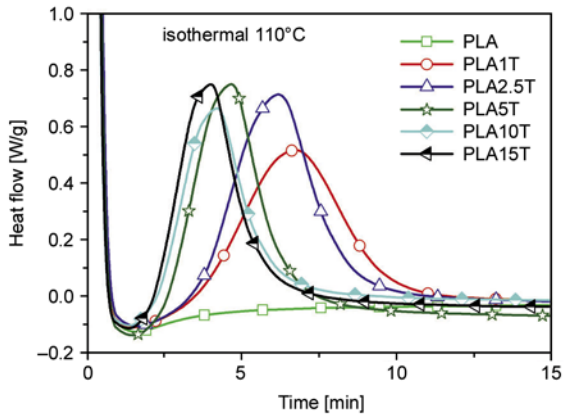

Figure 4. PLA and PLA/talc composites heat flow [W/g] versus *t* [min] at the isothermal temperature (T_i) of 110°C

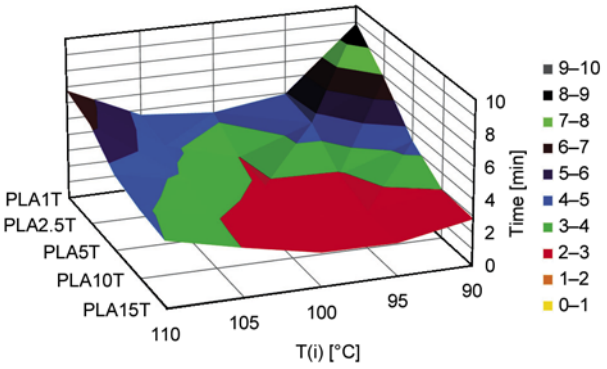

Figure 5. DSC isothermal analysis of PLA/talc composites: T_i versus t_{max}

Table 3. PLA, PLA/talc composites crystallinity percentage after isothermal and after annealing

Sample	χ [%] after isothermal DSC					χ [%] after annealing 2 h at 100°C
	90°C	95°C	100°C	105°C	110°C	
PLA	7.8	21.2	27.4	28.6	17.3	24.5
PLA1T	26.9	27.9	29.5	33.5	34.3	26.8
PLA2.5T	27.8	27.7	32.8	31.3	34.8	27.2
PLA5T	28.3	28.4	30.5	30.9	34.0	29.3
PLA10T	27.8	29.6	31.6	33.0	34.6	29.2
PLA15T	26.8	29.3	31.0	31.2	36.9	30.1

widely used to describe the isothermal crystallization processes in polymers.

If the following two assumptions are made:

(a) Nucleation rate is either zero (i.e. crystallization occurs due to the growth of pre-existing nuclei) or constant.

(b) Isotropical growth rate is proportional to either time t or $t_{1/2}$ (depending whether the devitrification is interface or diffusion controlled) then the classical Kohnogorov-Johnson-Mehl-Avrami (KJMA) equation can be derived to be Equation (2) [25]:

$$\chi(t) = \chi_\infty[1 - \exp(-kt^n)] \quad (2)$$

where $\chi(_t)$ is the volume crystallinity at time t; χ_∞ is the volume crystallinity after infinite time (estimated by using ΔH_∞); k is the overall kinetic rate constant and n is the Avrami exponent (which depends on the nucleation and growth mechanism of the crystal).

The evolution of the crystallinity with time can be estimated by using the degrees of crystallization (α) as expressed by the ratio of enthalpy determined by DSC using Equation (3):

$$\alpha = \frac{\chi(t)}{\chi_\infty} = \frac{\Delta H(t)}{\Delta H_\infty} \quad (3)$$

The value of α at different times (t) is calculated by integrating this curve of enthalpy at selected times and calculating the ratio between this value and the total area of the curve.

Taking the double logarithm of Equation (2) gives Equation (4):

$$\ln[-\ln(1 - X_t)] = \ln(k) + n\ln(t) \quad (4)$$

The plot of $\ln[-\ln(1 - X_t)]$ vs $\ln(t)$ should be linear and the parameters k and n can be determined by curve fitting the experimental data with slope n and intercept $\ln(k)$.

The physical interpretation of the Avrami constants k and n is difficult and open to interpretation. Originally n was held to have an integer value between 1–4 which reflected the nature of the transformation in question. In the derivation above for example the value of 4 can be said to have contributions from three dimensions of growth and one representing a constant nucleation rate. If the nuclei are preformed, and thus present from the beginning, the transformation is only due to the 3-dimensional growth of the nuclei and n has a value of 3. An interesting condition occurs when nucleation occurs on specific sites (such as grain boundaries or impurities) which rapidly saturate soon after the transformation begins. Initially nucleation may be random and growth unhindered leading to high values for n (3, 4). Once the nucleation sites are consumed the formation of new particles will cease. Furthermore if the distribution of nucleation sites is non-random then the growth may be restricted to 1 or 2-dimensions. Site saturation may lead to n values of 1, 2 or 3 for surface, edge and point sites respectively.

The k parameter is a temperature-dependent factor which is generally taken in the Arrhenius form (Equation (5)):

$$k = k_0 \cdot \exp\left(-\frac{E}{RT}\right) \quad (5)$$

where E is the average activation energy for the overall crystallization process. For isothermal transformation according to Equation (5) we have Equation (6):

$$\ln(k) = \ln(k_0) - \frac{E}{RT} \quad (6)$$

The activation energy for crystallization can be determined by plotting $\ln(k)$ vs $1/T$ and $\ln(k)$ is directly connected to the activation energy. Figure 6 presents plots of $\ln[-\ln(1 - X_t)]$ vs $\ln(t)$ for the PLA/talc microcomposites at 110°C. The curves present an early and a nonlinear end part but in the figure only the parts used to do the fitting are

Table 4. Crystallization parameters $\ln(k)$ and n for PLA and PLA/talc microcomposites

Temperature	90°C		95°C		100°C		105°C		110°C	
Sample	n	ln(k)	N	ln(k)	n	ln(k)	n	ln(k)	n	ln(k)
PLA	–	–	–	–	3.06	–13.06	–	–	–	–
PLA1T	2.12	–4.40	2.37	–3.03	2.36	–2.54	2.37	–2.59	2.30	–3.43
PLA2.5T	2.03	–3.75	2.21	–2.98	2.57	–2.05	2.35	–2.20	2.50	–3.12
PLA5T	–	–	–	–	2.31	–1.61	2.27	–1.93	2.39	–2.57
PLA10T	–	–	–	–	–	–	2.26	–1.59	2.30	–2.18
PLA15T	–	–	–	–	–	–	–	–	2.29	-2.04

reported. The crystallization parameters ln(k) and n obtained after fitting are summarized in Table 4. Where there are no data was impossible to do the calculation. For neat PLA there is only one data at 100°C (Figure 7).

The ln(k), and thus the activation energy, decreases increasing the amount of talc. The ln(k) for pure PLA is –13.06 so the activation energy is higher than PLA/talc composites. For the sample where it was possible to evaluate the ln(k), it has a minimum value at 100°C according to what already reported for t_{max}.

For PLA the Figure 7 shows a nonlinear long early part, as in the other case but longest, and after a linear part fitted with the orange line with n values very near to 3 (Table 4). So the nuclei are preformed and the transformation is only due to the 3-dimensional growth of the nuclei. For PLA/talc composites instead at all the T_i under consideration the n factor is 2.3±0.2 and remains instead quite constant (except for a little change at 90°C) thus the mechanism of nucleation and growth of the crystal is more similar to a two dimensional growth on a lamellar structure as it can be expected from an epitaxial growth mechanism. Thus the micro talc change the mechanism of PLA crystallization strongly reducing the activation energy needed as Kolstad [5] already demonstrated. The mechanism of growth is directly linked to the presence of talc particles that works as nucleating agent with a 2d growth mechanism.

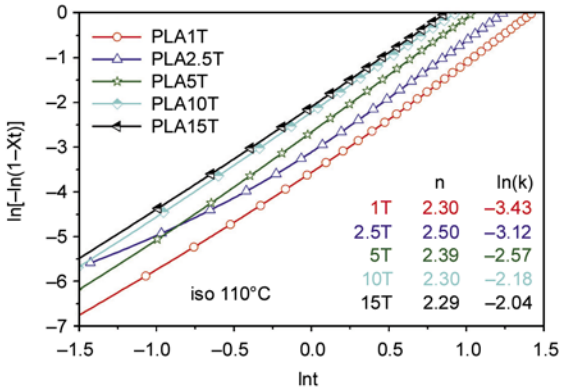

Figure 6. Plots of ln[–ln(1 – X_t)] vs ln(t) for the microcomposites at 110°C

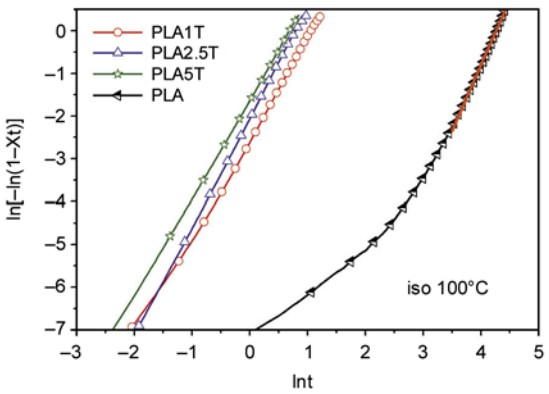

Figure 7. Plots of ln[–ln(1 – X_t)] vs ln(t) for the PLA at 100°C

3.4. Mechanical properties

In Figure 8 are reported the DMTAs of PLA and talc filled samples. For concentration higher than 5 wt% the addition of talc into PLA improves modulus as expected. The storage modulus is increased at 30°C and this is due to the reinforcing effect of talc. Under 5 wt% of talc content no relevant differences are highlighted thus the increase of crystalline percentage seems not to affect the storage modulus of PLA.

Considerable improvements of rigidity were instead observed at higher temperatures upon addition of talc for all loadings. In Figures 8 and 9 all the data obtained from DMTA tests of all samples at 30 and 85°C and the peak temperatures of tanδ are summarized. Because of the low modulus the test of PLA must be stopped at about 80°C instead also at low loading (i.e. 1 wt%), where the addition of talc into PLA that leads to no change in the storage modulus at 30°C, the composites show an increase of modulus at higher temperature (Figure 8): the 1 wt% of talc is enough to allow the PLA to reach the test end (100°C).

At high temperature the addition of 5, 10 and 15 wt% of talc leads to increases of storage modulus respectively of 260, 430 and 600 MPa thus the increases of the storage modulus are directly correlated to talc percentage. These increases at high temperature could be associated to the reinforcement effect of particles in the polymer matrix or to the crystallization induced by talc on the PLA.

To better understand the role on reinforcement of the PLA crystals and of the filler, DMTA were repeated on samples annealed for 2 hours at 100°C to permit the maximum crystallization. After the annealing the samples were tested on DSC to verify the reached crystallinity. The results are reported in Figure 9 and Table 3. The crystallinity after annealing (Table 3) is 25% for neat PLA and increase with the talc content to 30% as expected from the previous DSC isothermal data. The total crystallinity of

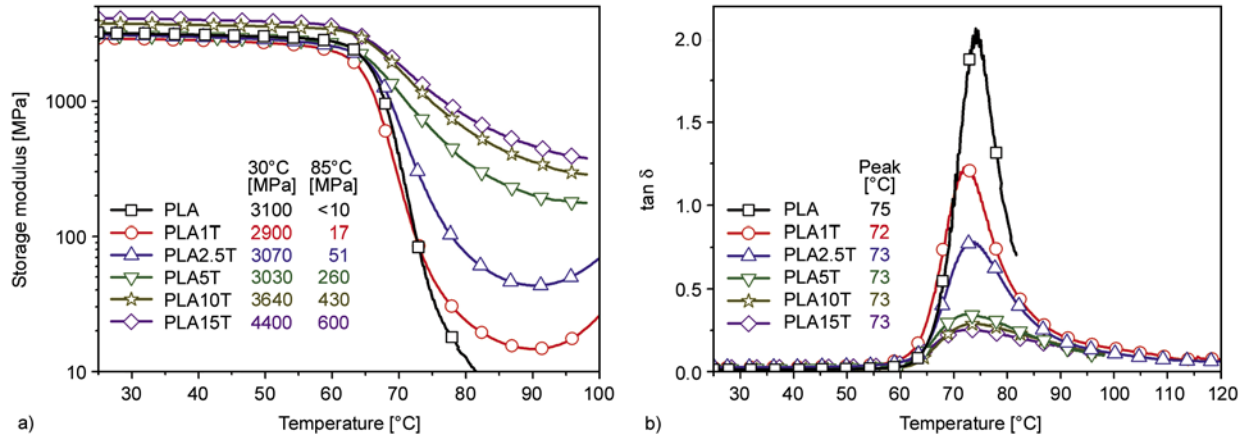

Figure 8. DMTA of PLA and PLA/talc composites. Storage modulus (a) and tan δ (b)

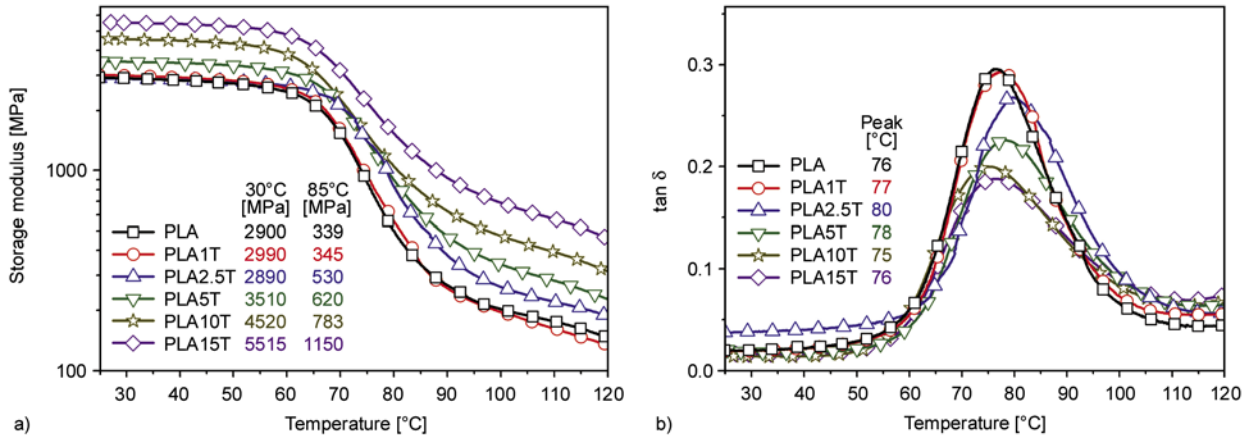

Figure 9. DMTA of PLA and PLA/talc composites after annealing (2 h at 100°C). Storage modulus (a) and tan δ (b)

the annealed samples is different from the corresponding samples measured with DSC. The differences are due to the thermal history of the samples: the DSC samples were quenched while the samples for mechanical analyses were heated from room temperature to isothermal condition for annealing. At 30°C the storage modulus is not influenced by talc and by the crystallinity level under the 2.5 wt% of talc content thus the main reinforcing effect in this case is due to the glassy state of PLA. Above this content (5 wt% and more) there is a linear increase of the storage modulus directly correlated to the talc addition. With the samples annealed the modulus increases faster with talc content than with un-annealed samples. This behaviour suggests that there is a synergistic effect between talc filler and crystallinity. At 85°C the storage modulus of pure PLA annealed is about 340 MPa and the sample reach the end of the test now fixed at 120°C. Thus, over the T_g, the crystallinity highly affects the thermo-mechanical properties of PLA. For annealed samples at high temperature the storage modulus directly increase with talc content and it seems due to the linear addition of talc effect and crystals presence.

Finally there is a small increase in the glass transition temperature (peak of tanδ) of the different samples after annealing (Figure 8, Figure 9). Probably during annealing the low molecular weight molecules, that are the molecules with the higher mobility, are included in the growing crystals. The low molecular weight molecules are the same that act as plasticizing agents for PLA amorphous part thus the result is an increase of the glass transition temperature.

4. Conclusions

To allow PLA utilization in engineering applications addition of selected fillers by melt-blending represents a good methodology for improving its performance. PLA based-composites obtained by addition of talc present considerable improvements

in the thermal and mechanical properties of PLA thus they are potentially interesting for technical applications. The incorporation of talc particles significantly accelerates the crystallization process of the PLA matrix.

The crystallization behaviour of PLA/talc composites during cooling is mainly influenced by the composition and the crystallization temperatures. The talc in PLA/talc composites can effectively increase the crystallization rate of PLA, even at a content of 1 wt%. The crystallization rate increased slightly as the talc content in the composite increased. The maximum speed of crystallization is reached with the annealing temperature of 100°C for the PLA and a lower (95°C) for talc high content samples.

The kinetics of crystallization obtained using the Avrami equation shows that PLA/talc microcomposites has a different growth kinetics that is more similar to a two dimensional growth on a lamellar structure such as an epitaxial growth. Moreover micro talc strongly reduces the activation energy.

At high temperature the modulus increase is due to a synergistic effect between crystals and filler, thus in order to have materials with good performances both the presence of a filler and PLA crystals are necessary.

References

[1] Shen L., Haufe J., Patel M. K.: Product overview and market projection of emerging biobased plastics: PRO-BIP 2009. Final Report, Utrecht University (2009).

[2] Lim L-T., Auras R., Rubino M.: Processing technologies for poly(lactic acid). Progress in Polymer Science, **33**, 820–852 (2008).
DOI: 10.1016/j.progpolymsci.2008.05.004

[3] Li H., Huneault M. A.: Effect of nucleation and plasticization on the crystallization of poly(lactic acid). Polymer, **48**, 6855–6866 (2007).
DOI: 10.1016/j.polymer.2007.09.020

[4] Bigg D. M.: Controlling the performance and rate of degradation of polylactide copolymers. in 'Annual Technical Conference – ANTEC 2003 Conference Proceedings, Nashville, USA', Vol 3, 2816–2822 (2003).

[5] Kolstad J. J.: Crystallization kinetics of poly(L-lactide-*co*-*meso*-lactide). Journal of Applied Polymer Science, **62**, 1079–1091 (1996).
DOI: 10.1002/(SICI)1097-4628(19961114)62:7<1079::AID-APP14>3.0.CO;2-1

[6] Nijenhuis A. J., Grijpma D. W., Pennings A. J.: Highly crystalline as-polymerized poly(L-lactide). Polymer Bulletin, **26**, 71–77 (1991).
DOI: 10.1007/BF00299350

[7] Kalb B., Pennings A. J.: General crystallization behaviour of poly(L-lactic acid). Polymer, **21**, 607–612 (1980).
DOI: 10.1016/0032-3861(80)90315-8

[8] Cohn D., Younes, H., Marom G.: Amorphous and crystalline morphologies in glycolic acid and lactic acid polymers. Polymer, **28**, 2018–2022 (1987).
DOI: 10.1016/0032-3861(87)90035-8

[9] Migliaresi C., de Lollis A., Fambri L., Cohn D.: The effect of thermal history on the crystallinity of different molecular weight PLLA biodegradable polymers. Clinical Materials, **8**, 111–118 (1991).
DOI: 10.1016/0267-6605(91)90018-B

[10] Urbanovici E., Schneider H. A., Brizzolara D., Cantow H. J.: Isothermal melt crystallization kinetics of poly(L-lactic acid). Journal of Thermal Analysis and Calorimetry, **47**, 931–939 (1996).
DOI: 10.1007/BF01979440

[11] Tábi T., Sajó I. E., Szabó F., Luyt A. S., Kovács J. G.: Crystalline structure of annealed polylactic acid and its relation to processing. Express Polymer Letters, **4**, 659–668 (2010).
DOI: 10.3144/expresspolymlett.2010.80

[12] Kishore K., Vasanthakumari R., Pennings A. J.: Isothermal melting behavior of poly(L-lactic acid). Journal of Polymer Science: Polymer Physics Edition, **22**, 537–542 (1984).
DOI: 10.1002/pol.1984.180220401

[13] Vasanthakumari R., Pennings A. J.: Crystallization kinetics of poly(L-lactic acid). Polymer, **24**, 175–178 (1983).
DOI: 10.1016/0032-3861(83)90129-5

[14] Tsuji H., Ikada Y.: Properties and morphologies of poly(L-lactide): 1. Annealing condition effects on properties and morphologies of poly(L-lactide). Polymer, **36**, 2709–2716 (1995).
DOI: 10.1016/0032-3861(95)93647-5

[15] Migliaresi C., Cohn D., de Lollis A., Fambri L.: Dynamic mechanical and calorimetric analysis of compression-molded PLLA of different molecular weights: Effect of thermal treatments. Journal of Applied Polymer Science, **43**, 83–95 (1991).
DOI: 10.1002/app.1991.070430109

[16] Haubruge H. G., Daussin R., Jonas A. M., Legras R., Wittmann J. C., Lotz B.: Epitaxial nucleation of poly (ethylene terephthalate) by talc: Structure at the lattice and lamellar scales. Macromolecules, **36**, 4452–4456 (2003).
DOI: 10.1021/ma0341723

[17] Ke T., Sun X.: Melting behavior and crystallization kinetics of starch and poly(lactic acid) composites. Journal of Applied Polymer Science, **89**, 1203–1210 (2003).
DOI: 10.1002/app.12162

[18] Fukada E.: Piezoelectricity of biopolymers. Biorheology, **32**, 593–609 (1995).
DOI: 10.1016/0006-355X(95)00039-C

[19] Turner J. F., Riga A., O'Connor A., Zhang J., Collis J.: Characterization of drawn and undrawn poly-L-lactide films by differential scanning calorimetry. Journal of Thermal Analysis and Calorimetry, **75**, 257–268 (2004).
DOI: 10.1023/B:JTAN.0000017347.08469.b1

[20] Rayner J. H., Brown G.: The crystal structure of talc. Clays and Clay Minerals, **21**, 103–114 (1973).
DOI: 10.1346/CCMN.1973.0210206

[21] Xiao H. W., Li P., Ren X., Jiang T., Yeh J-T.: Isothermal crystallization kinetics and crystal structure of poly(lactic acid): Effect of triphenyl phosphate and talc. Journal of Applied Polymer Science, **118**, 3558–3569 (2010).
DOI: 10.1002/app.32728

[22] Avrami M.: Kinetics of phase change. I. General theory. Journal of Chemical Physics, **7**, 1103–1112 (1939).
DOI: 10.1063/1.1750380

[23] Avrami M.: Kinetics of phase change. II. Transformation-time relations for random distribution of nuclei. Journal of Chemical Physics, **8**, 212–224 (1940).
DOI: 10.1063/1.1750631

[24] Avrami M.: Granulation, phase change, and microstructure kinetics of phase change. III. Journal of Chemical Physics, **9**, 177–184 (1941).
DOI: 10.1063/1.1750872

[25] Sun N. X., Liu X. D., Lu K.: An explanation to the anomalous avrami exponent. Scripta Materialia, **34**, 1201–1207 (1996).
DOI: 10.1016/1359-6462(95)00657-5

eXPRESS Polymer Letters Vol.5, No.10 (2011) 859–872
Available online at www.expresspolymlett.com
DOI: 10.3144/expresspolymlett.2011.85

Synergetic role of nanoparticles and micro-scale short carbon fibers on the mechanical profiles of epoxy resin

G. Zhang[1*], *Z. Rasheva*[1], *J. Karger-Kocsis*[2,3], *T. Burkhart*[1]

[1]Institute for Composite Materials, University of Kaiserslautern, 67663 Kaiserslautern, Germany
[2]Department of Polymer Technology, Faculty of Engineering and Built Environment, Tshwane University of Technology, Pretoria 0001, Republic of South Africa
[3]Department of Polymer Engineering, Faculty of Mechanical Engineering, Budapest University of Technology and Economics, H-1111 Budapest, Hungary

Received 8 February 2011; accepted in revised form 11 April 2011

Abstract. It was demonstrated in our previous work that the combined carbon nanofibers (CNFs) and microsized short carbon fibers (SCFs) in epoxy (EP) leads to significant improvements in the mechanical properties of the matrix. In this work, the effect of nano-SiO_2 particles, having an extremely different aspect ratio from CNFs, on the tensile property and fracture toughness of SCFs-filled EP was studied. It was revealed that the combined use of SCFs and silica nanoparticles exerts a synergetic effect on the mechanical and fracture properties of EP. Application of SCFs and the nanoparticles is an effective way to greatly enhance the modulus, strength and fracture toughness of the EP simultaneously. The synergetic role of the multiscale fillers was explained by prominent changes in the stress state near the microsized fillers and the plastic zone ahead of the crack tip. The synergetic role of multiscale fillers is expected to open up new opportunities to formulate high-performance EP composites.

Keywords: *nanocomposites, epoxy, fracture toughness, mechanical properties, short carbon fibers*

1. Introduction

Epoxy resins (EPs) are nowadays being extensively utilized in engineering applications such as aerospace, automotive, sport and electronic device due to their good mechanical properties and ease in processing. It is a continually challenging task for polymer scientists and engineers to improve the fracture toughness of EP simultaneously with other mechanical properties, e.g. stiffness and strength.

Various methods were developed in the last four decades to toughen EPs. Thermoplastic fibers significantly toughen brittle epoxy resin [1]. Microsized rubber particles [2–4], thermoplastic particles [5, 6], inorganic particles [7–10] were also proven to toughen EP systems. Rubber particles are effective toughening agents in thermosets because they trigger the localized shear yielding in the related matrices. However, rubber toughening is accompanied with obvious reductions of the modulus and creep resistance of the matrix. Thermoplastic particles can improve the toughness of EP with slight sacrifices of modulus and yield stress [6]. Microsized short fibers (diameter and length in micron scale), e.g. short carbon fibers [11, 12] (SCFs) and short glass fibers [13–16] were also employed to enhance the toughness of polymers. Inorganic particles and short fibers are especially attractive in EP matrices because they can improve the fracture toughness and the modulus (stiffness) at the same time. The toughening mechanism of rigid microparticles may comprise a combination of crack deflection, crack pinning, particle debonding and micro-

*Corresponding author, e-mail: ga.zhang@ivw.uni-kl.de

shear banding of matrix [8, 9, 17–22]. Compared with rigid particles, the toughening mechanisms achieved by short fibers, especially for randomly distributed fibers with a high aspect-ratio, are more complicated. Due to the relatively high aspect-ratio of short fibers, pull-out and fracture of fibers are important contributions to the toughness response [13–16].

Even though microsized fillers can effectively stiffen and toughen the EP matrix, when it is under stress, stress concentration can occur locally near the fillers and induce critical failure of the composite system [21]. In case of microsized short fibers, it should be taken into account that intensive stress concentration occurs at the fiber ends and this can promote fiber slip and may also cause some loss in strength [13, 23]. Thus, in many cases, the ductility of the matrix, being reinforced with microsized rigid fillers or randomly oriented fibers can be markedly reduced and the strength can only be moderately enhanced or it is even reduced.

In the last two decades, polymer nanocomposites gained intensive interest because of the exceptionally large specific area of the nanofillers available for interaction with the polymer matrix. Inorganic nanoparticles are one kind of common nanofillers being investigated for toughening of polymer matrices. Unlike microsized inorganic particles, inorganic nanoparticles will not lead to significant stress concentration due to their much smaller size which guarantees a good integration with the matrix [21]. It was reported that nanoparticles can simultaneously improve the stiffness, strength and toughness of EPs [21, 24, 25]. In addition, nanoparticles may toughen EP even at a very low loading [25, 26]. The debonding of nanoparticles [21, 25, 27, 28] and plastic void growth [25, 28], shear yielding of matrix [21, 27] are believed to be the main factors of toughening mechanisms.

In many cases only EP nanocomposites filled with nanoparticles at low concentrations are of practical interests because the introduction of nanofillers at high concentrations will complicate the manufacture process and lead to high costs, as well. From the point of view of the mechanical performance, nanocomposites do not necessarily present superior properties to microcomposites. Adachi *et al.* [10] compared the *E*-moduli of EP composites reinforced with spherical micro- and nano-silica particles. The contents of the fillers varied from 5 to 35 vol%. They did not find a significant effect of the particles size on the *E*-modulus, which was still controlled by the volume fraction. Wetzel *et al.* [21] found that the stiffening effect of large rod-like $CaSiO_3$ particles on EP is stronger than that of the alumina nanoparticles. The $CaSiO_3$ particles have a diameter of 3–5 μm and length to width (aspect) ratio of 3–4. Even though exceptionally good filler/matrix interaction exists in EP nanocomposites, the nanoparticles constrain the matrix deformation less than microparticles because the former, being in nearly molecular dimensions, are better integrated into the polymer microstructure [21]. Indeed, many research works proved that with low-loading nanoparticles, the modulus of the high-performance epoxy matrix can only be moderately increased [24–27]. A direct comparison of the mechanical properties of EP micro- and nanocomposites will supply engineers with a solid knowledge for selecting appropriate materials according to the needs of real applications.

Recent studies [29, 30] indicated that the inclusion of nanoparticles much improves the mechanical properties [29] and fatigue life [30] of continuous glass fibers reinforced EPs (GFRP). It was also revealed that to integrate low-loadings CNT into continuous glass fibers (GFRP) [31] and continuous carbon fibers [32, 33] reinforced EP (CFRP) significantly improves the mechanical and fracture properties, compared to conventional composites. Even though the mechanisms are still unclear, it was noticed that nanofillers seem to enhance the fibers/matrix adhesion [31–33]. These pioneer works give hints to enhance the mechanical properties of conventional EP composites reinforced with microsized (non-continuous) fillers by adding low-loading nanofillers.

Indeed, it might be of great interests to combine the advantages of micro- and nanofillers. This may be a promising composite formulation route to combine microfillers at medium to high concentrations, and nanofillers at low concentrations into polymer matrices. It was revealed in our previous work that combined use of SCFs and carbon nanofibers (CNFs) in EP resin leads to a synergetic role on the mechanical properties of the matrix [34]. The composites filled with combined SCFs and CNFs displays better mechanical properties than the materials rein-

forced only with SCFs or CNFs. However, a combination of two kinds of nanofillers, e.g. CNFs and nanoparticles, was not associated with synergetic effects [34]. It is assumed that that the common use fillers with distinctly different scale sizes is the key issue for eventual synergism. With this context, it is important to know if nanofillers, having distinctly different ratios from CNFs, will also play synergetic roles with the microsized SCFs. As abovementioned, inorganic nanoparticles are one kind of common nanofillers. In the present work, we studied the effect of nano-SiO_2 particles on the mechanical properties of EP composites filled with SCFs. Special attentions were paid to the contributions of the respective SCFs, nanoparticles and their combinations.

2. Experimental

2.1. Materials and preparation

All materials in the present work were prepared on the basis of a commercially available epoxy resin (DER331 by DOW, USA) with an epoxide equivalent weight 182–192 g/equiv. Cycloaliphatic amine hardener (HY 2954; Huntsman, USA) was used to cure the epoxy materials. Fumed spherical silica nanoparticles (Aerosil R8200) with hexamethyldisilazane modification were supplied by Evonik (Germany). The diameter and the specific surface area of the nanoparticles are respectively about 12–14 nm and 160 m^2/g. The nanoparticles were used as-received without any further treatment. Milled polyacrylonitrile (PAN)-based carbon fibers (Tenax® A-385) were supplied by Tenax GmbH (Germany). The diameter and the length of the fibers are respectively 7 μm and 40–70 μm. The SCFs were supplied without sizing treatment and were used as-received. Three series of epoxy composites, i.e. microcomposites filled with SCFs, low-loading nanoparticles-filled nanocomposites, and multiscale composites reinforced with both SCFs and low-loading nanoparticles, were compared in this study. The loading of the silica nanoparticles varied from 0.5 to 5.0 vol%. Pure EP and SCFs-filled EP (with SCF fractions from 5 to 15 vol%) served as reference materials. The volume fractions of all the fillers were calculated by considering their weights and (bulk) densities. The densities of pure EP, SCF and SiO_2 nanoparticles are 1.14, 1.74 and 2.00 g/cm^3, respectively.

Table 1. Compositions of materials studied

Series	Material codes	Matrix [vol%]	SCF [vol%]	Nano-SiO_2 [vol%]
Pure epoxy	EP	100	–	–
Microcomposites	5CF	95	5	–
	10CF	90	10	–
	15CF	85	15	–
Nanocomposites	1Si	99	–	1
	3Si	97	–	3
	5Si	95	–	5
Multiscale composites	10CF0.5Si	89.5	10	0.5
	10CF1Si	89	10	1
	10CF2Si	88	10	2
	10CF3Si	87	10	3

The nanoparticles adhere to each other due to the inherent Van der Waals force between the particles, resulting in nanoparticle agglomerates. The silica nanoparticles in the EP were dispersed by using a high-energy vacuum dissolver (Dispermat, VMA-Getzmann, Germany). At an extremely high rotation speed (5800 rpm) of teeth vested metal disc, the dissolver provides high shear forces to break up the agglomerates in the liquid EP in vacuum, followed by degassing. The SCFs were dispersed in the EP with a moderate rotation speed in order to avoid breakage of the fibers. The multiscale composites were prepared by firstly dispersing, with the extremely high rotation speed, the needed amounts of nano-SiO_2 in EP and by subsequent introduction of the SCFs in the nano-SiO_2/EP compounds. Afterwards, the compounds were blended with the curing agent HY2954 by stirring for 15 min. Finally the mixture was poured into release agent-coated metallic moulds and cured at 70°C for 8 hours, followed by 8 hours at 120°C.

The detailed compositions of the materials are disclosed in Table 1. For simplification purpose, the composite materials were referenced according to the type and the fraction of the fillers as shown in the left column of Table 1. For example, 10CF1Si refers to the multiscale composite filled with 10 vol% SCF and 1 vol% nano-SiO_2.

2.2. Glass transition temperature

Assessment of the glass transition temperature (T_g) was necessary as it is known that especially the nanofillers may affect the curing of the EP and this results in slight or prominent changes in the T_g [35]. T_g of the composites were determined by differential scanning calorimetry (DSC) using a DSC821

apparatus (Mettler-Toledo GmbH, Switzerland). All tests were performed in nitrogen atmosphere with a sample mass of about 20 mg. The sample was heated from 20 to 200°C at a rate of 10°C/min. The T_gs were assessed by the mid-point of the T_g steps.

2.3. Tensile tests

Tensile tests were performed at room temperature (21°C) on a Zwick 1474 (Zwick, Germany) universal testing machine at a constant crosshead speed of 0.5 mm/min. The measurements followed DIN EN ISO 527 using dumbbell shaped specimens. The specimens having a 4 mm thickness were machined from the molded plates. The length overall of dumbbell specimens is 75 mm. The length and width of narrow section are 30 and 5 mm, respectively. The displacement of each specimen during tension was accurately measured by an extensometer with an initial extension span of 20 mm. *E*-moduli were calculated with 0.05–0.25% strain. All presented data corresponds to the average of at least five measurements.

2.4. Fracture toughness

The fracture toughness K_{IC} and the critical energy release rate G_{IC} was determined by means of compact tension (CT) tests according to the standard ISO 13586 on at least five specimens at a crosshead speed of 0.5 mm/min. The CT specimens were cured in a metallic mold and then both sides were polished by abrasive papers until all visible marks disappeared. A notch was machined and then sharpened by tapping a fresh razor blade into the material, so that a sufficiently sharp natural crack was initiated. The thickness and the width of specimens were 4 and 30 mm, respectively.

In order to analyze material-failure mechanisms, the fracture surfaces of the tensile and CT test specimens were inspected in a scanning electron microscope (SEM, ZEISS SupraTM 40VP, ZEISS, Germany) after being coated a thin gold layer.

3. Results and discussion

3.1. Glass transition temperature

Table 2 shows the T_gs of the composites studied. The SCFs does not significantly influence the T_g. Only a slight decrease in T_g, if there is any, is noticed with the addition of SCFs. The effect of nanoparticles on the T_g is non-monotonic and seems to be rather complex. With respect to the nanocomposites, the addition of nanoparticles in the range of 1 to 3 vol% depresses the T_g. Further increase of the loading from 3 to 5 vol%, however, gives rise to the T_g. Compared with the microcomposite, i.e. 10CF, the nanoparticles in the multiscale composites slightly arise the T_g.

The change in T_g for EP nanocomposites is a controversial issue. Some researchers have found that T_g of nanocomposites increases as a function of the filler-loading [21, 36], whereas others observed the opposite [28, 37–41], and again others found non-monotonic trends [42, 43]. In general, the restricted mobility of polymer chains in the vicinity of the nanofillers is believed to arise the T_g [21, 35, 36, 40, 42]. However, the free volume at the nanofiller-resin interface can lower the T_g [39, 40, 42]. Moreover, a possible plasticizing effect of uncured or less cured epoxy resin, caused by the presence of nanoparticles, can lower the T_g [38, 40, 41]. The mechanisms how nanoparticles decrease the cross-link degree of EP is still not clear. Although the kinetically-controlled curing reaction is advancing also in presence of nanofillers, it may become hindered in the diffusion-controlled stage [35, 37]. Note that selective absorption of the resin or the hardener at the silica surface can lead to an off-stoichiometry in the interphase. This is associated with a marked difference in the cross-link density locally. We assume that the preferential adsorption at the nanoparticles can decrease the T_g due to the lower cross-link density near the filler-matrix interface. If this is the case, such a 'core-shell'-type structure (core:rigid silica, shell: EP with lower cross-linking then the bulk) can promote the cavitation of the nanoparticles and enhance the ductility of the material. The complexity of the underlying chemistry does not allow the reasoning of the observed change in the T_g.

3.2. Tensile properties

Figure 1a shows representative stress-strain curves of pure EP, nanoparticles-filled EP, SCFs-filled EP

Table 2. T_gs of materials studied

Material codes	EP	5CF	10CF	15CF	1Si	3Si	5Si	10CF0.5Si	10CF1Si	10CF2Si	10CF3Si
T_gs [°C]	133.4	131.4	130.1	130.5	129.4	128.1	136.8	133.7	131.9	130.8	130.8

and multiscale-fillers reinforced EP. Pure EP first exhibits a linear stress-strain response (between 0 and 0.3%, approximately) showing an *E*-modulus of about 2.71 GPa. The transition from elastic to nonelastic behavior was interpreted in terms of 'strain-softening' due to nonrecoverable deformation with increasing strain [44, 45]. Figure 1b shows the slopes, defined in [44] secant modulus E_{sm}, of the local points on the curves in Figure 1a as a function of strain. The data with strain from 0 to 0.3% was not shown due to the scattering of the data. The tendency of the so-called secant might give hints on debonding of fillers from polymer matrix in the loading process [44]. From Figure 1b, at a low strain

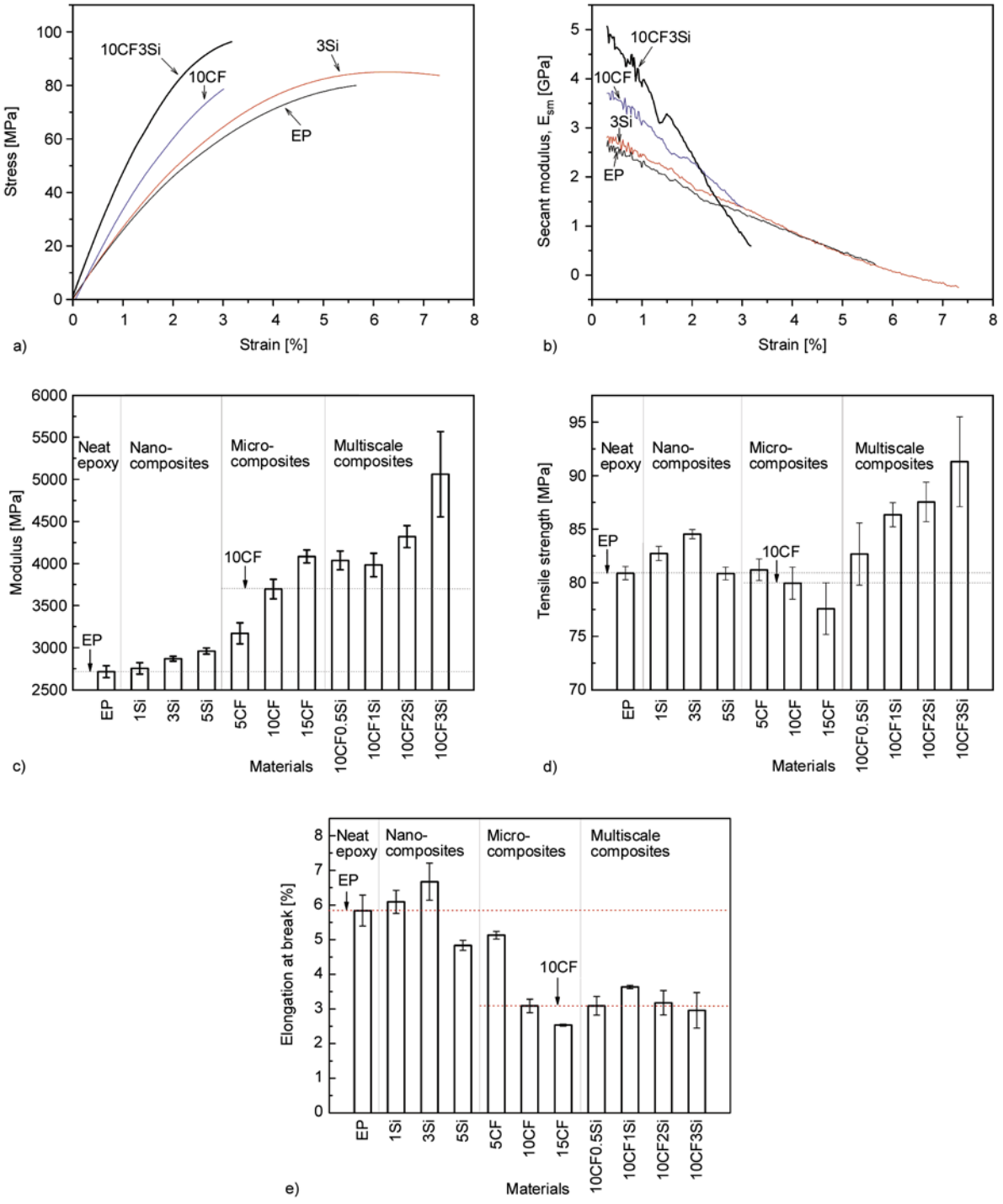

Figure 1. Stress-strain curves of typical materials studied (a), secant moduli of the materials in a (b), and the tensile characteristics: *E*-modulus (c), tensile strength (d) and elongation rate at break (e) of epoxy composites. Dash lines in (c), (d) and (e) indicating the levels of two reference materials, i.e. pure epoxy and SCFs/EP, are added for easier comparisons.

the secant modulus of the nanocomposite (3Si) is higher than EP. However, when the strain is higher than ~4.5%, the two materials have similar modulus. With respect to the SCF-composite, the secant modulus declines rapidly with increasing the strain due to debonding of SCFs, before critical failures take place. The 'strain-softening' effect of the multiscale composite (10CF3SiO_2) is more evident compared to 10CF. The enhanced 'strain-softening' of the multiscale composites compared with the SCF-composite will be discussed below.

The mean values of *E*-moduli, tensile strengths and elongations at break of the materials studied were displayed in Figure 1c – Figure 1e. The low-loading nanoparticles lead to a slight but significant increase in modulus (cf. Figure 1c). The tensile strength of epoxy is moderately increased with nanoparticles varying from 1 to 3 vol%. (cf. Figure 1d). A further increase of the nanoparticle loading to 5 vol% leads to a decrease in tensile strength. With a nanoparticle loading less than 3 vol%, the elongation rate is slightly increased. Filled with 5 vol% nanoparticles, however, the material exhibits a reduced ductility (cf. Figure 1e).

The reinforcing effect of SCFs is more prominent than that of the nanoparticles. Incorporation of 10 vol% SCF dramatically increases the *E*-modulus of the matrix. The *E*-modulus of the EP linearly increased with increasing the SCF fraction. The effect of randomly distributed SCFs on the strength is more dependent on the fiber-matrix interface than on their alignment [46, 47]. The incorporated SCFs in the present work do not lead to obvious improvement in tensile strength and even a slight decrease can be noticed if the SCF fraction is higher than 10 vol% (cf. Figure 1d). So, the constraint matrix deformability and the stress concentrations at the fibers significantly reduce the ductility of the matrix (Figure 1d). Therefore, in spite of the highly improved modulus, the tensile strength remained unaffected or even deteriorated due to the presence of SCFs (cf. Figure 1d).

The combination of the microfillers and the nanofillers leads to impressive improvements in modulus and strength data of the EP (cf. Figure 1c and Figure 1d). The modulus and strength of the multiscale composites increase with increasing the nanoparticle loading. Note that among the systems studied, application of multi-scale fillers was the only way to achieve improvements in modulus and strength at the same time. In addition, it is interesting to note that the enhancements in the modulus and strength owing to the multiscale fillers are significantly higher than the superposition of the separate contributions by respective fillers, as realized in the SCFs-filled and the nanoparticles-filled EP (cf. Figure 1c and Figure 1d). Therefore, the multiscale fillers have synergetic effects on the stiffeness and strength of the EP matrix. The elongation at break values of the multiscale composites are similar to those of the composites filled only with SCFs (cf. Figure 1e).

Figure 2a shows a typical fracture surface of the nanocomposites filled with nanoparticles (1Si). The crack propagation direction is indicated by an arrow. Numerous dimples can be recognized on the fracture surface (cf. Figure 2a).

With respect to the reinforcing effect of SCFs, according to the modified rule of mixture [48, 49], the stiffening (reinforcing) efficiency depends on the fiber aspect ratio and fiber orientation, as shown in Equations (1) and (2):

$$E = (\eta E_f - E_m)V_f + E_m \quad (1)$$

with

$$\eta = \eta_0 \eta_1 \quad (2)$$

where η is defined as a stiffening efficiency and η_0 and η_1 respectively the length efficiency factor and the orientation efficiency factor, respectively. E_f and E_m refer to the moduli of the fiber and the matrix, respectively. V_f is the volume fraction of the fibers. According to the linear relationship between the modulus and the volume fraction of SCFs (cf. Figure 1c), the η is determined to be about 0.05 for the EP+SCF composites. The stiffening efficiency of SCFs in this work agrees well with that achieved in polyethersulphone (PES) and polyphenylene sulphide (PPS) systems reinforced by randomly aligned SCFs [50]. Figure 2b and Figure 2c show representative tensile fracture surfaces of SCFs-filled epoxy (10SCF) with low and high magnifications, respectively. The EP matrix fails in a brittle manner except some ribs formed due to coalesce of cracks in different planes. Figure 2c displays a typical SCF-matrix interface taken from the fracture surface of 10CF. It is clear that the SCF-matrix interface was strongly involved in the cracking. The

propagation of local failure at SCF-matrix interface can be hindered by adhering points as indicated by dash-line arrows in Figure 2c.

Figure 2d, 2e and 2f display SEM pictures taken from the tensile fracture surface and SCF-matrix interface, respectively, of the multiscale composite (10CF3Si). Due to the large shear force provided by the dissolver, the nanoparticles were homogeneously distributed into the epoxy matrix although small agglomerates remain present in the matrix. Typically, the size of the small agglomerates is less than 100 nm, with some exceptions which are in submicron scales (cf. Figure 2e and Figure 2f). Comparing the fracture surfaces of the 10CF3Si and 10CF

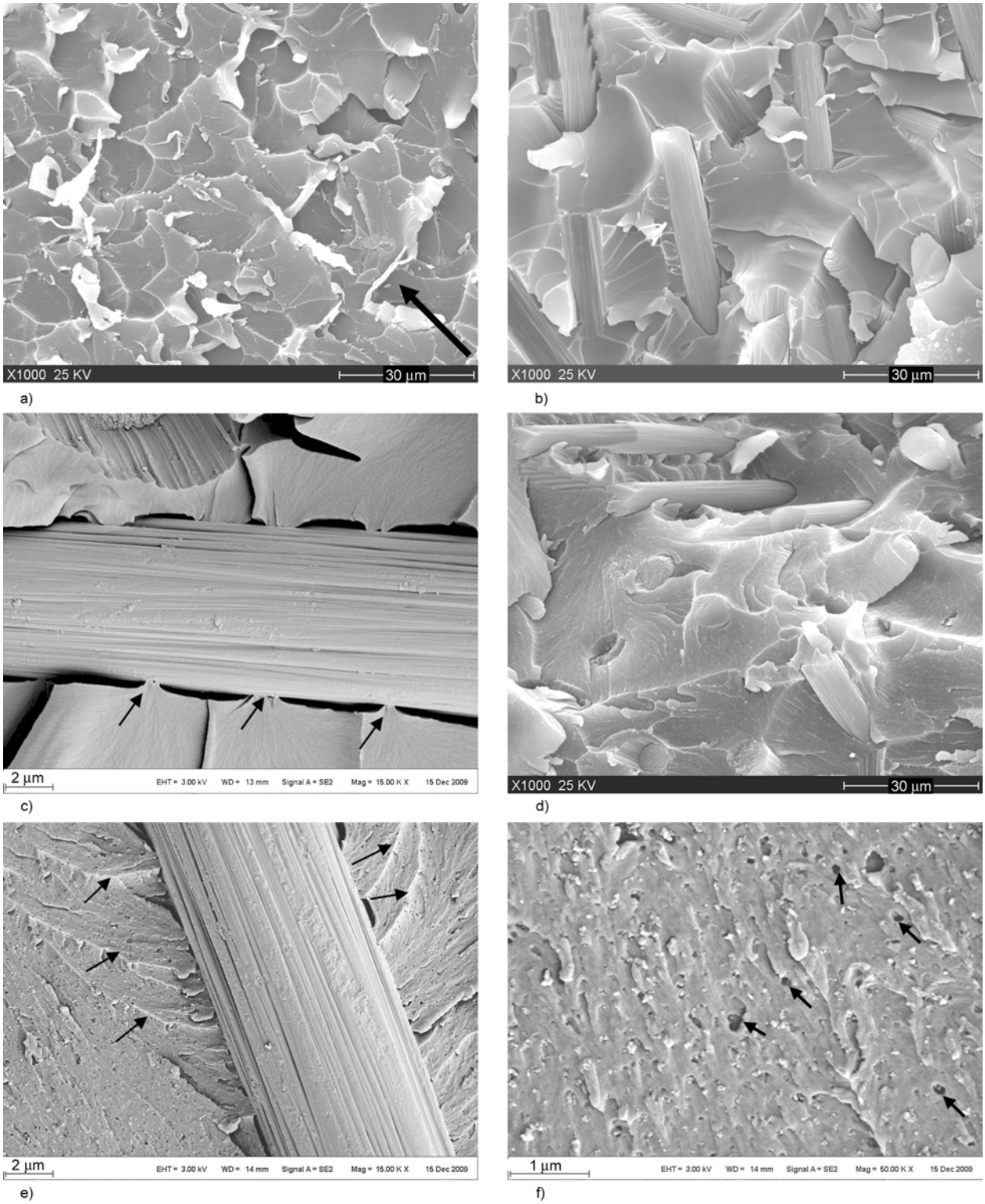

Figure 2. Fracture surfaces taken from tensile specimens 1Si (a), 10CF (b) and (c), 10CF3Si (d), (e) and (f)

(Figure 2d and Figure 2b), two features are clear. First, the fiber-matrix interface of the multiscale composite is far less damaged than in the SCF composite. Second, extensive plastic deformations and numerous microcracks can be resolved in the matrix of the multiscale composites. Some of the microcracks are indicated in Figure 2e by arrows. These microcracks were produced in the particle-particle ligaments and the particle-SCF ligaments due to the cavitation and debonding of nanoparticles. Figure 2f displays a local zone on the fracture surface of the multiscale composite at high magnification. It is clear that debonding of nanoparticles takes place. Significant matrix plastic dilatation, indicated by arrow in Figure 2f, can be found around the debonded nanoparticles. The obvious plastic dilatation of epoxy matrix is believed to form due to the cavitation of nanoparticles [4, 51, 52]. Nanoparticles first cavitate and induce crack bifurcation and pinning. As a result, before the onset of a critical crack numerous microcracks are produced. This triggers extensive shear yielding of the matrix (cf. Figure 2f). It is worth of noting that the supposed core-shell like structure of the nanoparticles strongly favors the cavitation. The sub-critical microcracks and the debonding of the nanoparticles are assumed to be the major mechanisms for the enhanced 'strain-softening' of the multiscale composite at a high strain.

According to the rule of mixture, the enhanced matrix stiffness due to the presence of nanoparticles will enhance the modulus of the multiscale composites, compared to the composites filled solely with SCFs. If we predict the modulus of the multiscale composites using the above mixture rule, the related moduli are only slightly higher than the conventional composite (10CF, cf. Figure 3). Comparing the predicted and experimental moduli, one can notice that the moduli of the multiscale composites are much higher than those predicted by the rule of mixture (cf. Figure 3). This suggests that the contribution of the nanoparticles on the modulus of the multiscale composites is much higher than predicted by additivity rule.

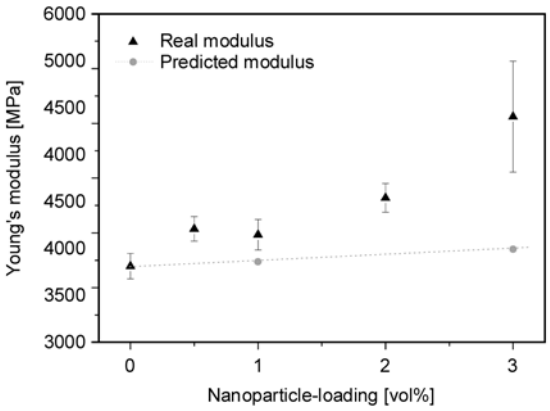

Figure 3. Difference between the real moduli of the hybrid composites and the predicted values using the mixture rule

During loading of the composites filled only with SCFs large local stresses develop in the matrix close to the fiber ends owing to stress concentration effects, and as a result larger local strains are signified in these regions [13, 15, 46]. The neighboring SCF are 'too far' in the brittle matrix, and thus they can hardly participate in the stress relief needed to avoid catastrophic fracture [13, 15, 46]. The scenario is different in the multiscale composites. The broken tensile specimens were polished in order to study with an optic microscope the morphologies under the fracture planes. Figure 4 illustrate the polished section of 10CF3Si. The diagram associated with Figure 4 shows the location from which observations were made. For the microcomposite, e.g. 10CF, no obvious cracking is noticed under the fracture plane [34]. However, multiple matrix cracks are observed under the fracture plane of the multiscale composite (the multiple cracking becomes less sharp on the graph due to the polishing). The multiple matrix cracks are also observed in case of the multiscale composites reinforced by combined SCFs and CNFs [34]. The formation of the multiple cracks gives hints that the stress field in the matrix between SCFs is homogenized with the presence of nanoparticles. This is due to the fact in the matrix in between the SCFs now well distributed nanoparticles are present which work for an efficient stress transfer and redistribution. Stress concentrations are relieved via cavitation of the nanoparticles making the matrix becomes more ductile. This is helpful in respect of the neighboring SCF which now can fulfill their reinforcing role accordingly. The outcome is a strongly enhanced strength as less stress concentration-induced premature failure occurs, which was found in fact (cf. Figure 1d). This failure sequence can also explain the observed changes in the fiber-matrix interfacial failure (cf. Figures 2c and 2e).

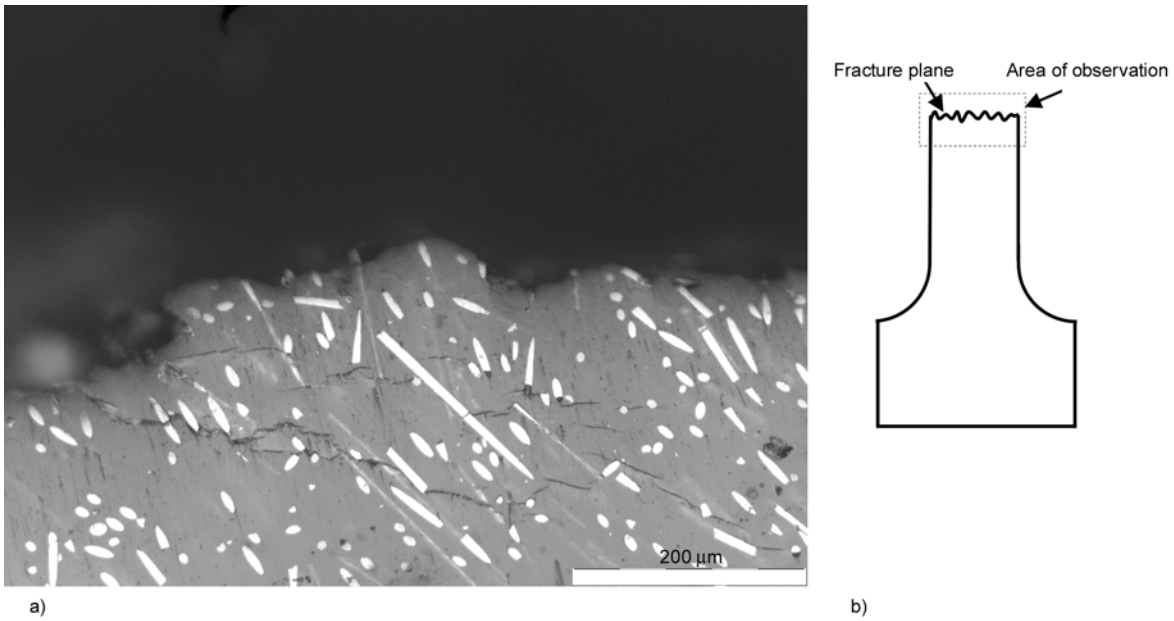

Figure 4. Optic micrographs of polished sections, perpendicular and near to the fracture planes (a), of 10CF3Si; the diagram associated shows the location observed (b)

For the composites filled only with SCFs the extra stress in the regions adjacent to a fiber end is associated with large local strain. The stress homogenization of the matrix due to the presence of nanoparticles enhances not only the *E*-modulus (Figure 1c), but also the ductility (elongation at break) of the multiscale composites. The data in Figure 1e indicates, however, remained or slightly enhanced ductility. The reason behind is the multiple microracking (cf. Figure 4) which is accompanied with an inherently small change in the elongation at break. Nevertheless, the multiple matrix cracking in Figure 4 evidence the stress relief proposed.

3.3. Fracture toughness

Figure 5a and Figure 5b show the fracture toughness, K_{IC}, and the critical energy release rate, G_{IC}, of the materials studied. The fracture toughness of the pure EP was 0.62 MPa·m$^{1/2}$ (cf. Figure 5a). The nanoparticles enhance the fracture toughness which increases monotonously with increasing nanoparticle concentration from 1.0 to 5.0 vol%. At 5.0 vol% nanoparticles content, the fracture toughness was increased by about 40%.With 5 vol% SCFs, the fracture toughness is increased by 47%. An increase in fiber-loading from 5 to 15 vol% leads to a steady increase in the fracture toughness. The addition of

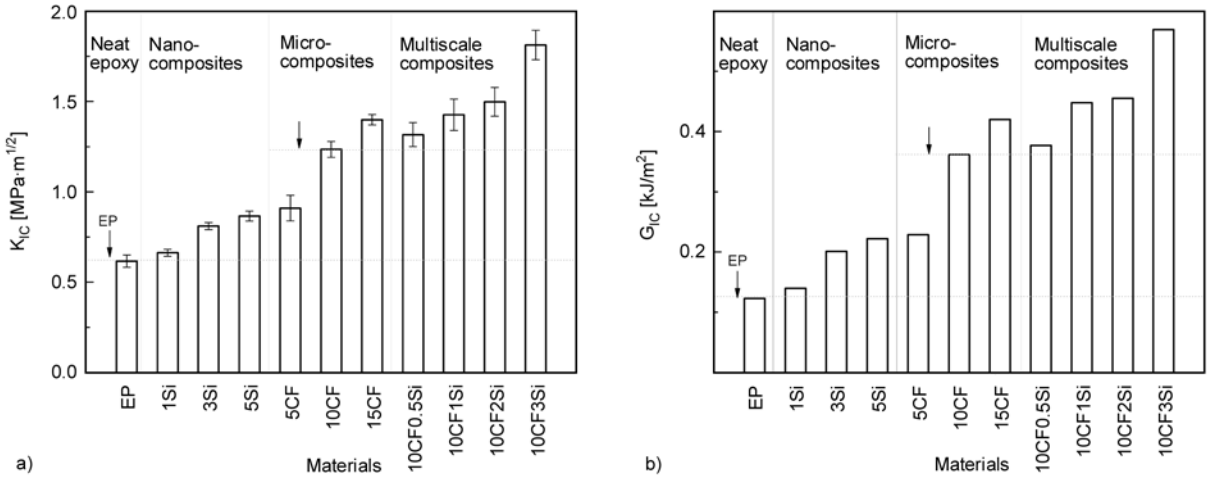

Figure 5. Fracture toughness, K_{IC}, (a) and critical energy release rate, G_{IC}, (b) of materials studied. Dash lines in (a) and (b) indicating the levels of two reference materials, i.e. pure epoxy and SCFs/EP, are added for easier comparisons.

10 vol% SCFs doubles the fracture toughness of the parent EP.

The multiscale composites present much higher fracture toughness than the corresponding micro-composite (10CF) and nanocomposites (1Si-3Si). It is interesting to note that the combination of nano-SiO_2 and SCF enhances the fracture toughness more than predicted by the additivity rule (cf. Figure 5a). For example, the combination of 10 vol% SCFs and 3 vol% nano-SiO_2 increases the fracture toughness of the pure EP by about 194%, while the superposition of the separate contributions of these two fillers, as respectively achieved in 3Si and 10CF, would result in a value of 132%. The tendency of G_{IC} is similar to that of K_{IC}. Figure 5b shows that both the nanoparticles and the SCFs increase the G_{IC} of the EP. As to the multiscale composites with a nanoparticle concentration 1 to 3 vol%, the combination of nano-SiO_2 and SCF leads to an improvement in G_{IC} which is significantly higher than the predicted one based on the rule of additivity.

Figure 6a shows the typical fracture surface of the nanocomposite filled with nano-SiO_2 (3Si). The fracture propagation direction is downward as indicated by an arrow, which is identical to all the other CT fracture surfaces presented in this paper. Numerous ribs can be detected on the fracture surface. Note that the fracture surface of pure epoxy is very smooth without hints for significant plastic deformation [34]. These ribs are formed when the cracks moving in slightly different planes coalesce, and they are believed to contribute to toughness improvement [4, 27]. Figure 6b illustrates the fracture surface of 3Si near the crack tip at high magnification. The nanoparticles cavitate and debond from the matrix and they induce crack bifurcation and pinning. As results of the cavitation and crack pinning, two or more fracture planes are produced. This is helpful for the matrix to dissipate energy by shear yielding, the onset of which is obvious by the ribs [21, 51, 52].

Figure 6c shows the CT fracture surface of 10CF. When plane strain conditions prevail, the typical crack path in short fiber reinforced composites is of zig-zag type, as was intensively analyzed by Karger-Kocsis and Friedrich [13–16]. Three major failure mechanisms dominate the fracture behavior of conventional composites filled with short fibers:

1. Pull-out and fracture of fibers, lying more or less perpendicular to the crack front;
2. Fiber/matrix debonding of fibers aligned more parallel to the fracture plane;
3. Stress concentration on fiber ends, followed by brittle fracture of the epoxy matrix;

All these events happen in a limited plastic zone (or termed damage zone).

Figure 6d displays a typical fracture surface of the multiscale composites (10CF3Si). Pull-out, fracture of fibers, and fiber/matrix debonding are also clearly observable on the fracture surface. Figure 6e and Figure 6f show the fracture surfaces at higher magnifications. Compared to the SCF-EP composites, the matrix fails less brittlely in case of the multiscale composites. Extensive micro-mechanical deformations of the matrix are clearly noticed in Figure 6d to Figure 6f. Similar to the nancomposites, the nanoparticles in front of the crack tip cavitate, debond, cause crack bifurcation, crack pinning and microcracks. By this way the nanoparticles can relieve the overstress on fiber ends in the vicinity of the crack tip. As consequence, compared to the conventional composite (10CF) [34], a larger plastic zone develops in which other SCFs can participate in the stress transfer (in case of multiscale composites), as schematically illustrated in Figure 7. Surely, this leads to enhancements in K_{IC} and G_{IC}, compared with SCFs-filled epoxy. Therefore, the contribution of the nanoparticles is twofold. First, they improve the fracture toughness triggering such mechanisms as cavitation, crack bifurcation and pinning etc. Second, they can relieve the overload near to the fiber ends in front of the crack tip via the above matrix-related failure events. The overall outcome is an enlarged plastic zone which is assumed to be the key factor for the synergisms reported.

As aforementioned, applaudable improvements in mechanical and fracture properties are also achieved in our recent work with combining SCFs with CNFs [34]. Basing on these works, it is assumed that the distinctly different dimensions of the combined fillers are the key factor for their synergetic roles. In the multiscale composite system, the nano-sized fillers can protect the micro-sized fillers by release stress concentration occurring near the microfillers. In comparison to nanoparticles, it seems that the

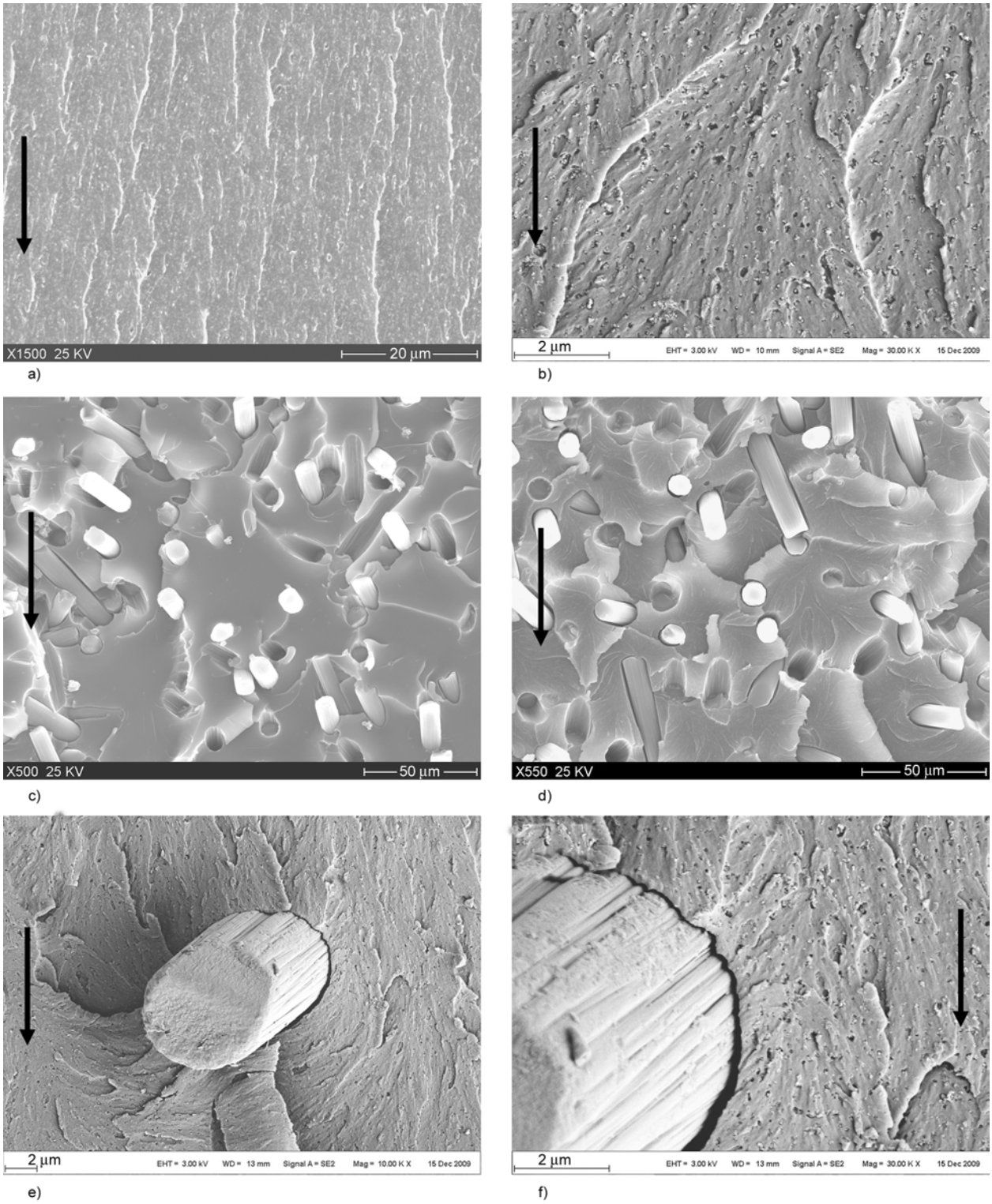

Figure 6. Fracture surfaces taken from CT tests of 3Si (a) and (b), 10CF (c), 10CF3Si (d), (e) and (f)

efficiency of CNFs is more efficient on improving the mechanical and fracture properties. That is, less CNF fraction is required for improving the SCFs-EP properties to the same extent as realized by nanoparticles. This can be related to the high aspect ratios of CNFs, which may lead to a more efficient stress transfer.

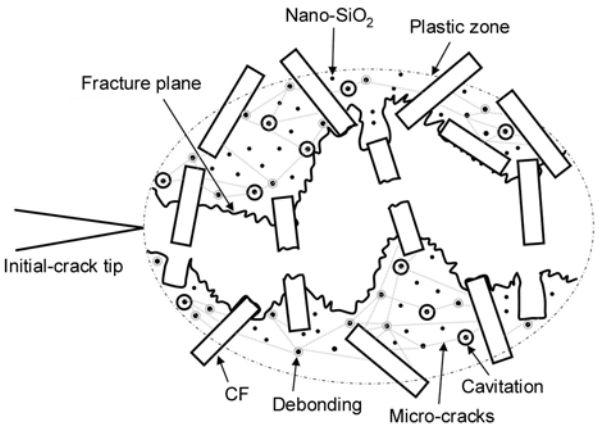

Figure 7. Schematic of plain-strain failure modes proposed for epoxy composites filled with SCFs and nanoparticles. The sizes of the fillers were not depicted in proportion

4. Conclusions

In the present work, mechanical and fracture properties of three series of epoxy composites were compared. The three series of composites are respectively I: microcomposites filled with micron SCFs ranging from 5 to 15 vol%, II: nanocomposites filled with silica nanoparticles up to 5 vol% and III: multiscale composites filled with the both fillers. Incorporation of multiscale fillers was associated with synergetic effects in respect to the tensile (*E*-modulus, strength) and fracture properties (K_{IC} and G_{IC}) of EP resin. Based on this work the following conclusions can be drawn:

1. Filled with nanosilica particles in low concentration range, the modulus of EP can only be slightly increased and the tensile strength is slightly increased or remained. The nanoparticles increase moderately the fracture toughness of epoxy. Filled with micro-sized SCFs, the modulus of epoxy is highly improved, however at cost of the elongation rate which is dramatically reduced. The tensile strength is remained or slightly reduced. The fracture toughness is improved with increasing the SCF fraction up to 15 vol%. With a SCF loading higher than 10 vol%, the fracture toughness of the EP can be almost doubled.
2. The combination of the multiscale fillers leads to a significant synergism in both of the tensile and fracture mechanical responses of the EP. The contributions of the combined fillers to the *E*-modulus, tensile strength, fracture toughness and fracture energy are markedly higher than those expected by the additivity rule considering the separate contributions of the respective fillers. The nanoparticles cavitate, induce crack bifurcation and crack pinning. Shear yielding of matrix and microcracks near SCFs take place. By this way, stress concentration near fibers, especially fiber ends, is efficiently relieved. As consequence, a larger plastic zone develops in presence of both nano-(SiO_2) and micro-fillers (SCF) than solely in the SCF-reinforced EP. This is believed to be the major reason for the synergetic effects observed for the EP with multiscale fillers.

Acknowledgements

This work is connected to the scientific program of the 'Development of quality-oriented and harmonized R+D+I strategy and functional model at BME' project. This project is supported by the New Széchenyi Plan (Project ID: TÁMOP-4.2.1/B-09/1/KMR-2010-0002).

References

[1] Teh S. F., Liu T., Wang L., He C.: Fracture behaviour of poly(ethylene terephthalate) fiber toughened epoxy composites. Composites Part A: Applied Science and Manufacturing, **36**, 1167–1173 (2005). DOI: 10.1016/j.compositesa.2004.08.007

[2] Sue H-J.: Craze-like damage in a core-shell rubber-modified epoxy system. Journal of Materials Science, **27**, 3098–3107 (1992). DOI: 10.1007/BF01154125

[3] Bagheri R., Pearson R. A.: Role of particle cavitation in rubber-toughened epoxies: 1. Microvoid toughening. Polymer, **37**, 4529–4538 (1996). DOI: 10.1016/0032-3861(96)00295-9

[4] Karger-Kocsis J., Friedrich K.: Microstructure-related fracture toughness and fatigue crack growth behaviour in toughened, anhydride-cured epoxy resins. Composites Science and Technology, **48**, 263–272 (1993). DOI: 10.1016/0266-3538(93)90143-5

[5] Nguyen F. N., Berg J. C.: Novel core–shell (dendrimer) epoxy toughenes: Processing and hot–wet performance. Composites Part A: Applied Science and Manufacturing, **39**, 1007–1011 (2008). DOI: 10.1016/j.compositesa.2008.03.005

[6] Cardwell B. J., Yee A. F.: Toughening of epoxies through thermoplastic crack bridging. Journal of Materials Science, **33**, 5473–5484 (1998). DOI: 10.1023/A:1004427123388

[7] Lee J., Yee A. F.: Fracture behavior of glass bead filled epoxies: Cleaning process of glass beads. Journal of Applied Polymer Science, **79**, 1371–1383 (2001). DOI: 10.1002/1097-4628(20010222)79:8<1371::AID-APP40>3.0.CO;2-O

[8] Lee J., Yee A. F.: Inorganic particle toughening I: Micro-mechanical deformations in the fracture of glass bead filled epoxies. Polymer, **42**, 577–588 (2001). DOI: 10.1016/S0032-3861(00)00397-9

[9] Lee J., Yee A. F.: Inorganic particle toughening II: Toughening mechanisms of glass bead filled epoxies. Polymer, **42**, 589–597 (2001). DOI: 10.1016/S0032-3861(00)00398-0

[10] Adachi T., Osaki M., Araki W., Kwon S-C.: Fracture toughness of nano- and micro-spherical silica-particle-filled epoxy composites. Acta Materialia, **56**, 2101–2109 (2008). DOI: 10.1016/j.actamat.2008.01.002

[11] Sanadi A. R., Piggott M. R.: Interfacial effects in carbon-epoxies. Part 3. Toughness with short fibres. Journal of Materials Science, **21**, 1642–1646 (1986). DOI: 10.1007/BF01114720

[12] Piggott M. R.: The effect of aspect ratio on toughness in composites. Journal of Materials Science, **9**, 494–502 (1974). DOI: 10.1007/BF00737854

[13] Karger-Kocsis J.: Instrumented impact fracture and related failure behavior in short- and long-glass-fiber-reinforced polypropylene. Composites Science and Technology, **48**, 273–283 (1993). DOI: 10.1016/0266-3538(93)90144-6

[14] Karger-Kocsis J.: Structure and fracture mechanics of injection-molded composites. in 'International encyclopedia of composites' (ed.: Lee S.M.) VCII Publishers, New York, Vol 5, 337–356 (1991).

[15] Karger-Kocsis J., Friedrich K.: Microstructural details and the effect of testing conditions on the fracture toughness of injection-moulded poly(phenylene-sulphide) composites. Journal of Materials Science, **22**, 947–961 (1987). DOI: 10.1007/BF01103535

[16] Friedrich K.: Microstructural efficiency and fracture toughness of short fiber/thermoplastic matrix composites. Composites Science and Technology, **22**, 43–74 (1985). DOI: 10.1016/0266-3538(85)90090-9

[17] Farber K. T., Evans A. G.: Crack deflection process-I. Theory. Acta Metallurgica, **31**, 565–576 (1983). DOI: 10.1016/0001-6160(83)90046-9

[18] Farber K. T., Evans A. G.: Crack deflection process-II. Experiment. Acta Metallurgica, **31**, 577–584 (1983). DOI: 10.1016/0001-6160(83)90047-0

[19] Lange F. F.: The interaction of a crack front with a second-phase dispersion. Philosophical Magazine, **22**, 983–992 (1970). DOI: 10.1080/14786437008221068

[20] Green D. J., Nicholson P. S., Embury J. D.: Fracture of a brittle particulate composite. Part 2. Theoretical aspects. Journal of Materials Science, **14**, 1657–1661 (1979). DOI: 10.1007/BF00569287

[21] Wetzel B., Rosso P., Haupert F., Friedrich K.: Epoxy nanocomposites – Fracture and toughening mechanisms. Engineering Fracture Mechanics, **73**, 2375–2398 (2006). DOI: 10.1016/j.engfracmech.2006.05.018

[22] Wetzel B., Haupert F., Zhang M. Q.: Epoxy nanocomposites with high mechanical and tribological performance. Composites Science and Technology, **63**, 2055–2067 (2003). DOI: 10.1016/S0266-3538(03)00115-5

[23] Sanadi A. R., Piggott M. R.: Interfacial effects in carbon-epoxies. Part 1. Strength and modulus with short aligned fibres. Journal of Materials Science, **20**, 421–430 (1985). DOI: 10.1007/BF01026510

[24] Zhang H., Tang L-C., Zhang Z., Friedrich K., Sprenger S.: Fracture behaviours of in situ silica nanoparticle-filled epoxy at different temperatures. Polymer, **49**, 3816–3825 (2008). DOI: 10.1016/j.polymer.2008.06.040

[25] Ma J., Mo M-S., Du X-S., Rosso P., Friedrich K., Kuan H-C.: Effect of inorganic nanoparticles on mechanical property, fracture toughness and toughening mechanism of two epoxy systems. Polymer, **49**, 3510–3523 (2008). DOI: 10.1016/j.polymer.2008.05.043

[26] Zhang H., Zhang Z., Friedrich K., Eger C.: Property improvements of in situ epoxy nanocomposites with reduced interparticle distance at high nanosilica content. Acta Materialia, **54**, 1833–1842 (2006). DOI: 10.1016/j.actamat.2005.12.009

[27] Rosso P., Ye L., Friedrich K., Sprenger S.: A toughened epoxy resin by silica nanoparticle reinforcement. Journal of Applied Polymer Science, **100**, 1849–1855 (2006). DOI: 10.1002/app.22805

[28] Johnsen B. B., Kinloch A. J., Mohammed R. D., Taylor A. C., Sprenger S.: Toughening mechanisms of nanoparticle-modified epoxy polymers. Polymer, **48**, 530–541 (2007). DOI: 10.1016/j.polymer.2006.11.038

[29] Uddin M. F., Sun C. T.: Strength of unidirectional glass/epoxy composite with silica nanoparticle-enhanced matrix. Composites Science and Technology, **68**, 1637–1643 (2008). DOI: 10.1016/j.compscitech.2008.02.026

[30] Manjunatha C. M., Taylor A. C., Kinloch A. J., Sprenger S.: The tensile fatigue behaviour of a silica nanoparticle-modified glass fibre reinforced epoxy composite. Composites Science and Technology, **70**, 193–199 (2010). DOI: 10.1016/j.compscitech.2009.10.012

[31] Qiu J., Zhang C., Wang B., Liang R.: Carbon nanotube integrated multifunctional multiscale composites. Nanotechnology, **18**, 275708/1–275708/11 (2007). DOI: 10.1088/0957-4484/18/27/275708

[32] Karapappas P., Vavouliotis A., Tsotra P., Kostoppoulos V., Paipetis A.: Enhanced fracture properties of carbon reinforced composites by the addition of multi-wall carbon nanotubes. Journal of Composite Materials, **43**, 977–985 (2009).
DOI: 10.1177/0021998308097735

[33] Yokozeki T., Iwahori Y., Ishibashi M., Yanagisawa T., Imai K., Arai M., Takahashi T., Enomoto K.: Fracture toughness improvement of CFRP laminates by dispersion of cup-stacked carbon nanotubes. Composites Science and Technology, **69**, 2268–2273 (2009).
DOI: 10.1016/j.compscitech.2008.12.017

[34] Zhang G., Karger-Kocsis J., Zou J.: Synergetic effect of carbon nanofibers and short carbon fibers on the mechanical and fracture properties of epoxy resin. Carbon, **48**, 4289–4300 (2010).
DOI: 10.1016/j.carbon.2010.07.040

[35] Allaoui A., Bounia N. E.: How carbon nanotubes affect the cure kinetics and glass transition temperature of their epoxy composites? – A review. Express Polymer Letters, **3**, 588–594 (2009).
DOI: 10.3144/expresspolymlett.2009.73

[36] Vassileva E., Friedrich K.: Epoxy/alumina nanoparticle composites. I. Dynamic mechanical behavior. Journal of Applied Polymer Science, **89**, 3774–3785 (2003).
DOI: 10.1002/app.12463

[37] Huang G. C., Lee J. K.: Isothermal cure characterization of fumed silica/epoxy nanocomposites: The glass transition temperature and conversion. Composites Part A: Applied Science and Manufacturing, **41**, 473–479 (2010).
DOI: 10.1016/j.compositesa.2009.12.003

[38] Ragosta G., Abbate M., Musto P., Scarinzi G., Mascia L.: Epoxy-silica particulate nanocomposites: Chemical interactions, reinforcement and fracture toughness. Polymer, **46**, 10506–10516 (2005).
DOI: 10.1016/j.polymer.2005.08.028

[39] Sun Y., Zhang Z., Moon K-S., Wong C. P.: Glass transition and relaxation behavior of epoxy nanocomposites. Journal of Polymer Science Part B: Polymer Physics, **42**, 3849–3858 (2004).
DOI: 10.1002/polb.20251

[40] Liu Y-L., Hsu C-Y., Wei W-L., Jeng R-J.: Preparation and thermal properties of epoxy-silica nanocomposites from nanoscale colloidal silica. Polymer, **44**, 5159–5167 (2003).
DOI: 10.1016/S0032-3861(03)00519-6

[41] Becher O., Varley R., Simon G.: Morphology, thermal relaxations and mechanical properties of layered silicate nanocomposites based upon high-functionality epoxy resins. Polymer, **43**, 4365–4373 (2002).
DOI: 10.1016/S0032-3861(02)00269-0

[42] Preghenella M., Pegoretti A., Migliaresi C.: Thermomechanical characterization of fumed silica-epoxy nanocomposites. Polymer, **46**, 12065–12072 (2005).
DOI: 10.1016/j.polymer.2005.10.098

[43] Barrau S., Demont P., Maraval C., Bernes A., Lacabanne C.: Glass transition temperature depression at the percolation threshold in carbon nanotube–epoxy resin and polypyrrole–epoxy resin composites. Macromolecular Rapid Communications, **26**, 390–394 (2005).
DOI: 10.1002/marc.200400515

[44] Meddad A., Fisa B.: Stress-strain behavior and tensile dilatometry of glass bead-filled polypropylene and polyamide 6. Journal of Applied Polymer Science, **64**, 653–665 (1997).
DOI: 10.1002/(SICI)1097-4628(19970425)64:4<653::AID-APP4>3.0.CO;2-M

[45] Sudár A., Móczó J., Vörös Gy., Pukánszky B.: The mechanism and kinetics of void formation and growth in particulate filled PE composites. Express Polymer Letters, **1**, 763–772 (2007).
DOI: 10.3144/expresspolymlett.2007.105

[46] Sanadi A. R., Piggott M. R.: Interfacial effects in carbon-epoxies. Part 1. Strength and modulus with short aligned fibres. Journal of Materials Science, **20**, 421–430 (1985).
DOI: 10.1007/BF01026510

[47] Bowyer W. H., Bader M. G.: On the re-inforcement of thermoplastics by imperfectly aligned discontinuous fibres. Journal of Materials Science, **7**, 1315–1321 (1972).
DOI: 10.1007/BF00550698

[48] Carman G. P., Reifsnider K. L.: Micromechanics of short-fiber composites. Composites Science and Technology, **43**, 137–146 (1992).
DOI: 10.1016/0266-3538(92)90004-M

[49] Krenchel H.: Fibre reinforcement. Akademisk Forlag, Copenhagen (1964).

[50] Lin G. M., Lai J. K. L.: Fracture mechanism in short fibre reinforced thermoplastic resin composites. Journal of Materials Science, **28**, 5240–5246 (1993).
DOI: 10.1007/BF00570071

[51] Karger-Kocsis J., Friedrich K.: Fatigue crack propagation and related failure in modified, andhydride-cured epoxy resins. Colloid and Polymer Science, **270**, 549–562 (1992).
DOI: 10.1007/BF00658286

[52] Sue H-J., Garcia Meitin E. I., Picklman D. M., Bott C. J.: Fracture mechanisms in rigid core-shell particle modified high performance epoxies. Colloid and Polymer Science, **274**, 342–349 (1996).
DOI: 10.1007/BF00654054

eXPRESS Polymer Letters Vol.5, No.10 (2011) 873–881
Available online at www.expresspolymlett.com
DOI: 10.3144/expresspolymlett.2011.86

Modification and mechanical properties of electrospun blended fibermat of PLGA and siloxane-containing vaterite/PLLA hybrids for bone repair

*G. Poologasundarampillai, K. Fujikura, A. Obata, T. Kasuga**

Department of Frontier Materials, Nagoya Institute of Technology, Gokiso-cho, Showa-ku, Nagoya 466-8555, Japan

Received 17 February 2011; accepted in revised form 11 April 2011

Abstract. Multi-syringe electrospinning has been successfully employed to produce a blended fibermat composed of poly(lactic-glycolic acid) (PLGA) fibers and a composite fiber for bone repair. The composite fiber, siloxane-containing vaterite (SiV)/poly(L-lactic acid) (PLLA), donated as SiPVH has the ability to release soluble silica species and calcium ions at a controlled rate. The SiPVH fibermats have demonstrated excellent bone regeneration ability *in vivo* at the front midline of the calvaria of rabbits. However, they are brittle and have low tensile strength resulting from the large particulate SiV (60 wt%) content. In this study, co-electrospinning of PLGA with SiPVH was performed in the hope of achieving a blended fibermat with improved mechanical properties. The co-electrospun fibermats showed good homogeneous blending of the PLGA and SiPVH composite fibers that had excellent flexibility. The blended PLGA-SiPVH fibermats had significantly improved mechanical properties compared to the SiPVH fibermats, where more than 20 times higher elongation to failure was achieved on comparison to the SiPVH fibermat. As well as strength, high porosity and large pore size are vital for the migration of cells into the centre of the graft. This was accomplished by heating the PLGA-SiPVH fibermats at 110°C for a fixed time, which induced the softening and flow of PLGA towards the more stable SiPVH fibers. Heating had successfully produced PLGA-SIPVH fibermats with large open pores and inter-fused SiPVH fibers, which also had better tensile mechanical properties than the SiPVH fibermat.

Keywords: *biopolymers, biocomposites, electrospinning, blended fibermat, mechanical properties*

1. Introduction

Large maxillofacial defects are often regenerated with barrier membranes [1–3]. Barrier membranes function by containing the regeneration site from ingression of soft tissue into the defect site, which is often filled with bone harvested from the patients and/or biological agents such as bone forming cells and growth factors [3]. These, also called guided bone regeneration (GBR) membranes are required to be biocompatible, integrate with host-surrounding tissue and have high mechanical properties and flexibility to maintain and support defect site and should also be easy to handle.

Fibrous membranes are promising as GBR materials due to their high and breathable interconnected porosity [3–8]. This allows efficient transport of nutrient and oxygen into and metabolic waste out of the regeneration site. The fibrous structure enhances cell attachment [9], therefore promotes soft tissue growth along the membrane while the porosity can be designed to inhibit in-growth. Electrospinning is a simple and versatile method to produce fibermats with fiber diameters ranging from nano-micrometer [10–12]. Electrospun materials are very promising for the regeneration of tissues and organs [13–15] due to the possibility of mimicking some of the

*Corresponding author, e-mail: kasuga.toshihiro@nitech.ac.jp

structural features of natural extra cellular matrix (ECM) [16]. Numerous studies show the enhanced cellular attachment and proliferation on the fibrous materials [9, 17, 18]. Several studies have also shown the higher mechanical properties, especially the elongation to failure, of the electrospun fibermats [19–22] and blended fibermats [23]. The mechanical properties of electrospun fibers depends greatly on the degree of alignment of the fibers within the mat, fiber lay-ups and interface properties of fiber-fiber contact [20, 24]. Therefore, the versatility of electrospinning presents a promising method of fiber production for biomedical application.

The current authors have previously employed electrospinning to fabricate bi-layered GBR membranes that were shown to be bioactive, biocompatible and mechanically strong while being flexible [25]. The bi-layered membranes consists of two layers, a PLLA fibermat layer and a siloxane-containing vaterite (SiV) / PLLA composite fibermat layer (SiPVH) [25, 26]. The PLLA layer acted as the soft tissue barrier membrane, where the interconnected porosity was optimised by tailoring the fiber diameter to inhibit cell migration into the depth of the fibermat. The SiPVH fibermat layer provides space for bone formation. Both, the PLLA and the SiPVH layers were bonded together by hot-pressing with a stainless steel mesh that was placed on top of the PLLA layer. Whereby, at regions on the fibermat in contact with the steel mesh fiber-fiber fusion was induced [26]. Early experiments on SiPVH dip-coated membranes showed MC3T3-E1 cells proliferate on the membrane and more so on the hydroxyl carbonate apatite (HCA) coated SiPVH [5]. Therefore, the authors had also coated the bi-layered membranes with a bone mineral-like apatite layer by soaking in simulate body fluid (SBF). The authors then performed *in vivo* experiments on New Zealand rabbits by placing the bi-layered GBR membranes at the 8 mm defects in the front midline of the calvaria of the rabbits [25]. They found enhanced bone formation on the SiVPVH composite layer at the sites where depressions (regions of fiber-fiber fusion) were made my stainless steel mesh. Their study of the fibermat morphology showed a unique melted structure which they proposed could have influenced the cells to proliferate and lay-down new bone faster at those sites [25, 26]. They also noted that the cells could only migrate through the non-depressed areas; therefore porosity for cell migration was important [25].

From an enhancement of bone regeneration point of view; it is highly desirable to obtain the melt-fused morphology throughout the fibermat, however the hot-pressing process closes majority of the pores, which are critical for cell migration. The hot-pressing process that leads to the desired unique morphology is also the major drawback in this material. Therefore innovative processing methods are required to overcome this hurdle in achieving the unique morphology. Here, in this study one such strategy is explored. The fabrication of the unique melted structure throughout the fibermat was attempted by electrospinning a blended fibermat and applying a heating procedure that induced partial melting and fusion of the poly(lactic glycolic acid) (PLGA) fibers. In addition to the melt-fused morphology, by co-spinning PLGA and SiPVH, the blended fibermat was expected to have improved mechanical properties, which is important for ease of handling, shaping to specific shape and finally to support the biological moieties and cells during the process of bone regeneration.

2. Experimental section

PLLA (Purasorb®; PURAC, The Netherlands) and PLGA (53% lactic, 47% glycolic) (Purasorb®; PURAC, The Netherlands) with average molecular weight (M_w) of 260 kDa and 160 kDa, respectively were used. Chloroform was purchased from Wako Pure Chemical Industries, Ltd., Osaka, Japan.

2.1. Preparation of SiV particles

The silicon-doped calcium carbonate (SiV) powders were prepared by a carbonation process as described by Yasue *et al.* [27] and later modified by Kasuga *et al.* [28]. Briefly, calcium hydroxide ($Ca(OH)_2$) and aminopropyltriethoxysilane (APTES) were mixed together in methanol, followed by a constant bubbling of CO_2 gas for 75 min at a rate of 2 l·min^{-1}. The resulting slurry was dried at 110°C, resulting in the formation of SiV powder with average particle size of 1 μm.

2.2. Preparation of PLGA-SiPVH blended fibermats

The SiPVH fibermats were prepared according to the procedure described by Obata *et al.* [25]. Briefly,

SiV particles containing fibers, SiPVH, was produced by electrospinning a composite solution of 60 wt% SiV and 40 wt% PLLA. The composite solution was prepared by melt blending SiV and PLLA at 200°C for 10 min with a kneader and dissolved in chloroform with 10 wt% polymer concentration. Electrospun fibers of PLGA were produced after dissolving in chloroform with 10 wt% polymer concentration. Samples were then electrospun on the Nanofiber Electrospinning Unit (NEU, Kato Tech Co, Japan). The mixtures for electrospinning were loaded into a glass syringe and pushed out at a flow rate of 0.50 μl·s^{-1} through a metallic needle (22 gauge for SiPVH and 19 gauge for PLGA) that was connected to a +20 kV electric field. The fibers were collected on a rotating drum that was positioned 15 cm from the tip of the needle. Blended fibermats were produced by electrospinning two separate solutions side-by-side. Blended fibermats containing fibers of PLGA-SiPVH were produced with a final thickness of 230 μm after spinning for 210 min.

2.3. Modification of blended fibermats

PLGA-SiPVH fibermats were cut into circular membranes with a diameter of 17 mm. These were heated in a drying oven at 90, 110 and 130°C for 15, 20, 25 and 30 min to obtain the heat-fused morphology of the PLGA-SiPVH fibermats. Previous work has demonstrated the enhanced cellular proliferation of MC3T3 cells on an HA coated SiPVH fibermat in comparison to an uncoated SiPVH fibermats [26]. Therefore, cut fibermats before and after heating were soaked in a solution containing ions with 1.5 times the concentration of conventional simulated body fluid (SBF) to obtain the HA coating. The 1.5 SBF solution consisting of 3.75 mM Ca^{2+}, 213.0 mM Na^{+}, 2.25 mM Mg^{2+}, 7.5 mM K^{+}, 222.45 mM Cl^{-}, 6.3 mM HCO_3^{-}, 1.5 mM HPO_4^{2-}, 0.75 mM SO_4^{2-}, 50 mM $(CH_2OH)_3CNH_2$ and 45.0 mM HCl was prepared using reagent grade NaCl, $NaHCO_3$, KCl, $K_2PO_4{\cdot}3H_2O$, $MgCl_2{\cdot}6H_2O$, HCl, $CaCl_2$, $NaSO_4$ and $NH_2C(CH_2OH)_3$. After immersion in 1.5 SBF solution for 24 h the membranes were washed with distilled water and dried at room temperature.

2.4. Characterisation of blended fibermats

Samples for scanning electron microscopic (SEM, JSM-6301F, JEOL, Japan) observations were coated with amorphous osmium using an Os coater (Neoc, Meiwafosis, Japan) and observed under 5 kV accelerating voltage and 15 mm working distance.

Tensile tests were performed on the AGS-G, Shimadzu, Japan machine equipped with a 50 N load cell. Rectangular samples with dimensions of 5 mm × 40 mm were cut out of the fibermats and tested with a grip-to-grip separation of 20 mm at a strain rate of 5 mm/min. Samples were tested until complete failure and SEM observations were performed on the failed samples.

3. Results and discussion

Figure 1 shows the SEM images of the PLGA-SiPVH blended fibermats. The SiPVH on comparison to PLGA fibers has a much rougher fibrous surface due to the presence of SiV particles in the SiPVH fibers. The SiPVH fibers also have a large average fiber diameter than the PLGA, this was due to the higher viscosity of the SiPVH (5312 mPa·s) electrospinning solution than PLGA (793 mPa·s). The fiber diameters measured from the SEM images of PLGA ranged from 1.5–10.0 μm and the average diameter of SiPVH was measured to be 18±5 μm. The fiber diameter of SiPVH was found to be more homogeneous than that of PLGA. The cross-sectional image of the PLGA-SiPVH fibermat (Figure 1b) shows that the polymer and SiPVH fibers were very well blended.

3.1. Heating of PLGA-SiPVH blended fibermats

Optical microscopy was performed on the samples heated at 90, 110 and 130°C for 15 and 30 min (data not shown). The PLGA-SiPVH fibermat heated at 90°C for 30 min showed only a very small change in original morphology. On the other hand, at 130°C complete melting and large run off of the PLGA fibers were observed at both 15 and 30 min of heating. Figure 2 shows the SEM images of the PLGA-SiPVH fibermats after heating at 110°C for 15, 20, 25 and 30 min. All the PLGA-SiPVH fibermats heated at 110°C showed PLGA softening and flow;

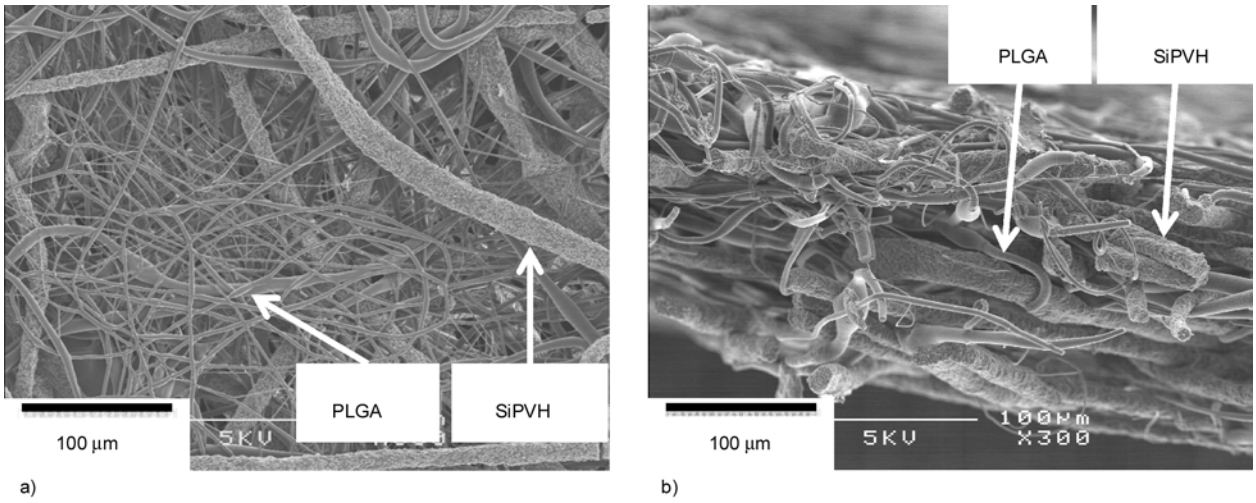

Figure 1. Surface (a) and cross-sectional (b) SEM images of the PLGA-SiPVH fibermat

this lead to fusion with the SiPVH fibers. An identical morphology was observed after heating for 15 and 20 min, here the initial as-spun PLGA fibrous network is still vaguely visible, more so in the 15 min heated sample. However, more coalescence of the PLGA was observed on the 20 min heated sample. On the other hand, heating for 30 min produced a large amount of flow where almost all the PLGA has aggregated towards the SiPVH fibers. However, heating for 25 min seems to have pro-

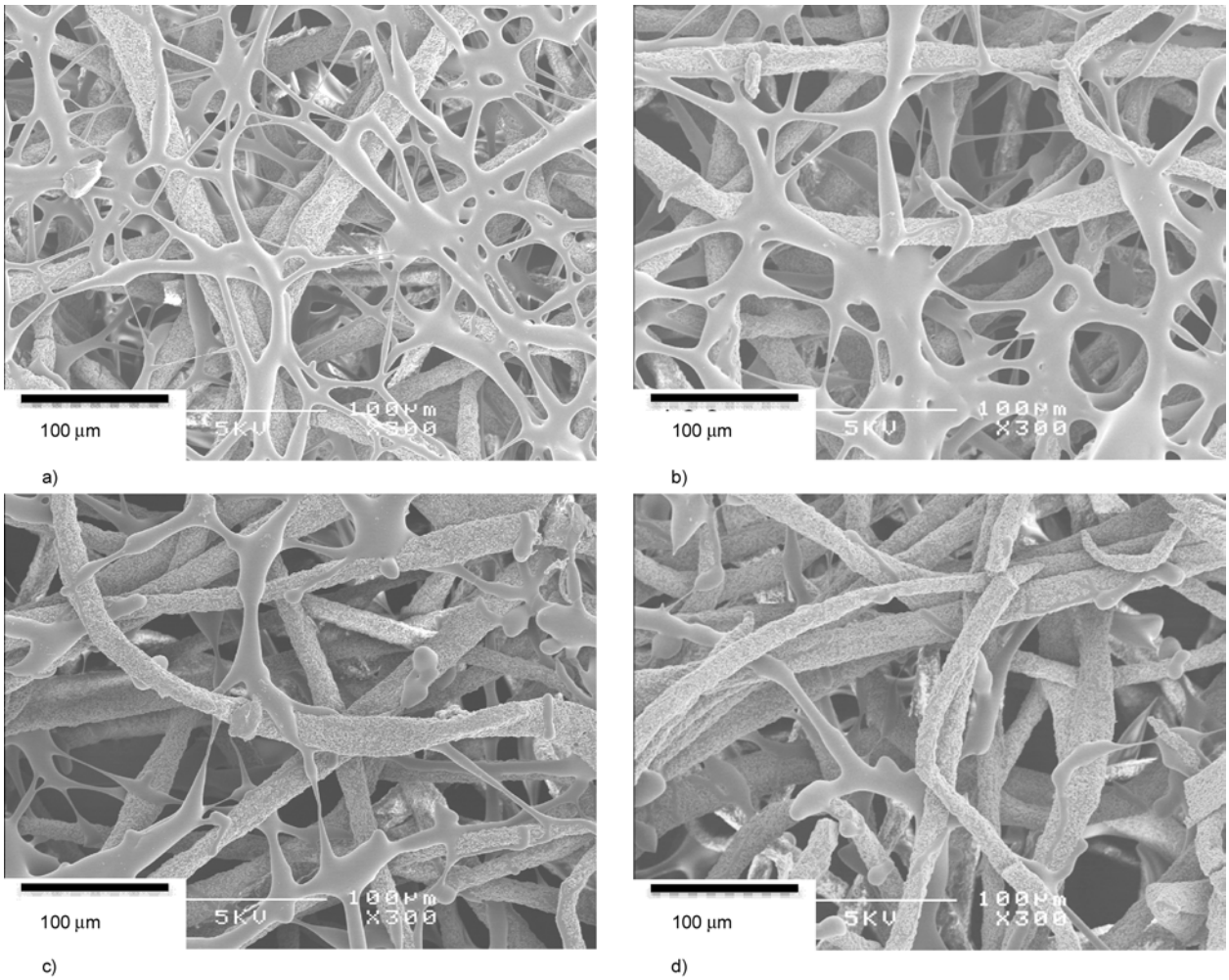

Figure 2. SEM images of the PLGA-SiPVH fibermat after heating at 110°C for (a) 15, (b) 20, (c) 25 and (d) 30 min

duced enough flow of PLGA fibers that has resulted in a fibermat morphology that has open pores of the order of 100 μm and a substantial proportion of PLGA still bridging the SiPVH fibers. This morphology could be beneficial for cell attachment, spreading and migration within the fibermat.

3.2. Morphology of the PLGA-SiPVH blended fibermats soaked in 1.5 SBF

Figure 3 shows the SEM images of the PLGA-SiPVH fibermats (Figure 3a) after soaking in 1.5 SBF for 24 h, (Figure 3b, d, e) after heating at 110°C for 25 min then soaking in 1.5 SBF and (Figure 3c) after soaking in 1.5 SBF for 24 h then heating at 110°C for 25 min. Firstly, the SiPVH fibers in all of the samples after soaking 1.5 SBF for 24 h were completely coated with a thick layer of HA (as shown in Figure 3d). As well, several particles of HA were also observed on the surface of PLGA, especially in the case of fine PLGA fibers that were observed to be completely coated (Figure 3e). Figure 3d, e shows the high magnification SEM images of Figure 3b; the HA particles on the SiPVH and PLGA surface have a globular cauliflower-like morphology. Secondly, the fibrous morphology of the as-spun-HA-coated (Figure 3a) and the heated and HA coated (Figure 3b, c) fibermats show a clear difference on the size of the pores in the fibermats. Where, from the SEM images the pore size seems to increase in the order as follows: as-spun-HA-coated (Figure 3a) < HA-coated-heated (Figure 3c)<heated-HA-coated (Figure 3b). The through-pore area fraction of the fibermats was calculated from the SEM images in Figure 3 using ImageJ. They were found to be 6.4, 16.2 and 9.2% for the as-spun-HA-coated, heated-HA-coated and HA-coated-heated, respectively. Although this not the true porosity of the fibermat but it gives an indication of the extent of porosity of each sample and demonstrates that the heating treatment signifi-

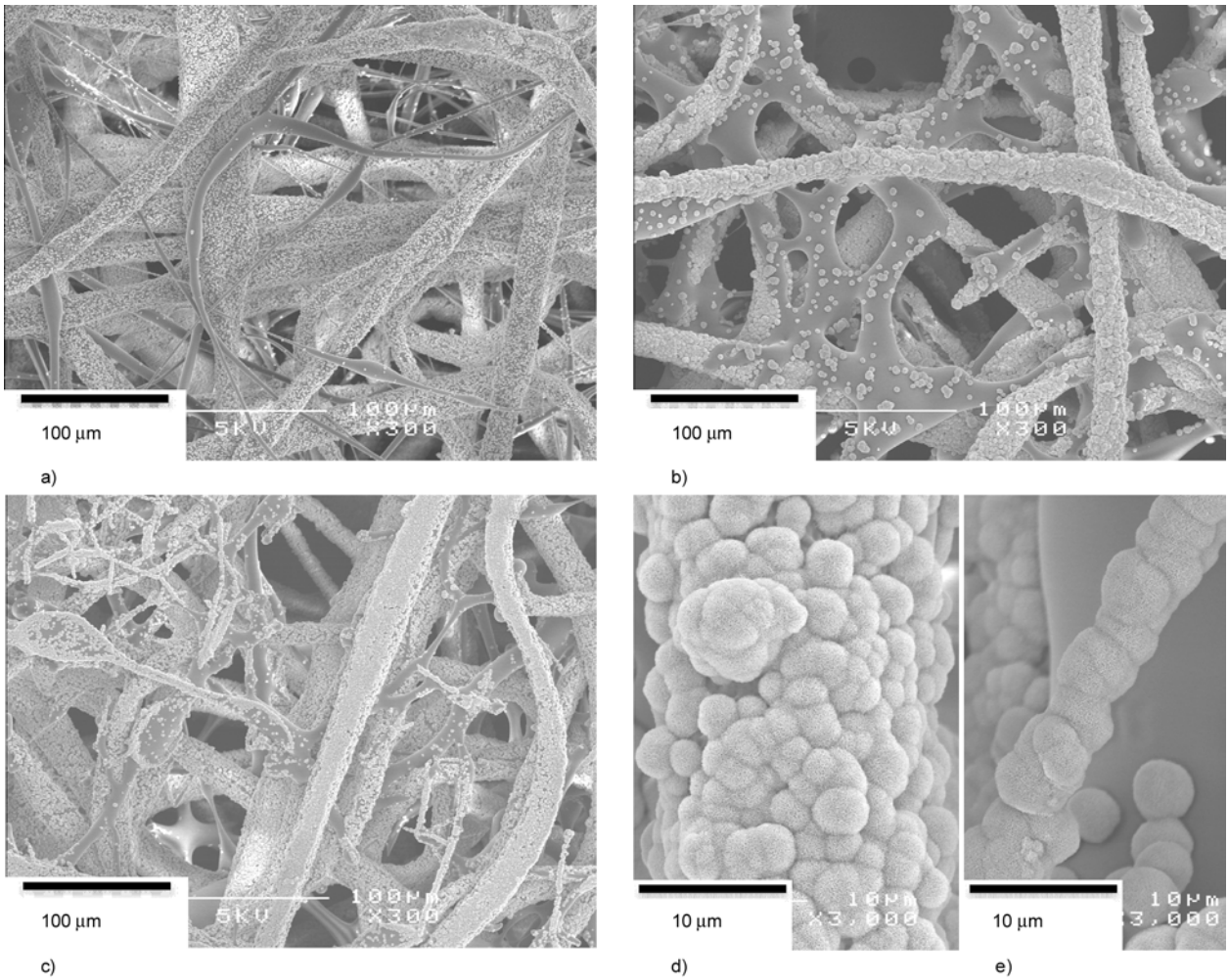

Figure 3. SEM images of the HA-coated PLGA-SiPVH fibermat (a) without heat application, (b) after heating and soaking, (c) after soaking and then heating and (d, e) high magnification images of (b)

cantly increases the porosity. The as-spun-HA-coated has the smallest pore space, this is expected since no heating was applied to result in the coalescence of the fine fibers of PLGA. While, in the case of the HA-coated-heated fibermat (Figure 3c) the HA coating on the fine PLGA fibers, where several fine PLGA fibers with HA coating (circled in Figure 3c) are clearly visible in the SEM image, has hindered its flow at the post-heating stage. This has reduced the coalescence of PLGA and hence the required effect of heating was not achieved. However, the heated-HA-coated fibermat (Figure 3b) has the desired morphology, where the SiPVH fibers are completely coated with HA and large interfiber distances can be seen. Therefore, for the blended PLGA-SiPVH fibermats, the processing conditions of heating at 110°C for 25 min followed by soaking in 1.5 SBF for 24 h is proposed to be ideal in achieving the desired fibermat morphology.

3.3. Mechanical properties of the PLGA-SiPVH blended fibermats

Figure 4a shows the tensile stress-strain curves and Figure 4b ultimate tensile strength (UTS) and elongation to failure of the as-spun SiPVH and blended PLGA-SiPVH fibermats and the heated PLGA-SiPVH fibermats. Both, the UTS and elongation before failure of all the PLGA-SiPVH blended samples were higher than that of SiPVH fibermats. The SiPVH fibermat had low UTS of 0.16 MPa and a brittle failure with a very low elongation to failure of 1.44%. The as-spun PLGA-SiPVH blended fibermat showed the largest elongation before failure of more than 30%. Both, as-spun and the 15 min heated samples had the highest UTS (~0.5 MPa), which then steadily decreased with heating time. Samples heated for 20 and 25 min at 110°C and then soaked in 1.5 SBF for 24 h were also tested in tension. A small decrease in the UTS was observed with soaking in SBF. This could be due to the degradation of PLGA in the 1.5 SBF solution, however the drop in UTS was minor.

The elongation to failure of the PLGA-SiPVH blended fibermats decreased drastically after heating, however still higher than that of SiPVH fibermat. Although, the 15 min-heated sample had relatively high UTS, the elongation before failure decreased to around 4%. Wei *et al.* [24] showed that the fracture energy decreases with increasing fiber-fiber fusion, where in this study longer heating time leads to higher fusion hence the elongation before failure is observed to decrease. Figure 5 shows the SEM images of the failure regions on the as-spun and heated samples of the PLGA-SiPVH blended fibermats after tensile testing. In the as-spun fibermat (Figure 5a–c) large plastic deformation before complete failure is evident, where several regions (circled in Figure 5a) of fiber stretching were observed on the whole fibermat. A higher magnification image of the circled area in Figure 5a is shown in Figure 5b, where the SiPVH fibers were seen to be completely fractured while the PLGA fibers have thinned to various thicknesses. Complete fracture of the sample took place when the cir-

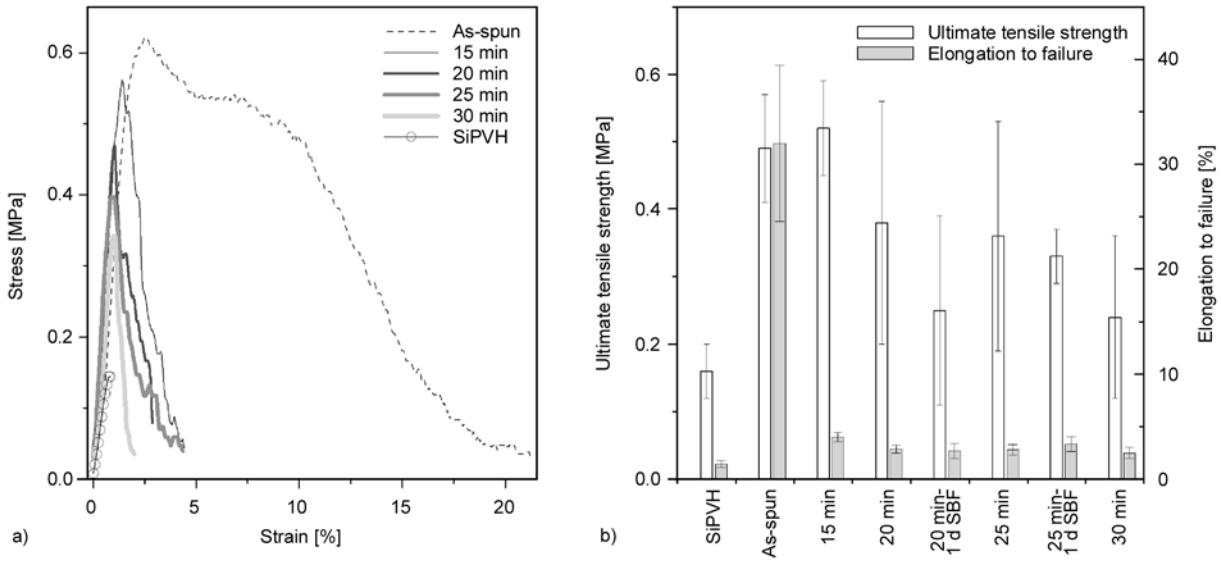

Figure 4. (a) Exemplary tensile stress-strain curves and (b) ultimate tensile strength and elongation to failure of the SiPVH fibermat and PLGA-SiPVH blended fibermats before and after heat treatment at 110°C for 15, 20, 25 and 30 min.

cle regions connected up along the width of the whole fibermat. Figure 5c shows a SEM image from the region of complete failure, which shows more thinned PLGA and fractured SiPVH fibers.

All the heated samples had a similar failure mechanism which was very different from that of the as-spun blended fibermats. Plastic deformation in the heated fibermats was observed to be very local and

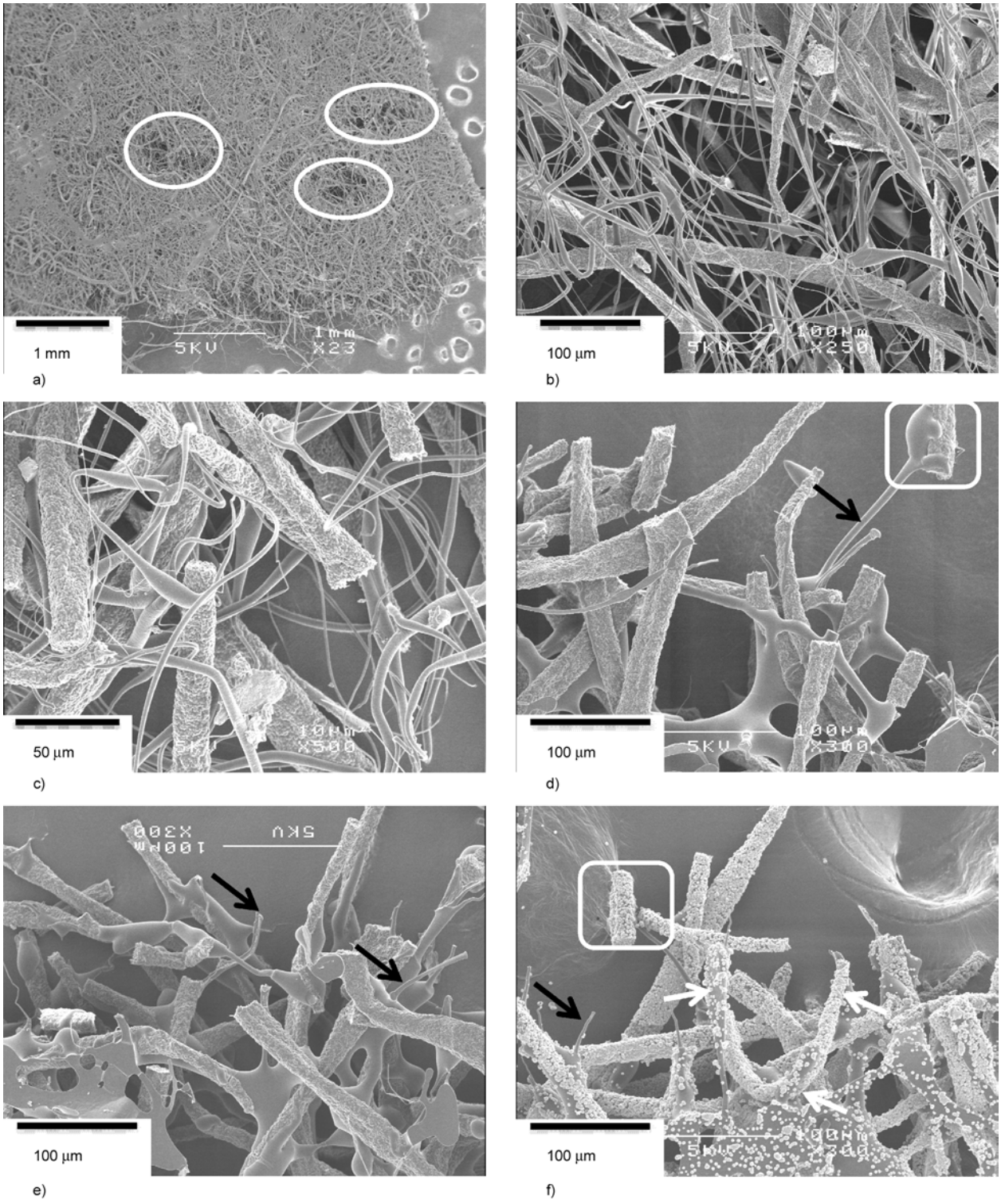

Figure 5. SEM images of the (a–c) as-spun and heated (d) 15 min, (e) 25 min and (f) 25 min-heated and soaked in 1.5 SBF PLGA-SiPVH fibermats after performing tensile tests. In the images the regions of local deformation in the as-spun PLGA-SiPVH are shown with ellipses, box in (d) and (f) show the fractured SiPVH fibers stabilised by PLGA, black arrows point to the PLGA strands that had plastically deformed and white arrows in (f) indicate a segment of SiPVH fiber stabilised by melt-fused PLGA.

confined to the region of final fracture. Figure 5d–f shows the SEM images of the failure zones of the heated samples. There are several important observations to be made. First, the fiber morphology close to the fracture zone had minimal disturbance after testing, a clear example for this is seen in Figure 5f, where a part of SiPVH fiber shaped 'U' (indicated by white arrows in SEM image) was not pulled out during testing. This indicates that the failure was brittle-like and that the melt-fused PLGA-SiPVH structure was very stable. Second, small strands of PLGA, indicated by black arrows in the SEM images, are the only PLGA polymer to undergo plastic deformation. Thirdly, these strands of PLGA are observed to hold the fractured pieces of SiPVH fibers in place (square boxes in SEM images), this is advantages after implantation if the SiPVH fibers were to fracture off; they could be held in implantation site by the PLGA. Finally, the failure region and mode of failure of the heated-HA-coated PLGA-SiPVH fibermat (Figure 5f) was identical to the hated-only fibermats. Therefore, the melt-fused PLGA-SiPVH fiber morphology obtained by heating at 110°C for 20 or 25 min and HA coated by soaking in 1.5 SBF could be promising for cell adhesion, spreading and migration. In vitro cell culture and in vivo animal studies are required to confirm this.

4. Conclusions

An attempt to mimic the morphology of the hot mesh-pressed bi-layered fibermat structure via a double syringe electrospinning and heating process was performed. The SEM images show clearly that the double syringe electrospinning of PLGA and SiPVH results in a well-blended fibrous structure. The PLGA-SiPVH fibermats have more than 30% elongation before failure and ~0.5 MPa ultimate tensile strength. On heating the PLGA fibers soften and flow towards the SIPVH fibers and adhere to it. This is found to indirectly, increase the pore size of the fibermat and result in multiple triple-points that connect the SiPVH fibers. Heating at 110°C for 20 min and more so after 25 min was found to produce a microstructure with pores of the order of 100 μm. The melt-fused PLGA-SiPVH fibermats after heating have higher elongation to failure and ultimate tensile strength on comparison to SiPVH-only fibermats. The melt-fusing by PLGA was also observed to provide stability to the SiPVH fibers while also increasing their strength.

Acknowledgements

This work was supported in part by Grant-in-Aids (B) (#20390499) from Japan Society for the Promotion of Science (JSPS), for Scientific Research in Institute of Ceramics Research and Education, NITECH and the JSPS International Training Program.

References

[1] Mayfield L., Nobréus N., Attström R., Linde A.: Guided bone regeneration in dental implant treatment using a bioabsorbable membrane. Clinical Oral Implants Research, **8**, 10–17 (1997). DOI: 10.1111/j.1600-0501.1997.tb00002.x

[2] Eickholz P., Kim T-S., Holle R.: Regenerative periodontal surgery with non-resorbable and biodegradable barriers: Results after 24 months. Journal of Clinical Periodontology, **25**, 666–676 (1998). DOI: 10.1111/j.1600-051X.1998.tb02504.x

[3] Yeh H-C., Hsu K-W.: Guided bone regeneration for fenestration defects in dental implants. Chang Gung Medical Journal, **26**, 684–689 (2003).

[4] Fujihara K., Kotaki M., Ramakrishna S.: Guided bone regeneration membrane made of polycaprolactone/calcium carbonate composite nano-fibers. Biomaterials, **26**, 4139–4147 (2005). DOI: 10.1016/j.biomaterials.2004.09.014

[5] Maeda H., Kasuga T., Hench L. L.: Preparation of poly(L-lactic acid)-polysiloxane-calcium carbonate hybrid membranes for guided bone regeneration. Biomaterials, **27**, 1216–1222 (2006). DOI: 10.1016/j.biomaterials.2005.08.010

[6] Lee E-J., Teng S-H., Jang T-S., Wang P., Yook S-W., Kim H-E., Koh Y-H.: Nanostructured poly(ε-caprolactone)–silica xerogel fibrous membrane for guided bone regeneration. Acta Biomaterialia, **6**, 3557–3565 (2010). DOI: 10.1016/j.actbio.2010.03.022

[7] Piattelli A., Scarano A., Paolantonio M.: Bone formation inside the material interstices of e-PTFE membranes: A light microscopical and histochemical study in man. Biomaterials, **17**, 1725–1731 (1996). DOI: 10.1016/0142-9612(96)87653-8

[8] Amano Y., Ota M., Sekiguchi K., Shibukawa Y., Yamada S.: Evaluation of a poly-l-lactic acid membrane and membrane fixing pin for guided tissue regeneration on bone defects in dogs. Oral Surgery, Oral Medicine, Oral Pathology, Oral Radiology and Endodontics, **97**, 155–163 (2004). DOI: 10.1016/j.tripleo.2003.09.009

[9] Stevens M. M., George J. H.: Exploring and engineering the cell surface interface. Science, **310**, 1135–1138 (2005). DOI: 10.1126/science.1106587

[10] Reneker D. H., Chun I.: Nanometre diameter fibres of polymer, produced by electrospinning. Nanotechnology, **7**, 216–223 (1996).
DOI: 10.1088/0957-4484/7/3/009

[11] Li D., Xia Y.: Electrospinning of nanofibers: Reinventing the wheel? Advanced Materials, **16**, 1151–1170 (2004).
DOI: 10.1002/adma.200400719

[12] Bhardwaj N., Kundu S. C.: Electrospinning: A fascinating fiber fabrication technique. Biotechnology Advances, **28**, 325–347 (2010).
DOI: 10.1016/j.biotechadv.2010.01.004

[13] Liang D., Hsiao B. S., Chu B.: Functional electrospun nanofibrous scaffolds for biomedical applications. Advanced Drug Delivery Reviews, **59**, 1392–1412 (2007).
DOI: 10.1016/j.addr.2007.04.021

[14] Li W-J., Laurencin C. T, Caterson E. J., Tuan R. S., Ko F. K.: Electrospun nanofibrous structure: A novel scaffold for tissue engineering. Journal of Biomedical Materials Research Part A, **60**, 613–621 (2002).
DOI: 10.1002/jbm.10167

[15] Zhang Y. Z., Su B., Venugopal J., Ramakrishna S., Lim C. T.: Biomimetic and bioactive nanofibrous scaffolds from electrospun composite nanofibers. International Journal of Nanomedicine, **2**, 623–638 (2007).

[16] Brightman A. O., Rajwa B. P., Sturgis J. E., McCallister M. E., Robinson J. P., Voytik-Harbin S. L.: Time-lapse confocal reflection microscopy of collagen fibrillogenesis and extracellular matrix assembly in vitro. Biopolymers, **54**, 222–234 (2000).
DOI: 10.1002/1097-0282(200009)54:3<222::AID-BIP80>3.0.CO;2-K

[17] Xie J., Li X., Xia Y.: Putting electrospun nanofibers to work for biomedical research. Macromolecular Rapid Communications, **29**, 1775–1792 (2008).
DOI: 10.1002/marc.200800381

[18] Jang J-H., Castano O., Kim H-W.: Electrospun materials as potential platforms for bone tissue engineering. Advanced Drug Delivery Reviews, **61**, 1065–1083 (2009).
DOI: 10.1016/j.addr.2009.07.008

[19] Wong S-C., Baji A., Leng S.: Effect of fiber diameter on tensile properties of electrospun poly(ε-caprolactone). Polymer, **49**, 4713–4722 (2008).
DOI: 10.1016/j.polymer.2008.08.022

[20] Baji A., Mai Y-W., Wong S-C., Abtahi M., Chen P.: Electrospinning of polymer nanofibers: Effects on oriented morphology, structures and tensile properties. Composites Science and Technology, **70**, 703–718 (2010).
DOI: 10.1016/j.compscitech.2010.01.010

[21] Lu J-W., Zhang Z-P., Ren X-Z., Chen Y-Z., Yu J., Guo Z-X.: High-elongation fiber mats by electrospinning of polyoxymethylene. Macromolecules, **41**, 3762–3764 (2008).
DOI: 10.1021/ma702881k

[22] Chandrasekaran A. R., Venugopal J., Sundarrajan S., Ramakrishna S.: Fabrication of a nanofibrous scaffold with improved bioactivity for culture of human dermal fibroblasts for skin regeneration. Biomedical Materials, **6**, 015001/1–015001/10 (2011).
DOI: 10.1088/1748-6041/6/1/015001

[23] Kim Y. B., Cho D., Park W. H.: Enhancement of mechanical properties of TiO_2 nanofibers by reinforcement with polysulfone fibers. Materials Letters, **64**, 189–191 (2010).
DOI: 10.1016/j.matlet.2009.10.038

[24] Wei X., Xia Z., Wong S-C., Baji A.: Modelling of mechanical properties of electrospun nanofibre network. International Journal of Experimental and Computational Biomechanics, **1**, 45–57 (2009).
DOI: 10.1504/IJECB.2009.022858

[25] Obata A., Hotta T., Wakita T., Ota Y., Kasuga T.: Electrospun microfiber meshes of silicon-doped vaterite/poly(lactic acid) hybrid for guided bone regeneration. Acta Biomaterialia, **6**, 1248–1257 (2010).
DOI: 10.1016/j.actbio.2009.11.013

[26] Wakita T., Obata A., Poologasundarampillai G., Jones J. R., Kasuga T.: Preparation of electrospun siloxane-poly(lactic acid)-vaterite hybrid fibrous membranes for guided bone regeneration. Composites Science and Technology, **70**, 1889–1893 (2010).
DOI: 10.1016/j.compscitech.2010.05.014

[27] Yasue T., Kojima Y., Arai Y.: Preparation of vaterite and control of its crystal shape (in Japanese). Gypsum Lime, **247**, 471–480 (1993).

[28] Kasuga T., Maeda H., Kato K., Nogami M., Hata K-I., Ueda M.: Preparation of poly(lactic acid) composites containing calcium carbonate (vaterite). Biomaterials, **24**, 3247–3253 (2003).
DOI: 10.1016/S0142-9612(03)00190-X

eXPRESS Polymer Letters Vol.5, No.10 (2011) 882–896
Available online at www.expresspolymlett.com
DOI: 10.3144/expresspolymlett.2011.87

Study of matrix micro-cracking in nano clay and acrylic tri-block-copolymer modified epoxy/basalt fiber-reinforced pressure-retaining structures

M. Bashar[1], *U. Sundararaj*[2], *P. Mertiny*[1*]

[1]University of Alberta, Department of Mechanical Engineering, 4–9 Mechanical Engineering Building, Edmonton AB, T6G 2G8
[2]University of Calgary, Department of Chemical and Petroleum Engineering, 2500 University Drive NW, Calgary AB, T2N 1N4

Received 9 January 2011; accepted in revised form 13 April 2011

Abstract. In fiber-reinforced polymer pressure-retaining structures, such as pipes and vessels, micro-level failure commonly causes fluid permeation due to matrix cracking. This study explores the effect of nano-reinforcements on matrix cracking in filament-wound basalt fiber/epoxy composite structures. The microstructure and mechanical properties of bulk epoxy nanocomposites and hybrid fiber-reinforced composite pipes modified with acrylic tri-block-copolymer and organophilic layered silicate clay were investigated. In cured epoxy, the tri-block-copolymer phase separated into disordered spherical micelle inclusions; an exfoliated and intercalated structure was observed for the nano-clay. Block-copolymer addition significantly enhanced epoxy fracture toughness by a mechanism of particle cavitation and matrix shear yielding, whereas toughness remained unchanged in nano-clay filled nanocomposites due to the occurrence of lower energy resistance phenomena such as crack deflection and branching.Tensile stiffness increased with nano-clay content, while it decreased slightly for block-copolymer modified epoxy. Composite pipes modified with either the organic and inorganic nanoparticles exhibited moderate improvements in leakage failure strain (i.e. matrix cracking strain); however, reductions in functional and structural failure strength were observed.

Keywords: *polymer composites, epoxy nanocomposites, filament winding, fracture toughness, matrix cracking*

1. Introduction

Filament winding is known to be one of the most economic and efficient methods for producing fiber-reinforced polymer (FRP) structures such as pipes and vessels. Pressure-retaining structures made from FRP are becoming increasingly popular, and are frequently considered as an alternative to conventional metallic structures. Improved performance in terms of high specific strength and corrosion resistance can be achieved with FRP pressure structures. However, the performance of these structures is dependent on the diverse and sustained loading conditions throughout their service life. It is therefore of great importance to understand their complex material behavior and damage mechanisms under different loading conditions and environmental effects.

In the design and application of composite pressure piping, functional and structural failure mechanisms must be considered [1–6]. In the case of functional failure (e.g. leakage) the structure is unable to contain the pressurized fluid, even though it is still able to sustain the applied mechanical loading. Structural failure (e.g. burst failure) is thus characterized by the pipe's inability to carry the applied loading. These types of failure usually occur as sep-

*Corresponding author, e-mail: pmertiny@ualberta.ca

arate events, but can happen as concomitant damage events depending on the applied loading situation. Functional failure is typically distinguished by fluid weepage and wetting of the outer wall. Due to fluid transmission through the wall, composite pressure structures have restricted application without any ancillary support medium (e.g. liner). Leakage is directly related to transverse matrix microcracking which is characterized by a reduction of composite stiffness as well as nonlinear stress-strain behavior. Functional failure is known to occur when transverse tensile loading normal to the fibers exceeds a certain threshold value [6].

Thermosetting polymers such as epoxy with their inherent brittleness are particularly prone to matrix cracking. One possible route to enhance ductility of thermosets is by dispersing rubbery phases inside the polymer matrix, i.e. liquid rubbers [7–13], thermoplastic spheres [14, 15], core-shell particles [16–18] and nanostructured block-copolymers [19–23]. Likewise, inorganic particles such as silica [7, 24], alumina [24], glass beads [25] and nano-clay [18, 26–30] are also known to enhance the toughness of the epoxy. Mechanism of epoxy toughening (i.e. particle cavitation, matrix shear yielding, multiple crazing, crack pinning and crack deflection) can be as diverse as the multifarious reinforcements available [31]. Irrespective of the operative resistance mechanism, the sole purpose of the dispersant is to aid the deformation process for dissipating energy. In FRP structures the presence of a fibrous reinforcement phase introduced additional complexity to polymer toughening. It is peculiar that toughness enhancements as observed in bulk polymers are not always transferrable to the same extent to fiber composite systems [32, 33].

Recently, polymer nanocomposites have become the forefront of composite research. Polymer nanocomposites are typically composed of a polymeric phase with one or more reinforcing nano-scale materials. Final properties of the resulting nanocomposites are dependent on the type of constituents used, their morphologies, interfacial characteristics, dispersion methods and preparation techniques. The nano-clay I.30E used in this study is an organically modified hydrous aluminosilicate with a platelike structure, having an aluminum octahedron layer sandwiched between silicon tetrahedron sheets. Studies have indicated that optimum properties of the resulting nanocomposite are obtained in an exfoliated structure, when individual silicate layers are completely dispersed into the polymer matrix [34–36]. The distance between the clay interlayer in the polymer matrix depends on such properties as the clay structure, curing agent, curing temperature and time, viscosity and the type of resin. Block-copolymers on the other hand have a structure consisting of rather long sequences of different repeating units. Commercially available M52N is an acrylic tri-block-copolymer which consists of rigid and rubbery blocks. This type of block-copolymer easily dissolves in epoxy resin and self-assembles on the nano-level due to the affinity between epoxy monomers and polymethylmethacrylate (PMMA), and repulsion between the epoxy monomers and the middle polybutylacrylate block (PBuA) [21, 22]. Various studies have been conducted on block-copolymer modified epoxy, most of which reported enhancements in toughness and ductility in the modified resin, while causing only minor reductions in stiffness and strength [19–23]. Similarly, nano-clay filled nanocomposites were found to increase toughness as well [26–29]. In clay modified materials an enhanced tensile strength and stiffness [26, 27, 34] were usually also observed while ductility was compromised.

The focus of the present study is to investigate methods for enhancing mechanical properties of the epoxy matrix by incorporating nanoparticles into the material system. The notion is to improve matrix toughness by adding nanoparticles into the substrate material to mitigate or prevent transverse matrix cracking in filament-wound pressure-retaining structures. With this intention in mind, two different types of nanoparticles were investigated, i.e. inorganic clay I.30E and organic tri-block-copolymer M52N. Several epoxy-nanoparticle formulations were developed and used as the matrix material for filament-wound composite piping. Morphology, mechanical and fracture studies of bulk epoxy nanocomposites were performed, and hybrid filament-wound epoxy composite pipes were subjected to biaxial stress testing.

2. Experimental procedure

2.1. Material system

The matrix material used in this study was EPON 826 bisphenol-A resin with EPI CURE 9551 non-

MDA polyamine curing agent; both are proprietary formulations of Hexion Specialty Chemicals (Columbus, Ohio, USA). The nanofiller used was Nanomer I.30E, $CH_3(CH_2)_{17}NH_3$-MMT, which is an primary alkylammonium ion modified Na-montmorillonite (Na-MMT) from Nanocor Inc. (USA). The other type of nano-phase material was an acrylic tri-block-copolymer M52N [PMMA/DMA PBuA PMMA/DMA] (where DMA stands for dimethacrylamide) synthesized by Arkema Inc. (Philadelphia, Pennsylvania, USA). The fiber reinforcement material was basalt fiber KV12 supplied by Kamenny Vek (Dubna, Moscow Region, Russia).

2.2. Epoxy nanocomposite formulation

Preparation and processing of epoxy nanocomposites from resin, curing agent and nanofillers involved such major steps as mixing, dispersion and degassing. Prior to dispersion into the epoxy precursor, nano-clay I.30E was dried in an oven at an elevated temperature of 120°C for a period of 24 hours. Afterwards, the nano-clay was allowed to cool down to room temperature. A specific amount of I.30E was first introduced into acetone, and pre-swelling in acetone was performed for six hours at room temperature. The solution was then mixed with pre-heated EPON 826 resin at 60°C by gentle stirring. Acetone promoted migration of epoxy inside the clay interlayer and also reduced resin viscosity. To obtain the desired level of resin viscosity for efficient ultrasonic mixing, the system temperature was slowly raised to 80°C. A 300 ml mixture of nano-clay and EPON 826 was subjected to sonication in a glass beaker for eight hours. The Sonifier (Branson model S-75) (Branson Ultrasonics Corporation, Danbury, CT, USA) operated at 75 W power output with 20 kHz output frequency. A step horn sonotrode with a 12.7 mm tip diameter was used to transmit ultrasonic energy. Sonication was followed by two hours of mechanical mixing. Finally, the mixture was degassed under vacuum until all excess acetone was completely stripped off from the solution.

M52N copolymer was dissolved directly by gradually adding block-copolymer powder to the epoxy resin at room temperature under steady mixing. The temperature was then increased and held stationary at 80°C until a homogenous solution and good optical transparency was observed. The dissolution time varied with copolymer concentration.

A stoichiometric amount of curing agent was mixed with the epoxy-nanofiller mixture at 60°C for five minutes by a mechanical stirrer running at 900 rpm. Formation of bubbles during curing agent addition necessitated a degassing cycle to be performed for 10~20 minutes. Finally, the resin mixture was poured into a stainless steel mold and cured at 120°C for two hours. Representative techniques were followed for epoxy nanocomposite formulations containing 1, 2 and 3 wt% I.30E or 1, 3 and 5 wt% M52N.

2.3. Hybrid nanocomposite pipe fabrication

Filament-wound basalt fiber/epoxy/nanoparticle tubes were manufactured containing various concentrations of either M52N or I.30E. Hybrid fiber-reinforced nanocomposite pipes were fabricated by pulling five continuous basalt fiber strands from their creels using a computer controlled WMS 4-axis filament winding machine (McClean Anderson, Schofield, WI, USA). While en-route to the mandrel, fiber strands were thoroughly impregnated with epoxy-nanoparticle formulation contained in a drum-type resin bath maintained at 30°C. Layers of resin wet fiber material were wound successively onto chrome-plated steel mandrels. Throughout the manufacturing process a numerically controlled tensioning system steadily applied 26.7 N tension to each fiber strand. Curing of the specimens occurred at 80°C for one hour and 120°C for 2.5 hours, followed by cooling down to room temperature. For

Figure 1. Tubular test specimen

mechanical testing, a rubber bladder liner was inserted inside each tubular specimen and the tube extremities were reinforced with aluminum end connections. The rubber bladder was designed to enable the assessment of functional as well as structural failure in the same experiment [5]. Composite pipes were also fitted with two strain gauge rosettes aligned parallel and perpendicular to the tube axis. All specimens had a $[\pm 60_3]_T$ fiber architecture, an inside diameter of 38.1 mm and a gage length of 90 mm. Figure 1 shows a test specimen with attached aluminum end connections.

2.4. Microstructure study

X-ray diffraction (XRD) analysis of the clay nanocomposites was carried out using a Rigaku Geigerflex 2173 (Rigaku Corporation, Tokyo, Japan) diffractometer with a vertical goniometer. The system is equipped with a Co tube and a graphite monochromator to filter K-beta wavelengths. All tests were run at 40 kV and 30 mA, and samples were scanned between $2\theta = 1$ to 30° changing the angle of incidence at a rate of 0.008 2θ s^{-1}.

Thin sections (5~10 μm) of the epoxy nanocomposite fracture surface were investigated by transmission optical microscopy (TOM). To prepare the thin sections, nanocomposite blocks were first placed in a Reichert Jung Ultra Microtome (C. Reichert Optische Werke AG, Vienna, Austria) and sectioned with a diamond cutter. These sections represent an area near the starter crack taken normal to the fracture surface and parallel to the crack propagation direction. The subsurface birefringent zone was explored under bright field and between cross polarizers using a Leica DMRXA microscope (Leica Microsystems, Wetzlar, Germany) directly connected to a Nikon DXM 1200 digital camera.

Representative samples of the cured nanocomposites having a thickness of about 40 nm were examined with a Morgagni 268 (FEI, Hillsboro, Oregon, USA) transmission electron microscope (TEM) at 80 kV. A Reichert Jung Ultra Microtome was again used to make the thin specimens. Some of the nanocomposite samples containing M52N block-copolymer were allowed to stain overnight in 4% osmic acid.

2.5. Mechanical testing of epoxy nanocomposites

Stress intensity factors K_I at failure of nanocomposite samples under plane-strain conditions were determined by three-point bending. The single edge notch bend (SENB) geometry was chosen according to the standard ASTM D5045 99, and testing was performed on a MTS 810 (MTS Systems Corporation, Eden Prairie, MN, USA) universal testing machine with a crosshead speed of 0.2 mm/min. Two methods were chosen to pre-crack specimens

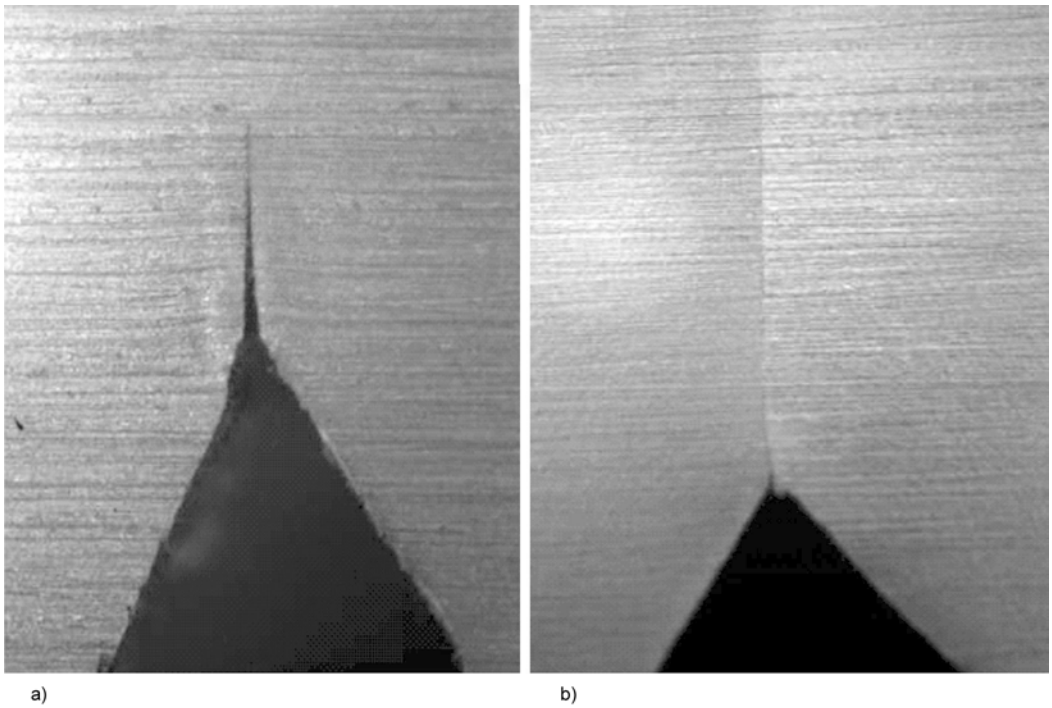

Figure 2. Pre-crack configurations: (a) blunt crack, (b) sharp crack [35]

prior to testing. A razor blade was inserted and pressed down to a depth of 1 mm inside a machined notch using the same MTS machine. This generated a blunt crack as shown in Figure 2a. The second method involved inserting and repeatedly tapping a razor blade with a hammer into the machined notch, which created a natural sharp crack (see Figure 2b). The stress intensity factor was calculated according to Equations (1–3):

$$K_{\mathrm{I}} = \frac{P}{BW^{1/2}} f(x) \tag{1}$$

with

$$x = \frac{\alpha}{W} \tag{2}$$

$$f(x) = 6x^{1/2} \cdot \frac{1.99 - x(1-x)(2.15 - 3.93x + 2.7x^2)}{(1+2x)(1-x)^{3/2}} \tag{3}$$

where P is the load at failure, B is the specimen thickness, W is the specimen width, and α is the overall crack length. In this study, stress intensity factors of sharp pre-cracked specimens were considered to provide the fracture toughness K_{IC} of the composite.

Uniaxial tensile tests were performed according to the standard ASTM D638 03 for the determination of the tensile modulus, tensile strength and tensile elongation at break of the neat epoxy and the nanocomposite samples. Dog bone specimens were mounted into the MTS 810 universal testing machine, and tested at a constant loading rate of 4.5 N/s.

2.6. Fractographic study

Fracture surfaces of single edge notch bend specimens were explored by a JEOL 6301F field emission scanning electron microscope (SEM) (JEOL Ltd., Tokyo, Japan) at an accelerating voltage of 5 kV. This instrument allowed for nanostructure evaluation with a high resolution of approximately ~3 nm. Before inspection, a conductive gold coating was applied to the I.30E nanocomposite fracture surface, while M52N modified epoxy fracture surface was coated with chromium.

2.7. Mechanical testing of hybrid nanocomposite tubes

Prior to mechanical testing of the hybrid fiber-reinforced nanocomposite pipes, fiber volume fractions were determined by resin burn-out tests, and nominal wall thicknesses were also calculated [6]. Corresponding data is summarized in Table 1. Tube samples made with M52N and I.30E exhibited, for the most part, decreasing fiber volume fraction with increasing nanofiller content. The reverse trend resulted for the wall thicknesses, which increased with rising nanofiller content. An increase in resin viscosity with nanofiller loading is assumed to have caused this behavior.

Multi-axial testing of the pipe specimens was performed by applying a monotonic 2-to-1 hoop-to-axial stress loading ratio ('pressure vessel loading') [2]. During each test a custom built multi-axial testing machine maintained a constant biaxial stress ratio by simultaneously applying internal pressurization and axial traction. All tests were preformed under load control conditions. A pressure intensifier supplied hydraulic oil for specimen pressurization at a rate of 4.63 kPa/s. Loading was continued until ultimate specimen failure (i.e. structural failure). The data acquisition system permitted recording of hoop and axial strains, axial load and stroke, internal pressure and pressure intensifier volume. Average hoop and axial stresses were determined applying thin-wall membrane theory according to standard ASTM D2992 06. Hoop and axial stresses were calculated according to Equations (4) and (5):

$$\sigma_{\mathrm{H}} = \frac{D(p_{\mathrm{i}} - p_0) - 2tp_0}{2t} \tag{4}$$

$$\sigma_{\mathrm{A}} = \frac{D^2(p_{\mathrm{i}} - p_0) - 4tp_0(D+t)}{4t(D+t)} + \frac{F}{\pi t(D+t)} \tag{5}$$

Table 1. Fiber volume fraction and nominal wall thickness for fiber-reinforced nanocomposite pipes

	Filler type	Filler matrix loading				
		0 wt% (neat epoxy)	1 wt%	2 wt%	3 wt%	5 wt%
Fiber volume fraction [%]	M52N	66.8	66.0		65.9	65.2
	I.30E		59.9	59.9	58.8	
Nominal wall thickness [mm]	M52N	1.306	1.333		1.341	1.355
	I.30E		1.472	1.472	1.499	

where D is the internal pipe diameter, t is the wall thickness, p_i and F are the internal pressure and axial force applied to the pipe, and p_0 is the atmospheric pressure.

2.8. Detection of pipe failures

Quantification of previously mentioned failure events was critical as this would typically standardize the performance of the composite pipes for their intended service condition. To identify functional and structural failure events from the same test setup, each pipe sample was fitted with the aforementioned internal rubber bladder, which enabled pressurization until catastrophic pipe failure. Prior to testing the inside of a rubber bladder as well as the annular volume in between the pipe and the bladder were filled with hydraulic fluid. Pressurization occurred from inside the bladder. In the course of the experiment, the initiation, accumulation and coalescence of matrix cracks provided pathways for fluid to escape through the composite structure. In this study, functional failure in the form of leakage was characterized by a prescribed fluid loss volume through the tube wall (i.e. a loss corresponding to 1% of the internal pipe volume). After a certain amount of fluid loss from the annulus, the inflating rubber bladder provides a seal inside the specimen. Pressurization was continued until rapid loss of fluid from the hydraulic system was ascertained indicating pipe burst, i.e. structural failure.

3. Results and discussion

3.1. Microstructure study

The morphology of the layered silicate in nanocomposites was studied by wide-angle X ray diffraction (WAXD). X-ray diffraction patterns of cured nanocomposites for various clay loadings are shown in Figure 3. Nanocomposites containing 1 and 2 wt% I.30E clay did not produce any distinguishable diffraction peak. In these nanocomposites the clay architecture can therefore be interpreted as exfoliated. Nevertheless, an intercalated structure cannot be fully ruled out as the traces exceed the detection limit of the WAXD ($2\theta \geq 1°$). Also shown in Figure 3 is the diffraction peak for a sample with 3 wt% clay, which shifted to the left implying that the clays preserved their characteristic stacked layer structure as tactoids with interlayer spacing d_{001} of 2.72 nm. From XRD traces the interlamellar distance of the pure organically modified clay I.30E was estimated to be d_{001} = 1.9 nm.

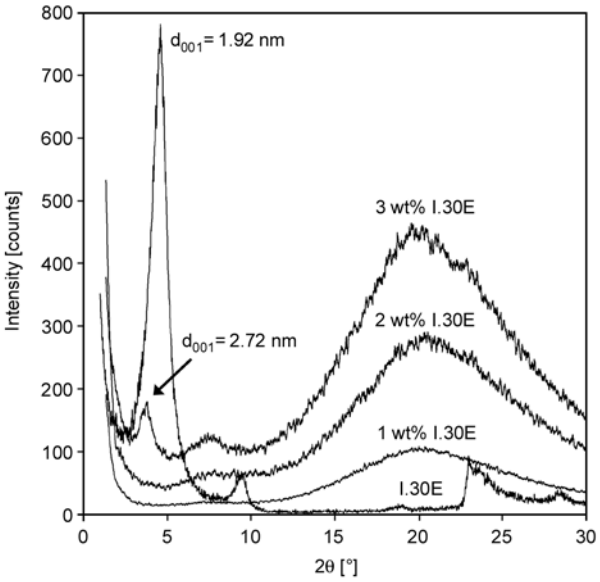

Figure 3. X-ray diffraction traces of pure I.30E and its nanocomposites

The TEM micrograph of a clay nanocomposite shown in Figure 4a displays partly exfoliated and predominantly intercalated layered silicate structures having adjacent silicate layers 10~15 nm apart from each other. Although most of the intercalated nano-clays are in submicron size, a few agglomerated micron size clay particles are also visible in the TEM micrograph, as exhibited in the lower magnification image of Figure 4b. In agreement with Messersmith and Giannelis [36] it was assumed that this type of aggregate formation is the result of chemical interaction between the silicate layer and the N–H group in the polyamine curing agent or from the alkyl ammonium ion modifier of the nanoclay. Figures 4c and 4d show randomly dispersed 20~30 nm spherical micelles of the block-copolymers, which consist of a PBuA rubbery core surrounded by a PMMA rigid shell [22]. Note that consistent with the particle size of both M52N and I.30E and the wavelength of visible light, the prepared nanocomposite samples were optically transparent.

Transmission optical microscopy allowed visualization of polymer deformation by identifying the birefringence and voided zone underneath the fracture surface. Assuming that a propagating crack would leave behind traces of a subsurface damage zone, TOM was employed to confirm the presence

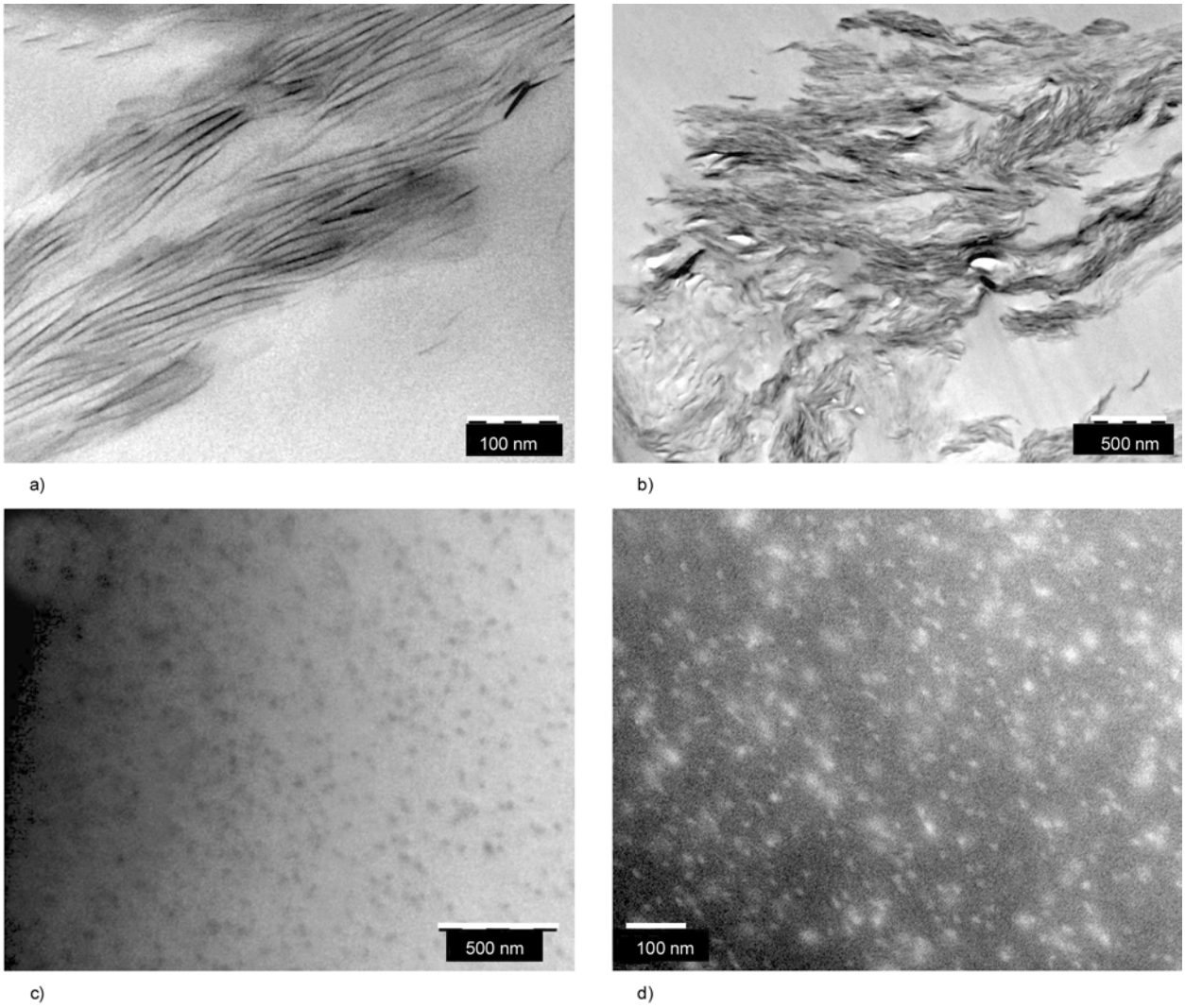

Figure 4. TEM images of nanostructures in epoxy nanocomposites: (a) intercalated clay I.30E (high magnification), (b) flocculated clay I.30E (low magnification), (c) spherical micelles of M52N block-copolymer without osmic acid staining and (d) with osmic acid staining

of the plastic zone. Figure 5 shows the existence of matrix deformation or shear banding for both pre-crack geometries under plane-strain condition. The birefringent region in the sharp crack is mainly confined in the process zone near the starter crack (see Figure 5b), whereas for the blunt crack the birefringent region shown in Figure 5c traverses the whole cross-section due to crack-tip plasticity. Dean and coworkers [19, 20] and Hydro and Pearson [21] reported similar subsurface localized matrix deformation for block-copolymer (i.e. PEO-PEP, PMMA-PBuA-PMMA) modified epoxy. TOM images taken under bright field and also in cross-polarized light conditions represent a toughened epoxy containing 1 wt% M52N. The size of the crack-tip plastic zone can be estimated theoretically according to the Irwin equation [7]. In a plane-strain condition, the Irwin equation, i.e. Equation (6) yields the radius of the plastic zone according to the following expression:

$$r_y = \frac{1}{6\pi}\left(\frac{K_{IC}}{\sigma_{ys}}\right) \tag{6}$$

where r_y is the radius of the plastic zone, K_{IC} is the plane-strain fracture toughness, and the value of the tensile yield stress σ_{ys} = 72.76 MPa was measured from uniaxial tensile testing. Theoretically determined radii of the plastic zone are 7.52 and 80.04 μm for the sharp and blunt crack geometry respectively. In terms of the linear elastic fracture mechanics, the stress situation at the crack-tip can adequately explain the damage behavior as observed by TOM microscopy. In plane-strain condition, a triaxial state of stress caused an intense stress field at the sharp crack-tip, thereby imposing restrictions

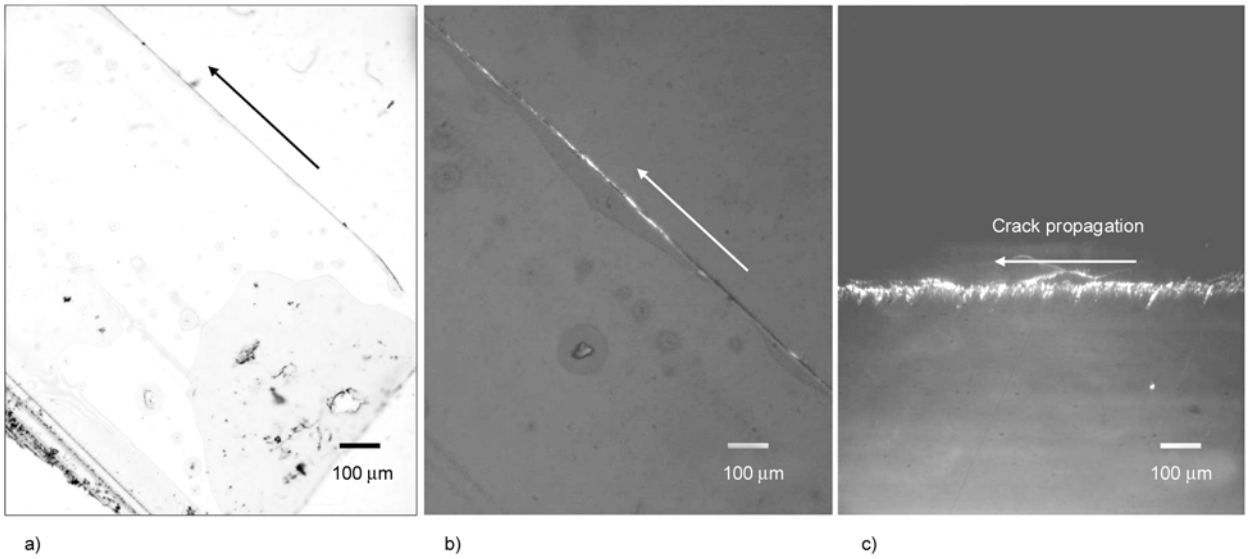

Figure 5. TOM images of epoxy block-copolymer nanocomposites: sharp pre-cracked fracture surface examined under (a) bright field, (b) cross-polarized light and (c) blunt pre-cracked surface under cross-polarized light

on the plastic zone size. For the blunt crack-tip the stress is distributed over a wider section (mimicking a state of plane-stress) that contributed to the formation of a relatively larger plastic zone. Later in this paper it will be shown that these differences in the stress field have a considerable effect on the toughening mechanism of the modified epoxy.

3.2. Mechanical testing of epoxy nanocomposites

Fracture toughness of the neat epoxy was estimated to be 0.78 MPa·m$^{0.5}$. In Figures 6 and 7 average stress intensity factors of neat epoxy and its nanocomposites are compared for the respective pre-crack geometries. (Note that in the following, error bars shown in graphs represent plus and minus one standard deviation for tests performed in triplicate or greater; lines represent first or second degree polynomial trend lines). It is shown that a sharp pre-cracked nanocomposite containing 5 wt% M52N yields an almost twofold improvement in toughness, which reveals a direct contribution of block-copolymer loading on fracture toughness. Pearson and Yee [12, 13] observed cavitation induced plastic deformation for rubber toughened epoxy, and Wu *et al.* [23] described a similar crack resistance phenomenon for nanostructured (micelle) block-copolymer modified epoxy. The present authors also observed similar phenomena during the fracture process. Hydrostatic tension ahead of the sharp

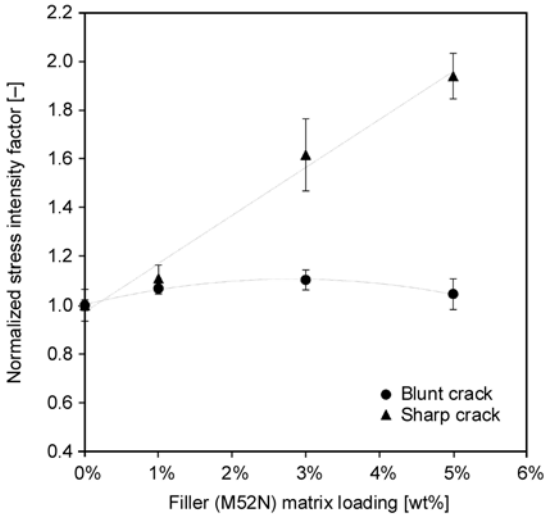

Figure 6. Critical stress intensity factor of nanocomposites relative to M52N block-copolymer concentration

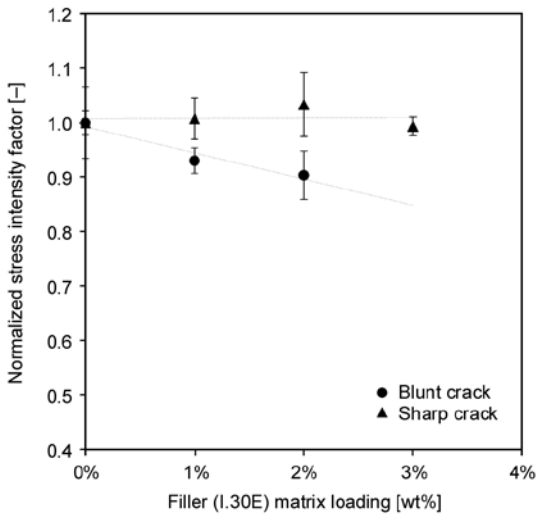

Figure 7. Critical stress intensity factor of nanocomposites relative to I.30E nano-clay concentration

crack-tip caused cavitation of the rubbery core of the block-copolymer resulting in localized shear deformation of the epoxy matrix; both are energy absorption mechanisms. In the case of blunt cracks only a minor enhancement in critical stress intensity became obvious (see Figure 6), which is assumed to be the effect of crack-tip plasticity evidenced by a large deformation zone shown in TOM microscopy in Figure 5c. Thus, without any discernible distinction in fracture energy between the block-copolymer modified epoxy and the neat epoxy the behavior with a blunt crack practically resembles tensile fracture. Subramaniyan and Sun [29] documented an equivalent effect of crack-tip zone plasticity in their study of organoclay and core-shell rubber toughened epoxy.

As presented in Figure 7 the behavior of nano-clay modified nanocomposites was rather different. For instance, only marginal or no improvement in fracture toughness was achieved for nanocomposites with 2 wt% I.30E and a sharp crack, and for samples with a blunt crack a moderated drop in fracture energy of up to 10% was observed. According to Zilg *et al.* [26] and Zerda and Lesser [27], a mostly intercalated structure rather than an exfoliated nanocomposite improves toughness by exposing additional surface area during the crack propagation process. However, clay nanocomposites prepared in this study behaved differently, primarily due to partial exfoliation of the nano-clay, and secondly, because of the relatively small size of the intercalated nano-clay. It will subsequently be shown (i.e. in Figures 10b and 10c) that most of the particles are indistinguishable on the micron level, indicating a rather uniform distribution of submicron size particles. The ultrasonic mixing process is considered to be the cause for the break down of clay agglomerates into the submicron size. It is well recognized that particle size, shape and structure significantly affect the fracture process in particulate reinforced polymers. In the subsequent section of this paper, micromechanisms are further explored and discussed in light of the insignificant effect of nano-clay on fracture toughness.

Tensile moduli of the neat epoxy and the nanocomposites are shown in Figure 8. In the case of acrylic block-copolymer modified epoxy, the modulus slightly decreased in response to increasing M52N concentration. A decrease of about 5~10% was observed for the range of M52N concentrations studied. Nanocomposites made from 1 wt% layered silicate I.30E resulted in more than 16% enhancement in stiffness compared to pure epoxy; moduli were increased even more for higher nano-clay loadings, which is in agreement with the findings of Lan and Pinnavaia [34]. Exfoliated clay platelets with 1 nm thick silicate layers having high in-plane bond strength and large surface area were expected to greatly improve mechanical properties of the nanocomposites [34]. The present study substantiated this notion as even predominantly intercalated nanocomposites generated significantly increased epoxy stiffness; to a certain extent, the intercalated particles of relatively small size caused a stiffening effect similar to that of exfoliated nano-clays.

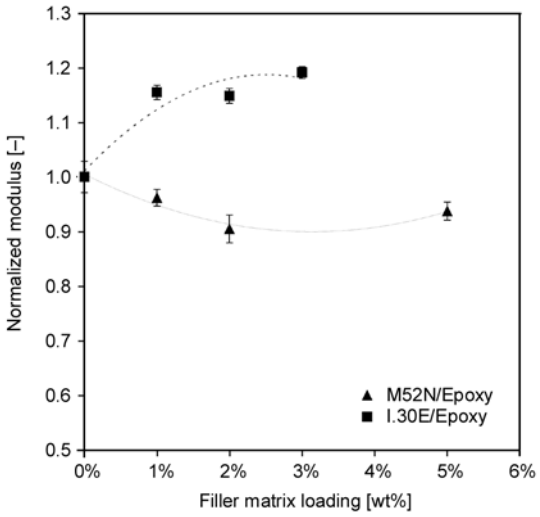

Figure 8. Tensile modulus of nanocomposites with respect to nanofiller loading

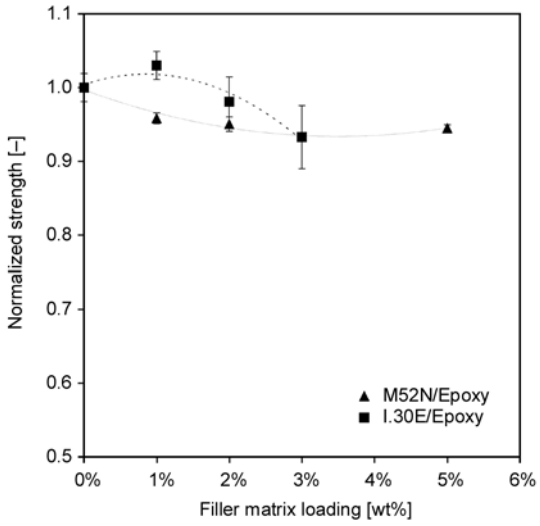

Figure 9. Tensile strength of nanocomposites with respect to nanofiller loading

Figure 9 correlates tensile strength of the nanocomposites with their corresponding nanofiller loadings. Notably, strength remained mostly unaffected by the block-copolymer addition, which is contrary to the common intuition about rubber modified thermosets [13, 14]. Possible reasons for this behavior are the nano-scale dispersion and greater compatibility of M52N block-copolymer towards epoxy. Addition of 1 wt% I.30E nano-clay in the matrix caused a slight increase in tensile strength but for higher nano-clay loadings a minor decrease was recorded.

3.3. Fractographic study

SENB fracture surfaces of the neat epoxy and its nanocomposites were extensively studied using SEM microscopy, see Figures 10 and 11. An arrow displayed in these micrographs indicates the crack propagation direction. The neat epoxy fracture surface was found to be flat and smooth, which is characteristic of brittle fracture behavior in a homogenous material. Relative to the unmodified epoxy, the extensively rough surface morphology of the nano-clay filled epoxy evidences repeated perturbation of the crack front from its original propagation path due to the presence of intercalated clay. Features shown in Figure 10b are consistent with bifurcation and/or deflection of the primary crack into multiple secondary cracks which are not necessarily coplanar [25]. Most of the clay tactoids shown in the micrographs are in the submicron size, but it is evident that a small fraction of particles were as large as ~10 μm. Due to the mostly small particle size and an apparently lower interparticle distance, deflected crack paths intersecting with each other generate a severely textured surface morphology as shown in Figures 10b and 10c, even though the clay concentrations were different for these nanocomposites. No indication of interfacial debonding between the epoxy network and the clay structures was discernible, suggesting excellent interfacial interaction. The morphology of the fracture surface also discounts the occurrence of effective crack pinning mechanisms. As reported in [25, 31], crack deflection mechanisms are not an efficient source of toughening, which correlates well with the rather insignificant toughening effect of the nano-clay.

In Figures 11a and 11b, acrylic block-copolymer modified epoxy exhibits a plane and featureless

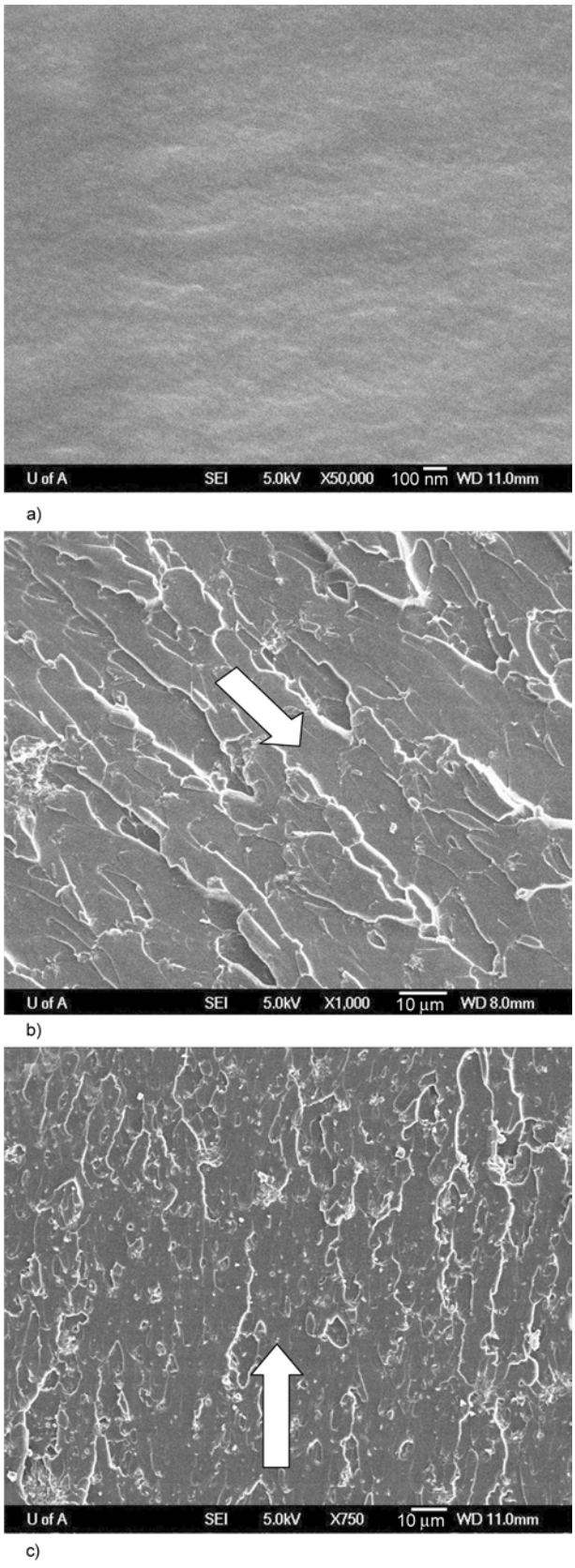

Figure 10. SEM images of nanocomposite fracture surfaces: a) neat epoxy, b) 1 wt% and c) 2 wt% I.30E nano-clay modified epoxy

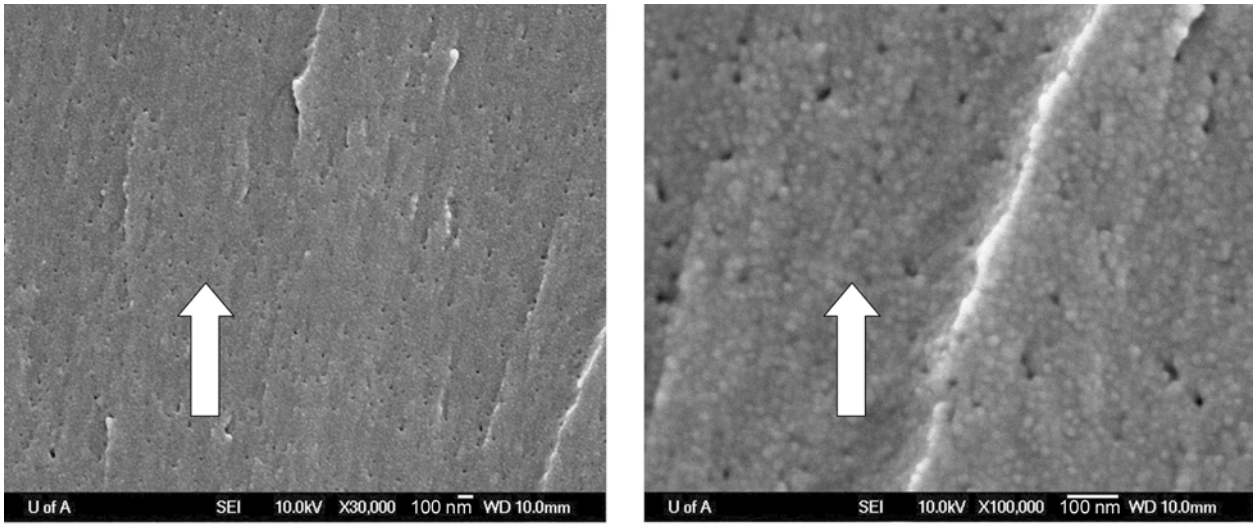

Figure 11. SEM images of M52N block-copolymer modified epoxy fracture surfaces at: a) low magnification and b) high magnification

crack surface with considerable epoxy-rich regions. Also evident in the same pictures is nanoscopic surface roughness. It appears that cavitation of the spherical micelles occurred during the fracture process, which is substantiated by the presence of minute spherical cavities with approximately ~20 nm size that are randomly dispersed in the polymer matrix. As mentioned previously, the cavitation process is considered to have initiated localized shear yielding of the matrix causing substantial dissipation of energy as evidenced by excellent improvements in fracture toughness [21, 23].

3.4. Mechanical testing of hybrid nanocomposite tubes

It is a common inference that transverse matrix cracking initiates near or at the fiber-matrix interface and then transmits through the resin matrix. Matrix cracks usually initiate at very low global strain levels due to high strain concentrations near the fiber resulting from the elastic discontinuity at the interface [1, 37]. Figure 12 depicts the influence of nanofiller loadings on maximum hoop strain, which usually is congruent with the leakage point at this loading ratio. Maximum hoop strain of the unmodified epoxy pipes was measured to occur at a mechanical strain of approximately 2400 με. For a 5 wt% M52N loading an increase in leakage failure strain of about 30% was observed. M52N significantly enhanced leakage failure strain and at the same time reduced stress non-linearity. These results correspond to those reported by Sjögren and

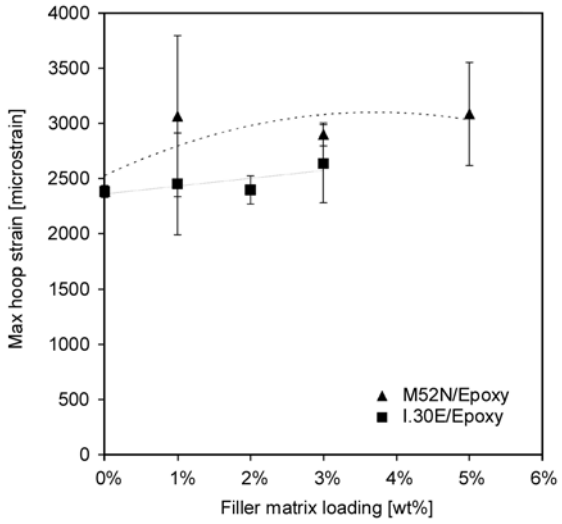

Figure 12. Maximum hoop strain of hybrid nanocomposite pipes as a function of nanofiller loading

Berglund [10, 11], who demonstrated a significant increase in transverse cracking strains as a direct consequence of the modifier concentration. Conversely, for nano-clay modified pipes the leakage failure strain remained practically unaffected, and a maximum of 10% increase in strain was observed for 3 wt% nano-clay in the matrix.

Failure stresses of hybrid fiber-reinforced nanocomposite pipes are summarized in Figures 13 and 14. The graph for M52N block-copolymer filled epoxy reveals that the hoop stress at leakage increased by only 4% with the addition of 1 % M52N (Figure 13). For the remainder of block-copolymer concentrations a less pronounced effect on leakage strength was noticed, and a simultaneous decrease in leak-

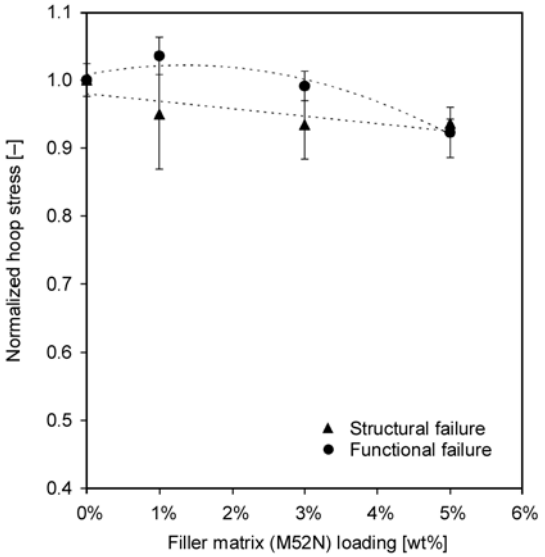

Figure 13. Hoop failure stress of hybrid nanocomposite pipes as a function of M52N block-copolymer loading

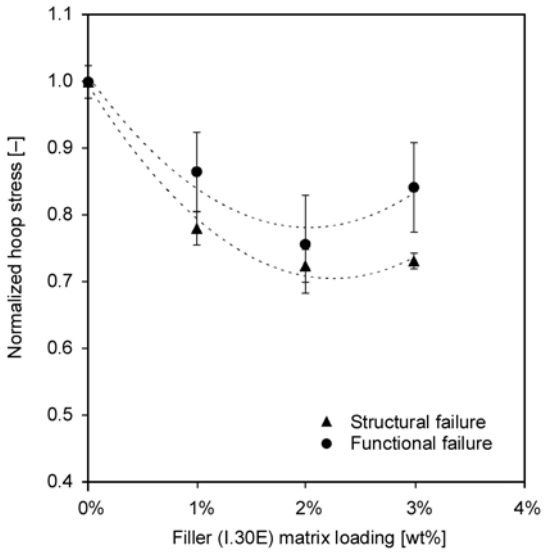

Figure 14. Hoop failure stress of hybrid nanocomposite pipes as a function of I.30E nano-clay loading

age and burst strength was observed for 5 wt% M52N. Test data for tubes made with I.30E modified polymer showed that the nano-clay imparted significant reductions in both the leakage and burst failure strengths (Figure 14). In summary, failure strength reductions were strongly correlated with I.30E loading, whereas strength values remained relatively stable when the polymer matrix was reinforced with M52N block-copolymer.

For pipes made with pure epoxy it was observed that transverse cracks initiate at low global strain in zones of high fiber packing followed by sudden unstable crack growth. Crack initiation likely occurred by adhesive debonding at the fiber-matrix interface where local strain concentrations are high. Transverse cracking associated with interfacial debonding was observed by various researchers [10, 11], and others have described the instantaneous crack propagation phenomenon [38, 39]. In the case of block-copolymer modified epoxy, the enhanced matrix ductility caused a build-up of strain energy until the sudden release of this energy resulted in initiation and subsequent crack propagation. It appears that matrix toughness significantly affected crack initiation and/or debonding processes due to improved polymer ductility. Delayed debonding may also be the outcome of better interfacial adhesion between the fiber and the matrix [11], possibly due to a sizing effect of the [PMMA/DMA-PBuA-PMMA/DMA] block-copolymer on the basalt fiber material [40]. As a consequence, increased strains at leakage failure were observed. However, the influence of M52N block-copolymer addition on the amount and/or extent of cracking was insignificant as evidenced by only minor improvements in leakage failure stresses. It is assumed that restrictions imposed by adjacent fibers on the crack-tip plastic zone affected the propagation of transverse cracks, and also restricted the ability of the spherical micelles to cavitate and cause matrix shear yielding. It has been reported that in a fiber-polymer composite, fibers appear to constrain the crack-tip deformation zone [32]. This effect is more pronounced in a toughened polymer than in a brittle matrix. As a result, the development of matrix crack networks and associated fluid leakage was not diminished anywhere near the extent that one may have expected based on fracture toughness improvements in pure block-copolymer modified epoxy resin.

Influenced by congruent trends between composite pipe leakage strengths and fracture energies ascertained for nanocomposite samples with a blunt crack, it was hypothesized that transverse matrix cracking in filament-wound pipes, which includes both the initiation and propagation of micro-cracks, resembles tensile fracture behavior in a brittle matrix material. As discussed by Subramaniyan and Sun [29] it appears that fracture behavior associated with propagation of blunt cracks is dominated by a stress concentration factor and not a stress intensity

factor at failure. It is postulated that to some extent these mechanisms were effective in the case of block-copolymer modified epoxy pipes. Further studies are underway in support of this statement, and interlaminar fracture toughness, microscopy studies and interface effects will be discussed in subsequent publications.

For the nano-clay modified epoxy material it was concluded that the presence of few flocculated clay particles provided an uneven distribution of stress concentration points throughout the epoxy matrix (see Figure 4b), which supposedly acted as initiation sites for transverse matrix cracks [18]. Considering that the leakage phenomenon is dominated by crack initiation events rather than crack propagation (of a dominant crack), and due to enhanced stress fields resulting from the interaction of clay aggregates and the applied loading, leakage strength of the composite pipes was degraded. Substantial matrix cracking further caused reduced structural strength. In the presence of a weakened fiber-matrix load-sharing mechanism, fibers failed at their weakest points at reduced global load levels. The degraded matrix also allowed fibers to realign along the direction of the resulting force, thus imposing additional loading upon the fibers.

4. Conclusions

Visual inspection of functionally failed fiber-reinforced composite pressure pipes commonly reveals multiple aligned, nearly homogenously distributed cracks, which form numerous interconnected fluid pathways from the inner to the outer pipe surface. The majority of these cracks are oriented parallel to the fiber direction with crossover undulation points indicating delimitation of the laminates. The common intuition about transverse matrix cracking is that it is the consequence of stress acting transverse to the fiber direction. For the fiber orientation selected in this study, it is presumably the axial tensile load which is predominantly responsible for transverse matrix cracking of the composite pipe. Based on these observations the notion was to reinforce the relatively brittle epoxy matrix with a nano-particulate phase with the intent to mitigate the progression of micro-cracks. Yet, the intended reinforcement effect could not be realized, despite a considerable improvement in fracture toughness for one type of the tested nanocomposite system.

Modification of epoxy with tri-block-copolymer M52N rendered significant improvements of epoxy toughness by a process of particle cavitation and localized shear deformation of the matrix. In contrast, I.30E clay exhibited almost negligible influence on epoxy toughness, where the fracture properties of the nanocomposites are dictated by the exfoliated and intercalated morphology of the clay.

It was hypothesized that the transverse cracking process for fiber composite pipes made with M52N block-copolymer toughened epoxy begins with prolonged straining followed by fiber-matrix interfacial debonding and immediate crack propagation. Crack progression was also effected by alteration of the crack-tip stress field by adjacent fibers. In case of the I.30E nano-clay modified epoxy pipes, transverse matrix cracking was further accelerated in the presence of micron size clay aggregates which acted as stress concentrators. Even though leakage failure strain improved moderately for some of the hybrid nanocomposite pipes, these enhancements proved insignificant for the leakage failure strength, and the damage mechanism was found to practically resemble that of the neat epoxy composite pipes.

References

[1] Jones M. L. C., Hull D.: Microscopy of failure mechanisms in filament-wound pipe. Journal of Materials Science, **14**, 165–174 (1979).
DOI: 10.1007/BF01028340

[2] Ellyin F., Carroll M., Kujawski D., Chiu A. S.: The behavior of multidirectional filament wound fibreglass epoxy tubulars under biaxial loading. Composites Part A: Applied Science and Manufacturing, **28**, 781–790 (1997).
DOI: 10.1016/S1359-835X(97)00021-3

[3] Martens M., Ellyin F.: Biaxial monotonic behavior of a multidirectional glass fiber epoxy pipe. Composites Part A: Applied Science and Manufacturing, **31**, 1001–1014 (2000).
DOI: 10.1016/S1359-835X(00)00041-5

[4] Meijer G., Ellyin F.: A failure envelope for ±60° filament wound glass fibre reinforced epoxy tubulars. Composites Part A: Applied Science and Manufacturing, **39**, 555–564 (2008).
DOI: 10.1016/j.compositesa.2007.11.002

[5] Mertiny P., Ellyin F., Hothan A.: An experimental investigation on the effect of multi-angle filament winding on the strength of tubular composite structures. Composites Science and Technology, **64**, 1–9 (2004).
DOI: 10.1016/S0266-3538(03)00198-2

[6] Mertiny P., Ellyin F.: Influence of the filament winding tension on physical and mechanical properties of reinforced composites. Composites Part A: Applied Science and Manufacturing, **33**, 1615–1622 (2002). DOI: 10.1016/S1359-835X(02)00209-9

[7] Hsieh T. H., Kinloch A. J., Masania K., Sohn Lee J., Taylor A. C., Sprenger S.: The toughness of epoxy polymers and fibre composites modified with rubber microparticles and silica nanoparticles. Journal of Materials Science, **45**, 1193–1210 (2010). DOI: 10.1007/s10853-009-4064-9

[8] Kinloch A. J., Shaw S. J., Tod D. A., Hunston D. L.: Deformation and fracture behaviour of a rubber-toughened epoxy: 1. Microstructure and fracture studies. Polymer, **24**, 1341–1353 (1983). DOI: 10.1016/0032-3861(83)90070-8

[9] Sultan J. N., McGarry F. J.: Effect of rubber particle size on deformation mechanisms in glassy epoxy. Polymer Engineering and Science, **13**, 29–34 (1973). DOI: 10.1002/pen.760130105

[10] Sjögren B. A., Berglund L. A.: Toughening mechanisms in rubber-modified glass fiber/unsaturated polyester composites. Polymer Composites, **20**, 705–712 (1999). DOI: 10.1002/pc.10394

[11] Sjögren B. A., Berglund L. A.: The effects of matrix and interface on damage in GRP cross-ply laminates. Composites Science and Technology, **60**, 9–21 (2000). DOI: 10.1016/S0266-3538(99)00096-2

[12] Pearson R. A., Yee A. F.: Toughening mechanisms in elastomer-modified epoxies. Part 2. Microscopy studies. Journal of Materials Science, **21**, 2475–2488 (1986). DOI: 10.1007/BF01114294

[13] Yee A. F., Pearson R. A.: Toughening mechanisms in elastomer-modified epoxies. Part 1. Mechanical studies. Journal of Materials Science, **21**, 2462–2474 (1986). DOI: 10.1007/BF01114293

[14] Höfflin F., Könczöl L., Döll W., Morawiec J., Mülhaupt R.: Toughening of epoxy resins modified with polyetherester block copolymers: The influence of modifier molecular architecture on mechanical properties. Journal of Applied Polymer Science, **76**, 623–634 (2000). DOI: 10.1002/(SICI)1097-4628(20000502)76:5<623::AID-APP3>3.0.CO;2-Z

[15] Kinloch A. J., Yuen M. L., Jenkins S. D.: Thermoplastic-toughened epoxy polymers. Journal of Materials Science, **29**, 3781–3790 (1994). DOI: 10.1007/BF00357349

[16] Bécu-Longuet L., Bonnet A., Pichot C., Sautereau H., Maazouz A.: Epoxy networks toughened by core–shell particles: Influence of the particle structure and size on the rheological and mechanical properties. Journal of Applied Polymer Science, **72**, 849–858 (1999). DOI: 10.1002/(SICI)1097-4628(19990509)72:6<849::AID-APP10>3.3.CO;2-I

[17] Lin K-F., Shieh Y-D.: Core-shell particles designed for toughening the epoxy resins. II. Core-shell-particle-toughened epoxy resins. Journal of Applied Polymer Science, **70**, 2313–2322 (1998). DOI: 10.1002/(SICI)1097-4628(19981219)70:12<2313::AID-APP2>3.0.CO;2-P

[18] Marouf B. T., Pearson R. A., Bagheri R.: Anomalous fracture behavior in an epoxy-based hybrid composite. Materials Science and Engineering: A, **515**, 49–58 (2009). DOI: 10.1016/j.msea.2009.03.028

[19] Dean J. M., Lipic P. M., Grubbs R. B., Cook R. F., Bates F. S.: Micellar structure and mechanical properties of block copolymer-modified epoxies. Journal of Polymer Science Part B: Polymer Physics, **39**, 2996–3010 (2001). DOI: 10.1002/polb.10062

[20] Dean J. M., Grubbs R. B., Saad W., Cook R. F., Bates F. S.: Mechanical properties of block copolymer vesicle and micelle modified epoxies. Journal of Polymer Science Part B: Polymer Physics, **41**, 2444–2456 (2003). DOI: 10.1002/polb.10595

[21] Hydro R. M., Pearson R. A.: Epoxies toughened with triblock copolymers. Journal of Polymer Science Part B: Polymer Physics, **45**, 1470–1481 (2007). DOI: 10.1002/polb.21166

[22] Gerard P., Boupat N. P., Fine T., Gervat L., Pascault J-P.: Toughness properties of lightly crosslinked epoxies using block copolymers. Macromolecular Symposia, **256**, 55–64 (2007). DOI: 10.1002/masy.200751006

[23] Wu J., Thio Y. S., Bates F. S.: Structure and properties of PBO–PEO diblock copolymer modified epoxy. Journal of Polymer Science Part B: Polymer Physics, **43**, 1950–1965 (2005). DOI: 10.1002/polb.20488

[24] Moloney A. C., Kausch H. H., Stieger H. R.: The fracture of particulate-filled epoxide resins. Journal of Materials Science, **18**, 208–216 (1983). DOI: 10.1007/BF00543827

[25] Lee J., Yee A. F.: Role of inherent matrix toughness on fracture of glass bead filled epoxies. Polymer, **41**, 8375–8385 (2000). DOI: 10.1016/S0032-3861(00)00186-5

[26] Zilg C., Mülhaupt R., Finter J.: Morphology and toughness/stiffness balance of nanocomposites based upon anhydride-cured epoxy resins and layered silicates. Macromolecular Chemistry and Physics, **200**, 661–670 (1999). DOI: 10.1002/(SICI)1521-3935(19990301)200:3<661::AID-MACP661>3.0.CO;2-4

[27] Zerda A. S., Lesser A. J.: Intercalated clay nanocomposites: Morphology, mechanics, and fracture behavior. Journal of Polymer Science Part B: Polymer Physics, **39**, 1137–1146 (2001). DOI: 10.1002/polb.1090

[28] Haque A., Shamsuzzoha M., Hussain F., Dean D.: S2-glass/epoxy polymer nanocomposites: Manufacturing, structures, thermal and mechanical properties. Journal of Composite Materials, **37**, 1821–1837 (2003). DOI: 10.1177/002199803035186

[29] Subramaniyan A. K., Sun C. T.: Toughening polymeric composites using nanoclay: Crack tip scale effects on fracture toughness. Composites Part A: Applied Science and Manufacturing, **38**, 34–43 (2007). DOI: 10.1016/j.compositesa.2006.01.021

[30] Miller S. G., Meador M. A.: Polymer-layered silicate nanocomposites for cryotank applications. in '48th AIAA/ASME/ASCE/AHS/ASC Structures, Structural Dynamics, and Material Conference, Waikiki, USA' Vol 8, 7530–7538 (2007).

[31] Garg A. C., Mai Y-W.: Failure mechanisms in toughened epoxy resins – A review. Composites Science and Technology, **31**, 179–223 (1988). DOI: 10.1016/0266-3538(88)90009-7

[32] Hunston D. L.: Composite interlaminar fracture: Effect of matrix fracture energy. Journal of Composites Technology and Research, **6**, 176–180 (1984). DOI: 10.1520/CTR10842J

[33] Bradley W. L.: Understanding the translation of neat resin toughness into delamination toughness in composites. Key Engineering Materials, **37**, 161–198 (1989). DOI: 10.4028/www.scientific.net/KEM.37.161

[34] Lan T., Pinnavaia T. J.: Clay-reinforced epoxy nanocomposites. Chemistry of Materials, **6**, 2216–2219 (1994). DOI: 10.1021/cm00048a006

[35] Bashar M. T., Mertiny P.: Performance of hybrid fiber-reinforced polymer nanocomposite pipes. in 'SAMPE 2010 Conference and Exhibition, Seattle, USA' p6 (2010).

[36] Messersmith P. B., Giannelis E. P.: Synthesis and characterization of layered silicate-epoxy nanocomposites. Chemistry of Materials, **6**, 1719–1725 (1994). DOI: 10.1021/cm00046a026

[37] Asp L. E., Berglund L. A., Talreja R.: Prediction of matrix-initiated transverse failure in polymer composites. Composites Science and Technology, **56**, 1089–1097 (1996). DOI: 10.1016/0266-3538(96)00074-7

[38] Wang A. S. D.: Fracture mechanics of sublaminate cracks in composite materials. Journal of Composites Technology and Research, **6**, 45–62 (1984). DOI: 10.1520/CTR10817J

[39] Parvizi A., Garrett K. W., Bailey J. E.: Constrained cracking in glass fibre-reinforced epoxy cross-ply laminates. Journal of Materials Science, **13**, 195–201 (1978). DOI: 10.1007/BF00739291

[40] Li Y., Lin Q., Chen L., Zhou X.: Assembly of triblock copolymer brush at glass fiber/polystyrene interface and its effect on interfacial shear strength. Composites Science and Technology, **69**, 1919–1924 (2009). DOI: 10.1016/j.compscitech.2009.04.008

eXPRESS Polymer Letters Vol.5, No.10 (2011) 897–910
Available online at www.expresspolymlett.com
DOI: 10.3144/expresspolymlett.2011.88

Enhancing mechanical properties of thermoplastic polyurethane elastomers with 1,3-trimethylene carbonate, epsilon-caprolactone and L-lactide copolymers via soft segment crystallization

S. S. Liow[1*], *V. T. Lipik*[1], *L. K. Widjaja*[1], *S. S. Venkatraman*[1], *M. J. M. Abadie*[1,2]

[1]School of Materials Science and Engineering, Nanyang Technological University, 50, Nanyang Avenue, Singapore 639798, Singapore
[2]Laboratory of Polymer Science and Advanced Organic Materials, LEMP/MAO, Université Montpellier 2, Place Bataillon, 34095 Montpellier Cedex 05, France

Received 11 February 2011; accepted in revised form 13 April 2011

Abstract. Multiblock thermoplastic polyurethane elastomers based on random and triblock copolymers were synthesized and studied. Dihydroxyl-terminated random copolymers were prepared by ring opening copolymerization of ε-caprolactone (CL) and 1,3-trimethylene carbonate (TMC). The triblock copolymers were synthesized by using these random copolymers as macro-initiator for the L-lactide (L-LA) blocks. These random and triblock copolymers were further reacted with 1,6-hexamethylene diisocyanate (HMDI) and chain extended by 1,4-butanediol (BDO). The polymer structure and chemical composition were characterized by ^{1}H NMR ^{13}C NMR and SEC. Their thermal and mechanical properties were studied by using DSC and Instron microtester. Multiblock polyurethanes based on random PCL-co-PTMC copolymers showed strain recovery improvement with increasing PCL content. However, these polyurethanes were unable to sustain deformation at body temperature due to the melting of PCL crystals and low hard segments content. With the presence of crystallizable PLLA blocks, mechanical properties were improved at body temperature without compromising their good strain recovery.

Keywords: *biodegradable polymers, thermoplastic polyurethanes, soft segment crystallinity, strain recovery, elastomers*

1. Introduction

Recently, there has been renewed interest in applying biodegradable thermoplastic elastomers (TPEs) for biomedical implants. TPEs are favored over chemically crosslinked networks because of their remoldability and easy processability. Unlike crosslinked elastomeric networks, TPE demonstrates elastomeric properties due to physical crosslinks that are formed as a result of microphase separation between hard and soft segments. Typically, soft segments can provide elasticity and flexibility while hard segments offer the necessary physical crosslink sites.

Polyurethanes (PU) and poly(urethane urea) (PUU) have been intensively studied for several decades for mainly tissue engineering scaffolds and vascular implants because of their compatibility, elasticity and ease of surface modification. The hard segment in PUs typically contains diisocyanate, and their modification is an accepted way to alter properties of thermoplastic PU and PUU. One can enhance elasticity of PU by using an aliphatic diisocyanate instead of aromatic diisocyanate; and improve tensile strength and Young's modulus by increasing hard segments content [1]. However, increasing the

*Corresponding author, e-mail: Liow0019@e.ntu.edu.sg

diisocyanate content is not desirable in a biodegradable system because of the potential toxicity concerns regarding the degradation products, although this is still a matter of debate [2, 3].

To achieve effective elastomeric properties in thermoplastic PU and PUU, soft segments modification, as an alternative, was investigated intensively. In previous studies, soft segments such as poly(ε-caprolactone) (PCL) [4, 5], the copolymer or blend of PCL and polylactide (PLA) [6, 7], triblock PCL-PEG-PCL with poly(ethylene glycol) (PEG) as middle block [8], PCL blended with poly(1,6-hexamethylene carbonate) (PHC) [9], and the copolymer of poly(trimethylene carbonate) and PCL (PTMC-co-PCL (50/50)) [10] with optimum composition and high molar mass, have shown high elongation, good flexibility and elasticity.

Very few groups have addressed the effect of soft segment crystallization on polyurethane properties. Skarja [11] has reported that soft segment crystallinity strongly affects the properties of PCL-based polyurethanes. When hard segments are unable to aggregate to act as physical crosslink points, soft segment crystal structure may act as reinforcement filler, results in increased ultimate tensile strength (UTS), initial modulus and strain-at-break. A recent study on PEO-based polyurethanes by Waletzko *et al*. [12] showed that increased crystallinity of the soft block results in decreased strain-at-break and higher permanent set: the higher crystallinity impeded proper stress transfer to the continuous phase. Highly crystalline regions decreased strain-at-break instead of acting as load-bearing reinforcement agents.

The objective of this study was to synthesize biodegradable thermoplastic polyurethane elastomers; a parallel objective was to study the effect of soft segment crystallization on the polyurethane properties. PCL-co-PTMC was chosen as the soft segment of the PU. PTMC homopolymer is a completely amorphous biodegradable polymer that exhibits glass transition temperature at –20°C [13]. As compared to PCL, at molar mass range between 40–50 kDa, PTMC showed 30 times lower tensile strength but twice the elongation at break [14]; however, when copolymerized with other polymer such as PCL, PTMC shows better mechanical characteristics. Asplund *et al.* [10] has recently showed that LDI-based PUU that using poly (CL-co-TMC) as soft segments achieved higher elongation than PUU that based on poly (CL-co-DLLA).

In this study, we tried to lower the potential toxicity of degradation products by using the lowest amount of diisocyanate. Detailed cytotoxicity studies will be published in a separate article. To replace the role of the diisocyanate hard segments, PCL-co-PTMC soft segment was further reacted with L-LA to form A-B-A structure, yielding 'pseudo hard segments' via PLLA crystallization. Kricheldorf and Rost [15] have recently studied a similar system, PLLA-b-(PCL-co-PTMC)-b-PLLA multiblock copolymers synthesized by using bismuth(III) hexanoate as catalyst. However, they focused on the polymerization mechanism studies without emphasizing the relationship between mechanical property and PLLA crystallization.

2. Materials and methods

2.1. Materials

1,3-trimethylene carbonate (TMC) (Boehringer-Ingelheim, Germany), ε-caprolactone monomer (CL) (Alfa Aesar, Singapore), L-lactide (LLA) (Sigma Aldrich, Singapore), 1,6-hexamethylene diisocyanate (HMDI) (Fluka, Singapore) were used without further purification. The initiator, 2, 2-dimethyl 1, 3-propanediol (DMP) (Fluka, Singapore) was dried in 37°C vacuum oven for 24 h to remove moisture before synthesis. The catalyst, tin (II) 2-ethylhexanoate ($SnOct_2$) (Sigma Aldrich, Singapore) and the chain extender, 1,4-butanediol (BDO) (Alfa Aesar, Singapore) were dried over molecular sieves (4 Å). Solvents including methylene chloride, hexane and anhydrous toluene were of analytical grade, and used as received.

2.2. Polyurethane synthesis

The synthetic approach of the multiblock polyurethanes studied in this work is based on combination of three reaction steps in one pot, as shown in Figure 1. The first step was to randomly copolymerize CL and TMC by ring opening co-polymerization with controlled CL/TMC molar ratio (15/85, 25/75, 50/50, 75/25 and 85/15) and target M_n of 5000 Da. The following process illustrates the general procedure used to make 20 g of PCL/PTMC-based polyurethane (15/85) (MP1 in Table 1). 17.5 grams of TMC, 0.436 g of initiator, 133.3 ml of anhydrous toluene, 3.42 g of CL monomer and 0.21 g of

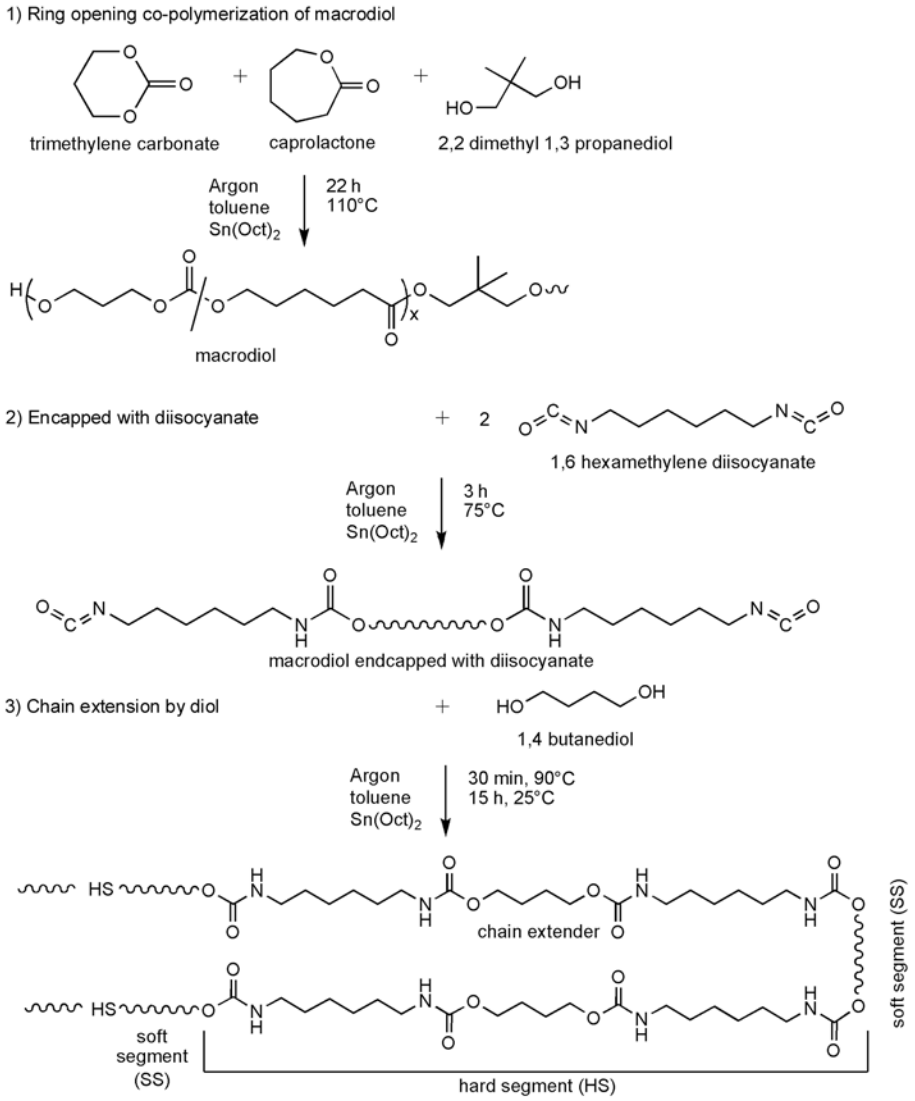

Figure 1. 3-step synthesis of multiblock polyurethanes based on PCL-co-PTMC

Table 1. Composition of soft segments and molar mass of (PCL-co-PTMC) multiblock polyurethanes

Multiblock PU (MP)	CL/TMC [mol%]*	M_w [Da][a]	M_w/M_n
MP1	15/85	57 100	1.60
MP2	25/75	59 300	1.62
MP3	50/50	58 700	1.63
MP4	75/25	69 800	1.75
MP5	85/15	78 700	1.83

MP = Multiblock Polyurethane
*Theoretical values
[a]Determined from SEC which was calibrated from polystyrene standards, chloroform as mobile phase

$SnOct_2$ (1 wt% of monomer weight) were added into a 250 ml round bottom reaction flask heated to 110°C for 22 hours under argon protection and continuous stirring. DMP was employed as initiator because $–CH_3$ showing distinctive peak at 0.95 ppm in ^{1}H NMR spectrum, allows accurate calculations of molar compositions and M_n.

In the second step, in the same flask, the resulting PCL-co-PTMC copolymer terminated by two reactive –OH groups was subjected to polycondensation reaction with 2-fold excess of hexamethylene diisocyanate (HMDI) (1.39 g) at 75°C for 3 hours, to yield diisocyanate terminated prepolymer. The third step was based on the addition of BDO (0.37 g) in a chain extension reaction, where the mixture temperature was raised to 90°C for 30 minutes under vigorous stirring (> 1000 rpm). The mixture was then cooled down to room temperature while the chain linking reaction was continued for another 15 hours, under constant stirring. The resulted product was purified by precipitation in cold methanol. The (PCL-co-PTMC): HMDI: BDO molar ratio was set

to 1:2.02:1. In this way multiblock polyurethanes were prepared with variation in soft segments composition. Hard segment content (wt%) was calculated by (g BDO + g HMDI)/ (g BDO + g HMDI + g soft segments). Each polyurethane contains 8 wt% of hard segments. MP1 ^{1}H NMR (400 MHz, $CDCl_3$): δ 4.77, 4.41, 4.23, 4.16, 4.12, 4.05, 3.95, 3.88, 3.66, 3.14, 2.31, 2.04, 1.66, 1.48, 1.40, 1.32, 0.99.

In the second series, multiblock polyurethanes (MP6–8) were prepared from A–B–A triblock copolymers, with variation of theoretical block 'A' length (1000, 2500, and 5000 Da). ROP of L-lactide (block 'A') was performed in the solution of PCL-co-PTMC random copolymer (block 'B'), when the first step was completed. It was initiated by both hydroxyl-ends of block 'B', at the presence of the catalyst from the first step. Steps two and three were repeated as described previously. MP6 ^{1}H NMR (500 MHz, $CDCl_3$): δ 5.15, 4.23, 4.16, 4.12, 4.05, 3.94, 3.87, 3.66, 3.15, 2.30, 2.04, 1.65, 1.58, 1.51, 1.37, 0.95.

2.3. Measurements

Molar mass of MP1-4 were determined by using Size Exclusion Chromatography (SEC) (Shimadzu LC-20AD prominence liquid chromatograph system equipped with three PLgel mixed-c columns in series and a Shimadzu RID-10A refractive index detector) (Kyoto, Japan). Monodisperse polystyrene standards were used for calibration. Measurements were made at 55°C with chloroform as eluent flowing at 1 ml/min. Samples were dissolved in chloroform (3 mg/ml) and 50 µl was injected. Besides, molar mass of MP6–8 were examined by using SEC system consisted of a Waters 510 HPLC pump, a Waters 410 differential refractometer detector (Milford, MA, USA) with tetrahydrofuran (THF) as mobile phase flowing at 1 ml/min. Samples were dissolved in THF (10 mg/ml) and 20 µl was injected. Measurements were made at room temperature.

Both ^{1}H NMR and ^{13}C NMR measurements were recorded in $CDCl_3$ on a Bruker 400 MHz (Bruker, Fällanden, Switzerland) or Varian VNMRS 500 MHz Spectrometer(Palo Alto, CA, USA). ^{1}H NMR signals were assigned according to several articles [13, 16–18] and ChemNMR ^{1}H estimation from ChemDraw. ^{13}C NMR spectroscopy was used to characterize the sequences of the triblock copolymer. From the dyads splitting of the ^{13}C NMR carbonyl signals of CL, TMC and LLA, the average block lengths of CL, TMC and LLA were calculated. Average block length of CL according to Equation (1) [16]:

$$\overline{L}_{CL} = \frac{I_{CL-CL}}{I_{CL-TMC}} + 1 \tag{1}$$

where $I_{CL–CL}$ is the signal intensity of the CL–CL dyad (signal a in Figure 2) and $I_{CL–TMC}$ is from CL–TMC dyad (signal b in Figure 2). Similar equation applied to TMC and LLA calculations.

Glass and melt transition temperatures were determined by Differential Scanning Calorimetry (DSC) (TA Instruments Q10-0095) (New Castle, DE, USA), under constant nitrogen flow. To ensure a consistent thermal history, samples (5 mg) were subjected to cool-heat-cool-heat treatment from –90 to 200°C with heating rate of 10°C/min and cooling rate of 20°C/min. The second heating data were analyzed. Typically, 2nd heating data are preferred for polymers rather than first heating, in order to wipe out the effects of polymer processing on the results. The degree of crystallinity (X_c) was calculated according to Equation (2):

$$X_c = \frac{\Delta H_f}{w \cdot \Delta H_f^0} \tag{2}$$

where ΔH_f is the heat of fusion of the sample, ΔH_f^0 is the heat of fusion of 100% crystalline PCL or PLLA and w is the weight fraction of CL or L-LA in the feed. For PCL and PLLA, the value of ΔH_f^0 used for the calculations was 139.5 J/g [19] and 93 J/g [20] respectively.

The stress-strain measurement was performed on Instron microtester 5848 (Norwood, MA, USA) equipped with 50 N load cell, at both room and body temperature (25 and 37°C). The polymer films were prepared by solution casting, methylene chloride (15% w/v) as solvent, in a Teflon dish. After drying in 37°C vacuum oven for 1 week, the films were punched into standard dumbbell shape (according to ASTM D 638 – 08, type V sample with thickness <4 mm) by using Schmidt press. Specimens were pulled at 10 mm/min in a temperature-controlled chamber. Testing result was discarded if the failure or necking occurred beyond gage length region.

Under the same operating condition, the cyclic tensile test was carried out. The sample was loaded and

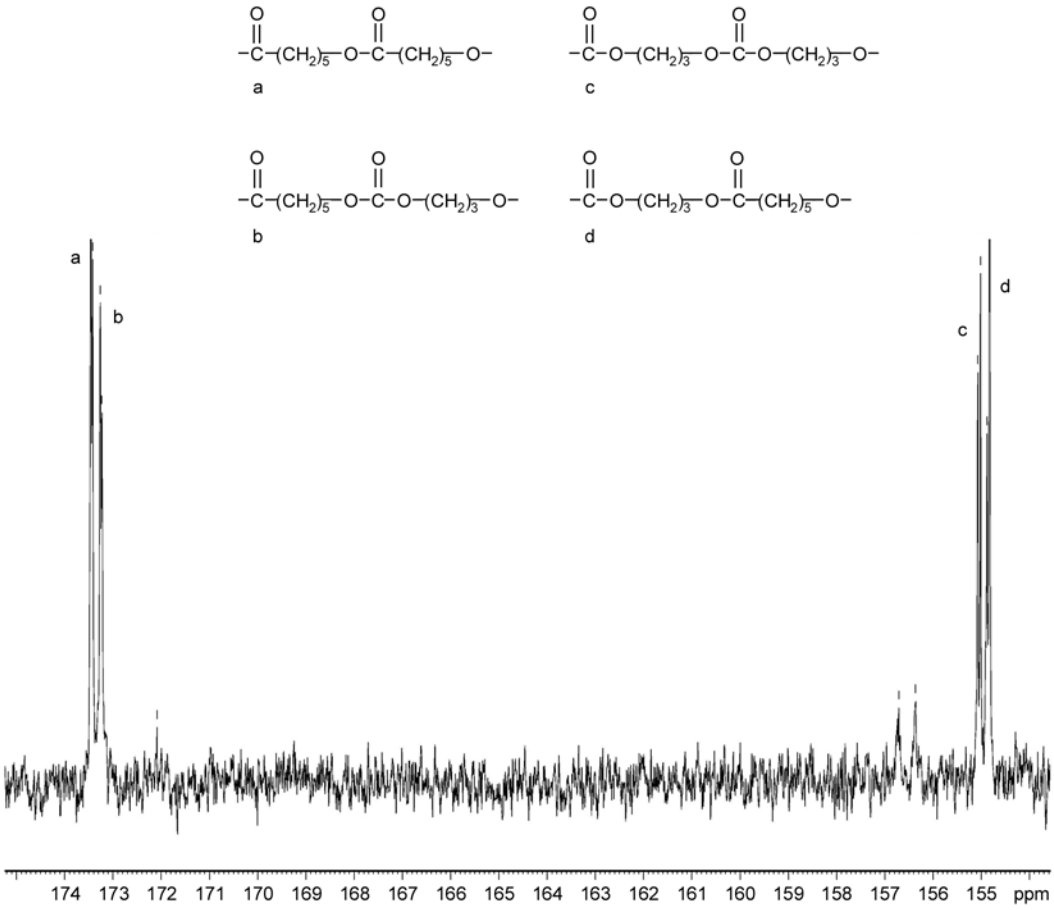

Figure 2. 101 MHz ^{13}C NMR spectrum (carbonyl region) of MP3 in $CDCl_3$

unloaded with 100% of the initial gage length per minute to 100% strain, for 3 cycles, or to 100–200–300% strain. The recovered strain (ε_R) was calculated as 100% strain minus permanent set. The permanent set of 100% strain was determined after a time of recovery (unloading) for 1 minute. For 200 and 300% strain, the recovery time was 2–4 minutes.

3. Results and discussion

3.1. Polyurethanes synthesis and characterization

(PCL-co-PTMC) polyurethanes

Multiblock polyurethanes, with various CL/TMC molar ratios, were synthesized by controlled ring opening co-polymerization (ROP) followed by polycondensation with HMDI and BDO. Targeted soft segment molar mass was achieved by controlling the total monomer/initiator ratio [21–23]. The mechanism of the cyclic esters ROP at the presence of $Sn(Oct)_2$ as catalyst was proposed in several studies [24, 25]. Table 1 showed the soft segment content and molar mass. The CL/TMC ratio was varied systematically to study PCL crystallinity on mechanical properties, while the hard segment content was fixed as low as 8 wt%.

[PLLA-b-(PCL-co-PTMC)-b-PLLA] polyurethanes

In the second series, multiblock polyurethanes were prepared from A–B–A triblock copolymers, which contained PCL-co-PTMC (50/50) as 'B' block, equivalent to soft segments of MP3 in Table 1, and PLLA as 'A' blocks. PLLA block length was controlled by total L-LA monomer/block 'B' macrodiol molar ratio. Table 2 showed the composition and molar mass of the second series. The hard segment content was fixed at 8 wt%.

3.2. Structural characterization

(PCL-co-PTMC) polyurethanes

NMR measurement in Table 3 showed the details of the soft segments molar mass, degree of polymerization of each segment with respect to one unit of initiator and average segment length. The random-

Table 2. 'A' block theoretical chain length and molar mass of [PLLA-b-(PCL-co-PTMC)-b-PLLA] multiblock polyurethanes

Multiblock PU (MP)	'A' block M_n [Da]*	M_w [Da][a]	M_w/M_n
MP6	1000	64 400	1.78
MP7	2500	80 200	1.77
MP8	5000	86 900	1.77

*Theoretical values
[a]Determined from SEC which was calibrated from polystyrene standards, THF as mobile phase

ness of PCL-co-PTMC soft segments was examined from ^{13}C NMR spectrum of carbonyl region in Figure 2. Average segment lengths were characterized by dyad splitting at 173.4 and 154 ppm, which corresponded to CL and TMC segments, respectively [13, 16]. From Figure 2 and Table 3, as expected, PCL-co-PTMC soft segments were completely and randomly copolymerized.

[PLLA-b-(PCL-co-PTMC)-b-PLLA] polyurethanes

Table 4 showed NMR data of purified triblock-based polyurethanes, including the calculated molar mass of block 'A' and 'B', degree of polymerization of each segment with respect to 1 unit of initiator, PLLA conversion and average segment length. The completion of the synthesis was examined from ^{1}H NMR spectrum. In Figure 3, ^{1}H NMR signals were assigned: $–CH_3$ signal from initiator (*a*), $–CH_2$ signals from CL (*d*), TMC (*j*) and CH signal from L-LA (*l*). The formation of urethane groups was indicated by $–CH_2$ from HMDI (*p*). The blockiness of PLLA blocks and the randomness of PCL-co-PTMC were analyzed from the carbonyl region of the ^{13}C NMR spectrum in Figure 4. Strong lactide signal (*e*) at 169.5 ppm represented the blocky polylactide structures with the absence of significant transesterification. In addition, the random sequence of CL and TMC segments agreed with MP3 in Figure 2.

3.3. Thermal properties

Microstructure of multiblock polyurethanes was studied by using DSC measurement. Generally, soft and hard segment crystallization, and the degree of phase separation can be estimated from thermal transitions such as glass transition temperature, melting temperature, and crystallization temperature. The polyurethane films for mechanical property study and the precipitated macrodiols were used in the thermal characterization.

(PCL-co-PTMC) polyurethanes

The second heating data were presented in Table 5, Figure 5 (macrodiols) and Figure 6 (multiblock polyurethanes). All polyurethanes in this study showed T_g below room temperature, indicating rubber-like amorphous structure. MP1–5 showed T_g close to T_g of their corresponding macrodiols SS1-5. The shift

Table 3. NMR measurement of (PCL-co-PTMC) multiblock polyurethanes

Multiblock PU (MP)	SS M_n [Da][a]	CL/TMC/DMP in feed*	CL/TMC/DMP found[a]	L_{CL}[b]	L_{TMC}[b]
MP1	5400	7:41:1	8:44:1	4.5	6.4
MP2	5200	12:35:1	13:36:1	2.7	4.3
MP3	5000	23:23:1	23:23:1	2.4	2.5
MP4	4600	34:11:1	30:10:1	4.8	2.4
MP5	4600	38:7:1	33:6:1	6.7	2.4

*Theoretical values
[a]Calculated from ^{1}H NMR peak integration of peak a, d and j
[b]Calculated from ^{13}C NMR spectra, using Equation (1)
DMP = 2,2 dimethyl 1,3 propanediol, the initiator of the PCL-co-PTMC random copolymers
SS = Soft segments

Table 4. NMR measurement of [PLLA-b-(PCL-co-PTMC)-b-PLLA] multiblock polyurethanes

Multiblock PU (MP)	'B' M_n [Da][a]	'A' M_n [Da][a]	CL/TMC/LLA/DMP in feed*	CL/TMC/LLA/DMP found[a]	PLLA conversion[a#]	L_{CL}[b]	L_{TMC}[b]	L_{LLA}[b]
MP6	4900	900	23:23:13:1	22:23:12:1	92%	2.6	2.5	7.2
MP7	4700	2100	23:23:34:1	22:22:29:1	85%	2.7	2.3	21.1
MP8	4900	4500	23:23:68:1	22:23:62:1	91%	2.7	2.4	42.2

*Theoretical values
[a]Calculated from ^{1}H NMR peak integration of peak a, d and j
[b]Calculated from ^{13}C NMR spectra, using Equation (1)
[#]Conversion = LLA found / in feed
DMP = 2,2 dimethyl 1,3 propanediol, the initiator of the PCL-co-PTMC random copolymers

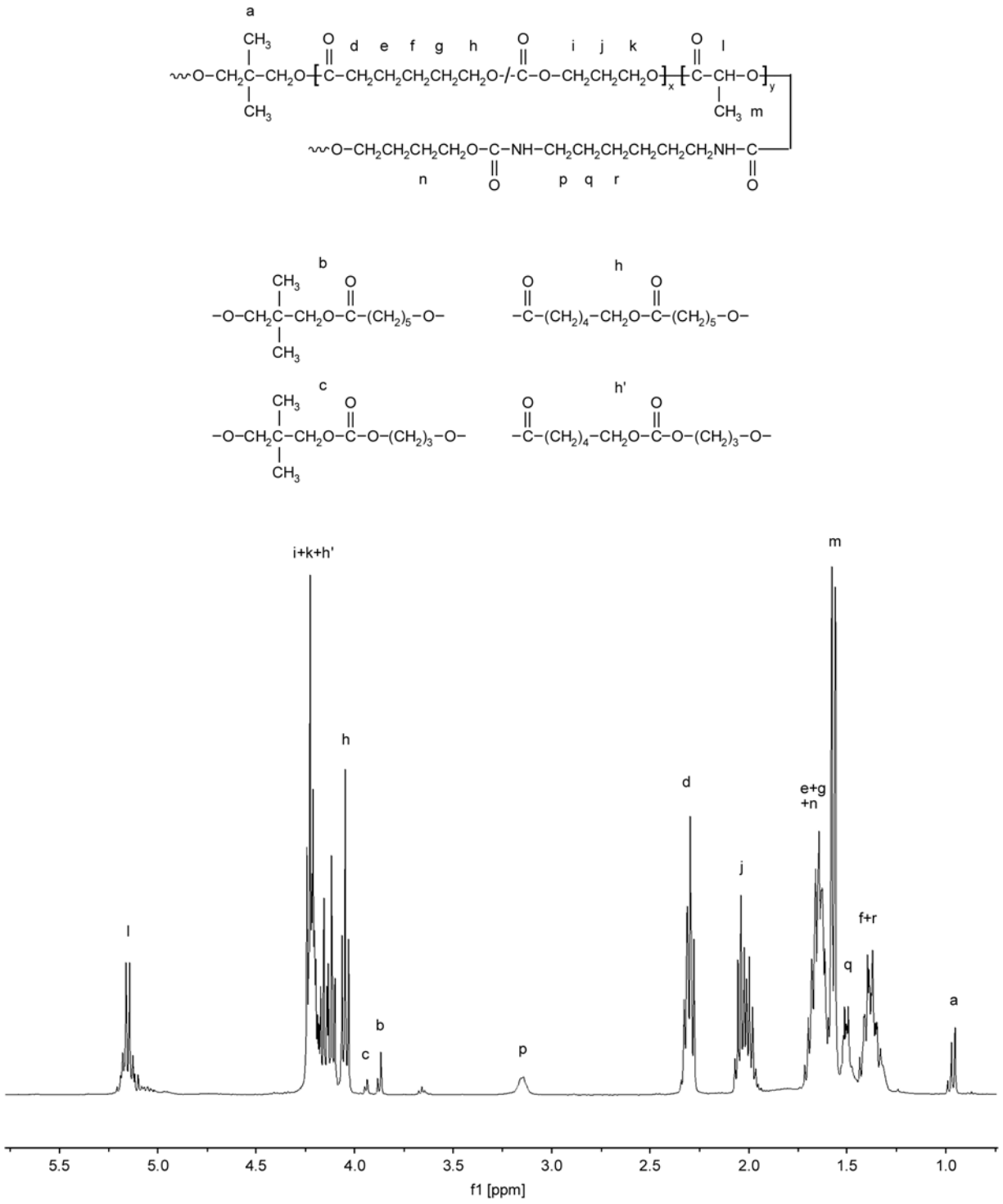

Figure 3. 500 MHz ^{1}H NMR spectrum of MP6 in $CDCl_3$

was attributed to the short uncrystallized HMDI-BDO blocks dispersion in the amorphous soft segments matrix [26]. To examine the degree of microphase separation between hard and soft segment, ΔT_g representing the difference between the T_g of polyurethane due to soft segments (MP1–5) and T_g of macrodiols (SS1–5), was calculated and listed in Table 5. Smaller ΔT_g reflects decreasing inter-phase interaction and solubilization, that is, increasing phase separation. In other words, polyurethane is well phase-separated if the ΔT_g is very small [1]. From Table 5, ΔT_g decreased with increasing CL molar fraction, suggesting that microphase separation between HS (HMDI-BDO)

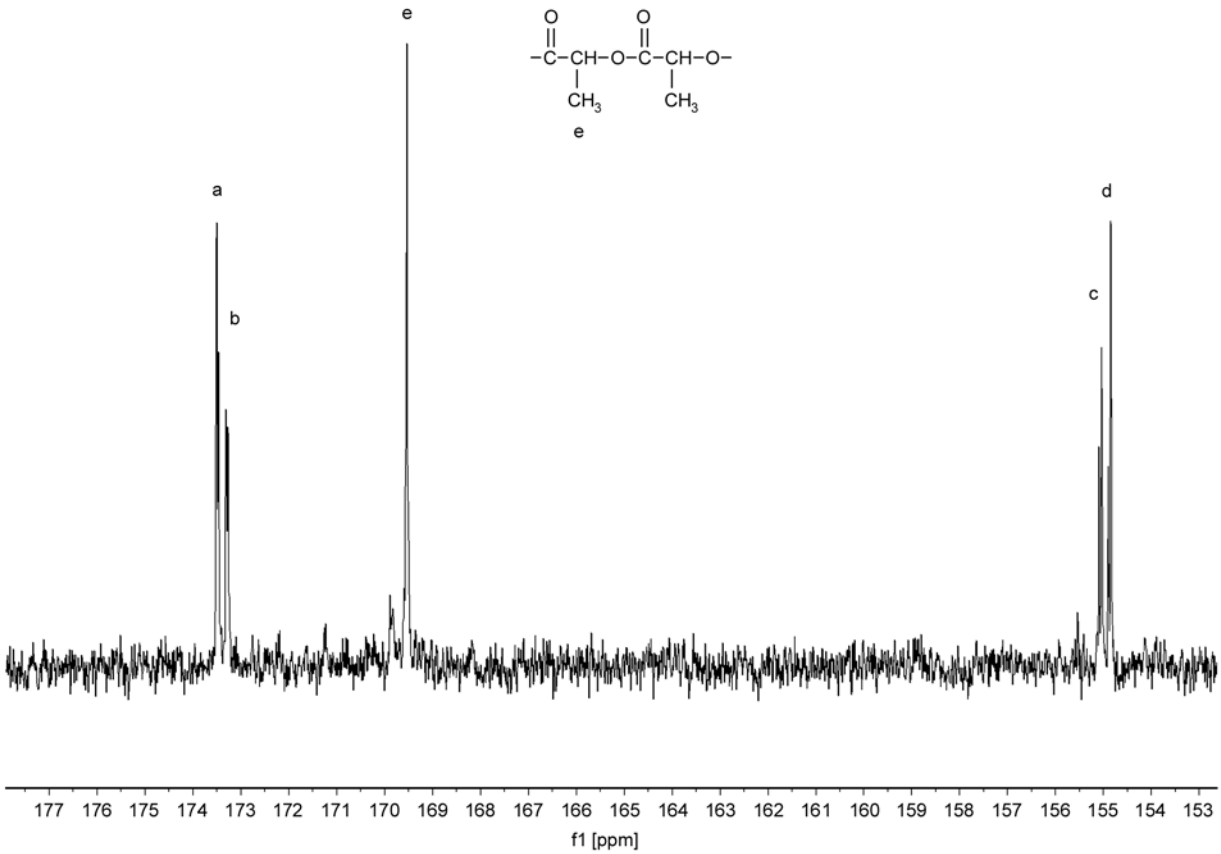

Figure 4. 101 MHz ^{13}C NMR spectrum (carbonyl region) of MP8 in $CDCl_3$

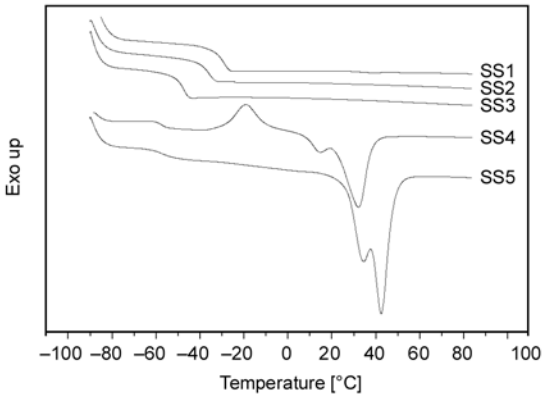

Figure 5. DSC second heating curves of precipitated macrodiols (SS1–5), from –90 to 90°C. The y-axis was shifted for better clarity

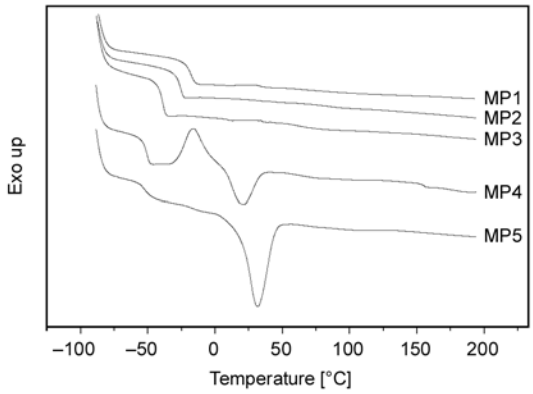

Figure 6. DSC second heating curves of (PCL-co-PTMC) multiblock polyurethane films (MP1–5) from –90 to 200°C. The y-axis was shifted for better clarity.

and SS (PCL-co-PTMC) became stronger. This is attributed to the effect of soft segment crystallization that could promote the phase separation, and is comparable to the studies reported on PU based on polycarbonates [27], PEO and PEO-PPO-PEO [28]. In the more extreme case, MP5 with 85% PCL showed T_g of –53 and –18°C, corresponding to PCL-rich and PTMC-rich two separated amorphous phases, which was not observed in SS5. The reason of the amorphous phase separation is unclear. It is believed that these short uncrystallized HMDI-BDO blocks tend to phase-separate from PCL and phase-mix with PTMC, thus, lead to non-continuous amorphous soft segment matrix. More characterizations such as AFM and DMA are required to further conclude the phase morphology.

Data in Table 5 suggests that crystallization is controlled by CL/TMC molar ratio in the soft seg-

Table 5. DSC data of the soft segments and (PCL-co-PTMC) multiblock polyurethanes

Polymer	T_g [°C]	T_c [°C]	T_m [°C]	ΔH_f [J/g][a]	X_c [%][d]	ΔT_g[e]
SS1	–29	–	–	–	–	–
SS2	–36	–	–	–	–	–
SS3	–47	–	–	–	–	–
SS4	–57	–26[b], –19[c]	32	58	41	–
SS5	–57	2[b]	42	60	43	–
MP1	–18	–	–	–	–	11
MP2	–26	–	–	–	–	10
MP3	–39	–	–	–	–	8
MP4	–51	–16[c]	20	16	12	6
MP5	–53, –18	–14[b]	31	36	26	4

The thermal properties of soft segments (SS) and their corresponding multiblock polyurethanes (MP) were included. DSC heating and cooling rate = 20°C/min. DSC data were observed from second heating curves, except T_c.
[a]Enthalpy of fusion values are per gram of PCL content in the soft segments or multiblock polyurethanes
[b]Crystallization temperature obtained from cooling curves
[c]Crystallization temperature obtained from second heating curve
[d]Degree of crystallinity based on heat of fusion of 100% crystalline PCL = 139.5 J/g
[e]The difference between T_g of SS and MP

ments. Soft segments crystallization were observed when CL/TMC molar ratio was 75/25 and higher. SS1–3 and MP1–3 did not show any melting transition because of their short average segment lengths (L_{CL} of 2.4–4.5 in Table 3). This is in contradiction with PCL-co-PTMC (50/50) copolymers studied by Pêgo *et. al.* [16]. L_{CL} of 3.93 was suggested to be long enough to crystallize. In our study, MP1 (15% PCL) with L_{CL} of 4.5 was unable to crystallize even though they were long enough, mainly due to the low %PCL. The degree of crystallization (X_c) and melting enthalpy of fusion (ΔH_f) dropped after chain extension, suggesting smaller, less stable and less organized crystallites were formed in the polyurethanes compared to the macrodiols in Figure 5 [28]. From the DSC analysis showing low degree of phase mixing with PCL, the main restriction of crystallization is due to the reduced chain mobility. MP5 with longer average L_{CL} of 6.7 was more readily to crystallize after chain extension as compare to MP4 (L_{CL} of 4.8 from Table 3).

As expected, hard segments transition was not observed in the second heating curves because the amount of HMDI and BDO were as low as 8 wt%. Pure HMDI-BDO hard segment melting transition ranging from 165–182°C was reported in previous studies [28–30].

[PLLA-b-(PCL-co-PTMC)-b-PLLA] polyurethanes

Figure 7 showed the DSC curves of MP6–8. In Table 6, DSC data of PCL-co-PTMC soft segments, triblocks and their corresponding polyurethanes showed that thermal properties was affected by

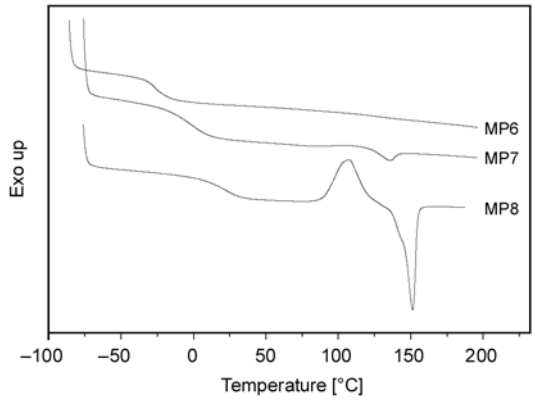

Figure 7. DSC second heating curves of [PLLA-b-(PCL-co-PTMC)-b-PLLA] multiblock polyurethane films (MP6–8) from –90 to 200°C. The y-axis was shifted for better clarity.

PLLA block length. Single T_g was observed in the PCL-co-PTMC soft segments, suggesting a continuous amorphous segments. T_g of triblock was increased after incorporation of PLLA blocks due to mixing of amorphous regions from PCL, PTMC and PLLA. The T_g were all below room temperature, suggesting a rubbery amorphous phase. Microphase separation in the second series was assessed by the difference between T_g of TB6–8 and MP6–8 (ΔT_g). ΔT_g was independent of PLLA block length. This could be attributed to two contrasting phenomena: hydrogen bonding between HMDI-BDO and the carbonyl group from PLLA esters can improve phase mixing; in contrast, crystallization from either segments can enhance phase separation [1].

From data shown in Table 6, the multiblock polyurethane crystallization is controlled by PLLA

Table 6. DSC data of the soft segments PCL-co-PTMC, triblock copolyesters and [PLLA-b-(PCL-co-PTMC)-b-PLLA] multiblock polyurethanes

Polymer	T_g [°C]	T_c [°C]	T_m [°C]	ΔH_f [J/g][a]	X_c [%][b]	ΔT_g[c]
SS3	–47	–	–	–	–	–
SS6	–49	–	–	–	–	–
SS7	–47	–	–	–	–	–
SS8	–47	–	–	–	–	–
TB6	–32	–	–	–	–	–
TB7	–10	74	137	39	41	–
TB8	20	82	154	49	53	–
MP3	–39	–	–	–	–	8
MP6	–27	–	–	–	–	5
MP7	–2	–	136	5	5	8
MP8	23	107	152	31	34	3

The thermal properties of soft segments PCL-co-PTMC (SS), triblocks (TB) and their corresponding multiblock polyurethanes (MP) were included. DSC heating rate = 10°C/min and cooling rate = 20°C/min. DSC data were observed from second heating curves. SS3 and MP3 data was included for comparison.

[a]Enthalpy of fusion values are per gram of PLLA content in the triblocks or multiblock polyurethanes

[b]Degree of crystallinity based on heat of fusion of 100% crystalline PLLA = 93 J/g

[c]The difference between T_g of TB and MP

block length. Triblock TB6 was found to be a continuous amorphous copolymer with the absence of any melting transition. Semicrystalline triblocks (TB7–8) were observed when the PLLA has average chain length (L_{LLA} in Table 4) higher than 21. Melting transition at 137–154°C were observed accompanied by high degree of crystallinity. After the addition of HMDI-BDO hard segments, although melting points remained unchanged, the enthalpy (and degree of crystallinity), expecially for MP7, dropped significantly. The decrease in enthalpy is possibly due to the disruption of PLLA crystallinity by the HMDI/BDO. It is not likely that this phenomenon is the result of the change in weight percentage of PLLA, since the enthalpies shown in Table 6 have been normalized.

Similar to series one, hard segments transitions was not observed in the second heating curves obtained from DSC measurement, because it was low in weight percent. With the presence of PLLA crystals, having melting transitions similar to HMDI-BDO hard segments, it may replace the role of hard segments as load bearing segments upon deformation.

3.4. Tensile properties

(PCL-co-PTMC) polyurethanes

Table 7 gave a summary of the mechanical properties including the initial modulus, ultimate tensile strength (UTS), the strain-at-break (ε_b) and the recovered strain after being stretched to 100–100–100% or 100–200–300% of the initial gage length.

As shown in Figure 8 and Table 7, at room temperature (25°C), the shape of the stress-strain curves for MP1–5 are typical for lightly crosslinked rubber: smooth transition from elastic to plastic region. MP1–3 showed low UTS which represented soft amorphous materials, which are in agreement with DSC results. MP4 and 5 showed significantly higher moduli, tensile strength, and strain-at-break than

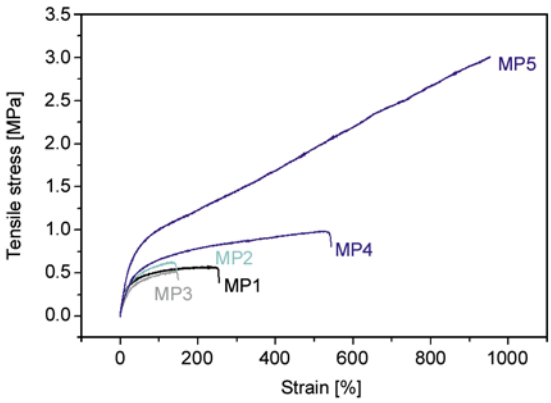

Figure 8. Stress-strain curves of MP1–5 at room temperature (25°C)

Table 7. Tensile measurements and cyclic deformation of (PCL-co-PTMC) multiblock polyurethanes at 25°C

Multiblock PU (MP)	CL/TMC [mol%]	Initial modulus [MPa]	UTS [MPa]	ε_b [%]	ε_{R1} [%/100%]	ε_{R2} [%/100%]	ε_{R3} [%/100%]
MP1	15/85	3.2±0.8	0.51±0.11	246±6	77	74	70
MP2	25/75	3.6±0.8	0.63±0.05	133±13	79	75	73
MP3	50/50	2.2±0.3	0.51±0.06	133±20	81	79	75
MP4	75/25	2.6±0.2	1.00±0.13	519±85	87	83[a]	76[b]
MP5	85/15	3.6±0.2	2.98±0.09	954[c]	75	57[a]	49[b]

Tensile test was conducted with number of sample n = 3–7 in each multiblock polyurethane

[a]In second cycle, sample was deformed to 200%, strain recovery is %recovered/200%

[b]In third cycle, sample was deformed to 300%, strain recovery is %recovered/300%

[c]Testing samples (n = 3) were not failed after machine limit, the standard deviation is not applicable

MP1–3, as a result of crystallizable PCL segments. MP1–5 showed UTS lower than traditional PU as the hard segment content was low and it did not crystallize. Their UTS and breaking strain were proportional to the degree of crystallinity. This is agreeable with the study conducted by Skarja [11]. The presence of PCL crystals was anticipated to act as physical network in a way that similar to hard segments [11]. They may absorb deformation energy through unfolding some of the isotropic crystalline lamellar and form new strain-induced crystalline lamellar perpendicular to the strain direction [31]. In Figure 8, MP5 showed the best tensile properties with PCL-co-PTMC 85/15 composition. It showed a dramatic increase in UTS and strain at break when compared to MP4 because MP5 has a relatively higher degree of crystallinity and melting point. Strain-induced crystallization in MP5 is extensive since its T_m (31°C) is close to room temperature thus mobility of the chain is high. However, MP4 has T_m slightly lower than room temperature. The crystalline region would have partially molten before it could be strain-crystallized.

[PLLA-b-(PCL-co-PTMC)-b-PLLA] polyurethanes

Second series of polyurethane elastomers with different PLLA block length were studied. Table 8 compared the tensile properties with MP3. Without PLLA blocks, MP3 showed low UTS and initial modulus that represented weak and soft materials. Polyurethanes based on triblock [PLLA-b-(PCL-co-PTMC)-b-PLLA] copolymers presented tougher and stronger behavior. At room temperature (25°C), the UTS and initial moduli increased proportional to the PLLA block length. This result is coherent with the mechanical tests of PLA-PTMC-PLA copolyesters reported by Zhang *et al.* [32].

In Figure 9, MP8 showed the highest initial modulus and UTS among all the polyurethanes in this study. In contrast, completely amorphous polyurethanes including MP6 and MP1–3 in this study showed limited elongation, low UTS and initial moduli. These can be attributed several factors that played significant role in the tensile properties of polyurethane. First, PCL or PLLA with moderate degree of crystallinity acts as reinforment filler to absorb deformation energy [12]. As noted in NMR and DSC measurement, PCL or PLLA segments crystallized in polyurethanes MP4, MP5, MP7 and MP8. Secondly, although all the HMDI-BDO segments of the multiblock polyurethanes were not crystalline, PLLA in the soft segments had high melting points which acted as additional hard seg-

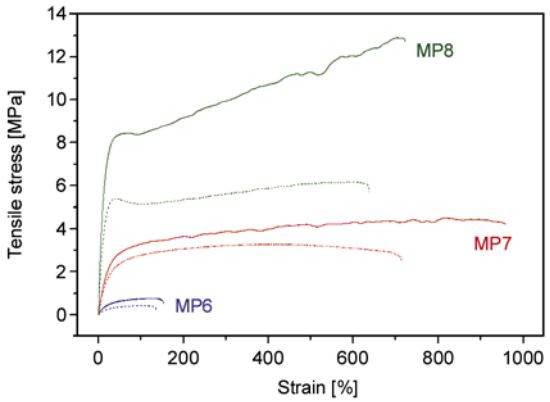

Figure 9. Stress-strain curves of MP6–8 at both room temperature (solid line) and body temperature (dotted line)

Table 8. Tensile test data of [PLLA-b-(PCL-co-PTMC)-b-PLLA] multiblock polyurethanes at room temperature and body temperature

Multiblock PU (MP)	PLLA block M_n [Da]*	Initial Modulus [MPa]	UTS [MPa]	ε_b [%]	ε_{R1} [%/100%]
25°C					
MP3	0	2.2±0.3	0.51±0.06	133±20	81
MP6	1000	3.6±0.4	0.65±0.10	116±14	88
MP7	2500	16.3±1.6	4.58±0.07	919[a]	93
MP8	5000	65.4±17.7^	12.90^	723^	79
37°C					
MP6	1000	2.8±0.2	0.49±0.06	126±14	88
MP7	2500	13.4±0.2	3.28±0.05	582±187	87
MP8	5000	52.1±1.8^	6.17^	637^	80

Tensile test was conducted with number of sample n = 2–3 in each multiblock polyurethane

*Theoretical value

[a]Testing samples (n = 3), one of them was not failed after machine limit, the standard deviation is not applicable

^Test was not triplicated due to films imperfection

ments. Lastly, MP6 and MP1–3 polyurethanes showed relatively low molar masses, and thus lowered tensile properties.

3.5. Temperature effect on tensile properties

Polyurethanes in the first series were unable to sustain deformation at body temperature (37°C). They became soft and too weak to be tested mechanically. The PU lost its structural integrity due to lack of hard segment crystallization to act as additional physical crosslinks at higher temperature.

Table 8 and Figure 9 showed that tensile properties of polyurethanes in the second series were temperature dependent. As temperature increased, UTS, initial modulus and strain-at-break decreased slightly. Unlike PCL crystals in the first series, PLLA crystals exhibited higher melting point that would not melt away at body temperature. Instead, the decrease in tensile properties is possibly due to the differences between T_g and testing temperature, especially for MP8 with T_g at 23°C. At room temperature (25°C), strain-induced crystallization was extensive, leading to high elongation. At body temperature, further away from its T_g, polymer chains gained higher mobility that allowed phase mixing between esters in the soft segments and urethanes in the hard segments [1].

3.6. Tensile cyclic hysteresis and strain recovery

As discussed in previous section, tensile strength and initial modulus of polyurethanes depend on structural rigidity that results from soft segments crystallinity, as the HMDI-BDO hard segments did not crystallize. MP8 showed the highest tensile strength and initial modulus. In contrast, stress hysteresis and strain recovery depend more on domain ductility and restructuring [1]. From our tensile cyclic test results, although MP8 showed the best tensile properties, it did not exhibit the highest strain recovery.

Table 7 showed the trend of strain recovery of the multiblock PU after tensile cyclic tests. In MP1–4, the % of strain being recovered was proportional to the %PCL in the random copolymer, except that MP5 demonstrated slightly lower strain recovery. The optimum CL/TMC composition to achieve highest strain recovery lies between 75/25 to 85/15, with moderate PCL crystallinity (X_c) between 12–26% (refer to Table 5). In Table 8, strain recovery

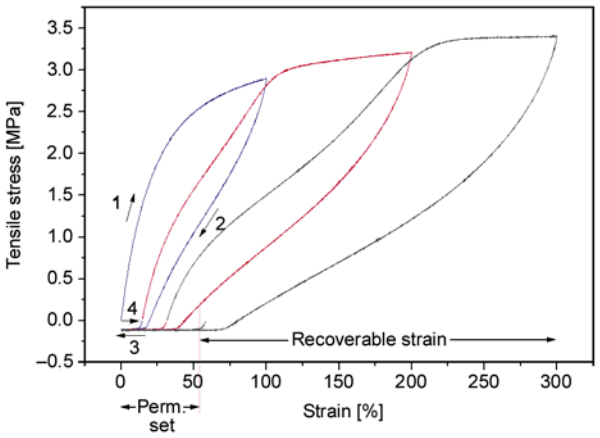

Figure 10. Tensile stress hysteresis of MP7 at 37°C, programming to 100–200–300% tensile cyclic loading-unloading

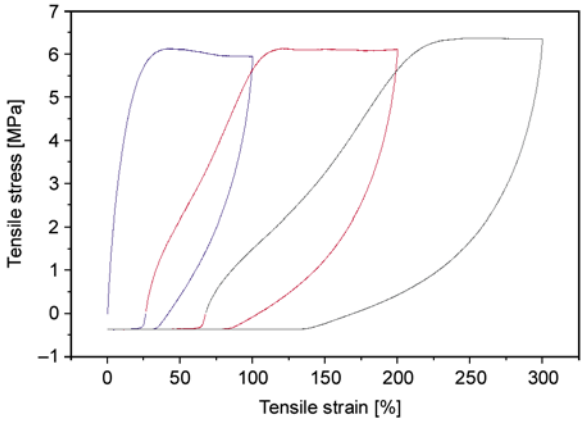

Figure 11. Tensile stress hysteresis of MP8 at 37°C, programming to 100–200–300% tensile cyclic loading-unloading

of MP6–8 with PLLA blocks were compared to MP3. It appears that the recoverable strain after 100% elongation was related to the PLLA block length. MP7 with low PLLA crystallinity (5%) showed the highest strain recovery of 93% in one minute. Similar to MP5 in the first series, MP8 in series two was not following the trend. It exhibited a slight drop in strain recovery, indicating the optimum PLLA crystallinity stayed between 5–34 %. These phenomena were attributed to PCL or PLLA crystallinity that impeded proper stress transfer to the continuous phase [12] and thus hindered domain restructuring. Moreover, their strain recoveries were barely affected by temperature, as shown in Table 8, because of the high PLLA melting point. Figures 10 and 11 depicted the cyclic tensile 100–200–300% of MP7 and MP8, respectively. MP7 exhibited strain recovery pattern that is smooth with

smaller hysteresis compared to MP8. More permanent set was evident in MP8 that showed yield point in the stress-strain curves (Figure 9).

4. Conclusions

The two sets of multiblock thermoplastic polyurethane elastomers reported in this study were different from previous studies in that the optimization of mechanical properties was studied by (i) crystallization of PCL in PCL-co-PTMC soft segments and (ii) crystallization of PLLA in PLLA-b-(PCL-co-PTMC)-b-PLLA triblock soft segments. First, the (PCL-co-PTMC) polyurethanes were synthesized and characterized. With low hard segment content, hard segment crystallinity was hardly observed. Increasing the PCL/PTMC molar ratio in the soft segments was found to have lowered the T_g, increased molar mass, and soft segments crystallinity. Mechanically, completely amorphous soft segments were shown to yield multiblock PUs which were soft and weak. The presence of moderate PCL crystallinity improved the tensile strength, initial modulus and strain-at-break while relatively low PCL crystallinity yielded the highest strain recovery. However, tensile properties of (PCL-co-PTMC) polyurethanes were greatly affected when being tested at body temperature due to the melting of PCL crystals. To solve this problem, 'pseudo hard segments' represented by PLLA blocks were introduced in the polyurethanes. When the (PCL-co-PTMC) polyurethanes were compared with [PLLA-b-(PCL-co-PTMC)-b-PLLA] polyurethanes, the presence of PLLA blocks significantly improved the tensile properties. PLLA soft segments with high melting point allowed the formation of additional physical crosslink points that can sustain deformation at body temperature, in addition to reducing potential toxicity due to high diisocyanate content. Similar to PCL crystals, the presence of moderate PLLA crystallinity improved the tensile strength and initial modulus while the highest strain recovery was achieved at low PLLA crystallinity. These polyurethanes are attractive as biomaterials for dynamic environment that demands high elasticity such as tissue engineering scaffolds and interventional cardiovascular devices, due to their excellent strain recovery and tensile properties at body temperature. Their thermal and mechanical properties are easily tunable by soft segment crystallinity.

Acknowledgements

This study was financially supported by Ministry of Education (MOE) Singapore. The authors are grateful to Dr. J. Kohn and Dr. D. Bolikal in New Jersey Center for Biomaterials (NJCBM), United States, for their advice and support in this study.

References

[1] Lamba N. M. K., Woodhouse K. A., Cooper S. L.: Polyurethanes in biomedical applications. CRC Press, Boca Raton (1998).

[2] Tuominen J., Kylmä J., Kapanen A., Venelampi O., Itävaara M., Seppälä J.: Biodegradation of lactic acid based polymers under controlled composting conditions and evaluation of the ecotoxicological impact. Biomacromolecules, **3**, 445–455 (2002). DOI: 10.1021/bm0101522

[3] Guelcher S. A.: Biodegradable polyurethanes: Synthesis and applications in regenerative medicine. Tissue Engineering Part B: Reviews, **14**, 3–17 (2008). DOI: 10.1089/teb.2007.0133

[4] Guan J., Sacks M. S., Beckman E. J., Wagner W. R.: Synthesis, characterization, and cytocompatibility of elastomeric, biodegradable poly(ester-urethane)ureas based on poly(caprolactone) and putrescine. Journal of Biomedical Materials Research, **61**, 493–503 (2002). DOI: 10.1002/jbm.10204

[5] Hassan M. K., Mauritz K. A., Storey R. F., Wiggins J. S.: Biodegradable aliphatic thermoplastic polyurethane based on poly(ε-caprolactone) and L-lysine diisocyanate. Journal of Polymer Science Part A: Polymer Chemistry, **44**, 2990–3000 (2006). DOI: 10.1002/pola.21373

[6] Kylmä J., Seppälä J. V.: Synthesis and characterization of a biodegradable thermoplastic poly(ester−urethane) elastomer. Macromolecules, **30**, 2876–2882 (1997). DOI: 10.1021/ma961569g

[7] Ryynänen T., Nykännen A., Seppälä J. V.: Poly(CL/DLLA-b-CL) multiblock copolymers as biodegradable thermoplastic elastomers. Express Polymer Letters, **2**, 184–193 (2008). DOI: 10.3144/expresspolymlett.2008.23

[8] Guan J., Sacks M. S., Beckman E. J., Wagner W. R.: Biodegradable poly(ether ester urethane)urea elastomers based on poly(ether ester) triblock copolymers and putrescine: Synthesis, characterization and cytocompatibility. Biomaterials, **25**, 85–96 (2004). DOI: 10.1016/S0142-9612(03)00476-9

[9] Hong Y., Guan J., Fujimoto K. L., Hashizume R., Pelinescu A. L., Wagner W. R.: Tailoring the degradation kinetics of poly(ester carbonate urethane)urea thermoplastic elastomers for tissue engineering scaffolds. Biomaterials, **31**, 4249–4258 (2010). DOI: 10.1016/j.biomaterials.2010.02.005

[10] Asplund J. O. B., Bowden T., Mathisen T., Hilborn J.: Synthesis of highly elastic biodegradable poly(urethane urea). Biomacromolecules, **8**, 905–911 (2007). DOI: 10.1021/bm061058u

[11] Skarja G. A.: The development and characterization of degradable, segmented polyurethanes containing amino acid-based chain extenders. PhD thesis, University of Toronto (2001).
[12] Waletzko R. S., Korley L. T. J., Pate B. D., Thomas E. L., Hammond P. T.: Role of increased crystallinity in deformation-induced structure of segmented thermoplastic polyurethane elastomers with PEO and PEO-PPO-PEO soft segments and HDI hard segments. Macromolecules, **42**, 2041–2053 (2009).
DOI: 10.1021/ma8022052
[13] Albertsson A-C., Eklund M.: Synthesis of copolymers of 1,3-dioxan-2-one and oxepan-2-one using coordination catalysts. Journal of Polymer Science Part A: Polymer Chemistry, **32**, 265–279 (1994).
DOI: 10.1002/pola.1994.080320207
[14] Domb A. J., Kumar N., Sheskin T., Bentolila A., Slager J., Teomim D.: Biodegradable polymers as drug carrier systems. in 'Polymeric biomaterials' (ed.: Dumitriu S.) Marcel Dekker, New York, 91–122 (2002).
[15] Kricheldorf H. R., Rost S.: Biodegradable multiblock copolyesters prepared from ε-caprolactone, L-lactide, and trimethylene carbonate by means of bismuth hexanoate. Macromolecules, **38**, 8220–8226 (2005).
DOI: 10.1021/ma050439h
[16] Pêgo A. P., Zhong Z., Dijkstra P. J., Grijpma D. W., Feijen J.: Influence of catalyst and polymerization conditions on the properties of 1,3-trimethylene carbonate and ε-caprolactone copolymers. Macromolecular Chemistry and Physics, **204**, 747–754 (2003).
DOI: 10.1002/macp.200390043
[17] Shen Y., Shen Z., Zhang Y., Yao K.: Novel rare earth catalysts for the living polymerization and block copolymerization of ε-caprolactone. Macromolecules, **29**, 8289–8295 (1996).
DOI: 10.1021/ma9518060
[18] Shen Y., Shen Z., Zhang Y., Huang Q., Shen L., Yuan H.: Random copolymerization of ε-caprolactone and trimethylene carbonate with rare earth catalysts. Journal of Applied Polymer Science, **64**, 2131–2139 (1997).
DOI: 10.1002/(SICI)1097-4628(19970613)64:11<2131::AID-APP9>3.0.CO;2-K
[19] Crescenzi V., Manzini G., Calzolari G., Borri C.: Thermodynamics of fusion of poly-β-propiolactone and poly-ε-caprolactone. Comparative analysis of the melting of aliphatic polylactone and polyester chains. European Polymer Journal, **8**, 449–463 (1972).
DOI: 10.1016/0014-3057(72)90109-7
[20] Fischer E. W., Sterzel H. J., Wegner G.: Investigation of the structure of solution grown crystals of lactide copolymers by means of chemical reactions. Colloid and Polymer Science, **251**, 980–990 (1973).
DOI: 10.1007/BF01498927
[21] Lipik V. T., Kong J. F., Chattopadhyay S., Widjaja L. K., Liow S. S., Venkatraman S. S., Abadie M. J. M.: Thermoplastic biodegradable elastomers based on ε-caprolactone and L-lactide block co-polymers: A new synthetic approach. Acta Biomaterialia, **6**, 4261–4270 (2010).
DOI: 10.1016/j.actbio.2010.05.027
[22] Liow S. S., Widjaja L. K., Lipik V. T., Abadie M. J. M.: Synthesis, characterization and photopolymerization of vinyl functionalized poly (ε-caprolactone). Express Polymer Letters, **3**, 159–167 (2009).
DOI: 10.3144/expresspolymlett.2009.21
[23] Dubois P., Jérôme R., Teyssié P.: Macromolecular engineering of polylactones and polylactides. 3. Synthesis, characterization, and applications of poly(iε-caprolactone) macromonomers) macromonomers. Macromolecules, **24**, 977–981 (1991).
DOI: 10.1021/ma00005a002
[24] Kowalski A., Duda A., Penczek S.: Kinetics and mechanism of cyclic esters polymerization initiated with tin(II) octoate, 1. Polymerization of ε-caprolactone. Macromolecular Rapid Communications, **19**, 567–572 (1998).
DOI: 10.1002/(SICI)1521-3927(19981101)19:11<567::AID-MARC567>3.0.CO;2-T
[25] Kricheldorf H. R., Kreiser-Saunders I., Stricker A.: Polylactones 48. $SnOct_2$-initiated polymerizations of lactide: A mechanistic study. Macromolecules, **33**, 702–709 (2000).
DOI: 10.1021/ma991181w
[26] Drobny J. G.: Handbook of thermoplastic elastomers. William Andrew Publishing, New York (2007).
[27] Kojio K., Furukawa M., Motokucho S., Shimada M., Sakai M.: Structure−mechanical property relationships for poly(carbonate urethane) elastomers with novel soft segments. Macromolecules, **42**, 8322–8327 (2009).
DOI: 10.1021/ma901317t
[28] Korley L. T. J., Pate B. D., Thomas E. L., Hammond P. T.: Effect of the degree of soft and hard segment ordering on the morphology and mechanical behavior of semicrystalline segmented polyurethanes. Polymer, **47**, 3073–3082 (2006).
DOI: 10.1016/j.polymer.2006.02.093
[29] Li Y., Ren Z., Zhao M., Yang H., Chu B.: Multiphase structure of segmented polyurethanes: Effects of hard-segment flexibility. Macromolecules, **26**, 612–622 (1993).
DOI: 10.1021/ma00056a010
[30] Kajiyama T., MacKnight W. J.: Thermal properties of polyurethanes. Enthalpies and entropies of fusion. Polymer Journal, **1**, 548–554 (1970).
[31] Toki S., Sics I., Burger C., Fang D., Liu L., Hsiao B. S., Datta S., Tsou A. H.: Structure evolution during cyclic deformation of an elastic propylene-based ethylene−propylene copolymer. Macromolecules, **39**, 3588–3597 (2006).
DOI: 10.1021/ma0600106
[32] Zhang Z., Grijpma D. W., Feijen J.: Triblock copolymers based on 1,3-trimethylene carbonate and lactide as biodegradable thermoplastic elastomers. Macromolecular Chemistry and Physics, **205**, 867–875 (2004).
DOI: 10.1002/macp.200300184

eXPRESS Polymer Letters Vol.5, No.10 (2011) 911–922
Available online at www.expresspolymlett.com
DOI: 10.3144/expresspolymlett.2011.89

Polystyrene grafted onto high-cis-1,4 polybutadiene backbone via 'living' radical polymerization with 2,2,6,6-tetramethylpiperidinyl-1-oxy (TEMPO) radical

Z. S. Yu[1,2*], *Y. Li*[1], *Y. R. Wang*[1]

[1]Department of Polymer Science and Engineering, Faculty of Chemical, Environmental and Biological Science and Technology, Dalian University of Technology, Dalian 116012, People's Republic of China
[2]Shanghai Research Institute of Petrochemical Technology, SINOPEC, Shanghai 201208, People's Republic of China

Received 25 February 2011; accepted in revised form 29 April 2011

Abstract. A stable nitroxide radical (2,2,6,6-tetramethylpiperidinyl-1-oxy, TEMPO) was employed to a grafting polymerization of styrene onto the high-*cis*-1,4 polybutadiene (PB) rubber initiated by 1,1-bis(*tert*-butylperoxy)cyclohexane (DP275B). The influence of TEMPO/DP275B ratio on the reaction progress, molecular structure, mechanical performance and fracture behavior of the toughened polystyrenes (PS) was systematically characterized. The results showed that a moderate amount of TEMPO used is favorable to the morphology and properties of the as-prepared products, which fracture with a semi-ductile mode. While increasing TEMPO dosage, both rubber grafting and particle size distribution become weaker, and as a result the material also tends to be very brittle and unstable under impact.

Keywords: *polymer composites, living radical polymerization, TEMPO, mechanical properties, fracture mechanism*

1. Introduction

Graft polymers became highly attractive materials and drew more and more attention due to their potential applications as e.g. compatibilisers, thickening agents, toughening and modifiers, etc. [1–5]. Graft copolymerization of vinyl monomers onto plastics is a very useful way to modify some special performances of the existing materials and expand their application range [6–10].

Compared with living ionic polymerization for graft polymers [11, 12], the advantages of living radical polymerization, e.g. nitroxide-mediated polymerization (NMP), are that the polymerization conditions required are less stringent, and the terminal group of initial graft segments (nitroxide group) is stable in air at room temperature and the intermediates can be isolated, stored and used as needed [9, 13]. Besides, the NMP method can combine the ease of polymerization with the fact that several monomers are capable of reaction [14]. Polymers with controlled molecular weight and narrow polydispersity can be synthesized by this controlled/stable free radical methodology [15, 16].

Several reports about the NMP method have recently appeared on the subject of the modification of polydienes or polymeric substrates through grafting copolymerization of vinyl monomers [17–24]. Commonly, the nitroxide moieties are firstly hung on the backbone of those substrates, which are endowed with functionalized group, and then in the presence of monomer, the grafts are grown from the nitroxide sites under thermal conditions. Howell *et al.* [25] reported a synthesis of PB (polybutadiene) with hanging nitroxide moieties to produce high-impact polystyrene (HIPS), and the grafting process was studied only by the comparison of the gel per-

*Corresponding author, e-mail: yvzx.sshy@sinopec.com

meation chromatography (GPC) of the grafted polymer with the functionalized polymer. In the fundamental studies of the controlled grafting of PS on PB by Bonilla-Cruz *et al.* [26], not only the functionalization mechanisms were proposed, but the structure and level of grafting control were investigated. Nevertheless, some aspects regarding the microstructural morphology and the mechanical performances of the final products have not been reported in literature.

In the present study, nitroxide-mediated polymerization has been conducted for synthesizing PB-*g*-PS copolymers in the presence of difunctional radical initiator (DP275B) and stable nitroxide radical (TEMPO), and the grafting polymerization behavior of the resulting product is characterized by size exclusion chromatography (SEC). Experiments are also designed to investigate the effect of nitroxide/initiator (TEMPO/DP275B) ratio on the polymerization kinetics behavior, phase inversion progress, and the structural and mechanical properties of as-produced resins. The corresponding toughening mechanisms are evaluated by means of scanning electron microscopy.

2. Experimental

2.1. Materials

High-*cis*-1,4-PB rubber (Trade name: BR9004) was supplied by Yanshan Petrochemical Co. (Beijing, China), and its molecular parameters are illustrated in Table 1. Styrene and ethylbenzene were obtained from Daqing Petrochemical Co. (Daqing, China). St was vacuum distilled over CaH_2 (Jinke Chemicals Co., Tianjin, China) just before polymerization. DP275B (80.7 wt% in ethylbenzene) was obtained from Qiangsheng Chemical Co. (Changshu, China) and used as received. TEMPO purchased from J & K Chemical Ltd. (Utah, USA), and solvents from Hongyan Chemical Co. (Tianjin, China) such as acetone, butanone, chloroform, methanol and tetrahydrofuran were used as received.

2.2. NMP preparation of PB-*g*-PS/PS composites

The NMP polymerization was carried out under nitrogen in a dried stainless steel reactor (1 l) equipped with an anchor-type magnetic stirring bar (Xiandali Petrochemical Ltd., Beijing, China). The typical polymerization process is as follows: firstly, BR9004 (30.0 g) added into the reactor was dissolved in styrene (370.0 g, 410.5 ml) under nitrogen by stirring at ambient temperature overnight to obtain a 7.5 wt% of rubber/monomer solution. After complete dissolution, DP275B (0.458 g, 1.42 mmol) and TEMPO (0 ~ 0.261 g, 0 ~ 1.66 mmol, Table 2) successively dissolved in ethylbenzene (30.0 g, 34.6 ml) were simultaneously charged into the reactor and dispersed in the previous rubber solution under the agitation. Then the system was heated by circulating heated oil to 105°C for pre-polymerization. The pre-polymerization continued at a pressure of 0.2 MPa while being stirred at a rate of 375 rpmn for 5 h. The partially polymerized system was transferred to a quick-opening plate reactor (Xiandali Petrochemical Ltd., Beijing, China) and further performed a post-polymerization at 150°C for 4 h. Finally, the produced polymer composite was dissolved in chloroform (1.41 kg, 0.95 l) and precipitated into methanol (1.19 kg, 1.5 l), and the obtained polymer was cut into granules and dried at 50°C in a vacuum oven under 10^{-1} Pa for 48 h to strip off the residual monomer and solvent.

Table 1. Molecular parameters of high-*cis*-1,4-PB substrate

Substrate	Microstructures [%]			$M_n \cdot 10^{-4}$	Polydispersity	Viscocity in styrene (5%) [mPa·s]
	vinyl-1,2	*cis*-1,4	*trans*-1,4			
BR9004	1.5	97.0	1.5	8.1	3.81	153.8

Table 2. Reaction conditions for NMP of styrene onto PB, where *R* = TEMPO/DP275B

Run	TEMPO [mmol]	DP275B [mmol]	R	$k_P'' \cdot 1000$ [min^{-1}]	Phase inversion point	
					x [%]	η [Pa·s]
1	0.00	1.42	0.00	5.58	14.7	3.71
2	0.47	1.42	0.33	3.31	19.2	3.34
3	0.95	1.42	0.67	2.66	23.6	2.02
4	1.66	1.42	1.17	1.51	30.5	1.90

k_P'', x and η are the abbreviation of apparent propagation rate constant, monomer conversion and system viscosity, respectively.

2.3. Separation of free PS from PB-*g*-PS

1.0 g of as-produced polymer composite was dissolved in 30.0 ml of mixed solvent (acetone/butanone = 50:50, v/v). Then, 15.0 ml of methanol was added into this solution for separating the two fractions. The PB-*g*-PS fraction was recovered as the precipitate at the bottom and the free PS (PS_f) fraction was recovered from the remaining emulsion formed. Both polymers were dried under vacuum and used for characterizations.

2.4. Characterization techniques

2.4.1. Characterizations of conversion, viscosity and grafting

Monomer conversion was detected by a 2WA-J Abbe refractometer (Shanghai Yice Apparatus & Equipment Co., China). The apparent viscosity was determined by a NDJ-1 rotary viscometer (Shanghai Precision & Scientific Instrument Co., China). The PS-grafted rubber phase was characterized for its grafting parameters, i.e. grafting degree (GD) and rubber phase volume fraction (RPVF), which could be calculated with Equations (1) and (2):

$$\mathrm{GD}[\%] = 100 \cdot \frac{m(\mathrm{Gel}) - m(\mathrm{PB})}{m(\mathrm{PB})} \tag{1}$$

$$\mathrm{RPVF}[\%] = 100 \cdot \frac{m(\mathrm{Gel})}{m(\mathrm{PS_f}) + m(\mathrm{Gel})} \tag{2}$$

where m(Gel), m(PB) and $m(PS_f)$ are the weights of the insoluble part, PB and PS_f in sample, respectively.

2.4.2. Size exclusion chromatography (SEC)

The number average molecular weight (M_n) and polydispersity of PS_f were determined by a Viscotek TDA302 SEC (Malvern Instruments, Malver, UK) with triple detection (refractive index, low-angle laser scatting and viscosity) in tetrahydrofuran (1.0 ml/min) at 40°C. PS reference standards in the range of $4000 \sim 1.6 \cdot 10^6$ were used for the calibration of the system.

2.4.3. Notched Izod impact testing

The notched specimens were prepared by the Model 2 Injection Test Sample Molding Apparatus (UK) and conditioned at 23°C for at least 48 h. The dimension of the specimens was $80 \times 10 \times 4$ mm^3. In middle part of their narrow face, a sharp notch tip of 2 mm depth was cut with a 6951 reciprocating notch-milling machine (CEAST, ITW Test and Measurement Italia S.r.l, Pianezza, Italy). The tests were preformed on a CEAST RESILE Impactor (ITW Test and Measurement Italia S.r.l, Pianezza, Italy) at room temperature.

2.4.4. Tensile testing

All of the dumbbell-type specimens for the tensile tests were also injection-molded. The standard distance (effective part) was fixed in 20 mm and the cross section was 4.0×2.1 mm^2. The tensile tests were conducted on an INSTRON 5567 universal material testing machine (Norwood, MA, USA) at a constant speed of 5 mm/min at 23°C.

2.4.5. Phase contrast microscope

The prepolymer samples drawn from reactor at various polymerization times were dropped on one glass slide and covered by another. Then the compacted films were naturally dried in air for observation. An OLYMPUS Ahimadzu BH-2 phase contrast microscope (Olympus Corporation, Tokyo, Japan) was used to observe the phase separation state and the phase inversion progress under a magnification of 200.

2.4.6. Transmission electron microscope (TEM)

TEM images were obtained with a FEI TECNAI20 TEM (FEI, Hillsboro, Oregon, USA) at an accelerating voltage of 200 kV. The as-prepared samples were firstly ultramicrotomed with a diamond knife on a LEICA ULTRACUT Ultramicrotome (Leica, Wetzlar, Germany) at –120°C to give ultrathin sections with a nominal thickness of 100 nm. Then the sections were transferred to Cu grids of 200 mesh, and stained with OsO_4 staining technique to enhance the contrast between rubber and matrix prior to the observation.

2.4.7. Scanning electron microscope (SEM)

Impact fracture surfaces of the specimens were coated with a thin gold layer on an EMITECH K550X Sputtering Coater (Quorum Technologies, East Grinstead, UK), and then observed to analyze the fracture nature and deformation mechanism. SEM analysis was performed by a FEI QUANTA200 SEM (FEI, Hillsboro, Oregon, USA) using a working voltage of 20 kV.

3. Results and discussion

3.1. Graft polymerization behavior

The PB-*g*-PS/PS composites were synthesized *via* NMP method in the simultaneous presence of TEMPO and DP275B. The polymerization conditions utilized are summarized in Table 2. In the initial stage of polymerization, the thermal decomposition of DP275B (1) firstly occurs at 105°C and several free radicals are generated as the primary products, such as *tert*-butoxy radical (3), 1,1-cyclohexyl-dioxide radial (4) and so on, as shown in Figure 1. Taking radical (4) as an example, due to the low reactivity of the oxygen-centered free radical with TEMPO [20], once formed, it would undergo addition with styrene to give a carbon-centered free radical (5), which can be trapped by nitroxide radical. As a consequence, the intermediate (6) is produced and temporarily in dormant state. Thus, an equilibrium between dormant spaces and nitroxide radicals is achieved and the polymerization rate can be controlled to some extent. In this case, with an enhancement of styrene conversion, the molecular weight of the PS_f polymer (7) is gradually increased [21].

Meanwhile, Figure 2 shows that the functionalized macroalkoxyamine (here labeled as FPB) can also be synthesized by heating the BR9004 rubber in the simultaneous presence of TEMPO and *tert*-butoxy radical (3) at 105°C. The radical (3) is formed directly from the initiator (1) and through the secondary decomposition of free radical (2) (Figure 1), and plays a significant role in the process of functionalization. Afterwards, a large amount of styrene monomers react with FPB to produce the PB-*g*-PS.

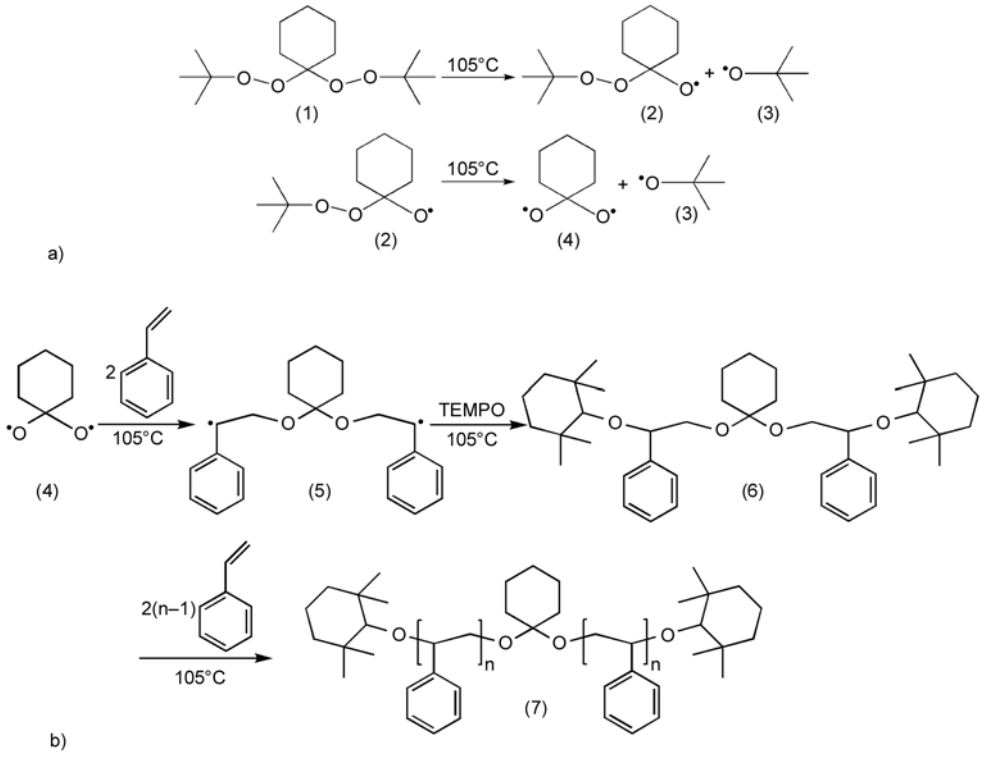

Figure 1. a) Thermal decomposition scheme of DP275B and b) TEMPO-mediated polymerization of styrene initiated by one kind of free radical

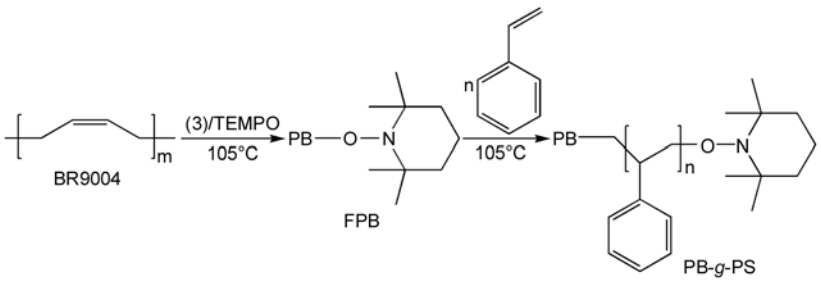

Figure 2. Reaction scheme of graft polymerization of styrene onto BR9004 rubber

Both length and molecular weights of the grafted PS chains are controllably enhanced with increasing monomer conversion [21].

3.2. Effect of R values on the polymerization kinetics

To acquire detailed information about the kinetic behavior of PB-*g*-PS/PS composite, the obtained monomer conversion (x) from Abbe refractometer method underwent a logarithmic calculation ($-\ln(1-x/100)$) and was plotted as the ordinate (Y-coordinate) (Figure 3a). And the slope of $-\ln(1-x/100)\sim t$ curve was the apparent propagation rate constants (k_P'') of monomer. The corresponding k_P'' results are shown in Table 2. As seen, $-\ln(1-x/100)$ exhibits approximately linear growth with the polymerization time under various R values. Evidently, the reaction rate of styrene mediated by TEMPO decreases with increasing TEMPO/DP275B ratio. This is mainly because that the carbon-centered free radicals generated in the prepolymerization process are successfully trapped by the TEMPO added, and to a certain extent, the prepolymerization rate can be efficiently controlled. Moreover, the inhibition effect of TEMPO radical on polymerization kinetics of styrene is obvious. As seen from Figure 3a, there exists an inhibition interval of about 60 minutes when adding inhibitor to the grafting polymerization system. This is also a clear evidence that inhibition typical for TEMPO occurred. Besides, the slightly changed inhibition interval under different TEMPO dosages may also account for a suitable amount of inhibitor in experimental range examined in favor of precise controllability of the grafting behavior.

3.3. Effect of R values on phase inversion

As known, rubber particles formed in phase inversion play an important role in resin-toughening. If phase inversion takes place incompletely, the products would present no excellent performance. So the study on phase inversion is of the utmost importance [27]. The relationship between the system viscosity (η) and the monomer conversion (x) under different R values is plotted in Figure 3b. When no TEMPO is added, the polymerization rate is very fast, and simultaneously, the viscosity also increases swiftly. It can be decreased obviously with increasing the TEMPO dosage at the same conversion-value of monomer. The phase inversion progress also tends to be remarkable, that is, the $\eta\sim x$ curve displays a significant elevating-descending-elevating change in phase inversion stage. Meanwhile, the conversion of styrene corresponding to the transition point is indeed improved (Table 2), which implies that a delayed phase inversion occurs.

A phase contrast microscope was applied for the optical observation of the phase inversion progress. At any R value, it presents a similar process of phase behavior change. Figure 4 illustrates the relative phase contrast photomicrographs of the samples before, at and after the phase inversion point when R value is 0.67. The light-colored region represents the resin phase and the dark-colored region represents the rubber phase. The reaction mixture is firstly a continuous phase consisting in PB dissolved in styrene/ethylbenzene. After a certain degree of monomer conversion, a second phase consisting in PS dissolved in styrene/ethylbenzene is formed and dispersed as irregular drops in the continuous rubber phase (Figure 4a). That is, at a certain spinodal,

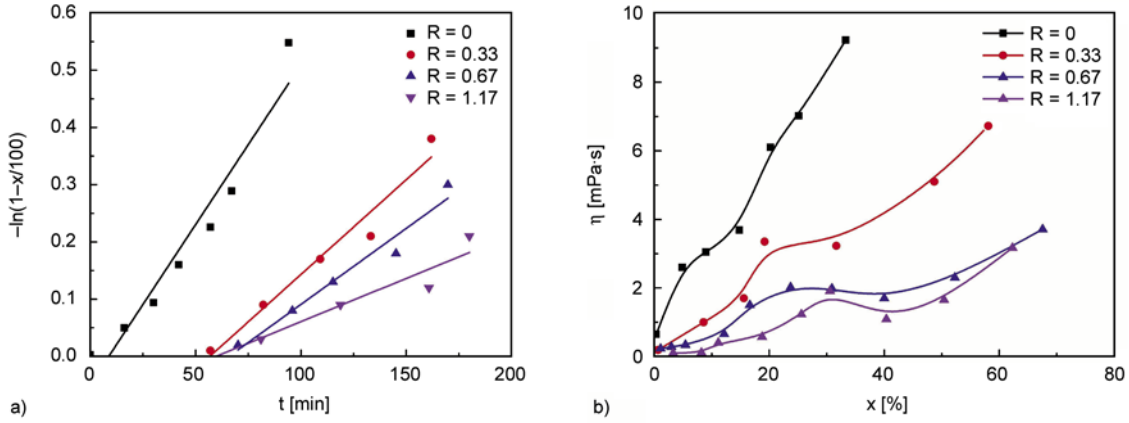

Figure 3. Effect of TEMPO/DP275B ratios on a) polymerization kinetics and b) phase inversion progress of styrene in BR9004 rubber system

PS polymers start to nucleate, due to the incompatibility of newly produced PS with original rubber substrate. Besides, these droplets gradually grow while the polymerization degree of monomer increases. As a result of the reaction evolution, the volume of said second phase increases gradually and two individual phases disperse semi-continuously (Figure 4b). At the point that the volume of PS phase becomes more dominant than of the rubber phase, phase inversion occurs. The continuous phase is now the PS phase dissolved in styrene/ethylbenzene and the dispersed phase is composed of the grafted or non-grafted rubber particles dissolved in styrene/ethylbenzene (Figure 4c). A similar behavior can be observed in systems containing dissolved polymers other than rubber [28–30].

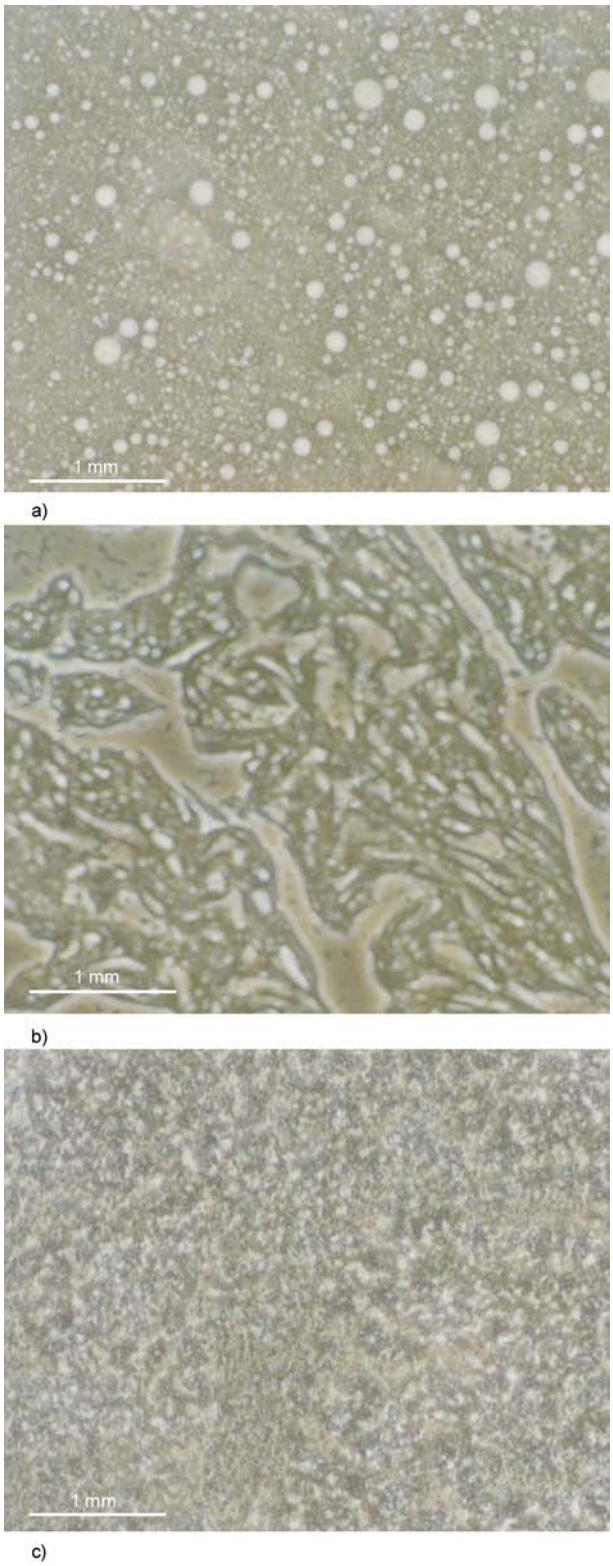

Figure 4. Phase contrast microphotographs of composite (R = 0.67): a) x = 11.2%; b) x = 23.6%; c) x = 39.1%

3.4. Stable polymerization behavior

Figure 5 displays the variation progress of grafting behavior under different TEMPO/DP275B ratio. When no TEMPO is added, the GD of 9004 rubber increases quickly in the first 100 min interval, and afterwards tends to be relatively slow, owing to the high viscosity of polymerization system and the scarce diffusion of reactive species. Otherwise, with the increasing TEMPO dosage, GD becomes more and more linearly related to the reaction time during the grafting progress. And the relevant increasing rate also lowers gradually as R increases from 0.33 to 1.17 due to an aforesaid depressed polymerization conversion and grafting rate. Those all results show that under a moderate dosage of TEMPO injected a relative stable polymerization behavior can be obtained.

As an auxiliary method, SEC analysis of the polymers was also carried out in order to elucidate the controlled polymerization progress. Figure 6 shows the comparative size exclusion chromatograms of PS_f separated from the resultant composite while there is no TEMPO added and the R value is 0.33,

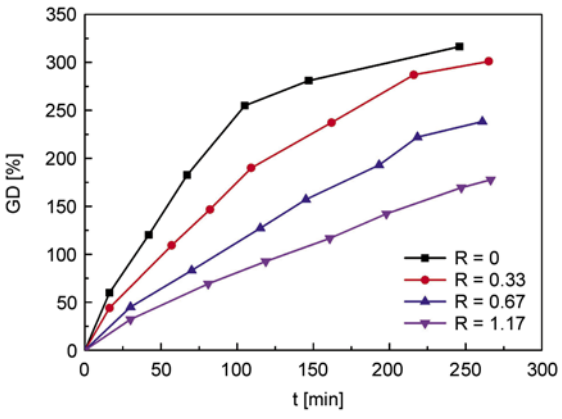

Figure 5. GD versus time under different R values

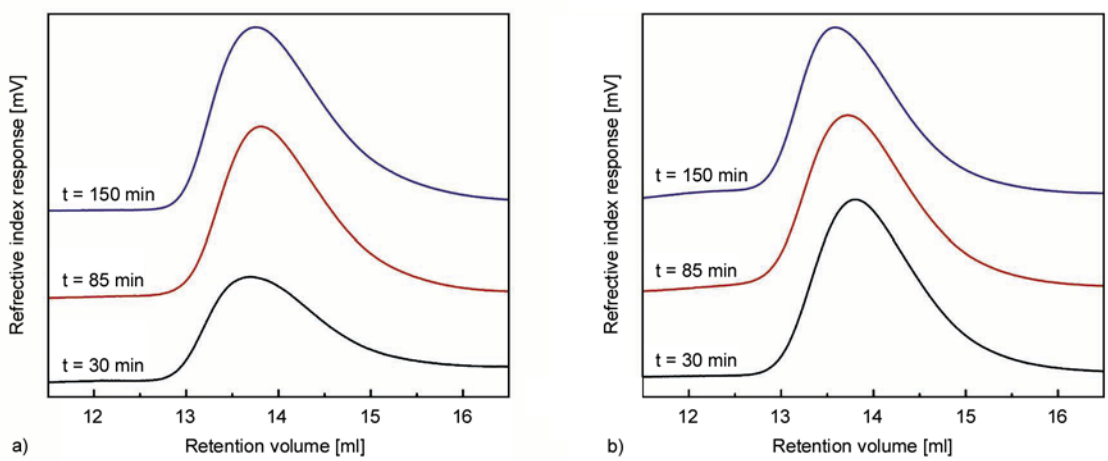

Figure 6. SEC curves of PS_f at different time when no TEMPO added (a) and *R* value is 0.33 (b)

Table 3. Molecular weight parameters of PS_f under different *R* values

t [min]	R = 0		R = 0.33	
	$M_n \cdot 10^{-4}$	Polydispersity	$M_n \cdot 10^{-4}$	Polydispersity
30	10.8	4.558	6.7	2.189
85	14.4	2.306	8.4	1.641
150	12.8	2.010	9.1	1.314

respectively. The relevant SEC results are listed in Table 3. Obviously, in the first case, once the polymerization occurs, PS macromolecules with higher molecular weight are formed besides those with lower molecular weight. This leads to a wider polydispersity value (>4.0). And the average molecular weight shows no significant variance and the polydispersity becomes narrower and decreases to 2.010. This can be attributed to the equilibrium of combination and disproportionation termination in typical free radical polymerization.

As for the second case, it maintains a relative narrower polydispersity value (<2.2) all the time; moreover, the maximum peak of the retention curve gradually shifts toward left, that is, higher molecular weight region, which indicates an increased average molecular weight of PS_f and a controlled growth of the end-functional chains. On the other hand, at the same reaction time (30 min), the PS_f phase presents a decreased molecular weight and a narrower polydispersity with the increase of TEMPO/DP275B ratio as shown in Figure 7. This also corroborates the foregoing conclusion of the controlled growth of chains and the stable polymerization behavior.

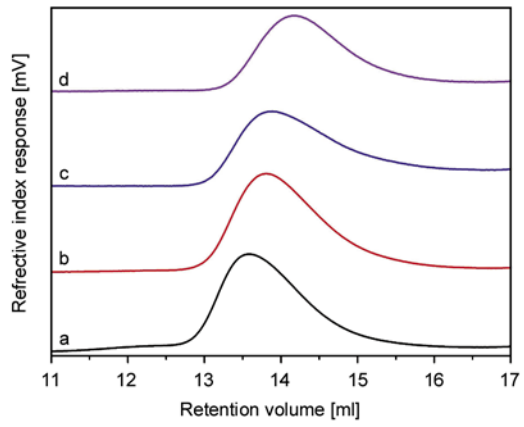

Figure 7. SEC curves of PS_f under different *R* values (*t* = 30 min): a) *R* = 0; b) *R* = 0.33; c) *R* = 0.67; d) *R* = 1.17

3.5. Morphological and mechanical properties

The structural and mechanical properties of the composites prepared with different TEMPO dosages are listed in Table 4. As shown, the yield stress and fracture stress have no great variance. However, the notched Izod impact strength and the elongation at break are quite different from each other; both show a significant downtrend with increasing the TEMPO/DP275B ratio. Therefore, *R* value has a strong influence on the impact property and fracture elongation by directly affecting the grafting level of elastomeric toughener. As one of the key factors, the interfacial performance has an important effect on the toughening modification. A moderate grafting level is beneficial to the distribution of rubber particles and the binding force between the two phases. On the other hand, the aforesaid great differences in toughness, to a large extent, are also attributable to the distinct morphological structures of as-prepared products. Figure 8 gives the TEM images of various PS composites obtained by changing *R* value. As illustrated from Figure 8a, the composite without

Table 4. Effect of R values on the molecular structures and mechanical properties of composites

R	Rubber phase		PS_f phase		Notched Izod impact strength [J/m]	Yield stress [MPa]	Fracture stress [MPa]	Elongation at break [%]
	GD [%]	RPVF [%]	$M_n \cdot 10^{-4}$	Polydispersity				
0.00	345.5	35.4	14.6	1.565	28.4	32.8	29.9	37.4
0.33	309.0	39.0	11.3	1.294	20.8	33.5	26.9	20.7
0.67	261.6	41.8	11.0	1.288	16.2	33.6	24.9	36.4
1.17	209.7	48.9	10.7	1.285	15.0	36.2	31.6	13.6

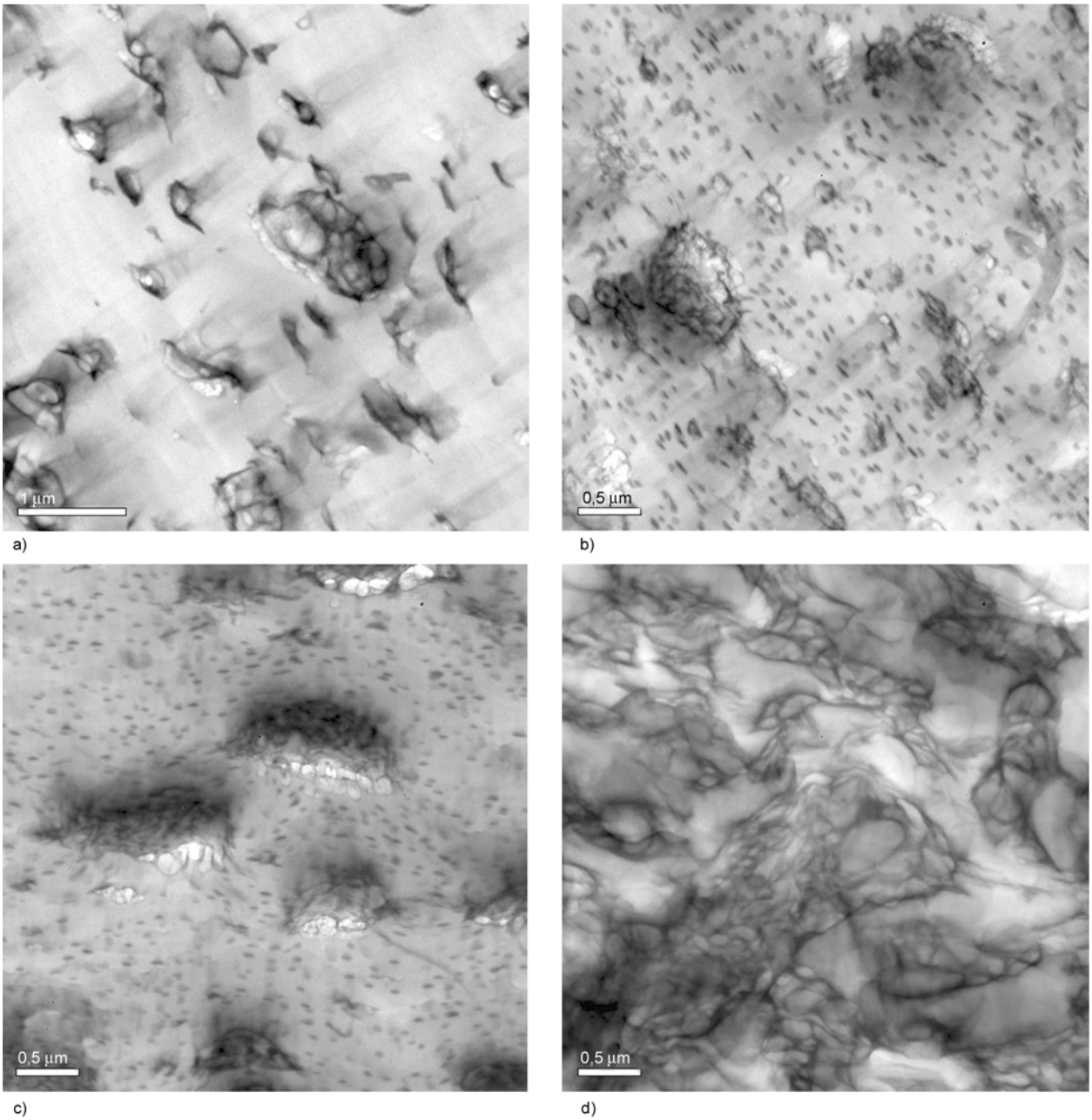

Figure 8. TEM images of composites under different *R* values: a) *R* = 0; b) *R* = 0.33; c) *R* = 0.67; d) *R* = 1.17

TEMPO possesses typical 'sea-island' structure with a wide distribution. A great many smaller particles (~300 nm) and a few larger ones (>1.0 µm) coexist. A large number of PS occlusions can be observed inside the larger particles while those smaller particles have almost no inclusions. The relatively clear interface and the hypodispersion of rubber phase may be due to the higher viscosity of polymeriza-

tion system and the random distribution of grafting chains on the rubber particle surface.

In the case of *R* value of 0.33 (Figure 8b), those smaller and larger particles in the composite similar to the former without TEMPO still exist. Besides, there appear homogeneously a mass of nanometer-grade granules without inner grafting, the size of which is lower than 100 nm. When *R* value is increased to 0.67, the number of larger particles increases and their size also tends to be uniform and is decreased to approximately 1.0 μm, which are attributable to the mediation action of TEMPO. Just because of those uniform larger particles having excellent stretching and yielding abilities under tensile, they endow the composite material with a higher elongation at break. However, the material shows poor anti-impact property while suffering an external impact force in that the existing micro-fine granules can not effectively terminate the development of crazes or restrain the propagation of cracks. Further increasing the TEMPO amount, the polymerization and chain extension occur very slowly. The relative lower grafting degree (209.7%) is not enough to disperse the rubber phase, indicating a poor two-phase interface. And the amount of as-produced PS phase is not up to that of rubber phase in a certain reaction interval, either. As a result, as shown in Figure 8d, the semi-continuous state or interpenetrating network of two-phase is formed [28], which is further unfavorable to impact resistance property.

3.6. Fractography

In order to deeply clarify the fracture mode and mechanism, the fracture surface morphologies of BR9004 rubber toughened PS composites with varying TEMPO/DP275B ratio after impact tests were observed by a scanning electron microscope. The corresponding images are shown in Figures 9–10, respectively. As can be seen from Figure 9a, the sample without TEMPO added totally shows a rather rough fracture surface and a certain degree of stress-whitening, suggesting that the plasticization and yielding phenomenon occur. Further amplifying the region, quite a few naked rubber particles and micron-grade cavities can be observed in the fractured surface. This means that the stress concentration releases effectively after the matrix stripping and the stress yielding. In a word, the dominating fracture mechanism in this case is the characteristic plasticization and yielding in the shear stress field.

In contrast, there are three distinct morphological domains on the fractured surface with *R* value of 0.33 as shown in Figure 10a. They are (i) mirror zone, (ii) rib-structure zone and (iii) rapid crack propagation zone, respectively. In the mirror zone (a range from notch to 500 μm), the fracture surface seems to be relatively flat and smooth, accompanied by only a few peeling patterns caused by the initiation and expansion of single or several crazes. While the crack propagates into the rib-structure zone, the rough band and the smooth band alternately appear (Figure 10b). The former are mainly

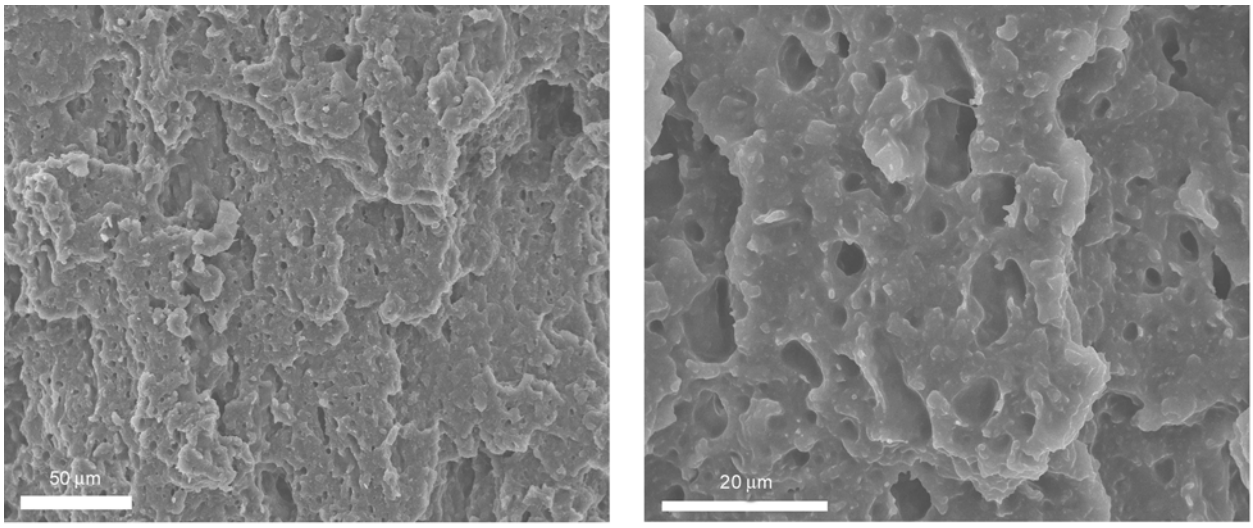

Figure 9. SEM images of fracture surface of composite without TEMPO added

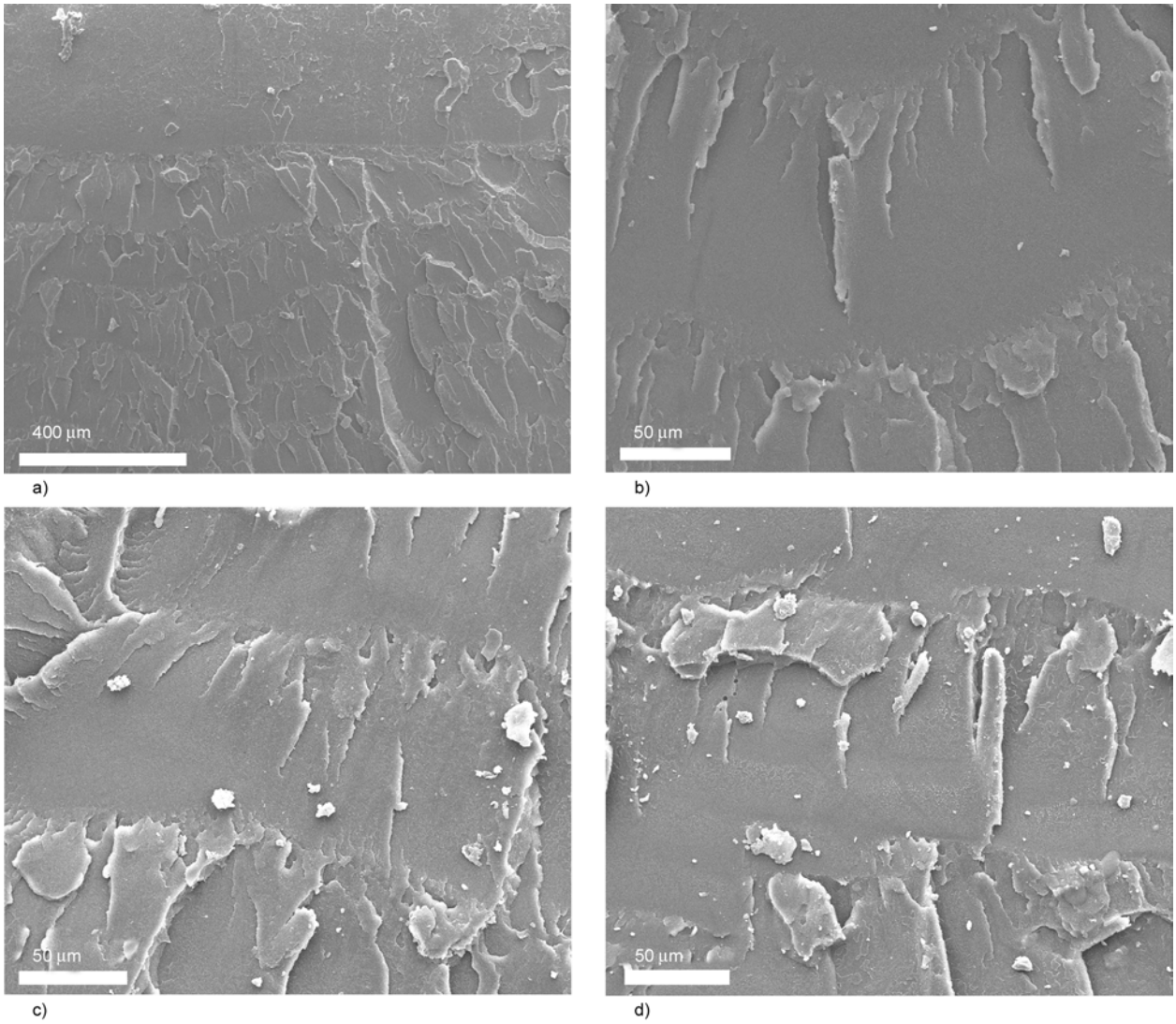

Figure 10. SEM images of fracture surface of composites with various *R* values: a) *R* = 0.33; b) *R* = 0.33; c) *R* = 0.67; d) *R* = 1.17

the dense cracks extending along the impact direction. Besides, stress-whiting is dramatic at the edge of those cracks, meaning a fatally tearing progress in the material. As for the latter, there exist almost no characteristics except a single crack from the rough band terminated here. Its appearance is the logical result of the external impact energy aggregating first and then releasing in the crack tip. In addition, with the cracks propagating, the spacing between rib-structures becomes narrower and narrower while the rough band gets wider and wider, demonstrating that the matrix material can not avoid unstable rupturing.

When *R* value is increased to 0.67 and 1.17, respectively, the composite materials basically present similar fracture surface morphology (Figure 10c–d). The substantive diversities lie in the peeling degree of craze patterns in the mirror zone, the band width and crack size in the rib-structure zone, and the propagating speed of cracks in the rapid crack propagation zone, etc. As seen, the more TEMPO is used, the more brittle the material becomes. Generally speaking, semi-ductile fracture occurs for the material with no or less TEMPO accompanied by pronounced cavitation and shear yielding, while for the material under the mediation of more TEMPO, alternate rough band and smooth band successively followed by fast developed cracks are obviously exhibited in the mode of quasi-brittle failure.

4. Conclusions

A well-controlled grafting polymerization of styrene onto the high-*cis*-1,4-PB rubber initiated by DP275B under the mediation of TEMPO. The grafting

progress, grafting parameters of rubber and molecular weight of PS_f while adding different TEMPO amount were determined, which showed that not only the grafting kinetics of styrene but the molecular weight of PS (free and grafted) can be well controlled besides a narrower polydispersity. The structure, mechanical properties and fracture mechanism of the composites were also evaluated. By adjusting the TEMPO/DP275B ratio to a certain degree, not only the finer rubber particles but the larger ones tended to be more homogeneous. Consequently, the material displayed relatively outstanding comprehensive mechanical properties. The relevant fracture mechanism was mainly cavitation and shear yielding. However, too much TEMPO applied was disadvantageous to the grafting and fine dispersion of rubber phase. Furthermore, the material exhibited poor physical properties and fractured in a quasi-brittle mode. Totally, three distinct fracture zones on its fractured surface suggested a fast propagating progress of crack and an unstable failure of material.

Acknowledgements

This work was financially supported by the National High Technology Research and Development Program of China (No. 2007AA03Z532) and the National Natural Science Foundation of China (No. 20774015). The authors wish to thank Senior Engineer Chaoxian Wang for instrumented impact and tensile testing and Senior Engineer Ying Liu for electron microscopy investigations.

References

[1] Sirqueira A. S., Soares B. G.: Mercapto-modified copolymers in elastomer blends. IV. The compatibilization of natural rubber/EPDM blends. Journal of Applied Polymer Science, **83**, 2892–2900 (2002). DOI: 10.1002/app.10283

[2] Lee D-Y., Subramaniam N., Fellows C. M., Gilbert R. G.: Structure–property relationships in modified natural rubber latexes grafted with methyl methacrylate and vinyl neo-decanoate. Journal of Polymer Science Part A: Polymer Chemistry, **40**, 809–822 (2002). DOI: 10.1002/pola.10165

[3] Whan J., Paul D. R. C.: Glass fiber-reinforced polyamide composites toughened with ABS and EPR-*g*-MA. Journal of Applied Polymer Science, **80**, 484–497 (2001). DOI: 10.1002/1097-4628(20010418)80:3<484::AID-APP1122>3.0.CO;2-5

[4] Taylor N. W., Bagley E. B.: Tailoring closely packed gel–particle systems for use as thickening agents. Journal of Applied Polymer Science, **21**, 113–122 (1977). DOI: 10.1002/app.1977.070210110

[5] Arnold M., Knorr J., Köller F., Bornemann S.: Modified polypropenes via metallocene catalysis. Journal of Macromolecular Science Part A: Pure and Applied Chemistry, **36**, 1655–1681 (1999). DOI: 10.1081/MA-100101619

[6] Stehling U. M., Malmstrom E. E., Waymouth R. W., Hawker C. J.: Synthesis of poly(olefin) graft copolymers by a combination of metallocene and 'living' free radical polymerization techniques. Macromolecules, **31**, 4396–4398 (1998). DOI: 10.1021/ma980141+

[7] Davis K. A., Matyjaszewski K.: Statistical, gradient, block and graft copolymers by controlled/living radical polymerizations. Advances in Polymer Science, **159**, 107–152 (2002). DOI: 10.1007/3-540-45806-9

[8] Hawker C. J., Bosman A. W., Harth E.: New polymer synthesis by nitroxide mediated living radical polymerizations. Chemical Reviews, **101**, 3661–3688 (2001). DOI: 10.1021/cr990119u

[9] Bani F., Abbasian M., Taromi F. A., Entezami A. A.: Polystyrene grafted to ABS backbone by living radical polymerization with TEMPO. Iranian Polymer Journal, **13**, 513–520 (2004).

[10] Yamanaka A., Izumi Y., Kitagawa T., Terada T., Sugihara H., Hirahata H., Ema K., Fujishiro H., Nishijima S.: The radiation effect on thermal conductivity of high strength ultra-high-molecular-weight polyethylene fiber by γ-rays. Journal of Applied Polymer Science, **101**, 2619–2626 (2006). DOI: 10.1002/app.24227

[11] Lu H. L., Chung T. C.: Synthesis of PP graft copolymers via anionic living graft-from reactions of polypropylene containing reactive p-methylstyrene units. Journal of Polymer Science Part A: Polymer Chemistry, **37**, 4176–4183 (1999). DOI: 10.1002/(SICI)1099-0518(19991115)37:22<4176::AID-POLA17>3.0.CO;2-O

[12] Kennedy J. P., Vidal A.: Block and graft copolymers by selective cationic initiation. III. Synthesis and characterization of bigraft copolymers. Journal of Polymer Science, Polymer Chemistry Edition, **13**, 1765–1781 (1975). DOI: 10.1002/pol.1975.170130803

[13] Moad G., Solomon D. H.: The chemistry of radical polymerization. Elsevier, Oxford (2006).

[14] Miwa Y., Yamamoto K., Sakaguchi M., Shimada S.: Well-defined polystyrene grafted to polypropylene backbone by 'living' radical polymerization with TEMPO. Macromolecules, **34**, 2089–2094 (2001). DOI: 10.1021/ma001449f

[15] Wayland B. B., Poszmik G., Mukerjee S. L., Fryd M.: Living radical polymerization of acrylates by organocobalt porphyrin complexes. Journal of the American Chemical Society, **116**, 7943–7944 (1994). DOI: 10.1021/ja00096a080

[16] Benoit D., Chaplinski V., Braslau R., Hawker C. J.: Development of a universal alkoxyamine for 'living' free radical polymerizations. Journal of the American Chemical Society, **121**, 3904–3920 (1999). DOI: 10.1021/ja984013c

[17] Solomon D. H., Rizzardo E., Cacioli P.: Polymerization process and polymers produced thereby. U.S. Patent 4581429, USA (1986).

[18] Roth M., Pfaendner R., Nesvadba P.: Grafting of ethylenically unsaturated monomers onto polymers. U.S. Patent 6521710, USA (2003).

[19] Roth M., Pfaendner R.: Grafting of ethylenically unsaturated monomers onto polymers. U.S. Patent, 6525151 (2003).

[20] Abbasian M., Namazi H., Entezami A. A.: 'Living' radical graft polymerization of styrene to styrene butadiene rubber (SBR) with 2,2,6,6-tetramethyl-1-piperidinyloxy (TEMPO). Polymers for Advanced Technologies, **15**, 606–611 (2004). DOI: 10.1002/pat.515

[21] Miwa Y., Yamamoto K., Sakaguchi M., Shimada S.: 'Living' radical graft polymerization of styrene to polypropylene with 2,2,6,6-tetramethylpiperidinyl-1-oxy. Macromolecules, **32**, 8234–8236 (1999). DOI: 10.1021/ma990998m

[22] Miwa Y., Yamamoto K., Sakaguchi M., Shimada S.: Well-defined polystyrene grafted to polypropylene backbone by 'living' radical polymerization with TEMPO. Macromolecules, **34**, 2089–2094 (2001). DOI: 10.1021/ma001449f

[23] Braunecker W. A., Matyjaszewski K.: Controlled/living radical polymerization: Features, developments, and perspectives. Progress in Polymer Science, **32**, 93–146 (2007). DOI: 10.1016/j.progpolymsci.2006.11.002

[24] Gromadzki D., Makuška R., Netopilik M., Holler P., Lokaj J., Janata M., Štěpánek P.: Comb copolymers of polystyrene-poly(*tert*-butyl (meth)acrylate) prepared by combination of nitroxide mediated polymerization and photoinduced *iniferter* technique. European Polymer Journal, **44**, 59–71 (2008). DOI: 10.1016/j.eurpolymj.2007.10.024

[25] Howell B., Zhu Y., Zeng W., Lyons J., Meunier D., Demirors M., Priddy D.: Application of living radical polymerization to enhance grafting of PS onto PBD. Polymeric Preprints, **40**, 73–74 (1999).

[26] Bonilla-Cruz J., Saldívar-Guerra E., Torres-Lubián J. R., Guerrero-Santos R., López-Carpy B., Luna-Bárcenas G.: Controlled grafting-from of polystyrene on polybutadiene: Mechanism and spectroscopic evidence of the functionalization of polybutadiene with 4-oxo-TEMPO. Macromolecular Chemistry and Physics, **209**, 2268–2283 (2008). DOI: 10.1002/macp.200800367

[27] Scheirs J., Priddy D. B.: Modern styrenic polymers: Polystyrenes and styrenic copolymers. Wiley, New York (2003).

[28] Freeguard G. F., Karmarkar M.: The production of rubber-modified polystyrene. I. Rheological behavior of the polymerizing system. Journal of Applied Polymer Science, **15**, 1649–1655 (1971). DOI: 10.1002/app.1971.070150708

[29] Molau G. E., Keskkula H.: Heterogeneous polymer systems. IV. Mechanism of rubber particle formation in rubber-modified vinyl polymers. Journal of Polymer Science Part A-1: Polymer Chemistry, **4**, 1595–1607 (1966). DOI: 10.1002/pol.1966.150040622

[30] Molau G. E.: Heterogeneous polymer systems. I. Polymeric oil-in-oil emulsions. Journal of Polymer Science Part A: General Papers, **3**, 1267–1278 (1965). DOI: 10.1002/pol.1965.100030402

eXPRESS Polymer Letters Vol.5, No.10 (2011) 923–935
Available online at www.expresspolymlett.com
DOI: 10.3144/expresspolymlett.2011.90

Effect of different dispersing additives on the morphology and the properties of polyethylene-based nanocomposite films

N. Tz. Dintcheva[1*], *F. P. La Mantia*[1], *V. Malatesta*[2]

[1]Dipartimento di Ingegneria Industriale, Università di Palermo, Viale delle Scienze, ed.6, 90128 Palermo, Italy
[2]Materials Science Department, Università Milano Bicocca, Via R. Cozzi 53, 20125 Milano, Italy

Received 10 February 2011; accepted in revised form 3 May 2011

Abstract. In this work, the use of a polar wax, e.g. amphiphilic Tegomer® E 525 (TEG) is investigated with the aim of modifying, and possibly improving, the dispersion of an organically modified nanoclay (OMMT), loaded at 5 wt%, in a polyethylene matrix (PE) at relatively low loading levels. We have indeed found that the incorporation of low loadings, e.g. 0.5 wt%, of TEG, an amphiphilic block co-polymer, into a PE/OMMT sample results in a substantial improvement of the clay dispersion in the nanocomposite and, consequently, of the mechanical and thermomechanical properties of the films. The achieved results are comparable to those obtained for systems containing traditional dispersing agents such as maleated PE (PEgMA) and ethylene-acrylic acid copolymer (EAA), at higher loadings, i.e. at 5 wt%. It has also been found that by increasing the polar wax content, i.e. 1–5 wt%, no useful improvement in the mechanical behaviour and morphology of the PE films was obtained. At high loadings of the polar wax relatively the short chains are arranged into the clay particles galleries and intercalation of the polyethylene chains between the clay platelets may be hindered. Additionally at high TEG loadings, the presence of the new polar groups of the wax also on external surfaces of the clay particles is expected to promote aggregation of the clay particles, with a loss of the beneficial effect of the more dispersed clay particles on the polymer mechanical/thermomechanical properties. The reported results strongly indicate that the amphiphilic TEG dispersing additive, may advantageously be used, at substantially lower loadings, as an alternative to incumbent PEgMA in the formulation of nanocomposites to improve their macroscopic performances.

Keywords: *mechanical properties, dispersing additives, polyethylene-based nanocomposite, polar wax, film formulation*

1. Introduction

It has been reported that thermoplastics filled with nanometer-sized materials show properties different from those of thermoplastics filled with conventional microsized particles. The incorporation of nanosized fillers has, indeed, been shown to have significant effects not only on some mechanical and thermomechanical properties e.g. elastic modulus, heat deflection temperature, but also on the transparency and haze characteristics of the polymers films. It is well documented that nanoclay incorporation into polymer films significantly enhances transparency, reduces haze and sizeably increases the film barrier properties. Clays, being hydrophilic, are easier to be nano-disperded in polar polymers. On the other hand preparation of clay-based nanocomposites by melt processing of polyolefins (PO's), thermoplastic olefins (TPO's) and other non-polar polymers is a technologically challenging task as the clay silicate layers have to be exfoliated by pure mechanical shear during the extrusion of the polymer. Extrusion conditions, extruder screw type and design strongly affect the exfoliation extent. In order to improve exfoliation, use of the more polar

*Corresponding author, e-mail: dintcheva@unipa.it

maleic anhydride-modified (maleated) POs, TPOs and organically modified clays may be required. The success of these materials requires also that the incorporation of the organically modified clay has negligible adverse effects on preparation, cost, processing stability and a host of other application specific performance properties.

When well dispersed low loadings (1–10 wt%) of nanoclays yield dramatic improvement of physical, thermal, and mechanical properties of polymer-based materials with a minimal increase in the polymer density as a result of the low inorganic loading [1–10].

It must be noted that the improvement of all these properties occurs only if the nanofiller particles are exfoliated, or at least intercalated, within the polymer matrix. Intercalation or exfoliation is the result of the incorporation of polymer macromolecules between the layers of the exfoliated clay particles and occurs only if the extrusion-induced thermo-mechanical stress is well transferred from the melt to the layered particles. A good adhesion between matrix and particles is then a necessary condition for a successful intercalation or exfoliation. When polymer melt and filler are not well adherent, e.g. in the case of a non-polar matrix such as polyolefins containing polar particles such as nanoclays, use of an adhesion promoter or compatibilizer, having polar groups is necessary [11–25].

In order to modify the clay morphology and consequently the final macroscopic properties in clay filled polyethylene, different commercial compatibilizers have been used. Sánchez-Valdes *et al.* [11] have used Zn-neutralized carboxylate ionomer, while, Shah *et al.* [12] used Na-neutralized poly(ethylene co-methacrylic acid), both Surlyn® by DuPont, in LDPE/clay nanocomposite formulation. Filippi and coworkers [13–14] have used as a compatibilizer, the ethylene-acrylic acids copolymers (Et-g-AA), namely Escor® by Exxon-Mobil. Xu *et al.* [15] have prepared HDPE/clay nanocomposites using a HDPE-g-AA co-polymer. The most widely used compatibilizer in polyethylene/clay formulations has been the maleic anhydride grafted polyethylene that allows obtaining an exfoliated clay morphology [16–23]. All the authors agree that the observed macroscopic benefits have been lower than those expected and calculated, for nanofilled polymer based systems, using different theoretical models.

Recently, a new type of polar compatibilizers, based on the oxidized polyolefin has been used in the polyethylene/silicate nanacomposite formulations. Durmuş *et al.* [24] concluded that the barrier and mechanical properties of the nanocomposites prepared with commercial grade oxidized polyethylene were better than those prepared with maleic anhydride grafted polyethylene. Furthermore, Luyt and Geethamma [25] have reported that the presence of oxidized paraffin slightly reduces the thermal stability of the LLDPE/clay sample.

In this work the use of a polar wax, e.g. amphiphilic Tegomer® E525 is investigated for the first time, with the aim of modifying, and possibly improving, the dispersion of an organically modified nanoclay (OMMT) in a PE matrix at relatively low loading levels. Interestingly the properties of the 0.5 wt% TEG containing PE/OMMT film are comparable to those of a PE/OMMT film containing a tenfold higher amount, i.e. 5 wt%, of the traditionally used maleic anhydride grafted polyethylene (PEgMA). These new results strongly indicate that the amphiphilic TEG dispersing additive may be advantageously used, at relatively low loading levels, as an alternative to PEgMA.

2. Experimental

2.1. Materials

The materials used in this work were:

– LLDPE, PE, (Clearflex FG166, M_w = 130 000 g·mol^{-1}, M_w/M_n = 3.8; $MFI_{190/2.16}$ = 0.27 g/10 min and ρ = 0.918 g·cm^{-3} at room temperature, Polimeri Europa, Rome, Italy);

– an organomodified clay, OMMT, (Cloisite® 15A from Southern Clay Products, Gonzales, TX, USA) was used to prepare the hybrid blend. Cloisite® 15A is a montmorillonite modified by dimethyl-dihydrogenated tallow-quaternary ammonium cation with a concentration of the organo-modified clay of 125 meq/100 g and density ρ = 1.66 g/cm^3. The OMMT was added at 5 wt% in all formulations;

– a maleic anhydride grafted polyethylene, PEgMA, with $MFI_{190°C/2.16\ kg}$ = 5 g/10 min (Polybond® 3009, from Crompton Corp., Middelbury CT, USA). The maleic anhydride level is 1 wt%, reported from the manufacturer. The PEgMA was added at 5 wt%;

Table 1. Sample composition and ration between dispersing additives and OMMT

Sample code	Composition wt/wt/wt%	Ratio between dispersing additive and OMMT
PE/OMMT	95/5	–
PE/PEgMA/OMMT	90/5/5	1.0
PE/EAA/OMMT	90/5/5	1.0
PE/TEG0.5/OMMT	94.5/0.5/5	0.1
PE/TEG1/OMMT	94/1/5	0.2
PE/TEG4/OMMT	91/4/5	0.8
PE/TEG5/OMMT	90/5/5	1.0

– an ethylene-acrylic acid copolymer, EAA, (Escor® 5001 from Exxon-Mobil Chemical Mediterranea, Milan, Italy) was used to prepare a compatibilized blend. The composite film has an acrylic acid content of 2.5 mol%, $MFI_{190°C/2.16\,kg}$ of 2.0 g/10 min and $\rho = 0.931$ g/cm^3. The EAA was added at 5 wt%;
– alternatively a polar wax e.g. Tegomer® E 525, TEG, (Evonik Goldschmidt Italia, s.r.l., Pandiono, Italy) , added at different wt%, i.e. 0.5, 1.0, 2.0, 4.0 and 5.0 was used to achieve a better dispersion of the nanoclay. TEG is a finely grained white powder with a melting point close to 100°C and a melt viscosity of 200 mPa·s at 140°C.

The composition of all nanocomposite films and ratio between the dispersing additives and OMMT were reported in Table 1.

2.2. Processing

The nanocomposite films were prepared considering two consecutive separate processing. In particular, first step was the compounding in twin screw extruder, in order to have a better additive dispersion and second step was the film formulation using a film-blowing apparatus.

First processing step: Compounding

The PE was melt-compounded with nanofiller and different dispersing additives (different type and loading) in a co-rotating inter-meshing twin-screw extruder (L/D = 35, D = 19 mm, OMC, Saronno, Italy), using a shear stress screw profile as reported in Figure 1. The temperature profile used was 120–120–160–170–180–180°C (die) and the residence time was about 120 s at 250 rpm. The extrudates were water-cooled, and granulated before the film formulation.

Second processing step: Film formulation

The films were prepared with a single-screw extruder equipped with a film blowing head and with a Brabender film-blowing unit (Braneder Technologie KG, Duisburg, Germany). The thermal profile was 120–140–170–190°C and the screw speed 60 rpm. The obtained film thickness was about 80 microns.

2.3. Characterizations

2.3.1. Mechanical test

The tensile properties were determined at room temperature and humidity, by using an Instron machine mod. 3365 (Instron, Norwood, MA, USA), according to ASTM test method D882. The specimens were cut from films in both the machine and transverse direction (machine, MD, and transverse, TD), and were tested at two strain rates: for modulus measurement purposes, the speed was 1 mm/min until a deformation of 10%, and that was subsequently increased to 500 mm/min until break. The data reported are the average values of ten tests per film sample, the reproducibility being ±5%.

2.3.2. Scanning electron microscopy (SEM)

SEM analysis was performed on the nitrogen fractured surfaces of all the films on a Philips (Netherlands, distributed by FEI, Hillsboro, Oregon USA) ESEM XL30 microscope.

2.3.3. X-ray analyses (X-ray)

Wide-angle X-ray analyses (WAXD) were performed at room temperature in the reflection mode on a Siemens D-500 X-ray diffractometer (Siemens

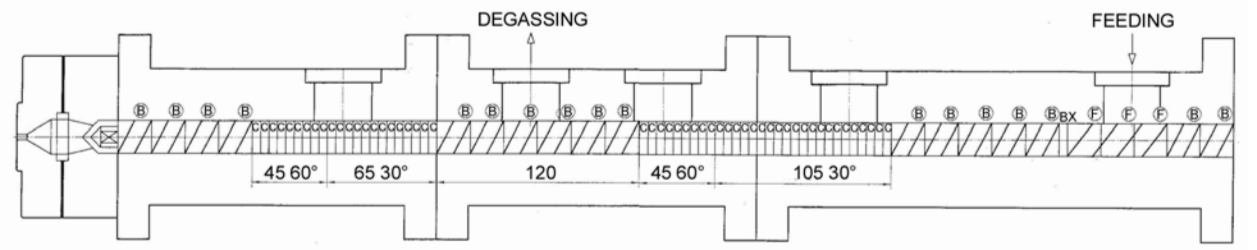

Figure 1. Screw profile of O.M.C. co-rotating intermeshing twin-screw extruder (L/D = 35, D =19 mm)

AG Munich, Germany) with Cu K_α radiation of wavelength of 0.1542 nm. A scanning rate of 10 deg/min^{-1} was used. The distances d_{001} between the silicate layers of the organoclay in the nanocomposite films were evaluated using the Bragg's equation $d_{001} = n\lambda/(2\sin\theta)$, where λ is the wavelength, θ is the incidence angle of the X-ray beam and n is an integer.

2.3.4. Transmission electron microscopy (TEM)

The analyses were carried out on the radial cross section for the film samples. Ultrathin films with thickness of about 100 nm for TEM observation were prepared by slicing the epoxy block containing PE nanocomposite films with a Leica Ultramicrotome (Leica Microsystems, Wetzlar, Germany). The ultra-thin films of the nanocomposite films were mounted on the holey carbon films on 300 mesh copper grids and then observed by JEOL JEM-2100 (Jeol Ltd., Tkyo, Japan) under accelerated voltage of 100 kV.

2.3.5. Rheological analysis

The rheological characterization, including measurements of complex viscosity was performed by using a Rheometric Scientific (Piscataway Township, NJ, USA) RDA II plate-plate rotational rheometer, operating at T = 180°C in the frequency range comprised between 0.1–500 rad/s.

2.3.6. Fourier transform infra-red analysis (FT-IR)

Fourier transform infra-red (FT-IR) spectra were evaluated using the Spectrum One Spectromoter by Perkin-Elmer (Weltham, MA, USA) and its Spectrum software. The spectra were obtained using 32 scans and a 4 cm^{-1} resolution. The powder samples were incorporated in KBr.

2.3.7. Nuclear magnetic resonance analysis (NMR)

^{13}C cross-polarization magic-angle spinning nuclear magnetic resonance (^{13}C de-coupled {^{1}H} CP-MAS NMR) spectra were obtained at room temperature on a Bruker Avance II 400 MHz (9.4 T) spectrometer (Bruker, Ettlingen, Germany) operating at 100.63 MHz for the ^{13}C nucleus with a MAS rate of 13 kHz for 1024 scans, a contact time of 1.5 μs, and a repetition delay of 1.5 ms.

3. Results and discussion

3.1. Rheological characterization

The viscosity measurements, in the frequencies range between 0.1–500 rad/s, were carried out and the flow curves are reported in Figure 2a. In general, the OMMT presence in the polymer matrix leads to a substantial viscosity increase in the whole frequencies region. Addition of adhesion promoters, in particular of PEgMA, further increases the complex viscosity, most sizeably, at the low frequencies values. Most interestingly the TEG presence, especially at low loadings (0.5 and 1 wt%), does not modify the rheological behaviour of the composites with their viscosity being substantially equal to that of the pristine polymeric matrix. Furthermore, the TEG presence, even at high loadings (4 and 5 wt%) leads to a much more pronounced decrease of the complex viscosity. The TEG additive has a very low viscosity, see 2.1, and obviously by increasing the TEG presence, the complex viscosity of the formulated nanocomposites decreases. In Figure 2b the flow curves of all investigated materials in high frequencies region are reported. The higher viscosity of PE/OMMT, in the range of 100–300 rad/s (typical shear rate range of extrusion operation) does not substantially worsen the processability of this material. The viscosity values of PE/

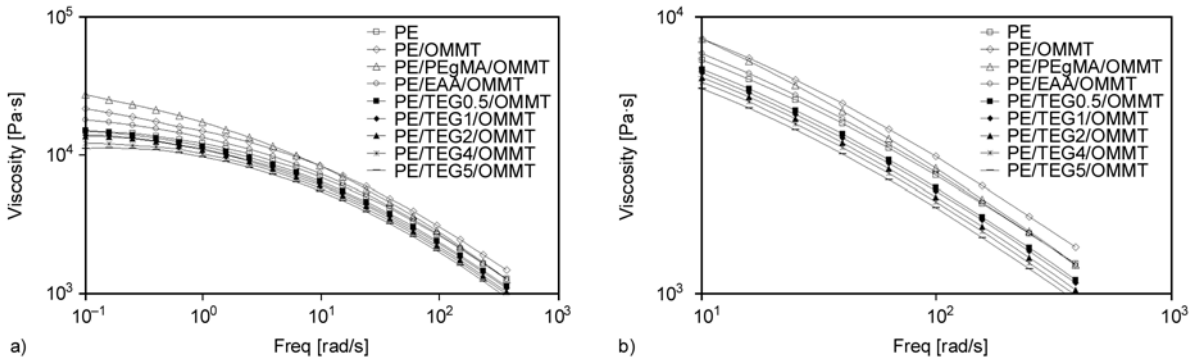

Figure 2. Complex viscosity of all the investigated materials

gMA/OMMT and PE/EAA/OMMT nanocomposites are, at higher frequencies, close to those of the unfilled polyethylene PE, and a comparable processability obtains. By contrast TEG, at high loadings, exerts a clear lubricating effect, while at low content, no modification of the processability was observed.

3.2. Mechanical characterization

In Figures 3–5, the mechanical properties, in particular, the elastic modulus, *E*, tensile strength, TS, and elongation at break, EB, are reported, in both the machine (MD) and transverse (TD) directions for polyethylene films (PE), either pristine or containing 5 wt% of organically modified montmorillonite (PE/OMMT), alone or together with adhesion promoters such as 5 wt% of maleic anhydride grafted polyethylene (PE/PEgMA/OMMT), of ethylene-acrylic acid copolymer (PE/EAA/OMMT) or of dispersing additives such as polar wax (PE/TEG%/OMMT) at different concentrations (0.5, 1, 2, 4 and 5 wt%). The obtained results suggest that the presence of OMMT nano-particles in the composite leads to an increase of the elastic modulus with no changes, or in some systems a slight decrease, in the ultimate properties, in keeping with what already reported in the literature [5–9]. In general, in order to obtain a better dispersion of the OMMT nano-particles and achieve good performances, use of dispersing additives and/or adhesion promoters is required [10–12, 14].

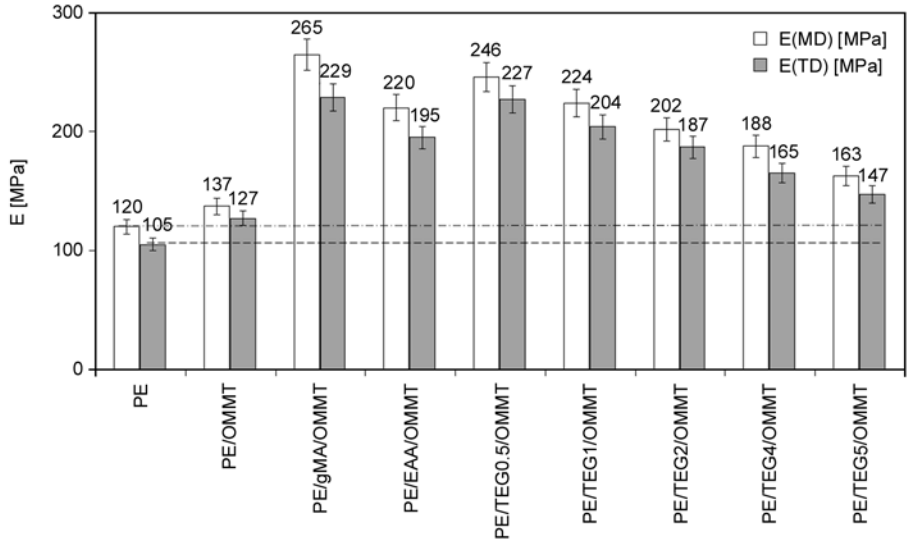

Figure 3. Elastic modulus of pristine PE film and PE/OMMT film without and with different dispersing additives in both machine (MD) and transverse (TD) directions

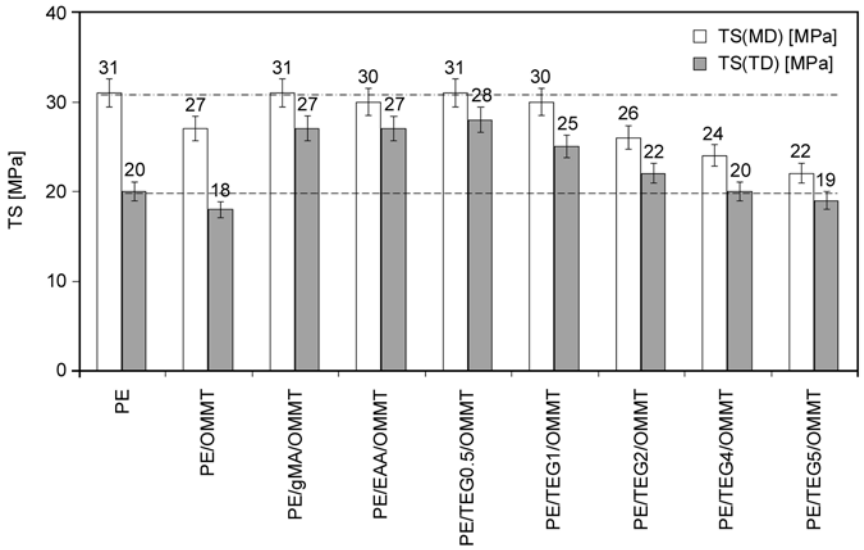

Figure 4. Tensile strength of pristine PE film and PE/OMMT film without and with different dispersing additives in both machine (MD) and transverse (TD) directions

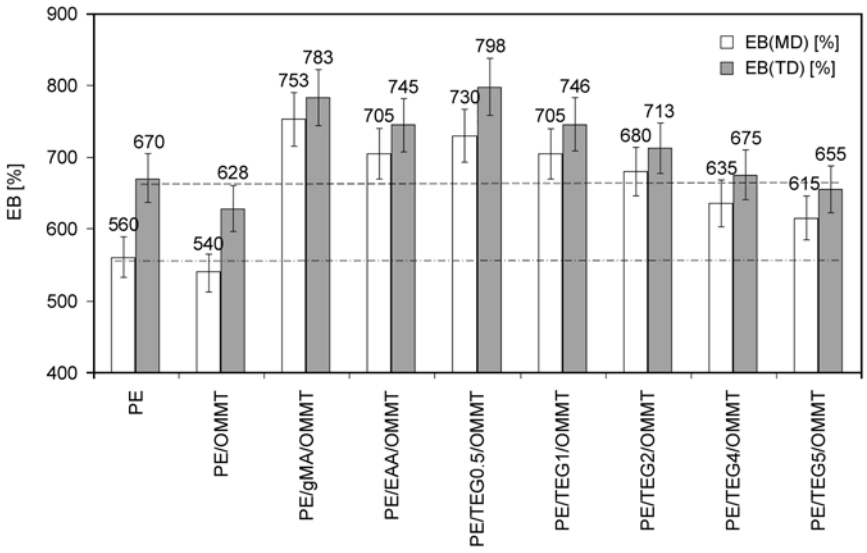

Figure 5. Elongation at break of pristine PE film and PE/OMMT film without and with different dispersing additives in both machine (MD) and transverse (TD) directions

It is interesting to note that the values of all the mechanical properties of films containing 5 wt% of PEgMA or 5 wt% of EAA are practically the same of films containing only 0.5 wt% of TEG. Increasing the concentration of TEG to 1 and 5 wt% does not produce further improvement of the films mechanical performances. It must also be noted that at high TEG loading, the films rigidity and properties at break drop. In particular, the elastic modulus of the PE/TEG5/OMMT film, in both the machine and transverse directions, decreases by about 50% with respect to the value of the PE/TEG0.5/OMMT film, even though the value is always higher than those of the pristine PE and PE/OMMT films. In parallel, a reduction of the tensile strength is observed upon a tenfold increase (i.e. to 5 wt%) of the TEG concentration. On the other hand at the higher concentration of TEG (e.g. 4 and 5 wt%) the elongation at break, EB, does not seem to increase.

Interestingly the inspection of the measured mechanical properties reveals that major improvements obtain at the lowest TEG loading, i.e. 0.5 wt%, and that the mechanical behaviour of the PE/TEG0.5/OMMT film is very similar, in both the machine and transverse directions, to that of both PE/PEgMA/OMMT and PE/EAA/OMMT films containing higher amounts (up to one order of magnitude) of either dispersing or compatibilizing agents.

Furthermore, no benefits are obtained in the film formulation for high TEG loading (see all discussed results).

This are, indeed, interesting results and the render the use of TEG, as a new dispersing additive and/or adhesion promoter, particularly advantageous in some film formulations given the low loading values required. Further confirmation of such envisioned advantages comes also from the analysis of the observed rheological changes reported and discussed in section 3.1.

3.3. Analysis of TEG by Fourier transform infra-red spectroscopy (FT-IR) and nuclear magnetic resonance (NMR)

The FT-IR and NMR analysis of the TEG sample was performed and the spectra are reported in Figures 6 and 7, respectively. In the FT-IR spectra different characteristic absorption areas were identified, in particular:

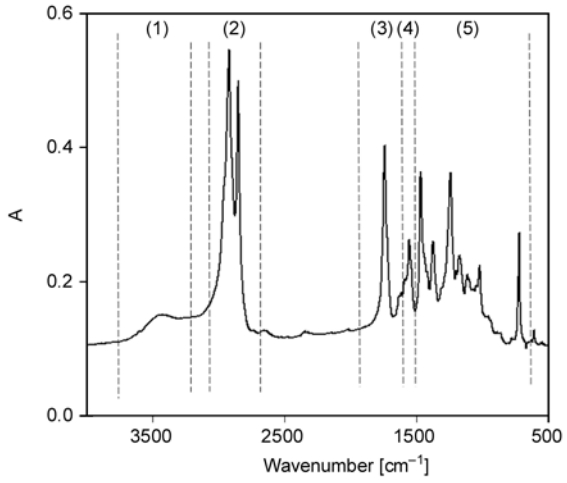

Figure 6. FT-IR spectra of TEG sample (in KBr)

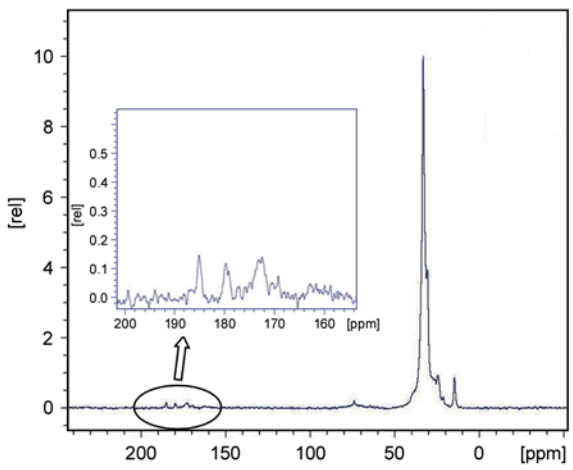

Figure 7. NMR analysis

Area 1: hydroxyl group region (3200–3700 cm^{-1}). The broad peaks in the spectra suggest the presence of hydroxyl bonds.

Area 2: C–H stretching in the alkanes (3000–2800 cm^{-1}). The TEG spectra shows well distinct absorption peaks at about 2918 cm^{-1} and about 2844 cm^{-1} due to the asymmetrical and symmetrical stretching vibration of the methylene groups, respectively.

Area 3: carbonyl region (1900–1600 cm^{-1}). The TEG spectra shows well distinct peak at 1738 cm-1 due to the presence of COX functional groups.

Area 4 (1640–1500 cm^{-1}): The TEG spectra reveals the presence of well a distinct peak at 1553 cm^{-1} due to the presence of secondary acyclic amides (–CONH); the absorption involves the coupling of the N–H bending and C–N stretching vibrations.

Area 5 (< 1500 cm^{-1}): The spectra show absorption peaks at about 1466 and 1370 cm^{-1} due to the in-plane bending and symmetric bending vibrations of methyl groups. Moreaover, a well distinct peak at 719 cm^{-1} is visible, due to the in-plane bending of the methylene groups.

The NMR analysis confirms the above FT-IR analysis. In particular, the well distinct peaks in the spectra at < 50 ppm can be attributed to the presence of numerous $–CH_2–$ and $–CH_3$ groups. The small peak between 50 and 100 ppm is due to the carbon atoms carrying hydroxyl groups. Furthermore, the small peaks between 150 and 200 ppm reveal the presence of amide and carboxyl groups.

The large amounts of methylene groups, confirmed by both analyses, suggest that TEG is a low molecular weight sample, according to the rheological data (see experimental part, i.e. description of the used materials).

The accurate FT-IR and NMR analyses suggest the presence of amides and carboxyl functionalities on the low molecular aliphatic chains in TEG polar wax structure.

3.4. Morphological analysis

3.4.1. X-ray analysis

In Figure 8, the X-ray traces of pristine OMMT, pristine TEG, PE/OMMT and PE/additive/OMMT, with of different dispersing additives are plotted, and Table 2 reports the interlayer distances of the investigated films, calculated using the Bragg's formula. All the OMMT-films show increased interlayer distance (main diffraction peak), with respect to the interlayer distance obtained for the pristine OMMT film. The latter film shows a secondary diffraction peak between 6 and 8 degrees, that is much smaller in the PE/OMMT system. The main peaks of PE/PEgMA/OMMT and PE/EAA/OMMT films are shifted to the left and the calculated interlayer distances are 3.56 and 3.37 nm, respectively. The presence of both compatibilizers leads to a decrease of the main peak intensity, see Figure 8a, that is more pronounced than that observed for the weakly intercalated PE/OMMT sample. As well known, the absence of the diffraction peak in X-ray trace suggests the presence of exfoliated clay morphology.

It is very interesting to highlight that the presence of TEG leads to an increase of the interlayer distance than the PE/OMMT sample but at high loadings, i.e. 1 and 5 wt%, the diffraction intensities significantly increase and the peaks are very intense, see Figure 8b. Furthermore, the sample PE/T0.5/OMMT shows lower diffraction intensity than the PE/OMMT one and this diffraction trace is similar

Table 2. Main peaks and calculated interlayer distance, using the Bragg's formula, of the investigated nanocomposite films

Sample	Main peak, 2θ	d_{001} [nm]
Cloisite® 15A	2.80	3.15
PE/OMMT	2.67	3.30
PE/PEgMA/OMMT	2.48	3.56
PE/EAA/OMMT	2.62	3.37
PE/TEG0.5/OMMT	2.58	3.42
PE/TEG1/OMMT	2.50	3.53
PE/TEG4/OMMT	2.42	3.65
PE/TEG5/OMMT	2.35	3.76
Tegomer® E525	1.85	4.77

to the trace obtained for the samples compatibilized with PEgMA and PEgAA.

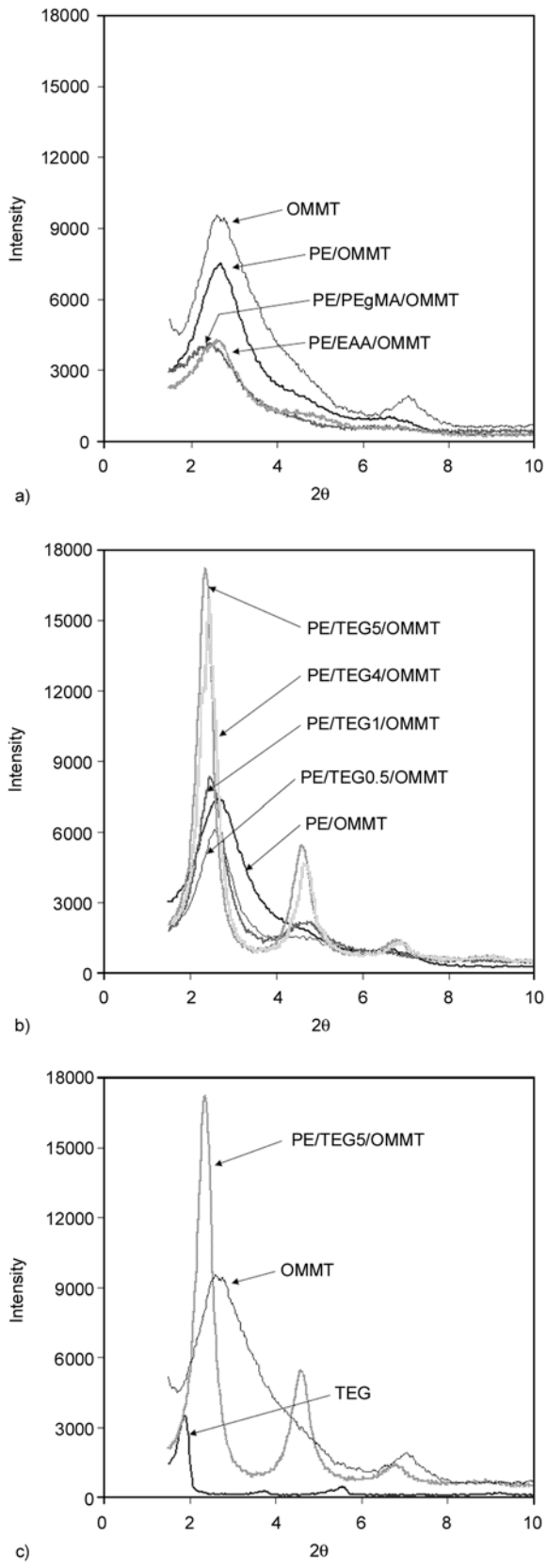

Figure 8. X-ray diffraction trace of all the investigated samples

In order to better understand the effect of the amphiphilic block co-polymer presence on the increase of the diffraction intensity, the X-ray analysis on the pristine TEG was performed. In Figure 8c, the X-ray trace of the pristine TEG, pristine OMMT and PE/TEG5/OMMT samples were shown. It is evident that the clay morphology modification occurs because of the polar wax (i.e. TEG) presence, given the very intense peaks and the increase in the intensity for PE/TEG5/OMMT sample. It seems that the small polar wax chains (having very low viscosity values, as reported in the experimental part), by strong interaction with the organic modifier, are able to penetrate the clay layers (the interlayer distance increase), but are not able to separate the layers into the clay tactoids, see Figure 9. Considering the strongly polar nature of the amphiphilic block co-polymer chains, it also could be hypothesized that the presence of wax chaina in the clay galleries inhibits the penetration of the polyethylene chains into the tactoid galleries; a similar hypothesis was made by Luyt and Geethamma [25]. In order to better explain the hypothesis of the easier intercalation into the clay galleries, but no exfoliation ability, of the TEG amphiphilic block co-polymer molecules than the PEgMA or EAA long polymeric chains, in Figure 9, the possible formation clay morphology in the nanocomposites is shown. Really, the penetration of PEgMA, partially EAA

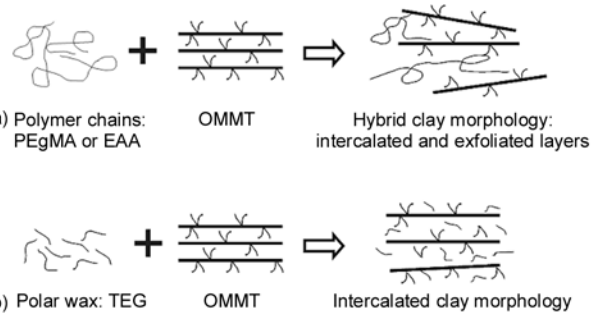

Figure 9. Clay morphology of PE/OMMT with different dispersing additives: (a) Formation of hybrid clay morphology, i.e. the PEgMA or EAA polymer chains are able to intercalate and in some cases to exfoliate the clay layers. The intercalation ability only of matrix chains, i.e. PE polymer chains, is very reduced, as well know. (b) Formation of preferentially intercalated morphology due to the reduced ability of the TEG molecules to separate the clay layers. The TEG molecules are high penetration ability considering their polar nature but reduced ability in layer separation due to their small dimension.

chains and PE macromolecules, during melt processing explains the intercalation effect and considering the specific intrinsic properties and nature explain also the exfoliation effect, i.e. that the long polymer chains are able to delaminate the tactoids. While the TEG molecules, having polar nature and small dimension are able to intercalate the clay tactoids during melt processing, in particular at high TEG loading, and the penetration of the PE chains into clay galleries are not favoured.

Furthermore, the physically-absorbed organic modifier on the clay particles surface it is likely to promote, especially at high TEG loading (e.g. 4 and 5 % wt.), the cluster formation of clay particles (see 3.4.2), by interaction among the wax polar groups, and, this would further inhibit the otherwise beneficial penetration of the polyethylene chains into the clay platelets that would improve the mechanical properties of the films.

3.4.2. Transmission electron microscopy analysis (TEM)

The TEM analysis of PE/OMMT (a), PE/PEgMA/OMMT (b), PE/TEG0.5/OMMT (c) and PE/TEG5/OMMT (d) films was carried out and the micrographs are reported in Figure 10. The PE/OMMT sample shows the presence in the system of clay clusters with dimensions larger than 200 nm. The isolated platelets are not visible, suggesting that the clay morphology is predominantly intercalated, in accord with the X-ray analysis results. The PE/PEgMA/OMMT sample shows clay tactoids with much smaller dimensions, and also a large number of isolated clay platelets are clearly visible, see Figure 10b. The presence of some tactoids leads to appearance of the diffraction peaks in the X-ray trace and the clay morphology is hybrid with a large number of exfoliated platelets.

The discussion about the clay morphology in the samples additivated with TEG, appears to be more complex. In fact, the micrographs of both investigated samples, i.e. PE/TEG0.5/OMMT (c) and PE/TEG5/OMMT (d) respectively, show the presence of large clay clusters, whose dimensions become larger at high TEG loading. These observations are in agreement with the X-ray analysis, in particular, the chains of the polar wax are arranged between the platelets of the clay and, due to their polar nature, significant particle re-aggregation occurs; this effect is, as noted above, more pronounced at highest TEG loading. Furthermore, it is reasonable to expect that the at high(er) TEG loadings some polar wax chains are also present on the external surface of the tactoids and this would promote, by polar-polar groups interaction, the clay particles re-aggregation.

In fact, the PEgMA presence leads to a formation of a large number exfoliated platelets and consequently the rigidity of the system increases without ductility loss. Moreover, the TEG presence leads to the formation of predominantly intercalated clay structures but at high loadings leads to some re-aggregation of the intercalated clay tactoids, most likely by association between the polar groups of TEG. It would then seem that this new morphology could be responsible for the observed worsening in the mechanical behaviour with respect to the PEgMA and EAA compatibilized samples; especially, at high TEG loading. At low TEG loading, i.e. 0.5 wt%, the polar wax chains are mainly intercalated into the tactoids and the re-aggregation particle process is not significantly pronounced.

3.4.3. Scanning electron microscopy analysis (SEM)

In order to evaluate the system morphology variations at microscopic level, the SEM micrographs at two different magnifications of the investigated films are reported in Figure 11. The morphology of PE/OMMT sample, not containing compatibilizer or dispersing additives is not uniform and also a poor adhesion between the clay particles and the matrix is observed. Furthermore, on the liquid nitrogen fractured surface of the PE/OMMT film are clearly noticeable some clay particles/cluster having micrometric dimensions. Addition of PEgMA at the 5 wt%, significantly improves the film morphology. The beneficial effect imparted by low loading of TEG, i.e. 0.5 wt%, is clearly evident from the inspection of the reported SEM micrographs. The fractured surface of this film is uniform and no re-aggregated clay clusters are observed. Interestingly, by increasing the TEG loadings, i.e. 1, 4 and 5 wt%, the above reported morphology improvement is no longer observed as seen in the reported micrographs, and these remarks are in full agreement with the observed differences in mechanical behaviour and other morphological analyses.

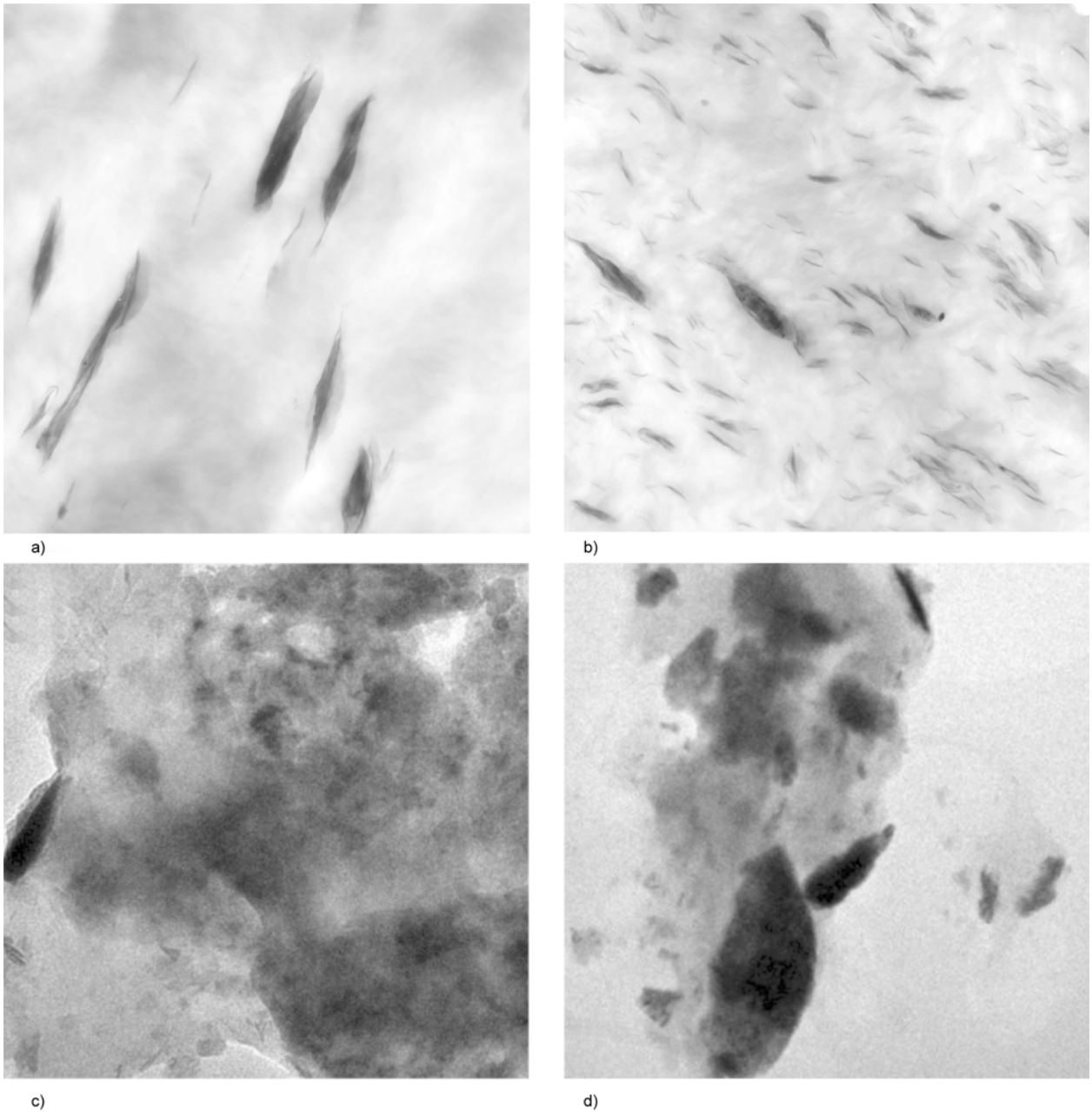

Figure 10. TEM micrographs of the investigated PE/OMMT (a), PE/PEgMA/OMMT (b), PE/TEG0.5/OMMT (c) and PE/TEG5/OMMT (d) films

4. Conclusions

In this work, a polar wax was used as dispersing additive in PE/OMMT film preparation with the aim of modifying, and possibly improving, the dispersion of an organically modified nanoclay (OMMT) in a PE matrix at relatively low loading levels. The obtained results suggest that the macroscopic properties of the films observed when the polar wax (TEG) was added at low concentration, i.e. 0.5 wt%, are similar to those obtained by adding PEgMA and EAA compatibilizers at 5 wt%. Furthermore, by increasing the TEG loading, i.e. 1–5 wt%, no improvement of the macroscopic performance was observed. At the higher loading levels the low molecular weight and polar nature of TEG chains promote its arrangement into the galleries of the organically modified clay and this somewhat hinders the polymer chains intercalation between the clay layers, with no improvement of the PE film mechanical and thermal properties. The obtained results suggest that the amphiphilic dispersing agent, at low loading levels, may advantageously be used as an alternative to PEgMA and EAA compatibilizers in the formulation of nanocomposite poly-

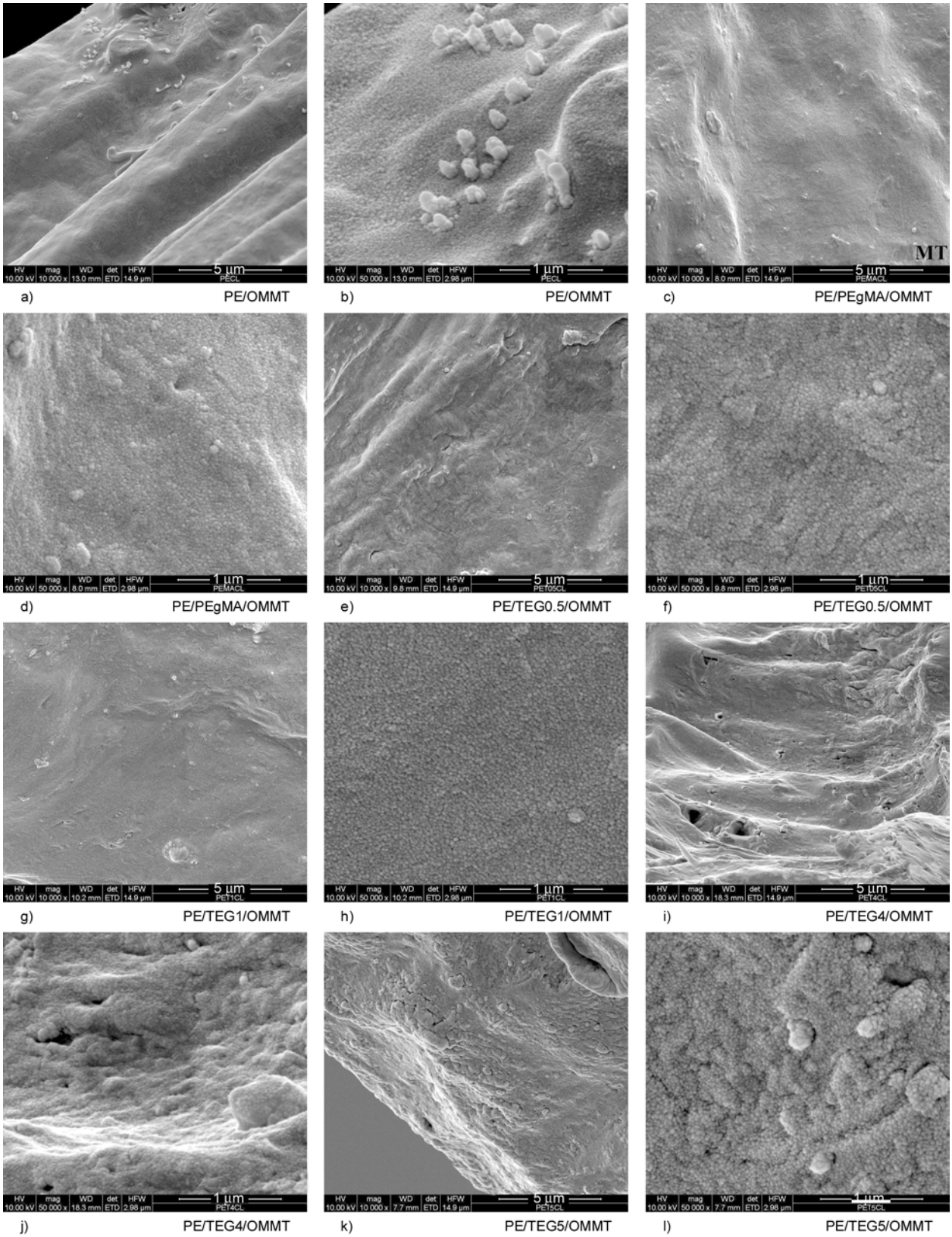

Figure 11. SEM micrographs at two different magnifications (10 000× and 50 000×) of the investigated films

olefin films, and its use would allow obtaining similar macroscopic performance improvement at substantially lower loading levels.

Acknowledgements

V.M. thanks Evonik Goldschmidt Italia s.r.l for kindly providing sample of Tegomer® E 525 polar wax.

References

[1] Alexandre M., Dubois P.: Polymer-layered silicate nanocomposites: Preparation, properties and uses of a new class of materials. Materials Science and Engineering R: Reports, **28**, 1–63 (2000).
DOI: 10.1016/S0927-796X(00)00012-7

[2] Pinnavaia T. J., Beall G. W.: Polymer-clay nanocomposites. Wiley, Chichester (2000).

[3] Ren J., Silva A. S., Krishnamoorti R.: Linear viscoelasticity of disordered polystyrene−polyisoprene block copolymer based layered-silicate nanocomposites. Macromolecules, **33**, 3739–3746 (2000).
DOI: 10.1021/ma992091u

[4] Dennis H. R., Hunter D. L., Chang D., Kim S., White J. L., Cho J. W., Paul D. R.: Effect of melt processing conditions on the extent of exfoliation in organoclay-based nanocomposites. Polymer, **42**, 9513–9522 (2001).
DOI: 10.1016/S0032-3861(01)00473-6

[5] Krishnamoorti R., Ren J., Silva A. S.: Shear response of layered silicate nanocomposites. Journal of Chemical Physics, **114**, 4968–4973 (2001).
DOI: 10.1063/1.1345908

[6] Ray S. S., Okamoto M.: Polymer/layered silicate nanocomposites: A review from preparation to processing. Progress in Polymer Science, **28**, 1539–1641 (2003).
DOI: 10.1016/j.progpolymsci.2003.08.002

[7] Hotta S., Paul D. R.: Nanocomposites formed from linear low density polyethylene and organoclays. Polymer, **45**, 7639–7654 (2004).
DOI: 10.1016/j.polymer.2004.08.059

[8] Zeng Q. H., Yu A. B., Lu G. Q., Paul D. R.: Clay-based polymer nanocomposites: Research and commercial development. Journal of Nanoscience and Nanotechnology, **5**, 1574–1592 (2005).
DOI: 10.1166/jnn.2005.411

[8] La Mantia F. P., Dintcheva N. T., Filippone G., Acierno D.: Structure and dynamics of polyethylene/clay films. Journal of Applied Polymer Science, **102**, 4749–4758 (2006).
DOI: 10.1002/app.25009

[9] Zhang M., Sundararaj U.: Thermal, rheological, and mechanical behaviors of LLDPE/PEMA/clay nanocomposites: Effect of interaction between polymer, compatibilizer, and nanofiller. Macromolecular Materials and Engineering, **291**, 697–706 (2006).
DOI: 10.1002/mame.200500399

[10] Durmus A., Kasgoz A., Macosko C. W.: Linear low density polyethylene (LLDPE)/clay nanocomposites. Part I: Structural characterization and quantifying clay dispersion by melt rheology. Polymer, **48**, 4492–4502 (2007).
DOI: 10.1016/j.polymer.2007.05.074

[11] Sánchez-Valdes S., López-Quintanilla M. L., Ramírez Vargas E., Medellín-Rodríguez F. J., Gutierrez-Rodriguez J. M.: Effect of ionomeric compatibilizer on clay dispersion in polyethylene/clay nanocomposites. Macromolecular Materials and Engineering, **291**, 128–136 (2006).
DOI: 10.1002/mame.200500330

[12] Shah R. K., Hunter D. L., Paul D. R.: Nanocomposites from poly(ethylene-*co*-methacrylic acid) ionomers: Effect of surfactant structure on morphology and properties. Polymer, **46**, 2646–2662 (2005).
DOI: 10.1016/j.polymer.2005.01.062

[13] Filippi S., Marazzato C., Magagnini P., Minkova L., Dintcheva N. T., La Mantia F. P.: Organoclay nanocomposites from ethylene–acrylic acid copolymers. Macromolecular Materials and Engineering, **291**, 1208–1225 (2006).
DOI: 10.1002/mame.200600217

[14] Filippi S., Dintcheva N. T., Scaffaro R., La Mantia F. P., Polacco G., Magagnini P.: Effects of organoclay on morphology and properties of nanocomposites based on LDPE/PA-6 blends without and with SEBS-*g*-MA compatibilizer. Polymer Engineering and Science, **49**, 1187–1197 (2009).
DOI: 10.1002/pen.21361

[15] Xu Y., Fang Z., Tong L.: On promoting intercalation and exfoliation of bentonite in high-density polyethylene by grafting acrylic acid. Journal of Applied Polymer Science, **96**, 2429–2434 (2005).
DOI: 10.1002/app.21708

[16] Pavliková S., Thomann R., Reichert P., Mülhaupt R., Marcinčin A., Borsig E.: Fiber spinning from poly (propylene)–organoclay nanocomposite. Journal of Applied Polymer Science, **89**, 604–611 (2003).
DOI: 10.1002/app.11870

[17] Zhai H., Xu W., Guo H., Zhou Z., Shen S., Song Q.: Preparation and characterization of PE and PE-g-MAH/montmorillonite nanocomposites. European Polymer Journal, **40**, 2539–2545 (2004).
DOI: 10.1016/j.eurpolymj.2004.07.009

[18] Wang Y., Chen F-B., Li Y-C., Wu K-C.: Melt processing of polypropylene/clay nanocomposites modified with maleated polypropylene compatibilizers. Composites Part B: Engineering, **35**, 111–124 (2004).
DOI: 10.1016/S1359-8368(03)00049-0

[19] Liang G., Xu J., Bao S., Xu W.: Polyethylene/maleic anhydride grafted polyethylene/organic-montmorillonite nanocomposites. I. Preparation, microstructure, and mechanical properties. Journal of Applied Polymer Science, **91**, 3974–3980 (2004).
DOI: 10.1002/app.13612

[20] Mlynarčíková Z., Kaempfer D., Thomann R., Mülhaupt R., Borsig E., Marcinčin A.: Syndiotactic poly (propylene)/organoclay nanocomposite fibers: Influence of the nano-filler and the compatibilizer on the fiber properties. Polymers for Advanced Technologies, **16**, 362–369 (2005).
DOI: 10.1002/pat.602

[21] Chow W. S., Abu Bakar A., Mohd Ishak Z. A., Karger-Kocsis J., Ishiaku U. S.: Effect of maleic anhydride-grafted ethylene–propylene rubber on the mechanical, rheological and morphological properties of organoclay reinforced polyamide 6/polypropylene nanocomposites. European Polymer Journal, **41**, 687–696 (2005).
DOI: 10.1016/j.eurpolymj.2004.10.041

[22] Lee J-H., Jung D., Hong C-E., Rhee K. Y., Advani S. G.: Properties of polyethylene-layered silicate nanocomposites prepared by melt intercalation with a PP-g-MA compatibilizer. Composites Science and Technology, **65**, 1996–2002 (2005).
DOI: 10.1016/j.compscitech.2005.03.015

[23] Dintcheva N. T., Marino R., La Mantia F. P.: The role of the matrix-filler affinity on morphology and properties of polyethylene/clay and polyethylene/compatibilizer/clay nanocomposites drawn fibers. e-Polymers, no. 054 (2009).

[24] Durmuş A., Woo M., Kasgöz A., Macosko C. W., Tsapatsis M.: Intercalated linear low density polyethylene (LLDPE)/clay nanocomposites prepared with oxidized polyethylene as a new type compatibilizer: Structural, mechanical and barrier properties. European Polymer Journal, **43**, 3737–3749 (2007).
DOI: 10.1016/j.eurpolymj.2007.06.019

[25] Luyt A. S., Geethamma V. G.: Effect of oxidized paraffin wax on the thermal and mechanical properties of linear low-density polyethylene–layered silicate nanocomposites. Polymer Testing, **26**, 461–470 (2007).
DOI: 10.1016/j.polymertesting.2006.12.015